A COMPARISON OF THE CONVERSION OF ISOPROPYL ALCOHOL BY NON-THERMAL PLASMA AND THERMALLY- DRIVEN CATALYSIS USING IN-SITU FTIR SPECTROSCOPY

Thesis submitted by:

ZEINAB TALIB ABDULWAHHAB MASHHADANI

For the degree of Doctor of Philosophy

Newcastle University

School of Engineering

November 2018

Declaration

I hereby declare that this thesis entitled ‘‘A COMPARISON OF THE CONVERSION OF ISOPROPYL ALCOHOL BY NON-THERMAL PLASMA AND THERMALLY- DRIVEN CATALYSIS USING IN-SITU FTIR SPECTROSCOPY’’ is the result of experiments carried out in the School of Engineering at Newcastle University. No part of this thesis has been submitted for a degree or any other qualification at Newcastle University or any other institution.

Zeinab Talib Abdulwahhab Mashhadani

November 2018

Acknowledgements

First and foremost I would like to thank my supervisor Prof. Paul A. Christensen for his supervision, knowledge, friendship, guidance and support throughout my project, without which this work would not have been possible. I could not have asked for a better supervisor than him.

I would like to thank my secondary supervisor Prof. Adam Harvey for the regular discussions and support during my project.

Secondly, I would like to thank Government of Iraq for a Scholarship, the Higher Committee for Education Development in Iraq HCED-Iraq, the Iraq Ministry of Oil and Petroleum Research and Development Center PRDC for the opportunity to study for a Ph. D. and for their financial support and Newcastle University for the invaluable support received during this research.

I would like to thank all of the members of Christensen Research Group, Dr. Abdullah Al-abduly, Dr. Pierrot Attidekou, Dr. Supandee Manelok, Halim Bin Md Ali and Ndubuisi Eje for their friendship throughout my studies.

Thanks also must go to Mr. Neville Dickman for his support during the in-situ FTIR NTP cells fabrication and Simon Daley for electronic work.

Finally, but by no means least, a very special thanks must go to my dad and my late mum, my husband, my kids, my sister and brother, my aunts and my husband's family for their love, support and encouragement that helped me to reach the end of this work. This thanks also extended to all members in PRDC.

List of Publications

Work published

1. Christensen, P.A., Mashhadani, Z.T.A.W, Md Ali, A.H.B., Carroll, M.A. and Martin, P.A., 2018. The Production of Methane, Acetone,"Cold" CO and Oxygenated Species from IsoPropyl Alcohol in a Non-Thermal Plasma: An In-situ FTIR Study. *The Journal of Physical Chemistry A*, *122*(17), pp.4273-4284.
2. Christensen, P.A., Mashhadani, Z.T.A.W. and Ali, A.H.B.M., 2018. In situ FTIR studies on the oxidation of isopropyl alcohol over SnO_2 as a function of temperature up to 600 °C and a comparison to the analogous plasma-driven process. *Physical Chemistry Chemical Physics*, *20*(14), pp.9053-9062.
3. Christensen, P.A., Ali, A.H.B.M., Mashhadani, Z.T.A.W. and Martin, P.A., 2018. A direct Fourier transform infrared spectroscopic comparison of the plasma-and thermally-driven reaction of CO_2 at Macor. *Plasma Chemistry and Plasma Processing*, *38*(2), pp.293-310.
4. Christensen, P.A., Ali, A.H.B.M., Mashhadani, Z.T.A.W., Carroll, M.A. and Martin, P.A., 2018. The Production of Ketene and C_5O_2 from CO_2, N_2 and CH_4 in a Non-thermal Plasma Catalysed by Earth-Abundant Elements: An In-situ FTIR Study. *Plasma Chemistry and Plasma Processing*, *38*(3), pp.461-484.

To be published

An in-situ FTIR Study of the Plasma- and Thermally-Driven Reaction of Isopropyl Alcohol at CeO_2 and a Comparison with the Analogous Processes at SnO_2 and Macor.

Posters and oral presentation

1. An in-situ FTIR Study of the Thermal-and Plasma-Driven Remediation of Isopropyl Alcohol, CEAM PG research conference held in Newcastle University at 2016 (poster).
2. The production of methane, acetone, "cold" CO and oxygenated species from isopropyl alcohol in a non thermal plasma: an in-situ FTIR study, CEAM PG research conference held in Newcastle University at 2017 (oral presentation).

3. The production of methane, acetone, “cold” CO and oxygenated species from isopropyl alcohol in a non thermal plasma: an in-situ FTIR study, IChemE Catalysis Special Interest Group Event: Unconventional Activation of Catalysts- Fundamentals and Applications held in Manchester University on Thursday 28 June 2018 (poster).

Awards

1. Second best poster at the PG chemical engineering CEAM conference held in Newcastle University at 2016.
2. Best poster at the IChemE Catalysis Special Interest Group Event: Unconventional Activation of Catalysts- Fundamentals and Applications held in Manchester University on Thursday 28 June 2018.

Abstract

In-situ Non-Thermal Plasma (NTP) InfraRed (IR) transmission and reflectance cells were designed, fabricated, modified and commissioned in order to facilitate the study of the catalysed NTP conversion of IsoPropyl Alcohol (IPA). IPA was chosen as the model compound because of its relevance to domestic air pollution and the significant body of infrared data on the reaction of the compound in thermal and NTP systems. As catalyst selection for NTP systems has often been made based on those materials active in the analogous thermal systems, the NTP experiments were supported by studies employing a Diffuse Reflectance Infrared Fourier Transform system and a commercial environmental chamber capable of being heated up to 600 °C in a controlled atmosphere.

The initial studies focussed on Macor, a ceramic comprising predominantly the oxides of Al, Mg and Si as they were intended to furnish benchmark data, as it was assumed that Macor would be inactive, but had a reasonable dielectric constant and was thermally stable. Macor did indeed prove inactive towards IPA on heating up to 600 °C: however, the material was highly active in the NTP process, with IPA reacting in the bulk of the plasma to produce acetone, which then reacted at the Macor to produce a polymer and isophorone. In addition, HCN, methane and cold CO, CO at ca. 115 K, were produced in the plasma bulk: the production of methane and cold CO was interpreted in terms of the fragmentation of acetaldehyde, produced but not directly observed, via a loose transition state.

SnO_2 and CeO_2 were also selected for study: in the former case primarily because of the wealth of IR data on the oxide from previous work in Newcastle, and the CeO_2 was selected for its known activity towards IPA and the concomitant IR data in the literature both from thermal and NTP studies.

IPA did not react in the plasma over SnO_2, but reacted to produce acetone and then CO_2 in the analogous thermal experiments. In contrast, IPA did react over CeO_2 in the plasma, giving the same products as with Macor and it also reacted at CeO_2 in the thermal experiments, to produce acetone and then CO_2, the products and their onset temperatures depending strongly on the pretreatment of the CeO_2 to remove adventitious adsorbed carbonates and bicarbonates. The NTP-driven process did not appear to be inhibited by these species.

Table of contents

List of Figures

List of Tables

List of Abbreviations

Nomenclature

A	The surface area of the dielectric / m^2
Å	Angstrom
A	Absorbance
Amps	Ampere
C	The total capacitance of the dielectric and gas /F
c	Concentration / M
C_d	The capacitance of the dielectric material between the two electrodes / F
C_g	The capacitance of the gas / F
cm	Centimetre
d	The gap width between electrodes / m
d	The thickness of the dielectric / m
dm	Decimetre
E	Electric field strength / Vm^{-1}
eV	Electron Volt
F	Farad
g	Gram
Hz	Hertz
I	The discharge current / Amps
K	Kelvin
kHz	KiloHertz
kV	KiloVolt
L	Optical path length / cm
M	Mega
m	Metre
M	Unit of concentration
m/z	mass-to-charge ratio
min	Minute
mm	Millimetre
nm	Nanometre
^oC	Celsius
P	Power / W
Pa	Pascal

pF	PicoFarad
ppm	Part per million
R	Reflectance of a sample at infinite depth
s	Second
S_R	Reference spectrum
Ss	Sample spectra
V	Volt
V_{max}	The discharge voltage / kV
V_{min}	The discharge onset voltage / kV
W	Watt
μm	Micrometre
μs	Microsecond

Greek symbols

λ	Wavelength
ε_g	Dielectric constant of background gas
ε_o	Vacuum permittivity / Fm^{-1}
ε_r	Dielectric constant
f	Discharge frequency
θ	Theta
Ω	Ohm
ε	Molar decadic extinction coefficient / M^{-1} cm^{-1}

Acronyms

AC	Alternating Current
APPJ	Atmospheric Pressure Plasma Jet
BOC	British Oxygen Company
CD	Coplanar Discharge
CPC	Combined Plasma Catalysis
DBD	Dielectric Barrier Discharge
DI	De-Ionised
DLaTGS	Deuterated Lanthanum alaine doped TriGlycine Sulphate
DRIFTS	Diffuse Reflectance Infrared Fourier Transform Spectroscopy
DTGS	Deuterated Tri-Glycine Sulfate
EHD	ElectroHydroDynamics

FTIR	Fourier Transform InfraRed
FWHM	Full Width at Half Maximum
HV	High Voltage
ICDD	International Centre for Diffraction Data
IPA	IsoPropyl Alcohol
IPC	In-Plasma Catalysis
IR	InfraRed
IVF	In-Vitro Fertilization
KM	Kubelka-Munk
LPGDR	Low Pressure Glow Discharge Reactor
MP	Microwave Plasma
MS	Mass Spectrometry
NTP	Non-Thermal Plasma
PACT	Plasma And Catalyst integrated Technologies
PBD	Packed Bed Discharge
PBP	Packed-Bed Plasma
PCD	Pulsed Corona Discharge
PDC	Plasma-Driven Catalysis
PEC	Plasma-Enhanced Catalysis
PPC	Post-Plasma Catalysis
PTFE	PolyTetraFluoroEthylene
RF	Radio Frequency
SBS	Sick Building Syndrome
SD	Surface Discharge
SOFCs	Solid Oxide Fuel Cells
SSPC	Single-Stage Plasma–Catalysis
TGA	ThermoGravimetric Analysis
TP	Thermal Plasma
US EPA	United States Environmental Protection Agency
UV	UltraViolet
VD	Volume Discharge
VOC	Volatile Organic Compound
WHO	World Health Organization
XRD	X-Ray Diffraction

Chapter 1. Introduction

This thesis reports work on the investigation of the non-thermal plasma driven, catalyzed remediation of IsoPropyl Alcohol (IPA) and to understand the chemistry of non-thermal plasma catalysis. IPA was chosen as a model of a Volatile Organic Compound (VOC). This chapter places the work in context, firstly producing an overview of VOCs and their effects on the environment and human health followed by a description of non-thermal plasma and then a review of the appropriate literature.

1.1. Volatile Organic Compounds

The term volatile organic compound refers to hydrocarbons having a low boiling point and high vapour pressure eg. ≥ 10 Pa at room temperature, one example of this type of compound is IPA with high vapour pressure around 5.3 KPa at 23.8 ºC [1][2].

VOCs are the most common air pollutants, and may be emitted from natural sources such as forest fires, vegetation, volcanoes and underground reservoirs of natural gas [3]. There are also four main categories of VOCs produced by human activities: (1) vehicles and aircraft; (2) organic solvents and products containing such solvents eg. paint, adhesive, domestic products, glue and inks; (3) production processes such as paper and food production, pharmaceutical, chemical and petrochemical industries eg. petrol storage and distribution, and (4) combustion processes [2][4].

VOCs are considered as a major source of the indoor pollution that can have detrimental effects on human health and the environment [5]. Thus, for example, VOCs are believed to be responsible for “Sick Building Syndrome” (SBS) [6] and, more recently, VOCs produced from cleaning agents have been postulated as having detrimental effects on pregnancy rates and adversely affecting the health of embryos in In-Vitro Fertilization (IVF) facilities [7][8].

With respect to SBS, it has been postulated that VOCs can be present in concentrations 2 to 5x higher in indoor air than in outdoor air [2]. Given that people spend 80-90 % of their lifetime indoor [9], then clearly VOCs have the potential to have a significant and detrimental effect upon human health. VOCs can be emitted from a variety of sources including: carpets, adhesives, solvents, cleaning products and wood products. as shown in table 1.1 [2][10][11].

Example of Household Products	Possible VOC Ingredients
Fuel containers or devices using gasoline, kerosene, fuel oil and products with petroleum distillates: paint thinner, oil-based stains and paint, aerosol or liquid insect pest products, mineral spirits, furniture polishes	BTEX (benzene, toluene, ethylbenzene, xylene), hexane, cyclohexane, 1, 2, 4-trimethylbenzene
Personal care products: nail polish, nail polish remover, colognes, perfumes, rubbing alcohol, hair spray	Acetone, ethyl alcohol, isopropyl alcohol, methacrylates (methyl or ethyl), ethyl acetate
Dry cleaned clothes, spot removers, fabric/leather cleaners	Tetrachloroethene (perchloroethene (PERC), trichloroethene (TCE))
Citrus (orange) oil or pine oil cleaners, solvents and some odor masking products	d-limonene (citrus odor), a-pinene (pine odor), isoprene
PVC cement and primer, various adhesives, contact cement, model cement	Tetrahydrofuran, cyclohexane, methyl ethyl ketone (MEK), toluene, acetone, hexane, 1, 1, 1-trichloroethane, methyl-iso-butyl ketone (MIBK)
Paint stripper, adhesive (glue) removers	Methylene chloride, toluene, older products may contain carbon tetrachloride
Degreasers, aerosol penetrating oils, brake cleaner, carburetor cleaner, commercial solvents, electronics cleaners, spray lubricants	Methylene chloride, PERC, TCE, toluene, xylene, methyl ethyl ketone, 1, 1, 1-trichloroethane
Moth balls, moth flakes, deodorizers, air freshers	1, 4-dichlorobenzene, naphthalene
Refrigerant from air conditioners, freezers, refrigerators, dehumidifiers	Freons (trichlorofluoromethane, dichlorodifluoromethane)
Aerosol spray products for some paints, cosmetics, automotive products, leather treatments, pesticides	Heptane, butane, pentane
Upholstered furniture, carpets, plywood, pressed wood products	Formaldehyde

Table 1.1. A summary of possible sources of Volatile Organic Compounds (VOCs) in commonly used products [11].

The health effects of exposure to IPA as an example of VOC vary from symptoms such as eye, noise and throat irritation, headache and dizziness, see table 1.2 [12], to serious health problems such as miscarriages, damage to the immune system of infants and children, damage to the liver, kidneys and central nervous system, as well as causing cancer when exposed to VOCs such as acetone and benzene on a daily basis at higher concentrations[2].

Type	Sources	Effects
CO	Heavy smoke areas, parking garages, from air intakes near heavy traffic roads	Headaches, dizziness
NO_x	Heavy smoke areas, parking garages, from air intakes near heavy traffic roads	Eye and throat irritations
O_3	Copy machines	Coughing, headaches, eye and throat irritations
Bacteria residues	Humidifiers, drainage pans of air conditioners	Various medical problems
VOC	Furniture-pressed wood, wallpaper, carpet, drapery, caulking, floor covering, felt tip markers	Headaches, dizziness, sore throats

Table 1.2. The potential effects of exposure to several examples of air pollutants [12].

As a consequence of the various harmful effects of VOCs on human health and the environment, various organizations in the world, for example the World Health Organization (WHO), the United States Environmental Protection Agency (US EPA) and the French Indoor Air Quality Observatory, have reported the statistics on VOC related deaths over the last few years [9] (and references therein). For example, WHO reported in 2012 that more than 7 million people (11.6 % of all global deaths) died due to indoor and outdoor air pollution, 4.3 millon of these deaths due to poor indoor air quality related to VOCs. In addition, in September 2016, a WHO report stated that more than 92 % of the people in the world live in areas exposed to air containing pollutants that exceed the WHO limits [13]. Furthermore, in May 2018, they reported that ca.17 % of adult lung cancer deaths, especially in women, were due to exposure to household air pollution emitted from cooking processes such as kerosene or solid fuels like wood, charcoal or coal [13].

In 2007, the French Indoor Air Quality Observatory published a study of indoor air quality for the first time based on a survey that covered 700 houses in France. The report stated that ca.

80-90 % of these houses had significant levels of aldehydes and hydrocarbons, and the latter are considered to be the most harmful type of pollutant [14].

There are different standards for air quality published by different environmental organizations and limits on the release of the common hazards that include VOCs [6].

There are different technologies available for VOC abatement, depending on parameters such as the type, concentration and the flow rate of the pollutant. The traditional techniques include thermal oxidation, catalytic oxidation, photocatalysis, adsorption, absorption, biofiltration, condensation and membrane separation [15][16]. However, these methods have various disadvantages eg: the generation of unwanted byproducts such as NOx, catalytic deactivation and poisoning with time, sensitivity to temperature and the need to sterilize the environment such as when employing biofiltration processes. In addition, some of these methods are not economically feasible, especialy when dealing with low concentrations of VOCs, eg. lower than 1 ppm [2][6][15].

Non-Thermal Plasma (NTP) could be an alternative method for VOC removal as it has several advantages over the other more traditional methods eg: it can be generated at atmospheric pressure and normal temperature, simple cell design and simple to scale up [17]. However, NTP technology may lead to the generation of harmful byproducts that could be more dangerous to human health and the environment than the initial VOCs such as HCN and NOx. In addition, NTP is costly in terms of energy when employed without a catalyst [2][17].

1.2. Principles of plasma

1.2.1. Plasma definition and occurrence

Plasma is widely regarded as the fourth state of matter and is characterized by the presence of atoms, molecules, ions, electrons and radicals having internal energies (with the exception of the electrons) unevenly distributed over the three degrees of freedom [18] as shown in fig. 1.1 [19].

Plasma can be considered as electrically conductive and sensitive to magnetic fields [20][21]. Plasma forms 99 % of the matter in the universe and is found in nature, for example: the sun, lightning and the Aurora Borealis [22][23], see fig. 1.2.

One of the most interesting examples of natural plasma is the Aurora Borealis, see fig. 1.2(b), which occurs when the streams of charged particles in the solar wind enter the earth's magnetic field, which is denser near the poles and this produces the Aurora. Lightning is another example of natural plasma see fig. 1.2(c), which is caused when the accumulation of charged particles inside clouds result in a large potential difference between the clouds and the earth: this essentially creates a plasma prior to lightning arcing between the clouds and the earth.

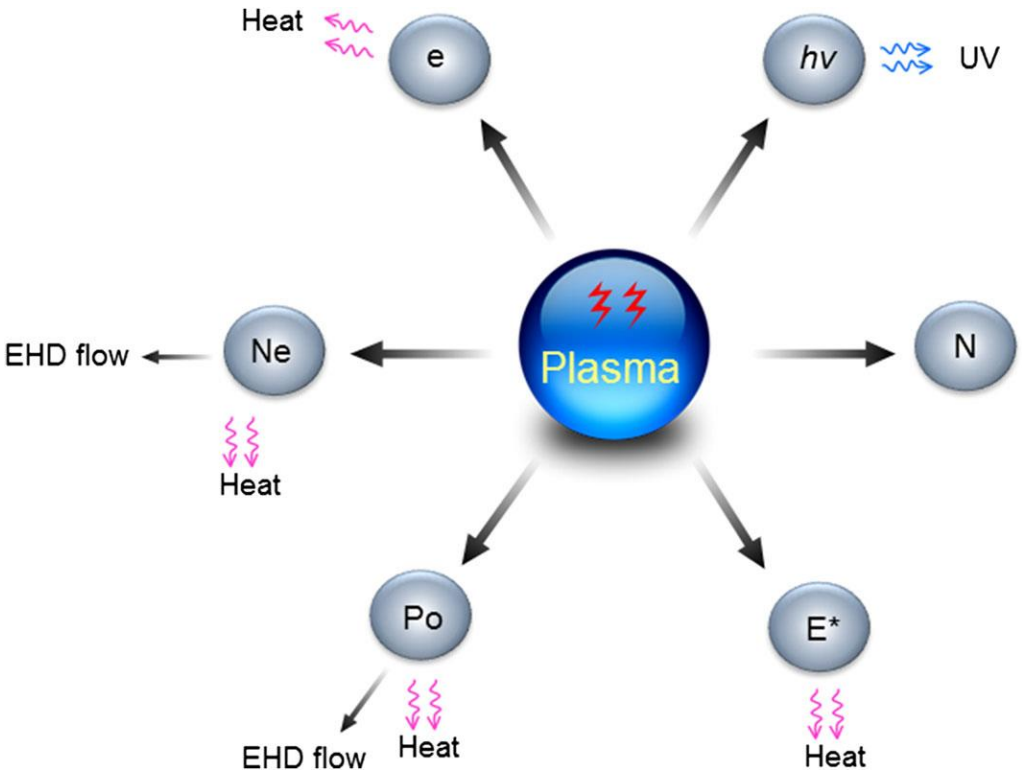

Figure 1.1. The major components of plasma: e = electron, hv = photon, N = neutral molecule or atom, E = excited molecule, Po = positive ion and Ne = negative ion [19].*

(a) **(b)** **(c)**

Figure 1.2. Examples of natural plasma: (a) the sun, (b) the Aurora Borealis and (c) Lightning [22] and references therein.

Plasma can also be produced artificially via the injection a sufficient amount of energy into a gas causing the formation of charged carriers [21-23]. There are various ways that energy can be delivered in order to generate plasma: by heating (eg. radiofrequency torch [24] and microwave plasma torch [25]), photoionization (eg. laser-plasma [21][26]) and by exposing neutral gas to beams of charged ions or electrons or by electrical discharge [21]; a schematic of these methods is shown in fig. 1.3. As can be seen from the figure, plasma can be generated by supplying sufficient heat (thermal energy) to a neutral gas using a flame and exothermic chemical reactions then generate the plasma via collisions between the electrons and the other neutral species. Mechanical methods such as adiabatic gas compression can also be used as another method of heat injection into the gas molecules to generate plasma. In addition, an energetic beam of electrons or ions can be used to supply energy to the gas reservoir by providing charged particles that then generate plasma, such as electrons, ions and photons that collide with the neutral species. The most widely method used for plasma generation is to employ an electric field across the carrier gas, this accelerates the few electrons present in the neutral gas to collide with the gas molecules and produce a cascade of electrons as well as ions and radicals.

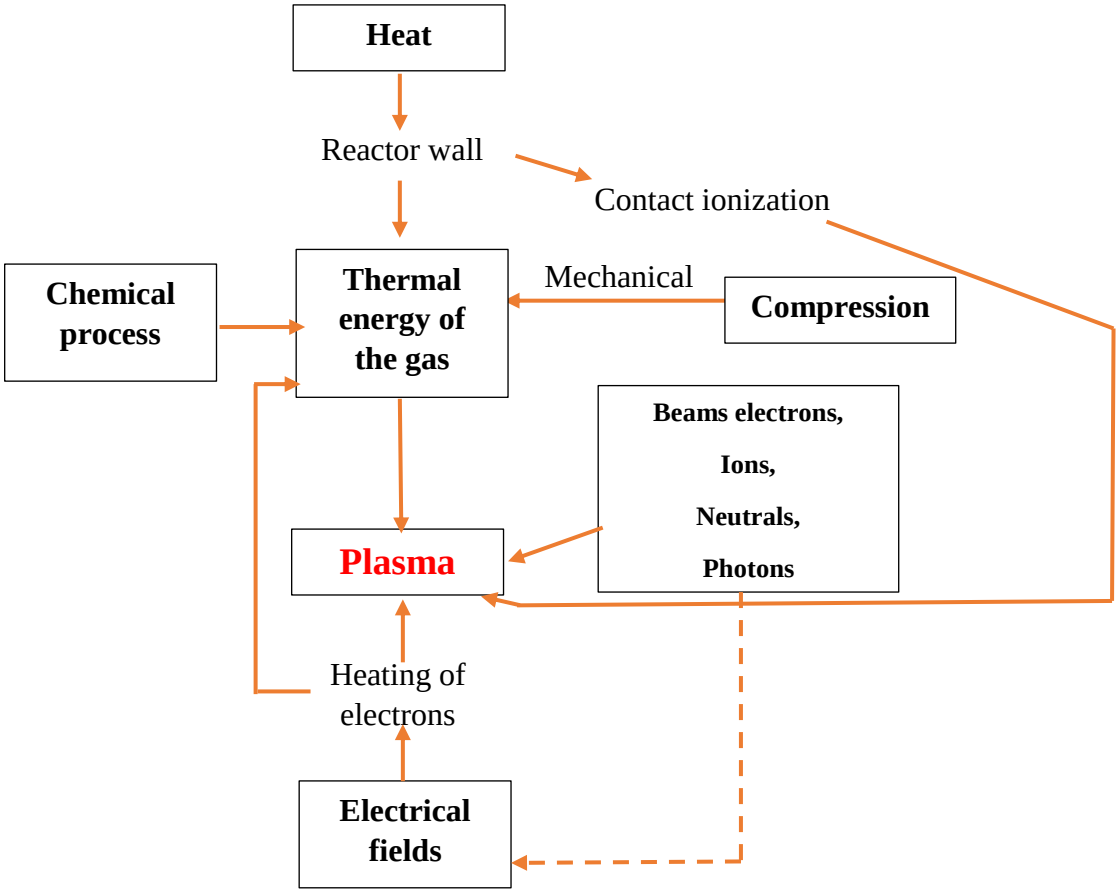

Figure 1.3. The principles of plasma generation [21].

1.2.2. Types of plasma

Artificial plasmas are generally classified as thermodynamic equilibrium (thermal or high temperature) plasmas or thermodynamic non-equilibrium (non-thermal or cold) plasmas, depending on the relative temperatures of the molecules and electrons in the plasma [27]. Thermal Plasmas (TPs) are those in which the temperature of the electrons and the atoms and molecules are equal and up to 10^4 K. In contrast, Non-Thermal Plasmas (NTPs) are those in which the temperature of the heavy species remain close to ambient, whilst the electron temperature is significantly higher, i.e. up to 10^4- 10^5 K [28-31]. Table 1.3 summarizes the main characteristics of thermal and non-thermal plasmas.

Properties	**Thermal plasma**	**Non-thermal plasma**
Electron temperature / K	10^4	$10^4 – 10^5$
Temperature of heavy species / K	10^4	300 - 1000
Electron density / m^{-3}	$\approx 10^{21} – 10^{26}$	$< 10^{19}$
Example	Arc plasma	Glow discharge

Table 1.3. The main characteristics of thermal and non-thermal plasmas [23][32].

For non-thermal plasma, inelastic collisions between the plasma species (electrons and heavy particles) initiate the plasma chemistry; in addition, a number of elastic collision can happen that lead to some slight heating of the heavy particles in the plasma regions whilst the electrons remain at high temperature [23][32].

1.2.3. The applications of plasma

Non-thermal plasma has various advantageous over thermal plasma, and these include: lower cost operation, ambient gas temperature, low heating losses, high removal efficiency and easy upscaling [17][33]. As a consequence, over the past few decades, NTPs have received significant attention and their application in, for example, industrial, environmental and medical fields [20][34][35], see table 1.4.

Thermal plasma	Non-thermal plasma
Arc welding	Generation of ozone
Arc gas heaters	Sterilization of medical equipment
Ion laser	Diesel exhaust treatment
Submerged arc welding	Propulsion in space

Table 1.4. Examples of the application of plasmas [36].

There are many companies producing commercial non-thermal plasma systems across a range of applications including: Enercon [37], Alternor [38], Plasma Etch [39], AcXys [40] (surface treatment/etching) and Ozonia [41], Lenntech [42], and Evoqua [43] (ozone for water treatment). Further, electro-static precipitation for industrial separation and gas cleaning dates back to 1907 [44]; however, none of these commercial systems rely upon plasma catalysis.

In the laboratory, topical chemical conversions using NTPs include [45]: ozone generation [46], the conversion of CH_4 to H_2 and C2-C4 derivatives [47], toluene to phenol and cresols [48], CO_2 and H_2O to syngas and synfuels [49], the treatment of volatile organic compounds [10], decontamination and disinfection [50], the deep desulfurization of diesel fuels [51], the treatment of flue gas [52] and the dry reforming of CO_2 and CH_4 [53].

1.3. Non-thermal plasma reactors

There are various reactor configurations to generate non-thermal plasma such as: Pulsed Corona Discharge (PCD), Dielectric Barrier Discharge (DBD), Atmospheric Pressure Plasma Jet (APPJ), Radio Frequency (RF), Microwave Plasma (MP) and Packed-Bed Plasma (PBP) [29].

Generally, the classification of NTP reactors is based on the reactor configuration and the discharge mode. The silent discharge or Dielectric Barrier Discharge (DBD) is the most common type of NTP generator [12][45][54][55] because it can be used under atmospheric pressure [56].

Typically, the DBD reactors employed in the laboratory are based on cylinders of Al_2O_3 or quartz with one high voltage electrode wrapped around the outer surface of the cylinder as a

foil and a metal rod, mounted along the axis of the cylinder, as the second electrode [57-59]. Where catalyst pellets are used, packed bed reactors are generally employed [58].

In general, Dielectric Barrier Discharge (DBD) reactors typically utilising non-thermal plasma consist of two metal electrodes across which is a pulsed or AC high voltage field, the electrodes are separated by a gap of several millimeters and at least one electrode is covered or coated with a dielectric material to protect the electrode from erosion, prevent arcing and enhance the discharge plasma power, see fig. 1.4, more details are provided below. Dielectrics include: ceramics, glass, quartz, polymer or other materials which also play a key role in stabilizing the plasma [44][54].

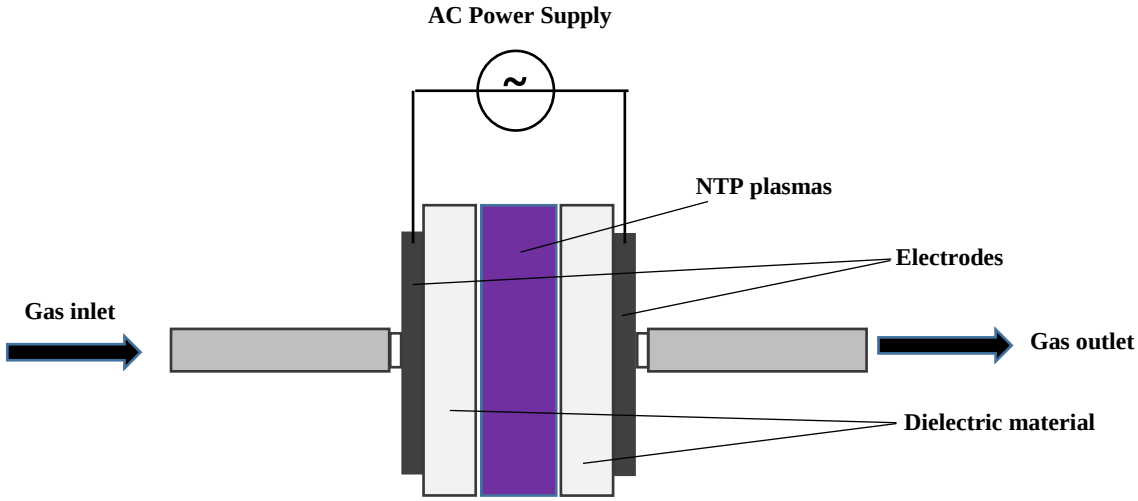

Figure 1.4. A typical non-thermal plasma Dielectric Barrier Discharge (DBD) reactor.

There are different types of DBD reactor depending upon the arrangement of the electrodes, i.e.: Volume Discharge (VD), Surface Discharge (SD), Coplanar Discharge (CD) and Packed Bed Discharge (PBD) [56] as shown in figs. 1.5(a)-(d). Figure 1.5(a) shows the VD reactor which consists of two plane electrodes, at least one which is covered with dielectric material, the feed gas passing between the dielectric and electrode. In this configuration, the active region of plasma consists of many tiny discharge columns or streamers. The Surface Discharge (SD) reactor, see fig. 1.5(b), consists of two electrodes: one of which is planar and positioned beneath the dielectric; the other is mounted as a thin plate or grid on the top surface of the dielectric. In this configuration, the plasma is generated as a thin layer over the surface of the dielectric material and near the surface electrode. The Coplanar Discharge (CD) reactor, see fig. 1.5(c), consists of two pairs of electrodes fixed inside the dielectric material with opposite polarity and

the discharge appears in the gas above the dielectric surface; in this reactor type the dielectric can be easily coated with catalyst or another dielectric material. In the case of Packed Bed Reactors (PBD), see fig. 1.5(d), the gap between the two electrodes is filled with dielectric or beads and the electrode arrangement can either involve coaxial plates or cylinders [60]. In this configuration, there are two types of discharge that occur in the gap: volume discharge occurs within the space between the beads, while surface discharge takes place over the surface of the beads and at the contact points between the beads and discharge electrodes or dielectric materials.

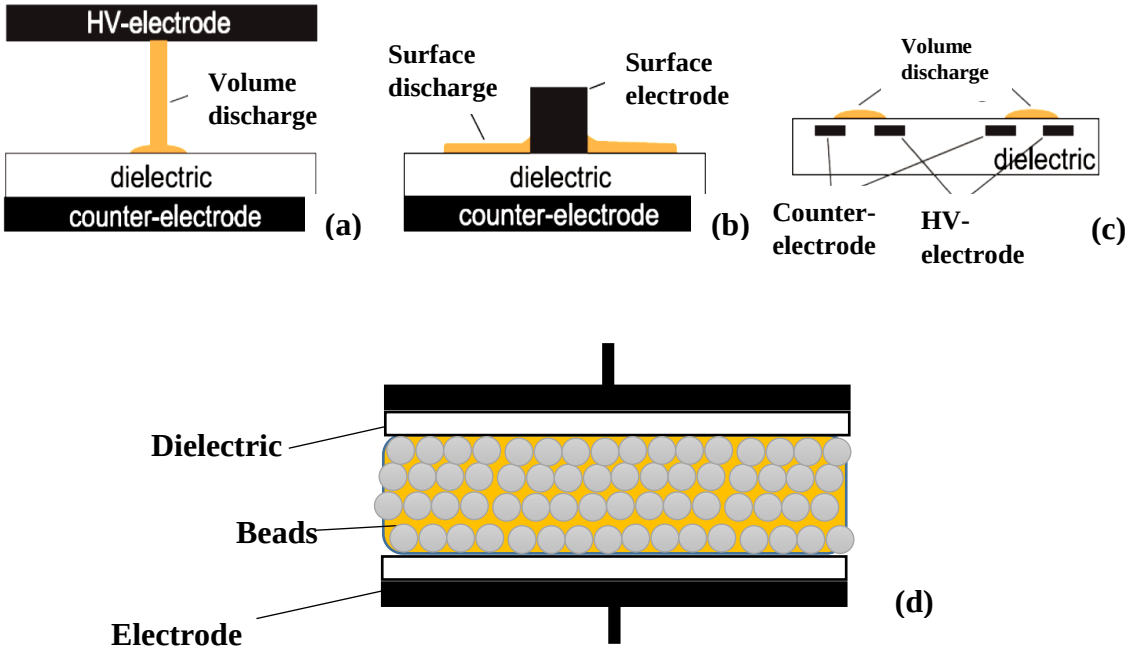

Figure 1.5. Schematic of the different types of dielectric barrier discharge reactor employing non-thermal plasma: (a) Volume Discharge (VD), (b) Surface Discharge (SD), (c) Coplanar Discharge (CD) and (d) Packed Bed Discharge (PBD) [56][60].

There are a number of industrial applications of DBD non-thermal plasma reactors, for example: ozone generation, surface modification of medical devices and biomaterials, high power CO_2 lasers, UV excimer lamps, plasma displays, pollution control in gas and liquid streams, chemical vapour deposition and medical applications [29].

1.4. The chemistry of non-thermal plasma

The chemistry which takes place in non-thermal plasma is quite complex and consists of a wide number of elementary processes. The primary and the secondary processes are defined as the elementary processes in terms of the timescales involved. Homogenous and heterogeneous reactions are considered the main types of reactions occurring in NTP. When an electrical field is applied between the electrodes, free electrons present in the gas are accelerated and energized. These free electrons are accelerated to very high energies (1-10 eV) and can collide with other atoms and molecules in the neutral gas. This leads to the ionization, excitation and/or dissociation of the neutral gas molecules as shown in table 1.5 [29][61].

Excitation	$e^- + A \quad A^* + e^-$
Ionization	$e^- + A \longrightarrow A^+ + e^- + e^-$
Dissociation	$e^- + A_2 \longrightarrow 2\,A + e^-$
Attachment	$e^- + A_2 \longrightarrow A_2^-$
Dissociative attachment	$e^- + A_2 \longrightarrow A^- + A$
Dissociative ionization	$e^- + A_2 \longrightarrow A^+ + A + 2e^-$
Electronic decomposition	$e^- + AB \longrightarrow A + B + e^-$
Charge transfer	$A^+ + B \longrightarrow A + B^+$

Table 1.5. The primary processes taking place in non-thermal plasma [29][61].

Figure 1.6 shows the typical timescales of the elementary processes in NTP. These chemical reactions include: the ionization, excitation, dissociation, light emission and charge transfer take place in the primary stage of plasma formation, which normally take around 10^{-8} seconds and result in the generation of electrons, ions, excited atoms and molecules, see table 1.5. During the secondary stage, recombination reactions between the electrons, ions, excited atoms and molecules generated as a result of the primary processes can take place, such as: ion + ion, radical + radical and radical + neutral species, leading to the formation of the final plasma products. These intermediate reactions take about 10^{-3} seconds, as shown in fig. 1.6 [61].

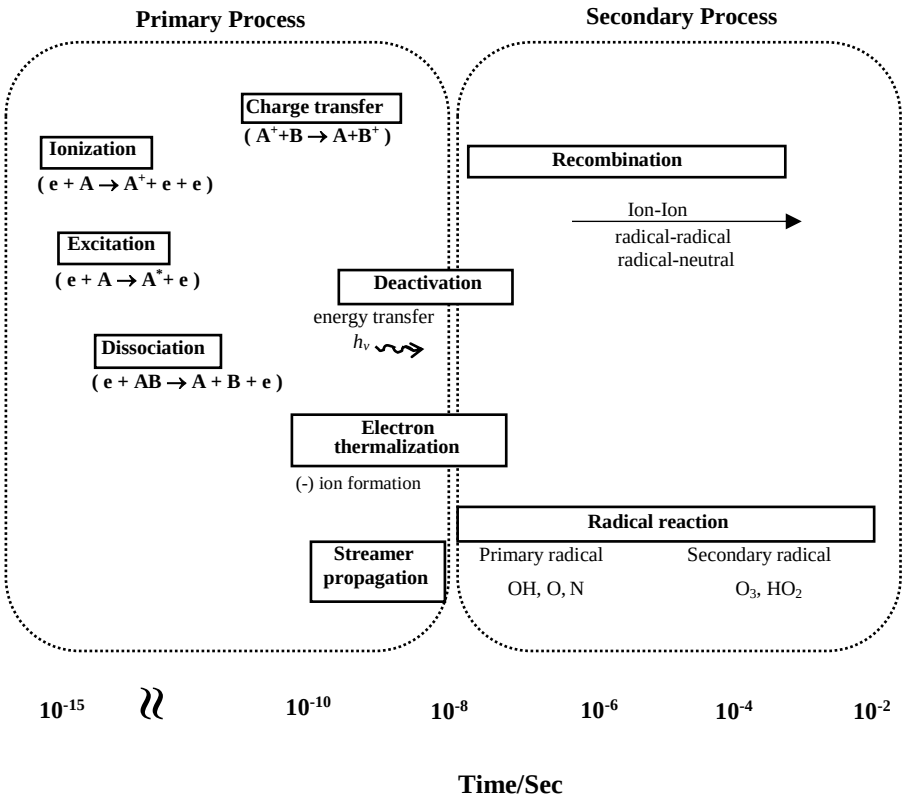

Figure 1.6. Schematic illustration of the timescales of the elementary processes in a Non-Thermal Plasma (NTP) [61].

1.5. The role of the dielectric in dielectric barrier discharge reactors non-thermal plasma

Initially, the gap between the two high voltage electrodes in NTP reactors was packed with dielectric pellets such as Al_2O_3 or $BaTiO_3$ and these were employed simply to increase the discharge power of the plasma via the discharge current I as described by the Manley equation [62][63]:

$$P = 4 f C_d V_{min}(V_{max} - V_{min} C_g/C) \qquad (1.1)$$

where C_d, C_g and C are defined as:

$$1/C = 1/ C_g + 1/ C_d \qquad (1.2)$$

and P is the discharge power (W), f is the discharge frequency (Hz), V_{min} is the discharge onset voltage (kV) required for plasma to be to initiated, V_{max} is the discharge voltage (kV), C_g is the

capacitance of the gas (F), C_d is the capacitance of the dielectric material between the two electrodes (F) and C is the total capacitance of the dielectric and gas (F). In addition, the discharge current (I, Amps) can be estimated from equation (1.3) [62]:

$$I = 4 f C_d(V_{max} - V_{min} C_g/C) = P / V_{min} \qquad (1.3)$$

V_{min} is primarily determined by the feed gas composition and the discharge gap width, while the discharge frequency (*f*) is set by the input power supply. The capacitance of the dielectric material is [63]:

$$C_d = \varepsilon_r \varepsilon_o A / d \qquad (1.4)$$

where ε_r is the dielectric constant or relative static permittivity, ε_o is the vacuum permittivity = 8.854×10^{-12} (F m^{-1}), A is the surface area of the dielectric (m^2) and d is the thickness of the dielectric (m). C_d depends on the dielectric constant and the geometric factors of the dielectric material such as A and d [63]. Table 1.6 shows the dielectric constants of some typical dielectric materials [64][65-69].

Dielectric materials	Dielectric constant
Teflon	1.89 - 1.93
SiO_2	3.8 - 3.9
Ceramic (Macor)	5 - 6
Glass	7 - 10
Al_2O_3	9.5 - 12
$ZrSiO_4$	10 - 12
TiO_2	80 - 170
$BaTiO_3$	1200 – 10 000 at (20–120 °C)
SnO_2	3 - 4
CeO_2	24.5

Table 1.6. The dielectric constants of typical dielectric materials [64][65-69].

From equations (1.1) and (1.2), at a constant input power and frequency, the discharge voltage is determined primarily by the capacitances of the dielectric material and background gas that fills the gap. Further, the relation between the capacitance of the dielectric and current is linear

and a higher capacitance lowers the discharge onset voltage at fixed of input power as shown in equation (1.3) [62].

An additional role of the dielectric is to increase the electric field strength (E) by decreasing discharge gap volume between the DBD electrodes [70]:

$$E=V_{max}\,\varepsilon_g / d \qquad (1.5)$$

where E = electric field strength (Vm^{-1}), V_{max} = discharge voltage (V), ε_g = dielectric constant of background gas and d= the gap width between electrodes (m).

Finally, the dielectric prevents arcing between the electrodes by increasing the resistance between them and produces a homogenous distribution of microdischarges: these are the thin and bright discharge channels, usually called filament discharges, inside the discharge gap due to the accumulation of the charges on the dielectric surface [71].

In fact, the dielectric barrier material is one of the key factors for the effective operation of the DBD plasma. In addition, the dielectric constant is one of the important properties of the dielectric barriers materials that can enhance the plasma generation: for example, Li et al. [63] studied the effect of using different dielectric barrier materials with different dielectric properties such as dielectric constant to investigate the efficiency and characteristics of these materials on the plasma reaction in a DBD reactor with respect to the decomposition of CO_2 to CO and oxygen. The planer reactor was fitted inside a Teflon shell and it was fed with CO_2 + N_2 (10: 90) through the gap between the dielectric material and the high voltage electrode. Both electrodes were made from stainless steel as two parallel layers (24 × 12 × 3 mm). The grounded electrode was covered with a 1mm thick of various barrier material and the gap between the dielectric material and the high voltage electrode was 1mm. The authors found that using $Ca_{0.7}Sr_{0.3}TiO_3$ with 0.5 wt% $Li_2Si_2O_5$ (to physically stabilize the $Ca_{0.7}Sr_{0.3}TiO_3$) as the dielectric was more effective than other ceramic dielectric materials with low permittivities such as alumina Al_2O_3 and silica glass SiO_2. Table 1.7 summarizes the data obtained by Li & co-workers. As can be seen, the dielectric constant has a significant effect upon the power and hence the conversion of CO_2.

Dielectric barrier	f / kHz	C_d /pF	ε_r	C_g / pF	V_{min} /kV	V_{max} / kV	P / W	CO_2 conversion %
SiO_2	10	9.8	3.9	2.5	3.3	5.1	1.8	3.8 %
Al_2O_3	10	21.3	11.0	2.5	3.4	5.2	4.5	4.7 %
$Ca_{0.7}Sr_{0.3}TiO_3$ + 0.5 wt% $Li_2Si_2O_5$	10	488.2	207.0*	2.5	1.9	3.0	40.7	15.6 %

** ε_r of $Ca_{0.7}Sr_{0.3}TiO_3$ before adding 0.5 wt% $Li_2Si_2O_5$ = 119.5.*

Table 1.7. The capacitance of dielectric materials employed by Li et al. [63].

Similar behaviour was shown by Meiners and co-workers [72]. They studied the influence of varying the dielectric constant and the thickness of the dielectric barrier material on the discharge power of a conventional VD-DBD. This reactor was made from two parallel metal electrodes with a 1 mm discharge gap between the barriers. Both electrodes were covered with different dielectrics including Al_2O_3, MgO, TiO_2 and $SrTiO_3$ of varying thicknesses. Air was used as a feed gas at a fixed flow rate of 1.2 dm^3 min^{-1} and a 12 kV, 14-16 kHz power supply was employed. The discharge current was significantly increased as the thickness of the dielectric barrier material was decreased from 2.0 to 0.5 mm due to strong microdischarge generation and increasing electron density in the plasma zone.

Importantly, it was found that certain dielectrics could act as catalysts and steer the reaction to yield different products (eg. Ni/SiO_2 [73], NiO/WO_3 vs Faujasite vs Mordenite [48][74]) but the trends observed when using a range of such catalysts are still not understood [73][75][76]. Consequently, catalyst selection for NTP processes has been based on those materials are active for the same chemical processes when carried out in conventional, thermal reactors operating under steady state conditions. However, plasmas are most certainly not in a steady state and hence this method of selection is not really valid, as was shown by the work described in this thesis.

1.6. The general principles of plasma catalysis

The combination of non-thermal plasma and catalysis technology may be termed as plasma catalysis or plasma enhanced catalysis. Using this approach can lead to enhanced energy

efficiency and decreased emission of harmful byproducts and increased reactant conversion [17][19].

Figure 1.7 shows the applications of plasma catalysis; eg. VOC and odor removal [77-79], NO_x reduction [80-83] and water treatment [84-86]. In addition, the use of plasma catalysis has been studied with respect to dry reforming, syngas production, hydrogen production, methanation, and ammonia synthesis [87].

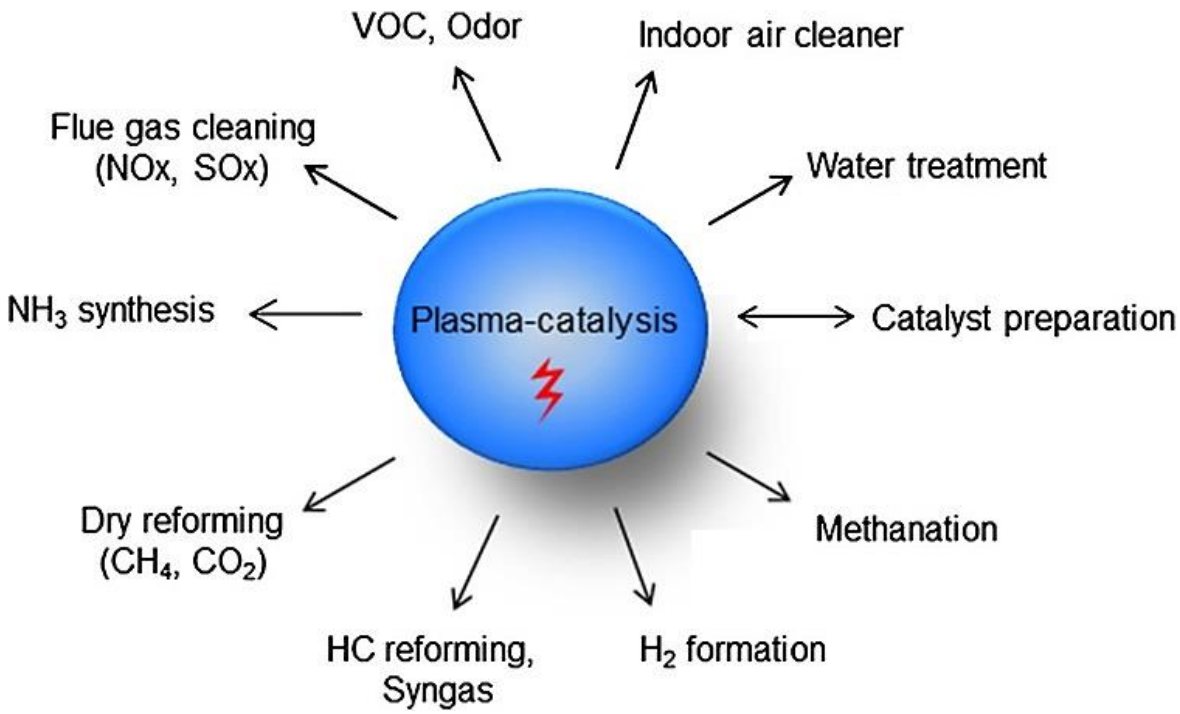

Figure 1.7. Applications of plasma catalysis [19].

1.7. The potential advantages of plasma catalysis chemistry

There are a number of significant potential advantages of plasma catalysis over conventional, thermal catalysis. Thus, the ions, radicals and vibrationally electronically excited species produced through the collisions between the high energy electrons generated in the NTP are only observed at temperatures > 1000 K in thermal systems [88]. In principle, almost 97 % of the plasma discharge power of low temperature plasmas can be converted into vibrational excitation of the gas feed molecules [89], and these species can exhibit enhanced sticking probabilities at catalyst surfaces and hence enhance the reactivity of endothermic processes [88][90]. The ions, radicals and excited species present in non-thermal plasma are essentially

unavailable in thermal systems; thus the key advantage of non-thermal plasma chemistry is that it makes a range of chemistries viable, where, by conventional means, they would require extremes of temperature and/or pressure that would be technically challenging and economically unfeasible. In summary, coupling NTP with catalysts offering novel chemical pathways with lower activation energies opens up the potential for a wholly new and exciting field of chemistry. In addition, it should be possible to enhance targeted reactions and suppress others by appropriate choice of catalyst, and feed gas, by controlling the number density of electrons and controlling the temperatures of the electrons and gaseous species.

Figure 1.8 summarizes the different plasma catalysis interactions inside the plasma region and at the catalyst surface eg. inside the in-plasma catalysis reactor (it is discussed below). As can be seen from the figure, plasma discharge type and the energy distribution of the electrons can be affected by catalysts introduced inside the discharge zone. As a result, new reactive species eg. electrons and radicals can be generated inside the plasma region, which can break the oxygen bond to produce active oxygen in case of using O_2 as a carrier gas. Hence, long lifetime species such as O_3, H_2O_2, NO and NO_2 may be produced due to the recombination of the short-lived species such as $O(^3P)$, $O(^1D)$, $N(^4S)$, $N(^2D)$, OH and HO_2 over the catalyst surface and possibly they can reach to the downstream post-plasma catalysis reactor (it is discussed below) and contact with a catalyst that employed in the second reactor. In addition, the electric field near the contact point between the dielectric pellets /or catalyst that presence in the discharge region of the reactor as a packing material will be increased and the residence time of the pollutants in the discharge zone due to the adsorption of VOC over the catalyst surface will be enhanced as well, and that can consequently affect VOC surface adsorption [91].

In contrast to the effect of catalyst on the plasma as stated above, plasma can effect the catalyst properties eg: by causing physical changes, by enhancing the dispersion of the active catalytic sites and increasing the oxidation state of the catalyst. In addition, the temperature inside the plasma region can be increased sufficiently to result in the thermal activation of the catalyst materials and new reaction pathways could be opened up [92][93]. Overall, it is possible that the removal efficiency of VOCs could be increased when combine plasma with catalysis [94].

In general, it is assumed that NTP systems consume more energy than the analogous thermal one. However, Whitehead [88] and references therein has reported that the overall activation energy for the destruction of air pollutants using NTP was similar to that observed for the thermal process.

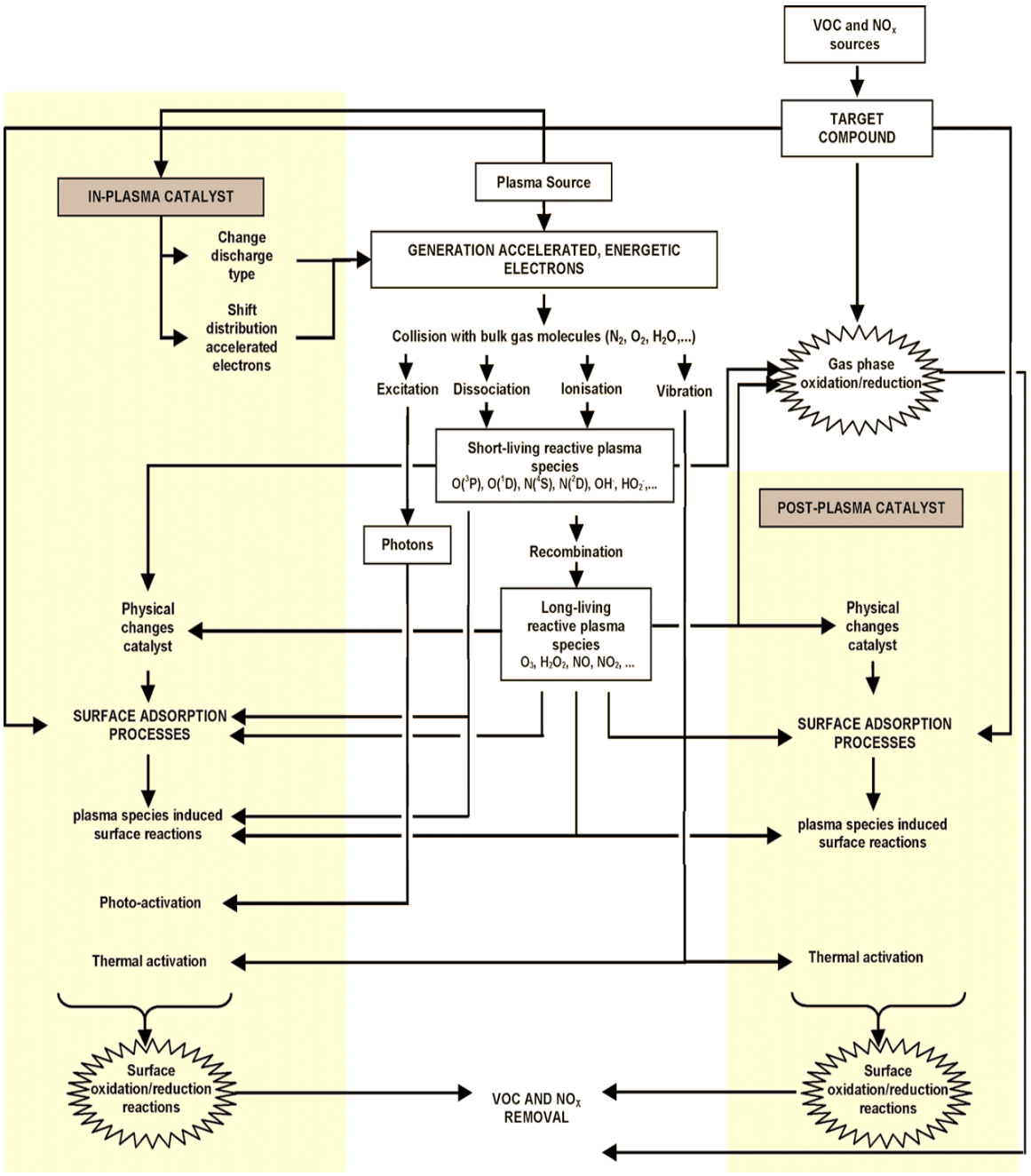

Figure 1.8. Schematic summary of plasma catalysis phenomenon [92].

A significant challenge of NTP-driven systems is perceived to be the high energy demand; however, companies such as Siemens [95] have adopted strategies involving the harnessing of the spillover of renewably-generated electricity to the production of fuels and chemical products, as matching the production of electricity from renewable energy to demand is very difficult, and often the surplus is simply spilled. The storage of this surplus energy chemically is seen as a possible solution to this problem; for example, the plasma-driven reduction of CO_2 to CO and O_2 is perceived as one possible chemical process, particularly as some industrial plants produce almost pure CO_2 as waste gas [96].

There could also be environmental benefits associated with plasma technology: thus, Martuzevicius and co-workers [97] compared conventional technologies with plasma systems for the destruction of volatile organic compounds, and found that NTP-based technology performed better with respect to the ozone layer depletion, acidification, eutrophication and human toxicity potential. The authors reported that "The relatively high demand of electrical energy causes lower positioning of plasma technologies in cases where no other materials are utilized and major waste is formed. On the other hand, many traditional end-of pipe technologies are associated with high amounts of process waste, which provides plasma technologies with an opportunity to establish them in the market as more efficient and in many occasions, more environment-friendly ones". Finally, plasma catalysis has not been researched sufficiently to exploit its very real potential.

1.8. Plasma catalysis reactor configurations

There are two categories of the plasma catalysis reactor depending on the location of catalyst: In-Plasma Catalysis (IPC) and Post-Plasma Catalysis (PPC). In IPC, the catalyst is located inside the NTP cell either as pellets or as a coating over the dielectric material or electrode. PPC consists of a two-stage process where the catalyst is located downstream of the reactor [92] as shown in fig. 1.9. In-plasma catalysis [77] is also known as: Plasma-Driven Catalysis (PDC) [98], Single-Stage Plasma–Catalysis (SSPC) [99], Plasma And Catalyst integrated Technologies (PACT) [100] or Combined Plasma Catalysis (CPC) [101][102]. PPC has been termed Plasma-Enhanced Catalysis (PEC) [98].

1.9. The challenges facing the exploitation of plasma catalysis chemistry

As state above, the potential of NTP-assisted catalysis in chemical synthesis is as yet largely unrealized: this is most likely due to the lack of analytical information on the processes taking place at the catalyst/plasma interface (interestingly, the US Plasma 2010 Committee report [103] concluded that the interactions of plasmas with solid surfaces is one of the six critical challenges that define the plasma research frontier; a view that is still popular today). The reason for the lack of understanding of plasma chemistry is the dearth of in-situ analytical studies able to provide molecular information and hence identify reactive intermediates, both adsorbed and in the gas phase. Hence the chemical mechanisms and kinetics involved are simply not understood [104][105]. This is reflected in the paucity of catalyst selection as discussed above and the simplicity (and unoptimised nature) of NTP reactor design [88][89] as discussed below.

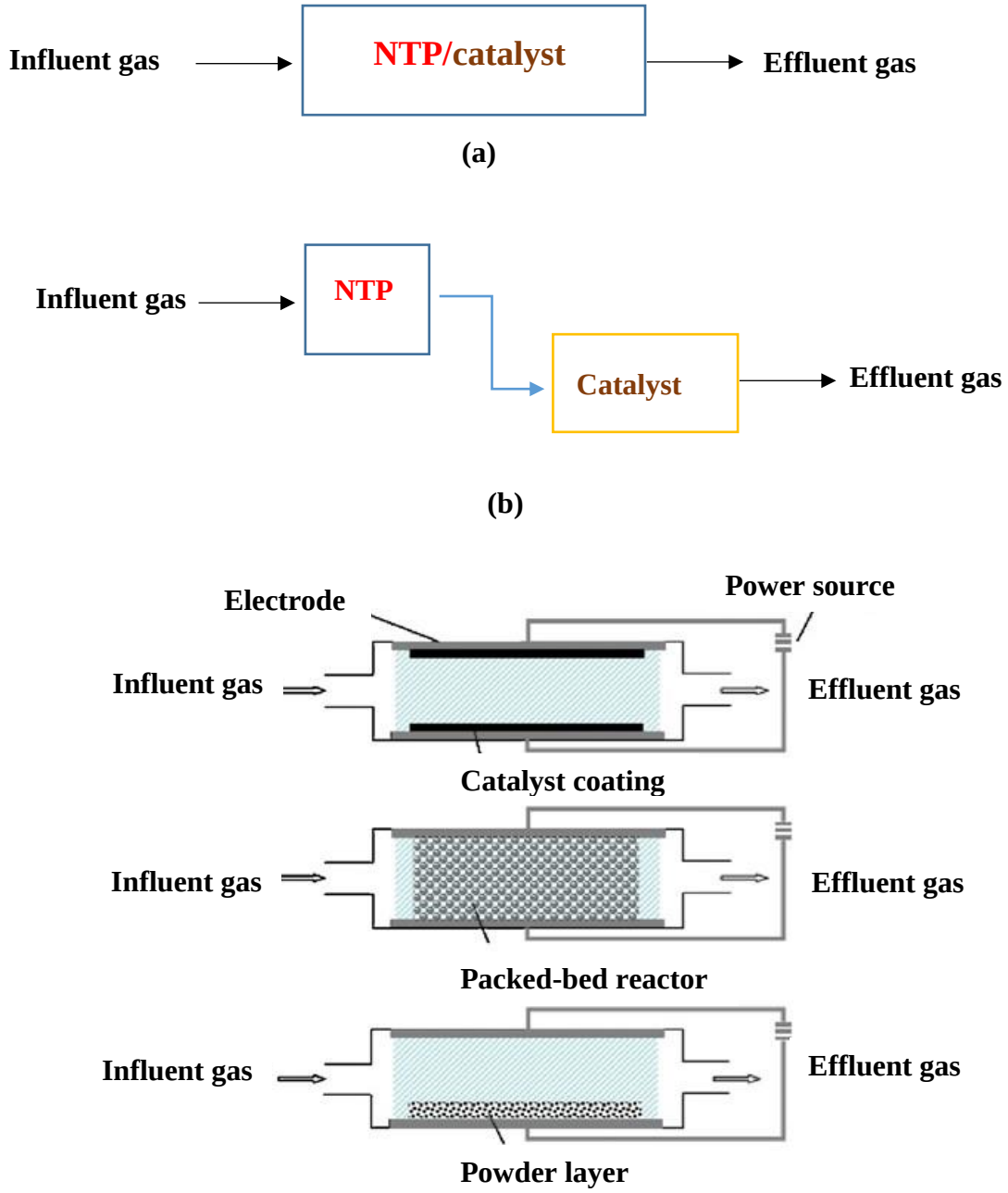

Figure 1.9. Schematic of (a) In-Plasma Configuration (IPC) and (b) Post Plasma (PPC). (c) The most common configuration employed in IPC reactor [92].

As state above, NTP reactors utilising catalyst are most commonly of the packed-bed type, either as a variant of the tube reactors described above with the gap filled with the catalyst/dielectric pellets or two plate electrodes separated by a gap filled with pellets [90]. It

is not at all clear these configurations are optimum, as there is no theoretical basis for their design: such a basis requires the chemistry taking place in the reactor to be modelled. All designs so far have essentially been empirical; they have not as yet been formulated on the basis of known or estimated rate constants or reaction mechanisms. The interaction of highly excited and reactive species with solid surfaces is largely unknown both in terms of the chemistry and the timescale over which such reactions take place [88]. Furthermore, whilst the potential synergy between NTP and catalysis is widely acknowledged in the NTP community, it has not been possible to include catalysis in models: indeed, even accounting for chemical reactions on the chemically simple surfaces of the HV electrodes has proven too challenging [106] due to the lack of chemical information on the species present. For example, in the absence of information on the identities of the species present in non-thermal plasmas, and at the solid (dielectric/catalyst)/plasma interface, all possible species need to be included in the model (eg. up to 150 molecules [107][108]) which increases computing time and decreases the accuracy of the model. The previous FTIR research strongly suggests that it should be possible to provide the hard experimental data required to aid effective modelling and hence reactor design [35].

1.10. The state-of-the-art in in-situ FTIR studies of non-thermal plasmas

Prior to the work in Newcastle [109-112], there were no papers in the literature that provided a direct comparison between in-situ FTIR studies on the thermally and plasma-driven conversion of air pollutants.

Whilst the plasma/catalyst surface has not been investigated extensively with in-situ infrared spectroscopy, such studies have started to appear. There are a number of studies on the downstream analysis of the exhaust from NTPs, see for example [113], but actual studies of the plasma glow with IR spectroscopy [35] or of the catalyst surface in contact with a plasma is only a recent phenomenon [6][114-118].

Christensen and Al-Abduly [35] studied the plasma glow region of a NTP using FTIR spectroscopy. The authors employed a plasma jet as shown in fig. 1.10, comprising a glass tube with a stainless steel rod as one HV electrode and a metal foil cylinder around wrapped the outside as the second electrode. A variety of gas mixtures eg. CO_2, CO_2 + air, N_2 + O_2, O_2, O_2 + N_2 + H_2O etc, were fed to the plasma jet and the plasma glow region monitored directly. In addition, the downstream plasma exhaust was monitored using UV Vis and FTIR spectroscopies. A number of species were observed in the plasma glow including: O_3, N_2O_5,

N_2O, HNO_3, CO_2, CO and an excited form of CO_2 (i.e. CO_2^*: this was the first report of the direct observation of an excited form of CO_2 in the plasma glow region of a NTP by infrared spectroscopy). The species was incorrectly identified as vibrationally-excited CO_2; recent work by Christensen et al. [109] showed this, in fact, to be rotationally-excited CO_2. O_3, N_2O_5, HNO_3 and N_2O were observed in the downstream exhaust from the plasma. The authors postulated that reactive species generated in the plasma glow region continued to react in the exhaust downstream of the plasma.

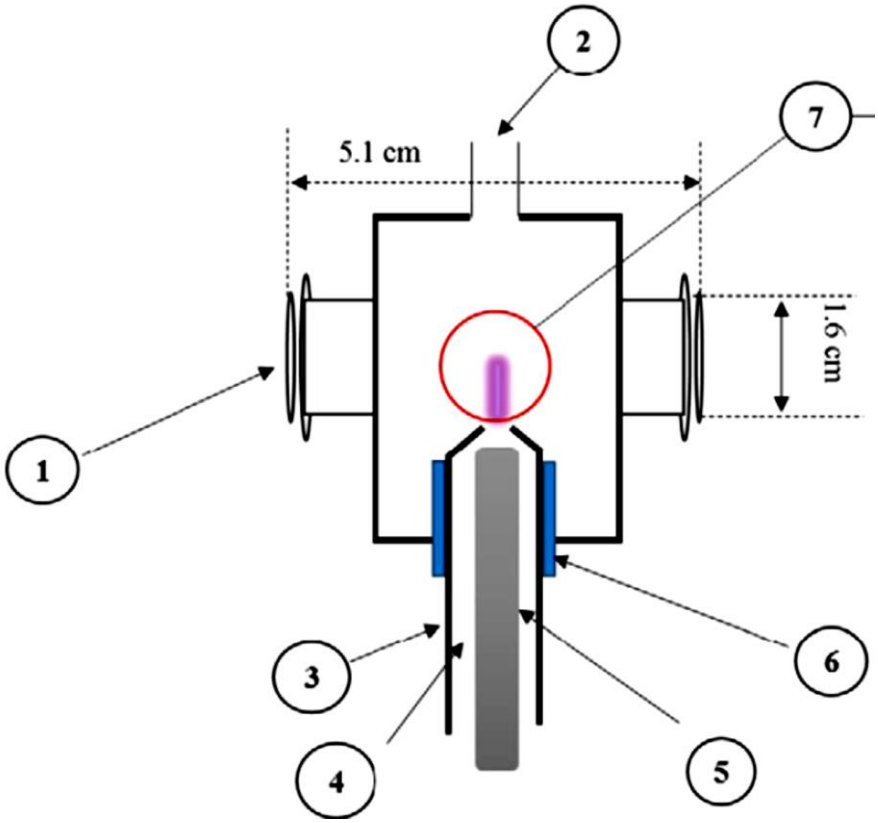

Figure 1.10. Non-thermal plasma jet transmission cell: (1) CaF_2 windows, (2) exhaust gas outlet, (3) Pyrex glass tube with a nozzle, (4) feed gas flow gap, (5) and (6) high voltage electrodes and (7) in situ sampling zone of the NTP glow [35].

Rivallan et al. [114] studied the gas phase reduction of CO_2 in Low Pressure Glow Discharge Reactor (LPGDR) at a catalyst wafer using step scan FTIR spectroscopy, see figs 1.11(a) and (b). The reactor comprised a Pyrex glass tube with two tungsten electrodes at either end with the sample wafer could be mounted behind one of the CaF_2 windows of the cell. The sample wafer could be a catalyst employed in the sample holder to study the plasma catalytic chemistry by coupling a mass spectrometer or gas FTIR cell in the exhaust stream; or it could be as a material employed inside the reactor and the plasma glow used to treat the material surface. CO_2/air was fed into and removed from the reactor by tubes positioned at the ends of the reactor.

The authors did not detect any reaction products or intermediates, although they did achieve a time resolution of ca. 400 μs.

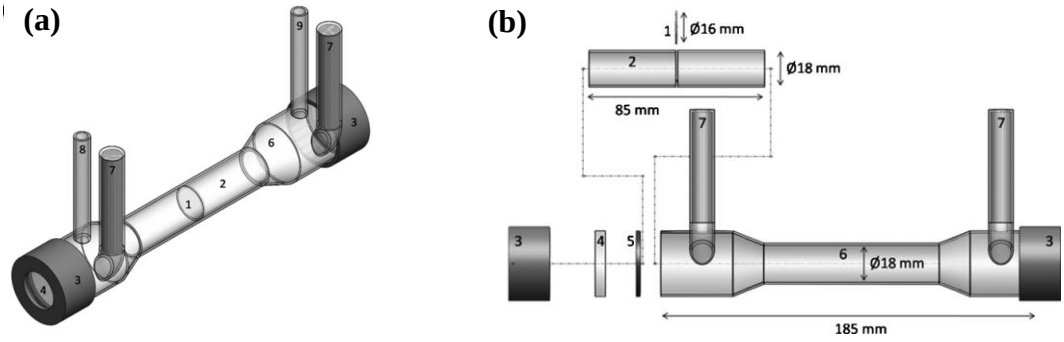

Figure 1.11. (a) Design and (b) expanded view of the LPGDR. 1. Sample wafer, 2. Pyrex tube sample holder, 3. Screw cap SVL 30, 4. CaF_2 window 30×5 mm, 5. Seal SVL 30, 6. Pyrex reactor with two fused electrodes, 7, 8 and 9: gas inlet and outlet of the reactor [114].

Li and co-workers [115] studied the deposition of Si from HexaMethylDiSilOxane (HMDSO) as a vapour phase in a low pressure radio frequency plasma using FTIR spectroscopy, see fig. 1.12. An IR beam was directed through the gas phase of the HMDSO that placed on the HV electrode which also act as the substrate, HV electrode was coated with a thin layer of Si. Simultaneously, the growth of the Si film was monitored with in-situ ellipsometry. IR spectra were recorded after one or more plasma pulses and a mass spectrometer was employed to analyse the exhaust gas. They found that O_2 admixture could be accelerate the deposition reaction of the thin film compared with the pure HMDSO plasma. In addition, O_2 admixture enhanced the formation of the SiO_x - like molecule structure of the films. Whilst the paper is interesting, the authors made no attempt to compare their data with data from thermally driven that can be used to generate SiO_x under high temperature.

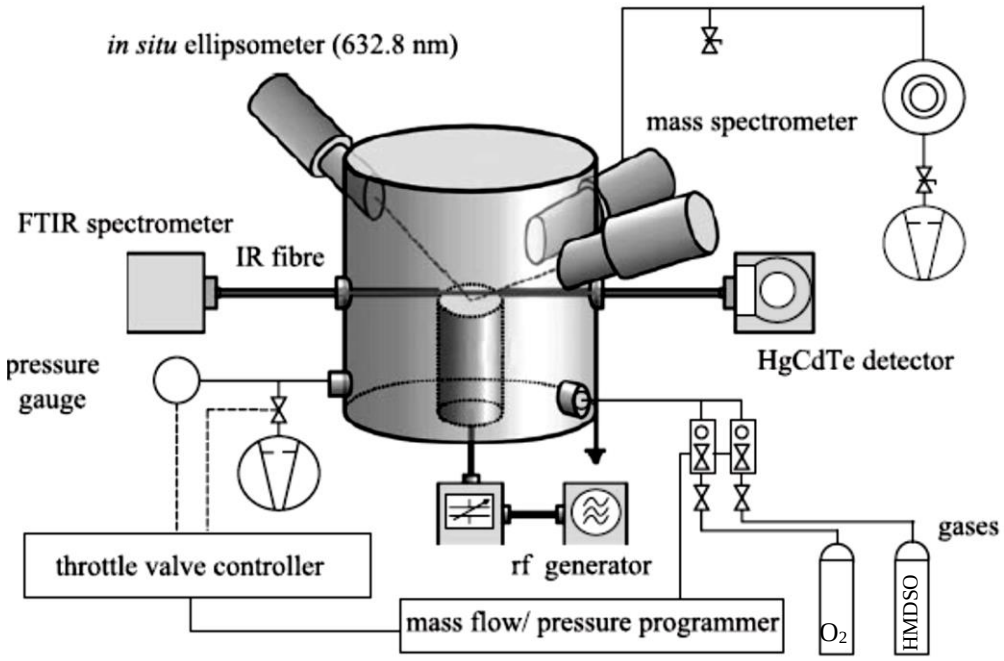

Figure 1.12. Schematic diagram of the experimental set-up employed by Li and co-workers [115].

Stere et al [116] investigated the atmospheric pressure NTP-driven and hydrocarbon assisted removal of NO_x (by conversion to N_2) from simulated diesel fuel (n-octane or toluene) at Ag/Al_2O_3 catalysts using in-situ DRIFTS. The authors employed a plasma jet, comprising a quartz tube with a central tungsten wire as one HV electrode and a metal ring as the second grounded electrode, see fig. 1.13. The He-fed jet was mounted in the DRIFTS cell such that the plasma contacted the catalyst, which was mounted by the IR beam. Mass spectrometry was employed to analyse the exhaust gas. The gas phase above the catalyst comprised the toluene or n-octane and O_2, NO and He as balance gas. The authors observed a number of species adsorbed on the Ag/Al_2O_3 catalyst during the NTP experiments. In the case of n-octane these includes, nitrate, acitate, carboxylate and isocyanate, and very weak absorptions due to CN^-. No isocyanate was detected in the toluene experiments and the only intermediate observed was adsorbed CN^-. The data on n-octane was similar to work reported on the analogous thermally-driven process where isocyanate was shown to be an intermediate in the formation of N_2 from NO_x.

Jia and Rousseau [6] reported studies on the CeO_2/plasma interface using in-situ infrared spectroscopy in a system they called Sorbent-Track, see figs. 1.14(a) and (b). A CeO_2 wafer was cradled in a glass U tube within which was one of the copper wire electrodes. The CeO_2

wafer was held in the centre of the Pyrex tube reactor perpendicular to the IR beam. The second Cu wire electrode as fed through the Pyrex tube wall to point at the wafer. The sample wafer was preheated first at 473 K for 2 hours and then cooled down to room temperature prior to the NTP experiment. The authors studied the reaction of acetone and IPA in air at a flow rate of ca. 500 cm^3 min^{-1} at the CeO_2 and found that acetone oxidized only to mesityl oxide, whilst IPA was fully oxidized to CO_2 via isopropoxide, acetone, mesityl oxide and acetate. Whilst very interesting data, the assignment of the features to various species were often based on single peaks and no attempt was made to confirm the assignments by comparison with authentic spectra of the species obtained using the same equipment.

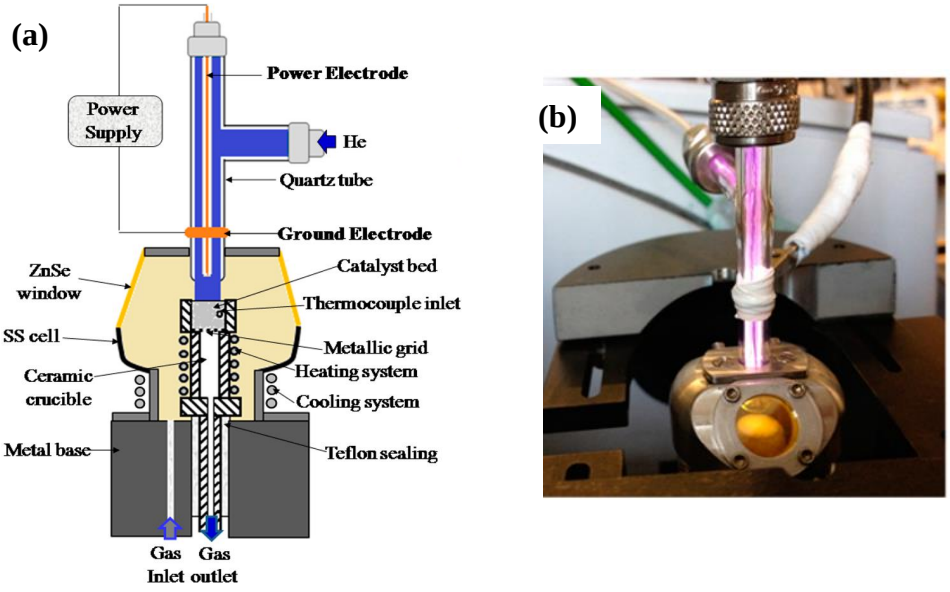

Figure 1.13. DRIFTS-MS setup: (a) Schematic sketch of the modified dome for the NTP-DRIFTS-MS measurements and (b) A photograph of the metallic dome with plasma on employed by Stere et al. [116].

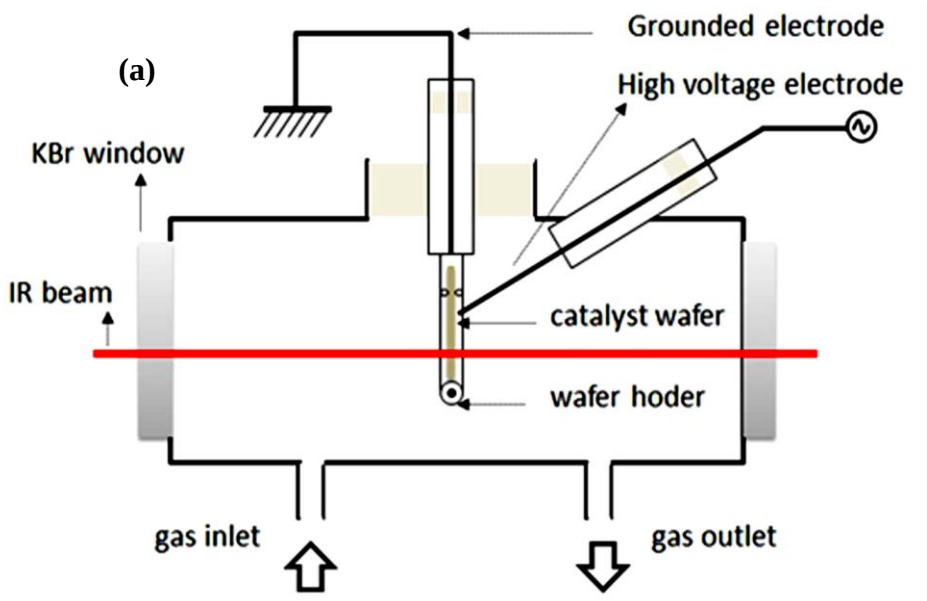

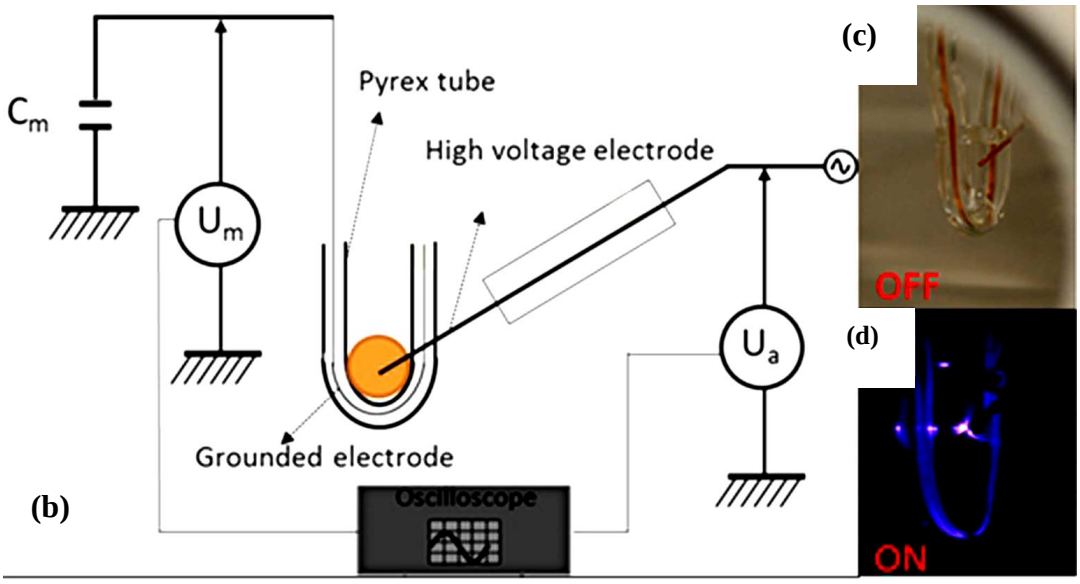

Figure 1.14. (a) Longitudinal view of sorbent track cell (Grounded electrode and high voltage electrode is copper wire; Catalyst wafer is placed in the IR pathway fixed by wafer holder of Pyrex tube.), (b) Electrical circuit of the in-situ DBD reactor (Pyrex tube is the insulating dielectric barrier), Photographs of catalyst wafer holder when Plasma: (c) off and (d) on [6].

A later paper by Rivallan et al. [117] reported the plasma- induced conversion of IPA over ɤ-Al_2O_3 using in-situ FTIR spectroscopy. The IR beam passed through both HV grid electrodes, one of which was mounted on the ɤ-Al_2O_3 wafer, see fig. 1.15. IPA and a 4:1 mixture of N_2 : O_2 were fed to the reactor at 600 mbar and 12 kV AC. Acetone was initially observed as an intermediate species due to the oxidation of IPA. The acetone was then converted into mesityl oxide as a result of aldolization. Finally, the mesityl oxide fragmented into acetaldehyde and isobutene. Again, whilst the paper is interesting, the authors made no attempt to compare their data with spectra from authentic samples.

Rodrigues et al. [118] used Diffuse Reflectance Infrared Fourier Transform Spectroscopy (DRIFTS) combined with non-thermal plasma to study the conversion of toluene and IPA (as model VOCs) at ɤ-Al_2O_3, TiO_2 and CeO_2 as shown in fig. 1.16. The high voltage electrodes were positioned inside the DRIFTS cell. The powder catalyst was placed directly on a copper 10 mm × 10 mm disc electrode and the second electrode was a copper tip 0.5 mm diameter, held above the powder. The authors studied the conversion of the VOCs as a function of the catalyst and voltage in air flowing at 30 cm^3 min^{-1}. The authors reported that IPA initially adsorbed on all three oxides and subsequently reacted to form acetone, propene, acetic acid and/or formic acid. No quantitative analysis was presented.

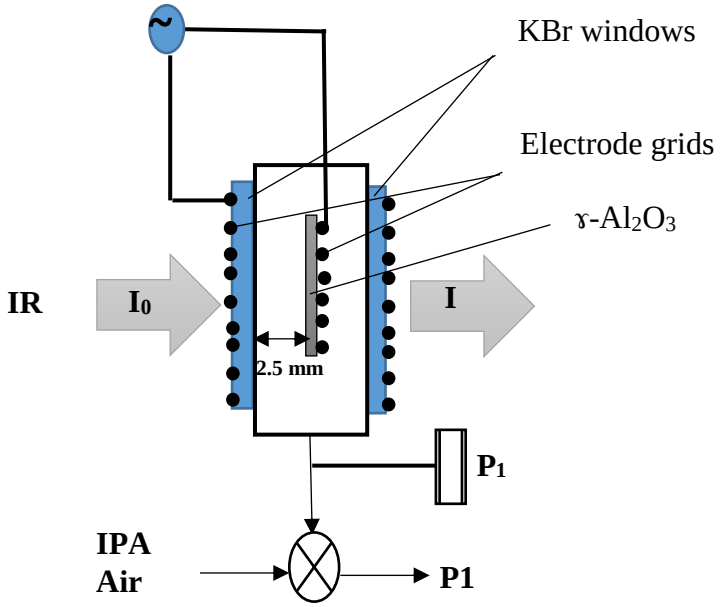

Figure 1.15. Schematic of the experimental system used by Rivallan et al. [117]; P_1 = pressure control, P1 = pumping stage.

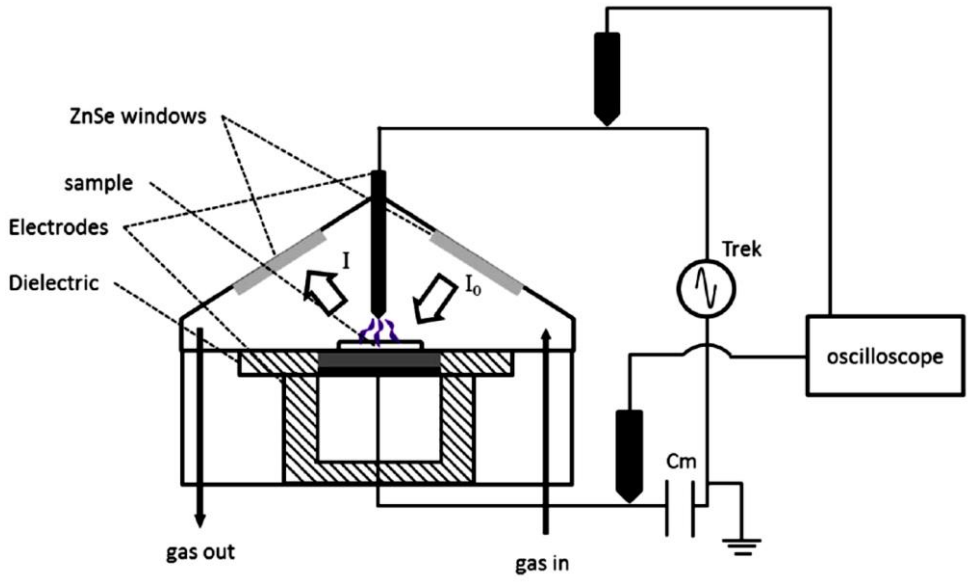

Figure 1.16. A Schematic of the IR/plasma cell employed by Rodrigues et al. [118].

As may be seen above, and in general, and even in the presence of ozone [119], the plasma-driven catalysed conversion of IPA generally leads to toxic products such as acetone and mesityl oxide rather than complete conversion to CO_2, and hence the requirement for an effective catalyst is clear.

1.11. Project aim and objectives

The aim of the work described in this thesis was to research the application of in-situ Fourier Transform InfraRed Spectroscopy to the study of the catalyzed and plasma driven conversion of IPA. In addition, the research seeks to assess the validity of catalyst selection for catalyzed NTP processes based on materials active in the analogous thermally-driven processes.

The objectives of the work was to design, fabricate and commission NTP-FTIR transmission and reflectance cells.

1.12. References

1. Olsen, E. and Nielsen, F., 2001. Predicting vapour pressures of organic compounds from their chemical structure for classification according to the VOC Directive and risk assessment in general. *Molecules*, *6*(4), pp.370-389.
2. Magureanu, M., 2012. VOC removal from air by plasma-assisted catalysis-experimental work. *Plasma Chemistry and Catalysis in Gases and Liquids*, pp.131-170.
3. Guenther, A., Geron, C., Pierce, T., Lamb, B., Harley, P. and Fall, R., 2000. Natural emissions of non-methane volatile organic compounds, carbon monoxide, and oxides of nitrogen from North America. *Atmospheric Environment*, *34*(12-14), pp.2205-2230.
4. Theloke, J. and Friedrich, R., 2007. Compilation of a database on the composition of anthropogenic VOC emissions for atmospheric modeling in Europe. *Atmospheric Environment*, *41*(19), pp.4148-4160.
5. Jarrige, J. and Vervisch, P., 2006. Decomposition of three volatile organic compounds by nanosecond pulsed corona discharge: Study of by-product formation and influence of high voltage pulse parameters. *Journal of Applied Physics*, *99*(11), p.113303.
6. Jia, Z. and Rousseau, A., 2016. Sorbent track: Quantitative monitoring of adsorbed VOCs under in-situ plasma exposure. *Scientific reports*, *6*, p.31888.
7. Hall, J., Gilligan, A., Schimmel, T., Cecchi, M. and Cohen, J., 1998. The origin, effects and control of air pollution in laboratories used for human embryo culture. *Human reproduction*, *13*(suppl_4), pp.146-155.
8. Agarwal, N., Chattopadhyay, R., Ghosh, S., Bhoumik, A., Goswami, S.K. and Chakravarty, B., 2017. Volatile organic compounds and good laboratory practices in the in vitro fertilization laboratory: the important parameters for successful outcome in extended culture. *Journal of Assisted Reproduction and Genetics*, *34*(8), pp.999-1006.

9. Thévenet, F., Sivachandiran, L., Guaitella, O., Barakat, C. and Rousseau, A., 2014. Plasma–catalyst coupling for volatile organic compound removal and indoor air treatment: a review. *Journal of Physics D: Applied Physics*, *47*(22), p.224011.
10. Xiao, G., Xu, W., Wu, R., Ni, M., Du, C., Gao, X., Luo, Z. and Cen, K., 2014. Non-thermal plasmas for VOCs abatement. *Plasma Chemistry and Plasma Processing*, *34*(5), pp.1033-1065.
11. 10 Easy Ways to Improve Indoor Air Quality (and Wellbeing) [Cited 2016 17 February]. Available from: https://www.pacificheatingcooling.com/how-to-improve-indoor-air-quality/.
12. Urashima, K. and Chang, J.S., 2000. Removal of volatile organic compounds from air streams and industrial flue gases by non-thermal plasma technology. *IEEE Transactions on Dielectrics and Electrical Insulation*, *7*(5), pp.602-614.
13. World Health Organization. Available from: http://www.who.int/phe/health_topics/outdoorair/databases/en/.
14. First French study on indoor air quality paints a grim picture [Cited 2007 23 October]. Available from: https://lavieverte.wordpress.com/2007/10/23/first-french-study-on-indoor-air-quality-is-not-encouraging/.
15. Khan, F.I. and Ghoshal, A.K., 2000. Removal of volatile organic compounds from polluted air. *Journal of Loss Prevention in the process Industries*, *13*(6), pp.527-545.
16. Das, D., Gaur, V. and Verma, N., 2004. Removal of volatile organic compound by activated carbon fiber. *Carbon*, *42*(14), pp.2949-2962.
17. Schiavon, M., Torretta, V., Casazza, A. and Ragazzi, M., 2017. Non-thermal Plasma as an Innovative Option for the Abatement of Volatile Organic Compounds: a Review. *Water, Air, & Soil Pollution*, *228*(10), p.388.
18. Gicquel, A., Cavadias, S. and Amouroux, J., 1986. Heterogeneous catalysis in low-pressure plasmas. *Journal of Physics D: Applied Physics*, *19*(11), p.2013.
19. Kim, H.H., Teramoto, Y., Ogata, A., Takagi, H. and Nanba, T., 2016. Plasma Catalysis for Environmental Treatment and Energy Applications. *Plasma Chemistry and Plasma Processing*, *36*(1), pp.45-72.
20. Fridman, A.A. (2012) 'Plasma Chemistry', (Cambridge: Cambridge University Press), pp. 1-11.
21. Conrads, H. and Schmidt, M. (2000) 'Plasma generation and plasma sources', *Plasma Sources Science and Technology*, 9(4), p. 441.

22. Baranoski, G.V. and Rokne, J.G., 2007, December. Rendering plasma phenomena: Applications and challenges. In Computer Graphics Forum (Vol. 26, No. 4, pp. 743-768). Blackwell Publishing Ltd.
23. A. Fridman and L. Kennedy, Plasma Physics and Engineering. Taylor and Francis, 2004.
24. Fauchais, P. and Vardelle, A., 1997. Thermal plasmas. *IEEE Transactions on Plasma Science*, *25*(6), pp.1258-1280.
25. Uhm, H.S., Hong, Y.C. and Shin, D.H., 2006. A microwave plasma torch and its applications. *Plasma Sources Science and Technology*, *15*(2), p.S26.
26. Carman, R.L., Forslund, D.W. and Kindel, J.M., 1981. Visible harmonic emission as a way of measuring profile steepening. *Physical Review Letters*, *46*(1), p.29.
27. Petitpas, G., Rollier, J.D., Darmon, A., Gonzalez-Aguilar, J., Metkemeijer, R. and Fulcheri, L., 2007. A comparative study of non-thermal plasma assisted reforming technologies. *International Journal of Hydrogen Energy*, *32*(14), pp.2848-2867.
28. Bahri, M. and Haghighat, F., 2014. Plasma-Based Indoor Air Cleaning Technologies: The State of the Art-Review. *CLEAN–Soil, Air, Water*, *42*(12), pp.1667-1680.
29. Abd Allah, Z. (2012) *Non Thermal Atmospheric Pressure Plasma For Remediation of Volatile Organic Compounds*, PhD thesis in the Faculty of Engineering and Physical Science, Manchester University.
30. Manheimer, W., Sugiyama, L.E. and Stix, T.H. eds., 1996. *Plasma science and the environment*. Springer Science & Business Media.
31. Lieberman, M.A. and Lichtenberg, A.J., 2005. *Principles of plasma discharges and materials processing*. John Wiley & Sons.
32. Tendero, C., Tixier, C., Tristant, P., Desmaison, J. and Leprince, P., 2006. Atmospheric pressure plasmas: A review. *Spectrochimica Acta Part B: Atomic Spectroscopy*, *61*(1), pp.2-30.
33. Shukla, P.K., 2001. A survey of dusty plasma physics. *Physics of Plasmas*, *8*(5), pp.1791-1803.
34. Taylan, O. and Berberoglu, H., 2014. Dissociation of carbon dioxide using a microhollow cathode discharge plasma reactor: effects of applied voltage, flow rate and concentration. *Plasma Sources Science and Technology*, *24*(1), p.015006.
35. Al-Abduly, A. and Christensen, P., 2015. An in situ and downstream study of non-thermal plasma chemistry in an air fed dielectric barrier discharge (DBD). *Plasma Sources Science and Technology*, *24*(6), p.065006.
36. Harry, J.E., 2013. *Introduction to Plasma Technology: Science, Engineering, and Applications*. John Wiley & Sons.

37. http://www.enerconind.com.UK/plasma-treatment/, 1996-2018.
38. http://www.alternor.com, 2011-2018.
39. http://www.plasmaetch.com.
40. http://www.acxys.com.
41. http://www.ozonia.com, 2012.
42. http://www.lenntech.com, 1998-2018.
43. http://www.evoqua.com, 2018.
44. Hammer, T., 2014. Atmospheric pressure plasma application for pollution control in industrial processes. *Contributions to Plasma Physics*, *54*(2), pp.187-201.
45. Kogelschatz, U., 2003. Dielectric-barrier discharges: their history, discharge physics, and industrial applications. *Plasma Chemistry and Plasma Processing*, *23*(1), pp.1-46.
46. Nassour, K., Brahami, M., Tilmatine, A., Nemmich, S., Miloua, F., Ramdani, N. and Zouzou, N., 2018. Comparative experimental analysis of ozone generation between surface and volume DBD generators. *IEEE Transactions on Dielectrics and Electrical Insulation*, *25*(2), pp.428-434.
47. Zhang, K., Mukhriza, T., Liu, X., Greco, P.P. and Chiremba, E., 2015. A study on CO_2 and CH_4 conversion to synthesis gas and higher hydrocarbons by the combination of catalysts and dielectric-barrier discharges. *Applied Catalysis A: General*, *502*, pp.138-149.
48. Youn, J.S., Bae, J., Park, S. and Park, Y.K., 2018. Plasma-assisted oxidation of toluene over Fe/zeolite catalyst in DBD reactor using adsorption/desorption system. *Catalysis Communications*, pp.36-40.
49. Nguyen, V.N. and Blum, L., 2015. Syngas and synfuels from H_2O and CO_2: Current status. *Chemie Ingenieur Technik*, *87*(4), pp.354-375.
50. V. Scholtz, J. Pazlarová, H. Soušková , J. Khuna and J. Julá, Biotechnol Adv (2015), http://dx.doi.org/10.1016/j.biotechadv.2015.01.002.
51. Ma, S., Zhao, Y., Yang, J., Zhang, S., Zhang, J. and Zheng, C., 2017. Research progress of pollutants removal from coal-fired flue gas using non-thermal plasma. *Renewable and Sustainable Energy Reviews*, *67*, pp.791-810.
52. Bai, M., Leng, B., Mao, S. and Li, C., 2016. Flue gas desulfurization by dielectric barrier discharge. *Plasma Chemistry and Plasma Processing*, *36*(2), pp.511-521.
53. Ashford, B. and Tu, X., 2017. Non-thermal plasma technology for the conversion of CO_2. *Current Opinion in Green and Sustainable Chemistry*, *3*, pp.45-49.
54. Ma, H., Chen, P., Zhang, M., Lin, X. and Ruan, R., 2002. Study of SO_2 removal using non-thermal plasma induced by dielectric barrier discharge (DBD). *Plasma Chemistry and Plasma Processing*, *22*(2), pp.239-254.

55. Chae, J.O., Demidiouk, V., Yeulash, M., Choi, I.C. and Jung, T.G., 2004. Experimental study for indoor air control by plasma-catalyst hybrid system. *IEEE Transactions on Plasma Science*, *32*(2), pp.493-497.
56. Pietsch, G.J., 2001. Peculiarities of dielectric barrier discharges. *Contributions to Plasma Physics*, *41*(6), pp.620-628.
57. Scarduelli, G., Guella, G., Ascenzi, D. and Tosi, P., 2011. Synthesis of liquid organic compounds from CH_4 and CO_2 in a dielectric barrier discharge operating at atmospheric pressure. *Plasma Processes and Polymers*, *8*(1), pp.25-31.
58. Zeng, Y., Zhu, X., Mei, D., Ashford, B. and Tu, X., 2015. Plasma-catalytic dry reforming of methane over γ-Al_2O_3 supported metal catalysts. *Catalysis Today*, *256*, pp.80-87.
59. De Bie, C., van Dijk, J. and Bogaerts, A., 2015. The dominant pathways for the conversion of methane into oxygenates and syngas in an atmospheric pressure dielectric barrier discharge. *The Journal of Physical Chemistry C*, *119*(39), pp.22331-22350.
60. Pietsch, G.J. and Gibalov, V.I., 1998. Dielectric barrier discharges and ozone synthesis. *Pure and Applied Chemistry*, *70*(6), pp.1169-1174.
61. Prantsidou, M., 2014. Plasma methods for the clean-up of organic liquid waste.
62. Manley, T.C., 1943. The electric characteristics of the ozonator discharge. *Transactions of the Electrochemical Society*, *84*(1), pp.83-96.
63. Li, R., Tang, Q., Yin, S. and Sato, T., 2006. Plasma catalysis for CO_2 decomposition by using different dielectric materials. *Fuel Processing Technology*, *87*(7), pp.617-622.
64. MACOR – Machinable Glass Ceramic Data Sheet [Cited 2016 19 January]. Available from: http://psec.uchicago.edu/ceramics/MACOR%20Data%20Sheet.pdf.
65. Clipper controls Inc [Cited 2016]. Available from: http://www.clippercontrols.com/pages/Dielectric-Constant-Values.html.
66. Ansari, S.A., Khan, M.M., Ansari, M.O., Kalathil, S., Lee, J. and Cho, M.H., 2014. Band gap engineering of CeO_2 nanostructure using an electrochemically active biofilm for visible light applications. *RSC Advances*, *4*(32), pp.16782-16791.
67. Tin dioxide semiconductor [cited 2013]. Available from: https://www.azom.com/article.aspx?ArticleID=8456.
68. Permittivity". schools.matter.org.uk. Archived from the original on 2016-03-11.
69. Schleife, A., Varley, J.B., Fuchs, F., Rödl, C., Bechstedt, F., Rinke, P., Janotti, A. and Van de Walle, C.G., 2011. Tin dioxide from first principles: Quasiparticle electronic states and optical properties. *Physical Review B*, *83*(3), p.035116.

70. Yu, Q., Kong, M., Liu, T., Fei, J. and Zheng, X., 2012. Characteristics of the decomposition of CO_2 in a dielectric packed-bed plasma reactor. *Plasma Chemistry and Plasma Processing*, *32*(1), pp.153-163.
71. Chirokov, A., Gutsol, A. and Fridman, A., 2005. Atmospheric pressure plasma of dielectric barrier discharges. *Pure and Applied Chemistry*, *77*(2), pp.487-495.
72. Meiners, A., Leck, M. and Abel, B., 2010. Efficiency enhancement of a dielectric barrier plasma discharge by dielectric barrier optimization. *Review of Scientific Instruments*, *81*(11), p.113507.
73. Nozaki, T., Muto, N., Kado, S. and Okazaki, K., 2004. Dissociation of vibrationally excited methane on Ni catalyst: Part 1. Application to methane steam reforming. *Catalysis Today*, *89*(1-2), pp.57-65.
74. Jeong, J.Y., Park, J., Henins, I., Babayan, S.E., Tu, V.J., Selwyn, G.S., Ding, G. and Hicks, R.F., 2000. Reaction chemistry in the afterglow of an oxygen− helium, atmospheric-pressure plasma. *The Journal of Physical Chemistry A*, *104*(34), pp.8027-8032.
75. Kasinathan, P., Park, S., Choi, W.C., Hwang, Y.K., Chang, J.S. and Park, Y.K., 2014. Plasma-enhanced methane direct conversion over particle-size adjusted MO_x/Al_2O_3 (M= Ti and Mg) catalysts. *Plasma Chemistry and Plasma Processing*, *34*(6), pp.1317-1330.
76. Thejaswini, H. C., Peglow, S., Sushkov, V., Hippler, R., 2014. Infrared Spectroscopy of CH_4/N_2 and C_2H_m/N_2 (m= 2, 4, 6) Gas Mixtures in a Dielectric Barrier Discharge. *Plasma Chem Plasma P.*, *34*(5), 1157-1170.
77. Holzer, F., Roland, U. and Kopinke, F.D., 2002. Combination of non-thermal plasma and heterogeneous catalysis for oxidation of volatile organic compounds: Part 1. Accessibility of the intra-particle volume. *Applied Catalysis B: Environmental*, *38*(3), pp.163-181.
78. Roland, U., Holzer, F. and Kopinke, F.D., 2005. Combination of non-thermal plasma and heterogeneous catalysis for oxidation of volatile organic compounds: Part 2. Ozone decomposition and deactivation of γ-Al_2O_3. *Applied Catalysis B: Environmental*, *58*(3), pp.217-226.
79. Ogata, A., Yamanouchi, K., Mizuno, K., Kushiyama, S. and Yamamoto, T., 1999. Decomposition of benzene using alumina-hybrid and catalyst-hybrid plasma reactors. *IEEE Transactions on Industry Applications*, *35*(6), pp.1289-1295.
80. Kim, H.H., Takashima, K., Katsura, S. and Mizuno, A., 2001. Low-temperature NOx reduction processes using combined systems of pulsed corona discharge and catalysts. *Journal of Physics D: Applied Physics*, *34*(4), p.604.

81. Bröer, S. and Hammer, T., 2000. Selective catalytic reduction of nitrogen oxides by combining a non-thermal plasma and a V_2O_5-WO_3/TiO_2 catalyst. *Applied Catalysis B: Environmental*, *28*(2), pp.101-111.

82. Miessner, H., Francke, K.P., Rudolph, R. and Hammer, T., 2002. NO_x removal in excess oxygen by plasma-enhanced selective catalytic reduction. *Catalysis Today*, *75*(1), pp.325-330.

83. Mok, Y.S., Koh, D.J., Kim, K.T. and Nam, I.S., 2003. Nonthermal plasma-enhanced catalytic removal of nitrogen oxides over V_2O_5/TiO_2 and Cr_2O_3/TiO_2. *Industrial & Engineering Chemistry Research*, *42*(13), pp.2960-2967.

84. Kušić, H., Koprivanac, N. and Locke, B.R., 2005. Decomposition of phenol by hybrid gas/liquid electrical discharge reactors with zeolite catalysts. *Journal of Hazardous Materials*, *125*(1), pp.190-200.

85. Wang, H., Li, J., Quan, X., Wu, Y., Li, G. and Wang, F., 2007. Formation of hydrogen peroxide and degradation of phenol in synergistic system of pulsed corona discharge combined with TiO_2 photocatalysis. *Journal of Hazardous Materials*, *141*(1), pp.336-343.

86. Bubnov, A.G., Burova, E.Y., Grinevich, V.I., Rybkin, V.V., Kim, J.K. and Choi, H.S., 2006. Plasma-catalytic decomposition of phenols in atmospheric pressure dielectric barrier discharge. *Plasma Chemistry and Plasma Processing*, *26*(1), pp.19-30.

87. Liu, C.J., Zou, J., Yu, K., Cheng, D., Han, Y., Zhan, J., Ratanatawanate, C. and Jang, B.W.L., 2006. Plasma application for more environmentally friendly catalyst preparation. *Pure and Applied Chemistry*, *78*(6), pp.1227-1238.

88. Whitehead, J.C., 2016. Plasma–catalysis: the known knowns, the known unknowns and the unknown unknowns. *Journal of Physics D: Applied Physics*, *49*(24), p.243001.

89. Fridman, A. Plasma Chemistry; Cambridge University Press: New York, 2008, p263.

90. Chen, H.L., Lee, H.M., Chen, S.H. and Chang, M.B., 2008. Review of packed-bed plasma reactor for ozone generation and air pollution control. *Industrial & Engineering Chemistry Research*, *47*(7), pp.2122-2130.

91. Veerapandian, S.K., Leys, C., De Geyter, N. and Morent, R., 2017. Abatement of VOCs using packed bed non-thermal plasma reactors: a review. *Catalysts*, *7*(4), p.113.

92. Van Durme, J., Dewulf, J., Leys, C. and Van Langenhove, H., 2008. Combining non-thermal plasma with heterogeneous catalysis in waste gas treatment: A review. *Applied Catalysis B: Environmental*, *78*(3-4), pp.324-333.

93. Vandenbroucke, A.M., Morent, R., De Geyter, N. and Leys, C., 2011. Non-thermal plasmas for non-catalytic and catalytic VOC abatement. *Journal of Hazardous Materials*, *195*, pp.30-54.

94. Van Durme, J., Dewulf, J., Sysmans, W., Leys, C. and Van Langenhove, H., 2007. Abatement and degradation pathways of toluene in indoor air by positive corona discharge. *Chemosphere*, *68*(10), pp.1821-1829.

95. Professor Paul Beasley, Head of R&D, Siemens plc UK, private communication.

96. Aerts, R., Somers, W. and Bogaerts, A., 2015. Carbon dioxide splitting in a dielectric barrier discharge plasma: a combined experimental and computational study. *ChemSusChem*, *8*(4), pp.702-716.

97. Martuzevicius, D.; Denafas, G.; Stasiulaitienė, I.; Abromaitis, V.; Ochmanaitė, V; Krugly, E.; Prasauskas, T. Report on Eco-Efficiency of Plasma-Based Technologies for Environmental Protection, Kaunas 2011, http://www.plastep.eu/fileadmin/dateien/Outputs/OP3-2.1_Eco-efficiency_report.pdf.

98. Kim, H.H., 2004. Nonthermal plasma processing for air-pollution control: a historical review, current issues, and future prospects. *Plasma Processes and Polymers*, *1*(2), pp.91-110.

99. Chen, H.L., Lee, H.M., Chen, S.H., Chang, M.B., Yu, S.J. and Li, S.N., 2009. Removal of volatile organic compounds by single-stage and two-stage plasma catalysis systems: a review of the performance enhancement mechanisms, current status, and suitable applications. *Environmental Science & Technology*, *43*(7), pp.2216-2227.

100. Chen, X., Rozak, J., Lin, J.C., Suib, S.L., Hayashi, Y. and Matsumoto, H., 2001. Oxidative decomposition of chlorinated hydrocarbons by glow discharge in PACT (plasma and catalyst integrated technologies) reactors. *Applied Catalysis A: General*, *219*(1), pp.25-31.

101. Chang, M.B. and Lee, H.M., 2004. Abatement of perfluorocarbons with combined plasma catalysis in atmospheric-pressure environment. *Catalysis Today*, *89*(1), pp.109-115.

102. Yu, S.J. and Chang, M.B., 2001. Oxidative conversion of PFC via plasma processing with dielectric barrier discharges. *Plasma Chemistry and Plasma Processing*, *21*(3), pp.311-327.

103. National Research Council, Plasma Science Committee and Plasma 2010 Committee, 2008. *Plasma science: advancing knowledge in the national interest* (Vol. 3). National Academies Press, http://www.nap.edu/catalog/11960/plasma-science-advancing-knowledge-in-the-national-interest p29-32.

104. Neyts, E.C., 2016. Plasma-surface interactions in plasma catalysis. *Plasma Chemistry and Plasma Processing*, *36*(1), pp.185-212.

105. Havran, V., Duduković, M.P. and Lo, C.S., 2011. Conversion of methane and carbon dioxide to higher value products. *Industrial & Engineering Chemistry Research*, *50*(12), pp.7089-7100.
106. Abd Allah, Z., Whitehead, J.C. and Martin, P., 2013. Remediation of dichloromethane (CH_2Cl_2) using non-thermal, atmospheric pressure plasma generated in a packed-bed reactor. *Environmental Science & Technology*, *48*(1), pp.558-565.
107. Kozák, T. and Bogaerts, A., 2014. Splitting of CO_2 by vibrational excitation in non-equilibrium plasmas: a reaction kinetics model. *Plasma Sources Science and Technology*, *23*(4), p.045004.
108. Sakiyama, Y., Graves, D.B., Chang, H.W., Shimizu, T. and Morfill, G.E., 2012. Plasma chemistry model of surface microdischarge in humid air and dynamics of reactive neutral species. *Journal of Physics D: Applied Physics*, *45*(42), p.425201.
109. Christensen, P.A., Ali, A.H.B.M., Mashhadani, Z.T.A.W. and Martin, P.A., 2018. A Direct Fourier Transform Infrared Spectroscopic Comparison of the Plasma-and Thermally-Driven Reaction of CO_2 at Macor. *Plasma Chemistry and Plasma Processing*, *38*(2), pp.293-310.
110. Christensen, P.A., Mashhadani, Z.T.A.W. and Ali, A.H.B.M., 2018. In situ FTIR studies on the oxidation of isopropyl alcohol over SnO_2 as a function of temperature up to 600° C and a comparison to the analogous plasma-driven process. *Physical Chemistry Chemical Physics*, *20*(14), pp.9053-9062.
111. Christensen, P.A., Mashhadani, Z.T., Md Ali, A.H.B., Carroll, M.A. and Martin, P.A., 2018. The Production of Methane, Acetone,"Cold" CO and Oxygenated Species from IsoPropyl Alcohol in a Non-Thermal Plasma: An In-situ FTIR Study. *The Journal of Physical Chemistry A*, *122*(17), pp.4273-4284.
112. Christensen, P.A., Ali, A.H.B.M., Mashhadani, Z.T.A.W., Carroll, M.A. and Martin, P.A., 2018. The Production of Ketene and C_5O_2 from CO_2, N_2 and CH_4 in a Non-thermal Plasma Catalysed by Earth-Abundant Elements: An In-situ FTIR Study. *Plasma Chemistry and Plasma Processing*, pp.1-24.
113. Schmidt-Bleker, A., Winter, J., Iseni, S., Dünnbier, M., Weltmann, K.D. and Reuter, S., 2014. Reactive species output of a plasma jet with a shielding gas device—combination of FTIR absorption spectroscopy and gas phase modelling. *Journal of Physics D: Applied Physics*, *47*(14), p.145201.
114. Rivallan, M., Aiello, S. and Thibault-Starzyk, F., 2010. Microsecond time-resolved Fourier transform infrared analytics in a low pressure glow discharge reactor. *Review of Scientific Instruments*, *81*(10), p.103111.

115. Li, K., Gabriel, O. and Meichsner, J., 2004. Fourier transform infrared spectroscopy study of molecular structure formation in thin films during hexamethyldisiloxane decomposition in low pressure rf discharge. *Journal of Physics D: Applied Physics*, *37*(4), p.588.
116. Stere, C.E., Adress, W., Burch, R., Chansai, S., Goguet, A., Graham, W.G. and Hardacre, C., 2015. Probing a non-thermal plasma activated heterogeneously catalyzed reaction using in situ DRIFTS-MS. *ACS Catalysis*, *5*(2), pp.956-964.
117. Rivallan, M., Fourré, E., Aiello, S., Tatibouët, J.M. and Thibault-Starzyk, F., 2012. Insights into the Mechanisms of Isopropanol Conversion on γ-Al_2O_3 by Dielectric Barrier Discharge. *Plasma Processes and Polymers*, *9*(9), pp.850-854.
118. Rodrigues, A., Tatibouet, J. M. and Fourre, E., 2016. Operando DRIFT Spectroscopy Characterization of Intermediate Species on Catalysts Surface in VOC Removal from Air by Non-thermal Plasma Assisted Catalysis. *Plasma Chemistry and Plasma Processing*, pp.1-15.
119. Barakat, C., Gravejat, P., Guaitella, O., Thévenet, F. and Rousseau, A., 2014. Oxidation of isopropanol and acetone adsorbed on TiO_2 under plasma generated ozone flow: Gas phase and adsorbed species monitoring. *Applied Catalysis B: Environmental*, *147*, pp.302-313.

Chapter 2. Experimental

This chapter describes the design, fabrication, characterization and modification of the InfraRed Non-Thermal Plasma IR NTP transmission and reflectance systems used to study the remediation of isopropyl alcohol. The synthesis of the SnO_2 nanopowders, the equipment and the techniques used to fabricate and characterize the SnO_2 nanopowders and the techniques used to characterize the CeO_2 nanopowders are also described.

2.1. Chemicals, materials, gases and equipment

The chemicals, materials, gases and equipment employed are summarized in table 2.1 and 2.2. All chemicals were used without further treatment.

Chemicals / Materials	Formula	Analysis	Supplier
Tin (IV) chloride pentahydrate	$SnCl_4.5H_2O$	Puriss min 98 %	Sigma-Aldrich
Silver nitrate	$AgNO_3$	99 %	Riedel-de Haen
Acetone	CH_3COOCH_3	Puriss 99 %	Fluka
Ethanol	C_2H_5OH	98 %	Fluka
Millipore water (DeIonised water, DI)	H_2O	18 MΩcm	Milli-Q system
Isopropyl alcohol	C_3H_8O	99.5 %	Sigma-Aldrich
Isophorone	3,5,5-Trimethyl-2-cyclohexen-1-one	97 %	Sigma-Aldrich
Potassium bromide	KBr	Spectroscopic grade	Alfa Aesar
Cerium (IV) oxide	CeO_2	99.995 %	Sigma-Aldrich
Nitrogen gas	N_2		Cryogenic boil-off
Nitrogen gas	N_2	N5.5 100 %	BOC
Argon gas	Ar	N5.5 100 %	BOC
Macor		Silicon 46 %, magnesium oxide 17 %,	Goodfellow Cambridge

		aluminium oxide 16 %, fluorine 4 %, potassium 10 % and boron 7 % [1]	
Ceramic wafer	Al_2O_3	96 %	Quik-ohm
Calcium fluoride windows	CaF_2	25 mm diameter, 3 and 2 mm thick	Crystran, UK
Stainless steel shim		0.07 mm	RS Components
Titanium mesh	Ti	50 % open area Thickness 0.07-0.1 mm	Dexment Corp, USA
Polytetrafluoroethylene	PTFE		RS Components
Stainless steel discs	316 S.S	25 mm	Holme & Dodsworth Metal
Stainless steel for the vessel	304 grade	90 mm diameter	Holme & Dodsworth Metal

Table 2.1. The chemicals, materials and gases employed in the work reported in this thesis.

Equipment	**Supplier**
Barnstead heating and stirring electromantle	MG Scientific
Harrier 15/80 centrifuge	MSE
Hydrothermal vessel	In house fabrication
MH-124 analytical balance	Fisherbrand
CB 162 hotplate and stirrer	Stuart
Ceramic boat	Shenzhen Jinghui Electronics Company Limited
Thermometer	Fisherbrand
N6C oven	Genlab Limited Thermal Engineers
Carbolite type 301 furnace (MC16-GB-C-1)	Barlword Scientific
Varian 670-IR spectrometer	Agilent
Varian 7000-IR spectrometer	Agilent

Specac environmental chamber and diffuse reflectance unit	Specac
Infrared Presslok holder	Thermo Scientific
NeonPro lamp transformer (NP100000-30)	Hyrite, China
Voltage controller	Carroll & Meynell
Gadget 13A Power meter (N67FU)	Maplin, UK
Flow meters	Roxspur Measurement & Control Ltd

Table 2.2. The equipment used in the work reported in this thesis.

2.2. Catalyst preparation

The tin oxide (SnO_2) nanopowders were synthesis by a hydrothermal process using a method adapted from that of Fujihara and co-workers [2] and Christensen et.al [3]. First, 7.01 gm of $SnCl_4.5H_2O$ was dissolved in 200 cm^3 DeIonised (DI) water with a resistivity 18 MΩcm to give a 0.1 M solution. The solution and a magnetic stirrer bar were transferred into a round-bottomed flask and the solution refluxed at ca. 95 °C for 3 hours to obtain a white slurry of SnO_2 as shown in figs. 2.1(a) & (b). The SnO_2 powder was then recovered by centrifuging and washing the solution many times with deionised water until no chloride ions were present, as shown by checking the aqueous layer after the centrifuge steps with 0.1 M $AgNO_3$ solution.

The stainless steel autoclave, cooling system and pressure system together comprised the hydrothermal equipment. These were designed and fabricated in-house and are shown in figs. 2.2(a) and (b). As can be seen from the figures, the white precipitate was transferred into a Teflon vessel with a round-bottom (melting point 327 °C and a volume of 80 cm^3) with lid, see fig. 2.2(a), and this vessel was inserted inside the stainless steel autoclave (with a round-bottom and volume of 150 cm^3) and sealed. The Teflon vessel was loosely sited in the stainless steel autoclave for safety, maintenance and cleaning issues, see fig. 2.2(b).

The autoclave was mounted in the oven, see fig. 2.2(c), at 180 °C for 24 hours under 10-15 bar pressure, after which it was allowed to cool to room temperature. The oven temperature was controlled using a thermocouple placed in the lid of the stainless steel reactor. The lid of the stainless steel reactor was also equipped with a pressure gauge, a relief valve set at 20 bar and a water cooling system to maintain the pressure inside the autoclave such that it did not exceed

the set point of 200 °C and 20 bar. For safety reasons, during the hydrothermal experiments, the temperature and pressure were recorded and compared with those expected on the basic of the plot of water boiling point versus pressure as shown in fig. 2.3. As can be seen from the figure, the pressure should be around 20 bar or less at a temperature of 200 °C. During the experiments if there was any deviation from this pressure, the experiment would be stopped immediately. Such a deviation could be due to overheating or a leak in the system, which can lead to explosion or insufficient pressure, respectively.

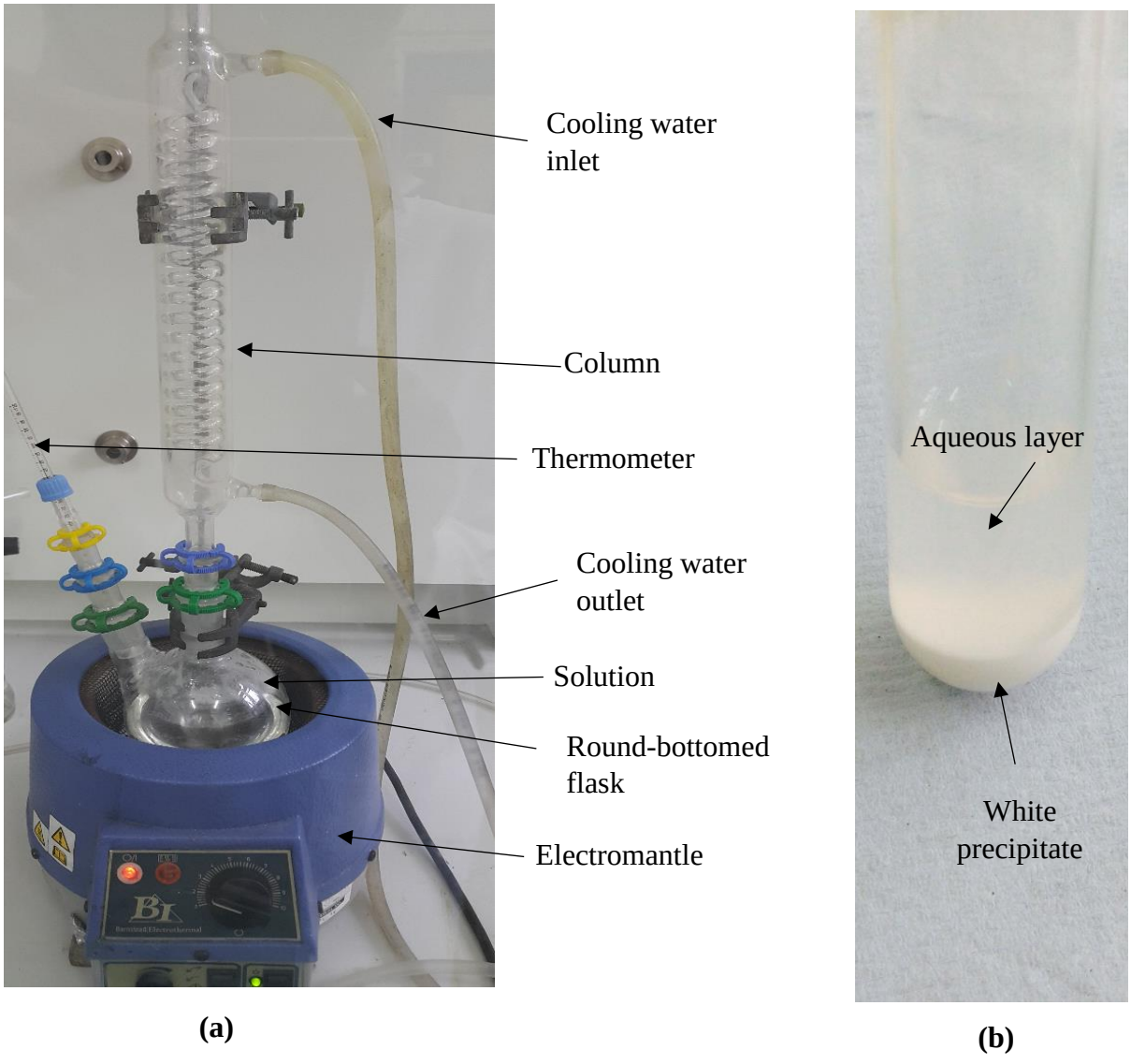

Figure 2.1. Photographs of (a) the reflux apparatus and (b) the white precipitate produced after the reflux process, centrifuging and washing with DI water.

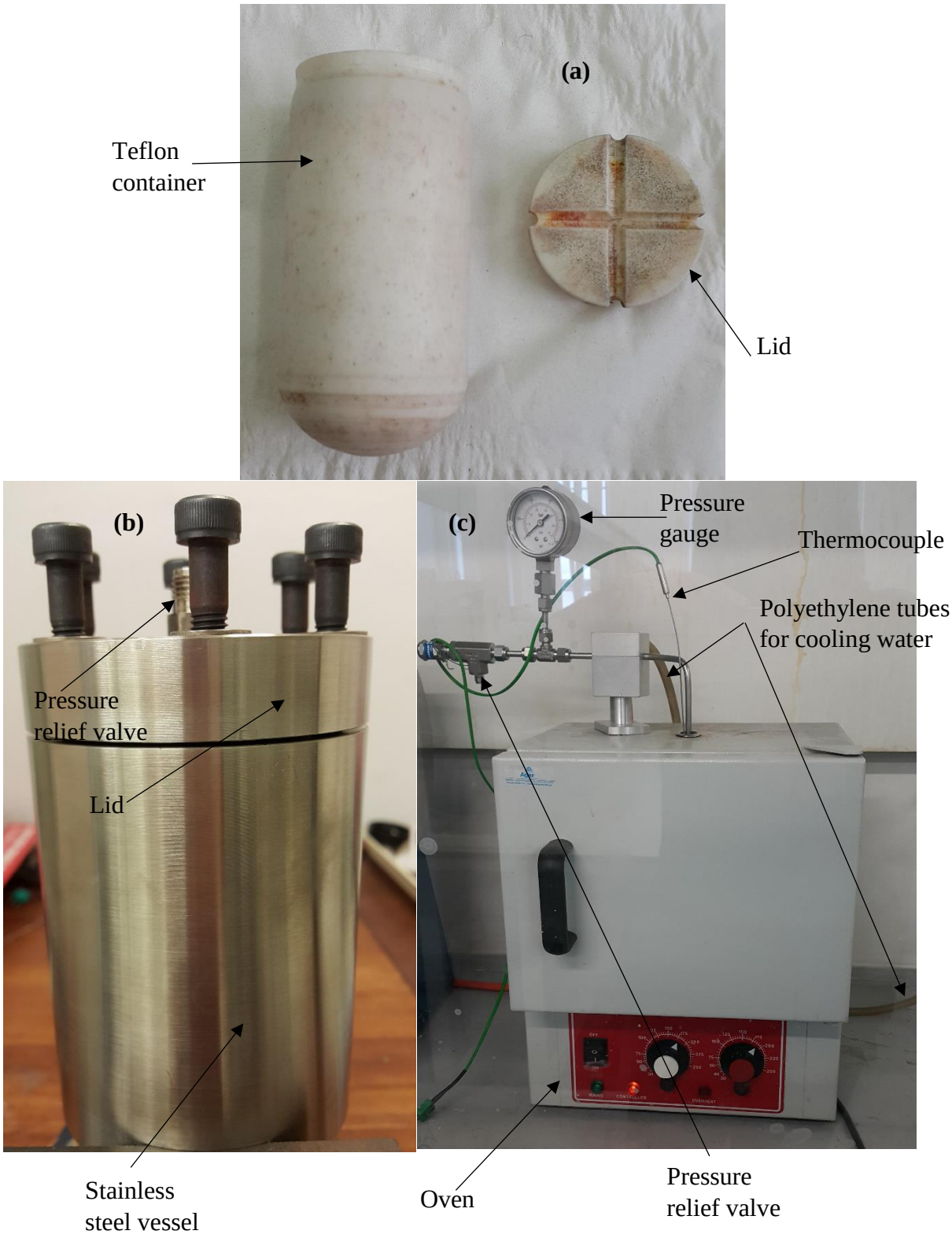

Figure 2.2. Photographs of the hydrothermal synthesis apparatus: (a) Teflon container, (b) stainless steel autoclave and (c) hydrothermal reactor.

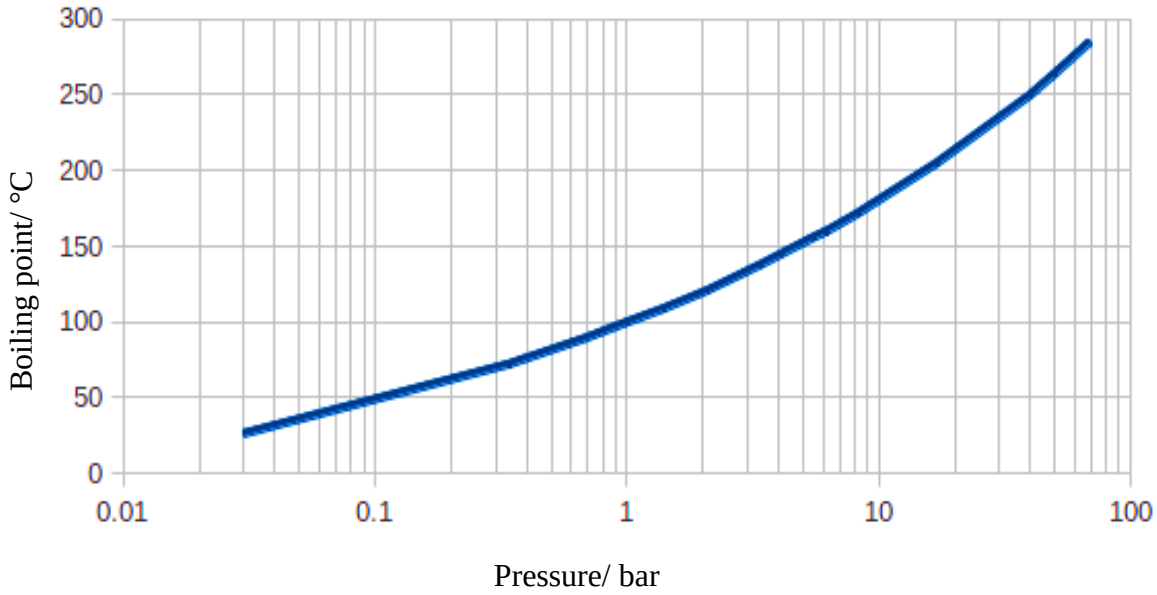

Figure 2.3. The variation of the boiling point of water vs. pressure [4].

After the hydrothermal step, the white wet precipitate was then rinsed with deionised water several times in the centrifuge until there was no more Cl^- ions present in sample (as determined by the addition of $AgNO_3$ solution) and transferred into an evaporating dish. The precipitate was then dried in an oven overnight at 60 °C and ground in a mortar and pestle as shown in figs. 2.4(a) - (c). Finally, the nanopowder was divided into two samples which were calcined in air in a recirculating air furnace at 400 °C and 700 °C: the synthesis procedure is summarized in fig. 2.5.

(a) **(b)** **(c)**

Figure 2.4. Photographs of the white slurry after: (a) the hydrothermal process, (b) drying in the oven for the overnight and (c) the grinding nanopowders after drying.

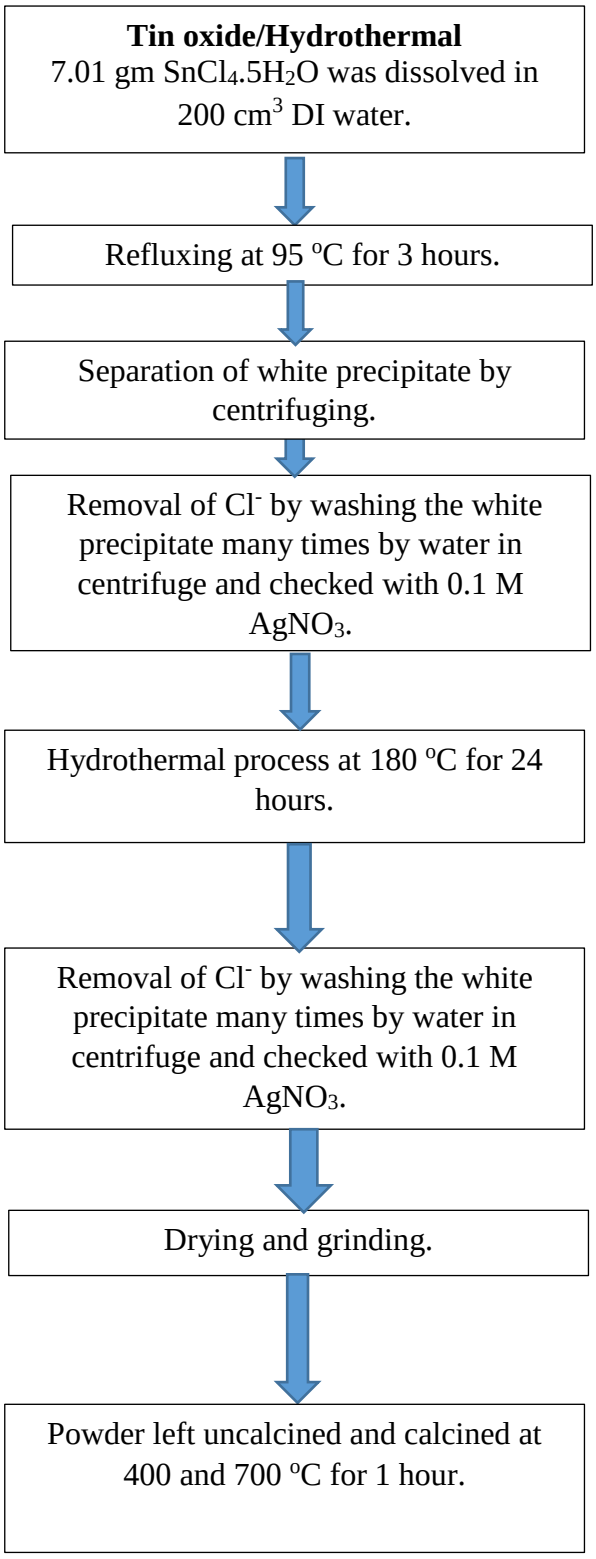

Figure 2.5. The procedure for preparing tin oxide nanopowders via the hydrothermal method.

2.3. X-ray diffraction

X-Ray Diffraction (XRD) data were obtained using PANalytical X'Pert Pro MPD, powered by a Philips PW3040/60 X-ray generator, fitted with an X'Celerator detector, see fig 2.6.

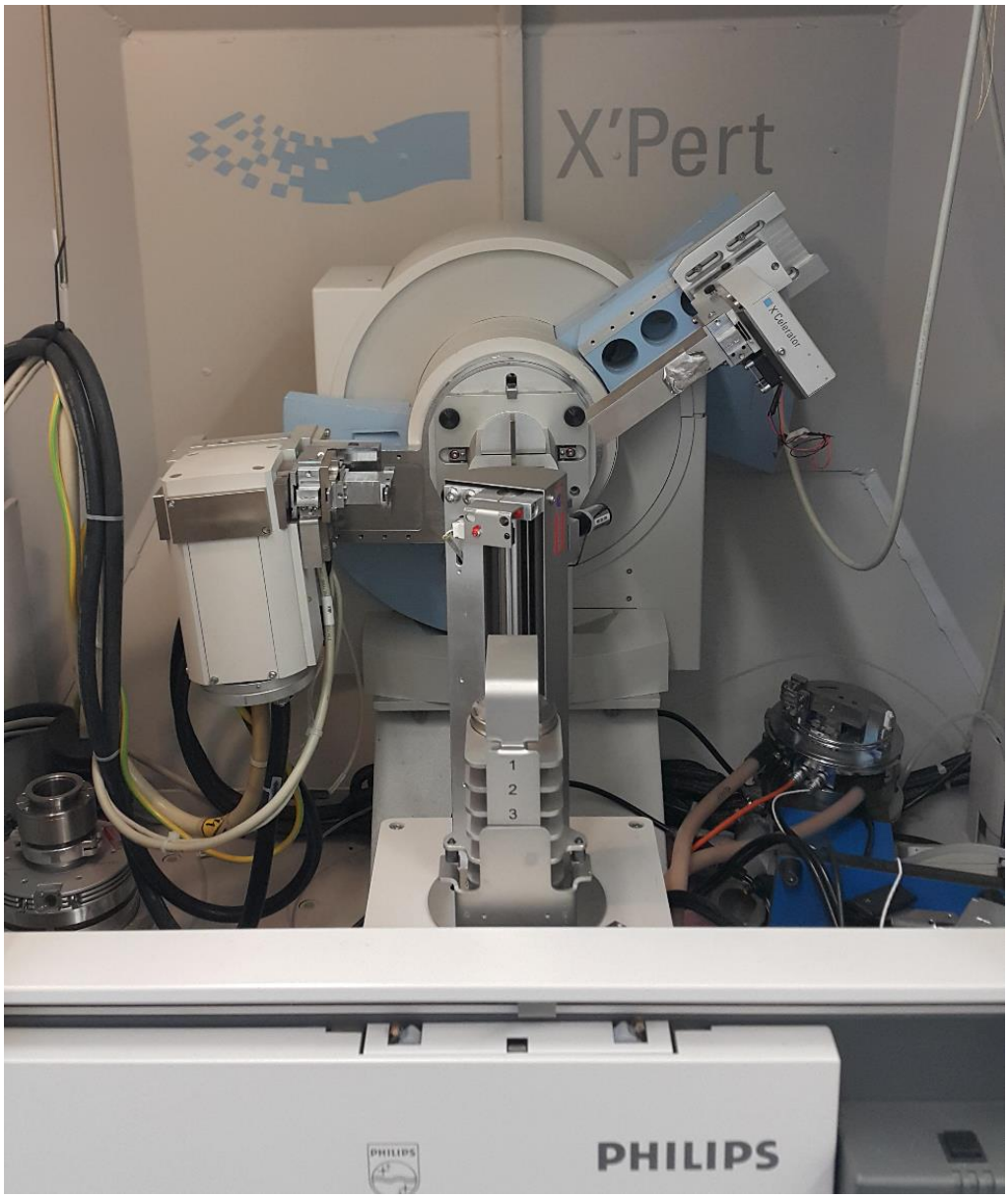

Figure 2.6. A photograph of the PANalytical X'Pert Pro MPD X-Ray diffractometer.

The powder sample was exposed to Cu-Kα X-ray radiation, which has a characteristic wavelength (λ) of 1.5418 Å. The X-ray source employed a Cu anode operating at 40 kV and a current of 40 mA. The ultra-fast X-ray detector X'Celerator uses RTMS (Real Time Multiple Strip) technology. This technology can simultaneously detect X-rays diffracted from a sample

over the range of 2θ angles during a scan using an array of a hundred channels. As a result, high quality diffraction data are produced by the X'Celerator in a significantly shorter time period than older style diffractometers would require.

By using the scanning X'Celerator detector with a nickel filter that can be fitted on the incident beam, the data were collected in reflection mode over the range 2-100°2θ with a step size of 0.0334°2θ and nominal time per step of 400 s. In addition, anti-scatter and divergence slits of 1/4 ° were used and fixed together with a 10 mm beam mask. Otherwise, all scans were carried out in 'continuous' mode.

The X'Pert accompanying software program PANalytical High Score Plus in conjunction with the ICDD Powder Diffraction File 2 Database (2004), ICDD Powder Diffraction File 4 - Minerals (2018), and the Crystallography Open Database (2016) were used to identify and analyse the catalyst phases.

Braggs Law was can be employed to determine the d-spacing according to:

$$2d_{hkl}\sin\Theta = n\lambda \quad (2.1)$$

where Θ is the angle of incidence of the X-ray radiation, d_{hkl} is the distance between atomic layers in the crystal, λ is the wavelength of the incident X-ray beam and n is an integer as shown in fig. 2.7.

To determine the average particle size, Scherrer's equation [5] was used using the Full Width at Half Maximum (FWHM) intensity of selected peaks as shown below:

$$t = 0.9\lambda/B.\cos\theta \quad (2.2)$$

where t is the particle size (Å), λ is the wavelength of the Cu Kα radiation (1.5406 Å), B is the FWHM in radians and θ is the Bragg angle.

All XRD tests were carried out by Mrs Maggie White, the School of Engineering, Newcastle University.

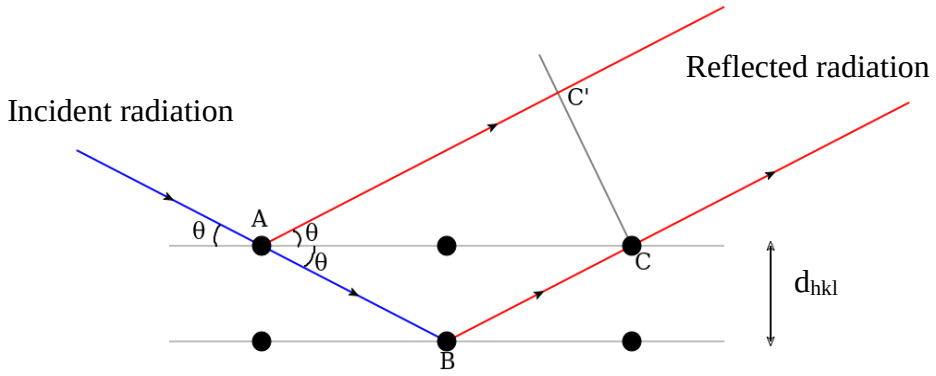

Figure 2.7. The incident and reflected X-rays at crystal planes.

2.4. Thermogravimetric analysis system

ThermoGravimetric Analysis **(**TGA) were carried out for CeO_2 sample in an atmosphere of flowing (40 cm^3 min^1) nitrogen, in a Netzsch STA 449C TG-DSC (ThermoGravimetry-Differential Scanning Calorimetry) system, see fig. 2.8, connected to a Netzsch Aeolos 403C Quadrupole Mass Spectrometer (QMS; m/z range 10-300). 55.5 mg of the CeO_2 was placed in an alumina crucible. A heating rate of 5 °C min^{-1} was used from 25 °C – 600 °C, the temperature held at 600 °C for 10 minutes then sample was cooled at 5 °C min^{-1} to room temperature. Run 1 was carried out on day1 and the sample left in air overnight. Run 2 was carried out on day 2 and the sample left in flowing nitrogen overnight and run 3 carried out the following day. The TGA measurements were carried out by Dr. Bernard Bowler, School of Engineering, Newcastle University.

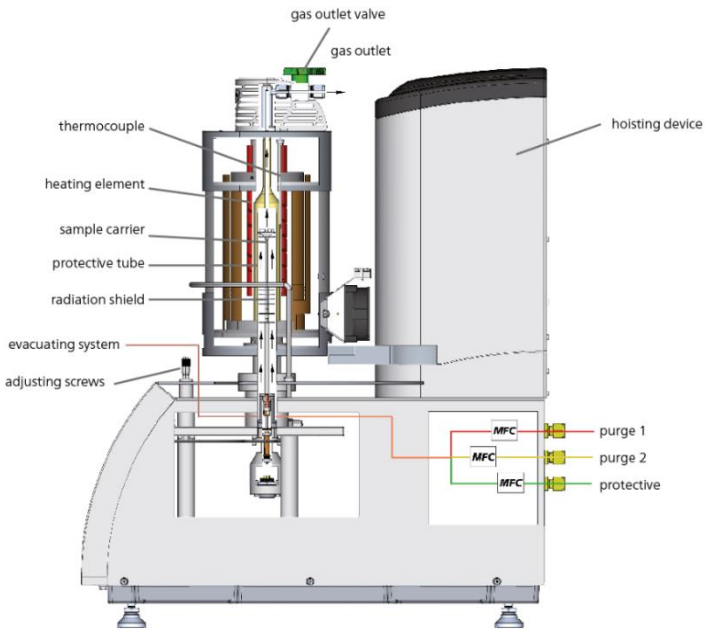

Figure 2.8. The Netzsch STA 449C TG-DSC equipment.

2.5. Thermal Fourier Transform Infrared Spectroscopy

In-situ thermal Fourier Transform Infra-Red Spectroscopy (FTIR) experiments as a function of temperature were carried out using a Varian 670-IR spectrometer equipped with a ceramic air-cooled infrared source, a Deuterated Lanthanum alaine doped TriGlycine Sulphate (DLaTGS) detector and a Specac environmental chamber and diffuse reflectance unit utilizing a ZnSe window [3][6], see fig. 2.9.

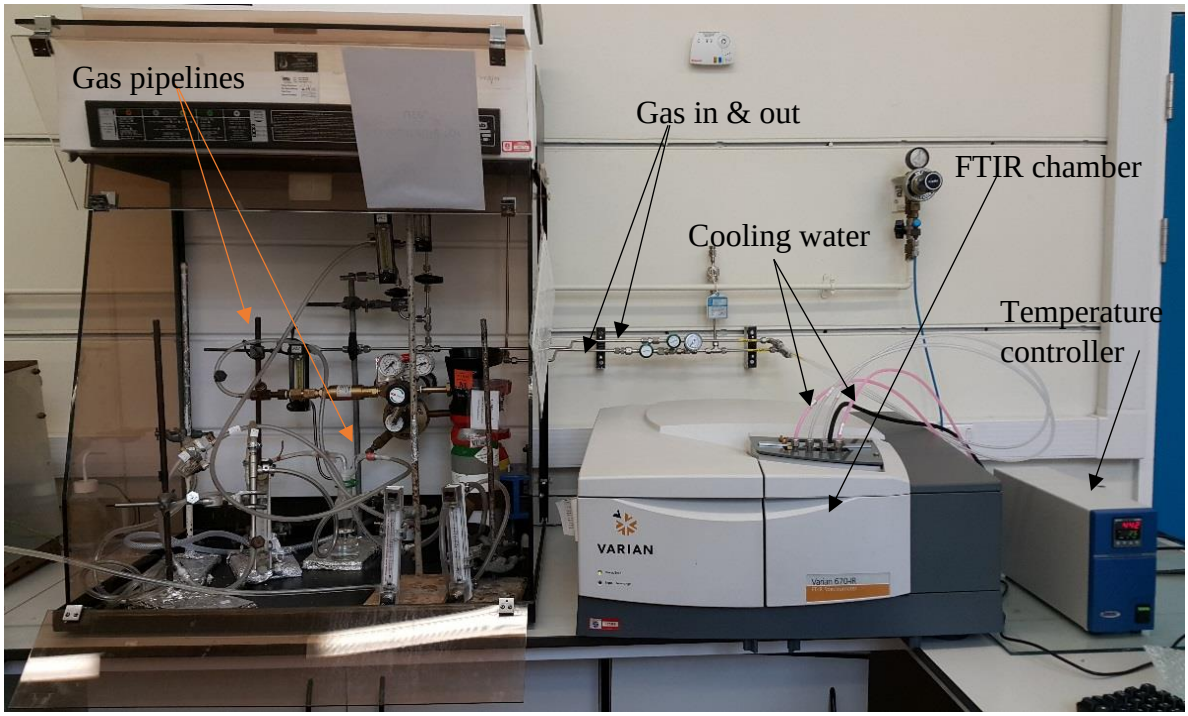

Figure 2.9. Photograph of the Varian 670-IR FTIR spectrometer.

The Specac reflectance accessory see figs. 2.10(a) & (b), allows IR spectra to be collected under controlled atmosphere conditions from room temperature up to 600 °C and pressures from vacuum to 34 atm. The IR beam was incident on the sample in the cell at angles from 20° to 76° with respect to the horizontal plane via a ZnSe window as shown in fig. 2.10(c) and a schematic diagram of the optical bench can be seen in fig. 2.10(d).

In the FTIR data analyses: S_S (sample) is the single beam spectra of the powder or solid sample and S_R (standard powder) is the single beam of the standard reference powder (spectroscopic grade KBr). Usually, the sample powder had to be diluted and this was done using the reference powder. A diffuse reflectance spectrum of the KBr using a mirror as reference was employed to check the purity of the KBr.

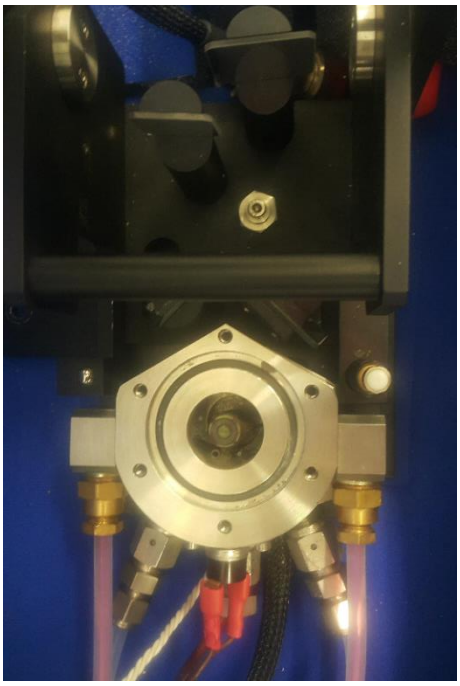

(a)

(b)

(c)

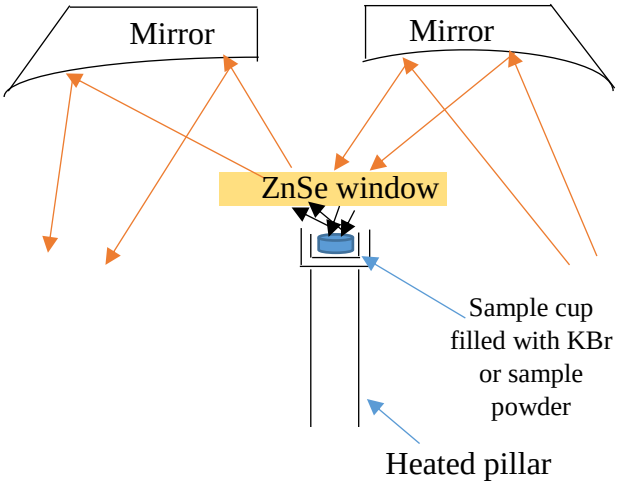

(d)

Figure 2.10. Photographs of: (a) the Specac accessory without cover, (b) the diffuse reflectance unit, (c) the cover with its ZnSe window and (d) schematic diagram of the optical bench and the sample holder.

Three different materials were assessed for catalytic activity: a Macor disk (12.5 mm diameter, 2 mm thick), nanoparticulate SnO_2 calcined at 400 ºC and 700 ºC, and CeO_2 powder. For each catalyst, the experiment was carried out using pure nitrogen gas (blank experiments) or nitrogen gas bubbled through a Dreschel bottle containing IPA at room temperature. In both cases, the gas flow rate of (N_2 or N_2/IPA) was fixed at 200 cm^3 min^{-1}.

Taking SnO_2 to exemplify a typical experiment: using pure KBr in the sample cup of the environmental chamber and a single beam spectrum (S_R, 100 co-added and averaged scans at 4 cm^{-1} resolution, ca. 2 minutes per scanset) was collected at 25 ºC under N_2 gas flow rate at 200 cm^3 min^{-1}. The KBr was then replaced by SnO_2/KBr (20 mg of SnO_2 + 80 mg of KBr) and a second reference spectrum (S_R, 100 co-added and averaged scans at 4 cm^{-1} resolution, ca. 2 minutes per scanset) taken under the same conditions (25 ºC under flowing N_2). This procedure allowed the option to choose the most appropriate reference spectrum. The chamber was then isolated from the gas flow and a sample spectrum Ss (S_S, 100 co-added and averaged scans at 4 cm^{-1} resolution, ca. 2 minutes per scanset) collected at 25 ºC. The temperature of the sample was then increased at 5 °C min^{-1} and a further spectrum collected at 50 ºC, after which spectra S_S were collected every 50 ºC up to 600 ºC. The experimental procedure and equipment are summarized in figs. 2.11(a) & (b).

When using powder samples, the single beam spectra were ratioed to give reflectance, R:

$$R = (S_S / S_R) \quad (2.3)$$

and then converted to an effective absorption using the Kubelka– Munk function [7]:

$$KM = (1-R)^2/2R \quad (2.4)$$

where KM is the Kubelka-Munk function and R is the reflectance of a sample at infinite depth. However, R cannot determined absolutely, but it is usually calculated by dividing the reflected intensity of the sample by the spectrum of a standard, for example KBr.

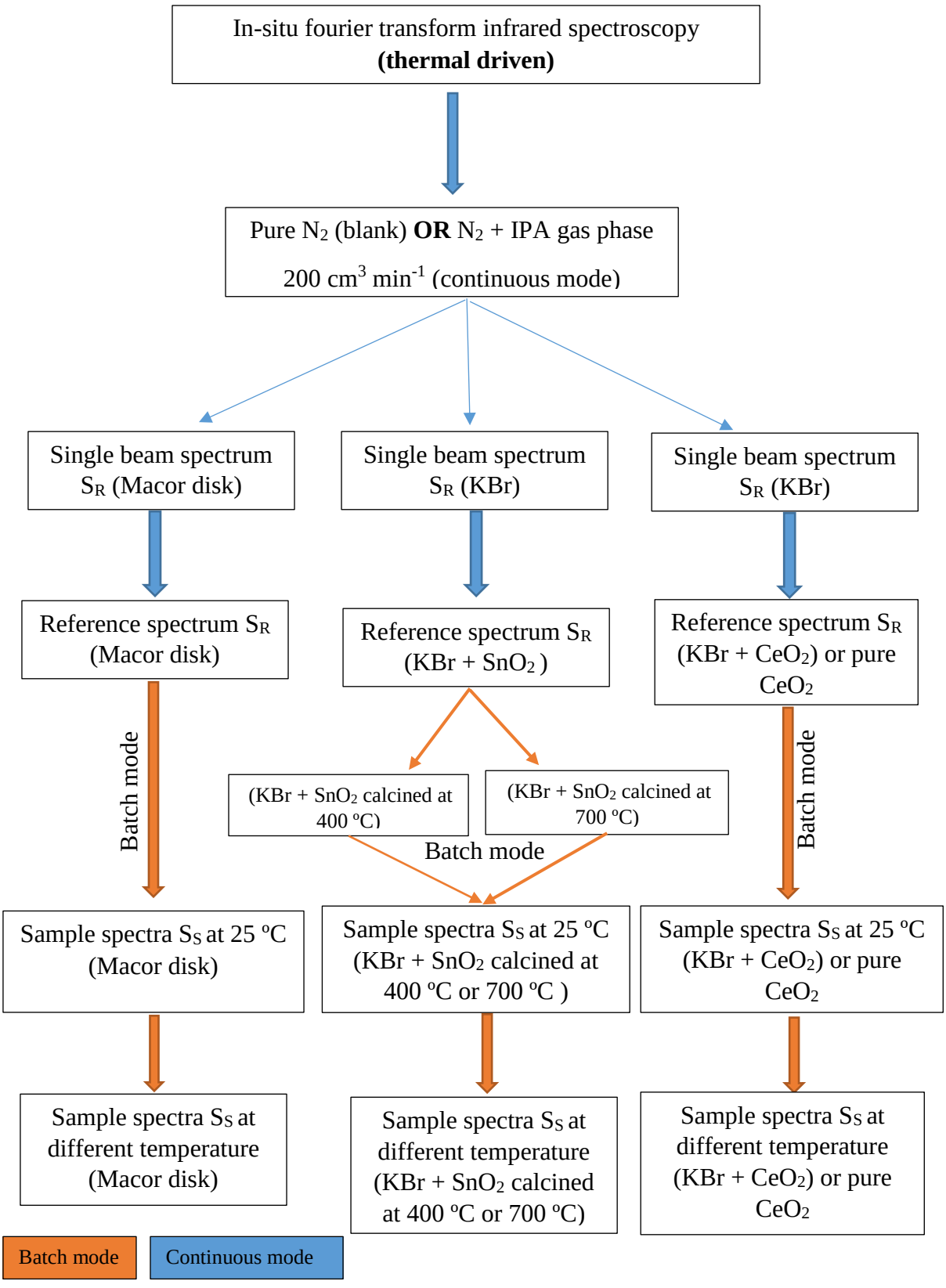
In-situ fourier transform infrared spectroscopy
(thermal driven)
Pure N2 (blank) OR N2 + IPA gas phase
200 cm3 min-1 (continuous mode)
Single beam spectrum SR (Macor disk)
Single beam spectrum SR (KBr)
Single beam spectrum SR (KBr)
Reference spectrum SR (Macor disk)
Reference spectrum SR (KBr + SnO2)
Reference spectrum SR (KBr + CeO2) or pure CeO2
Batch mode
(KBr + SnO2 calcined at 400 ºC)
(KBr + SnO2 calcined at 700 ºC)
Batch mode
Batch mode
Sample spectra SS at 25 ºC (Macor disk)
Sample spectra SS at 25 ºC (KBr + SnO2 calcined at 400 ºC or 700 ºC)
Sample spectra SS at 25 ºC (KBr + CeO2) or pure CeO2
Sample spectra SS at different temperature (Macor disk)
Sample spectra SS at different temperature (KBr + SnO2 calcined at 400 ºC or 700 ºC)
Sample spectra SS at different temperature (KBr + CeO2) or pure CeO2
Batch mode
Continuous mode

(a)

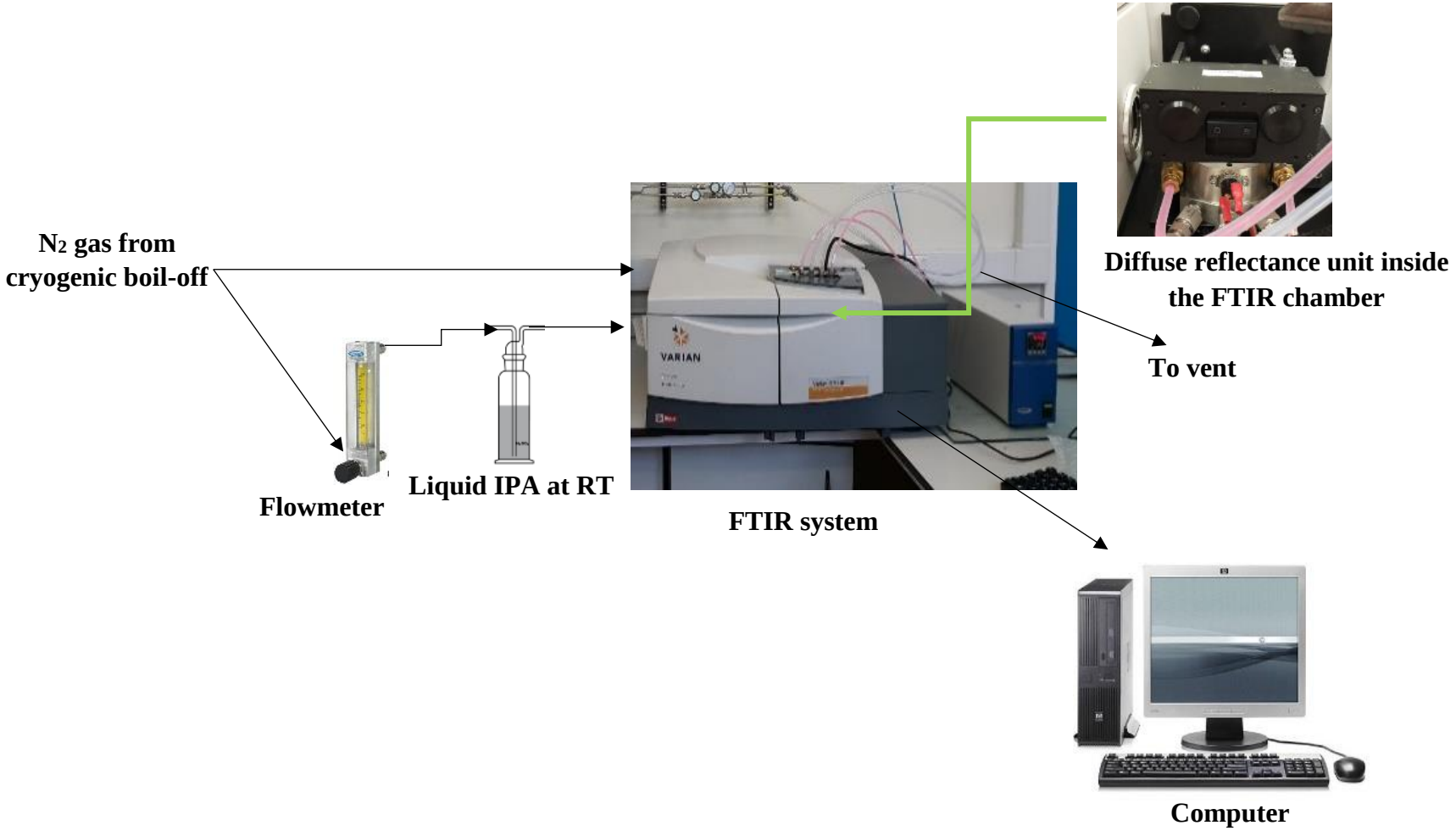

Figure 2.11. (a) The experimental procedure and (b) a schematic diagram of the thermal experiments.

The KM function is employed to annul the effect specularly reflected light, see fig. 2.12. This data manipulation results in difference spectra in which peaks with positive amplitude arise from the gain of absorbing species in S_S with respect to S_R, and peaks with negative amplitude to the loss of absorbing species. In order to remove unchanging absorptions, spectra were simply subtracted from each other (eg $KM_{600\ ^oC} - KM_{300\ ^oC}$); ie. no subtraction factor was employed.

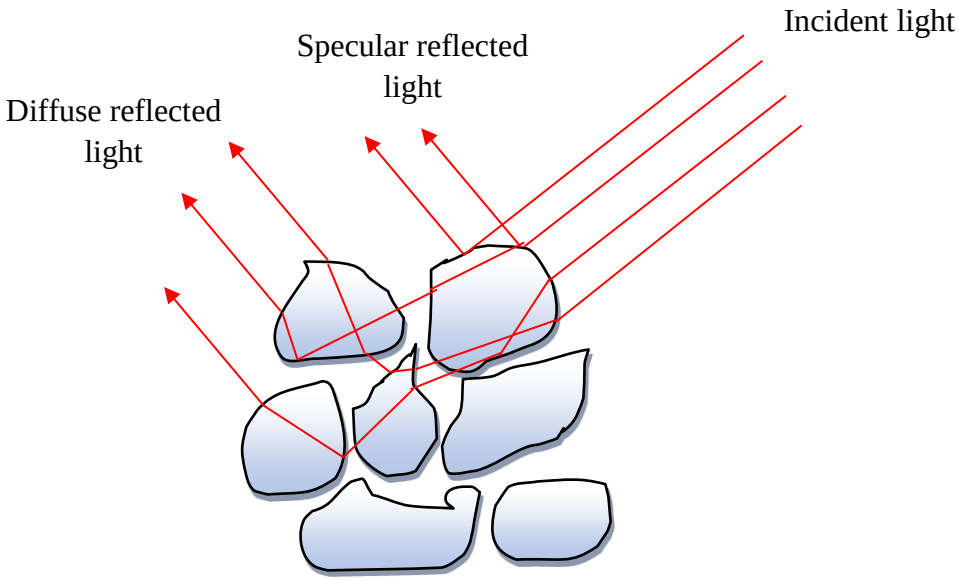

Figure 2.12. A schematic representation of the specular and diffuse reflection of light from a powdered sample.

When using the Macor disc, the single beam spectrua were simply manipulated to give absorbance spectra:

$$A = \log_{10} (S_R / S_S) \quad (2.5)$$

2.6. The Plasma Fourier Transform Infrared Spectrometer

An Agilent FTS7000 FTIR spectrometer with a Deuterated Tri-Glycine Sulfate (DTGS) detector was employed, see fig. 2.13. The IR beam was passed through the plasma via the two CaF_2 windows to the detector via an Amtir-1 filter, 25 mm x 2 mm (Spectra-Tech, USA) to remove visible light, and the IR beam intensity was reduced where necessary using metal grids to prevent detector saturation.

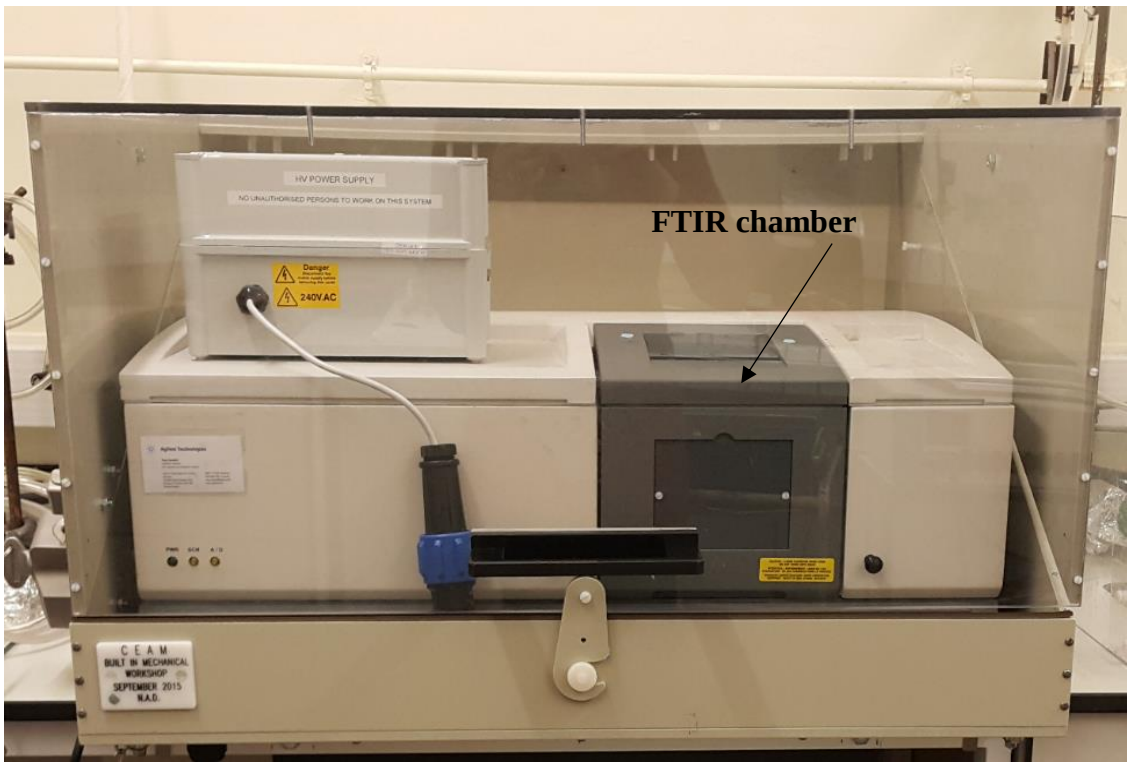

Figure 2.13. A photograph of the Agilent FTS7000 spectrometer.

2.7. The infrared non-thermal plasma transmission cell

An in-house built, NTP transmission cell was employed as shown in figs. 2.14(a) & (b).

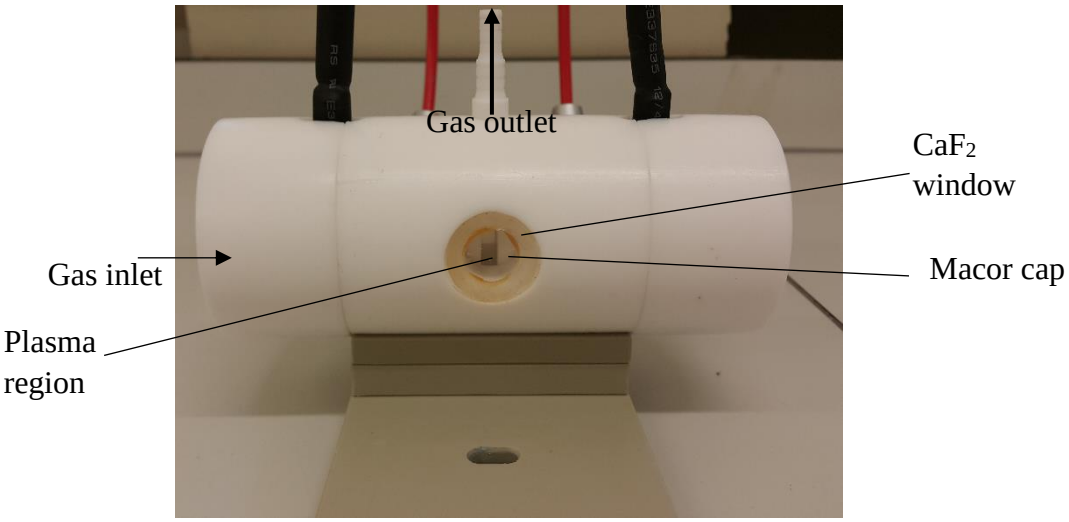

(a)

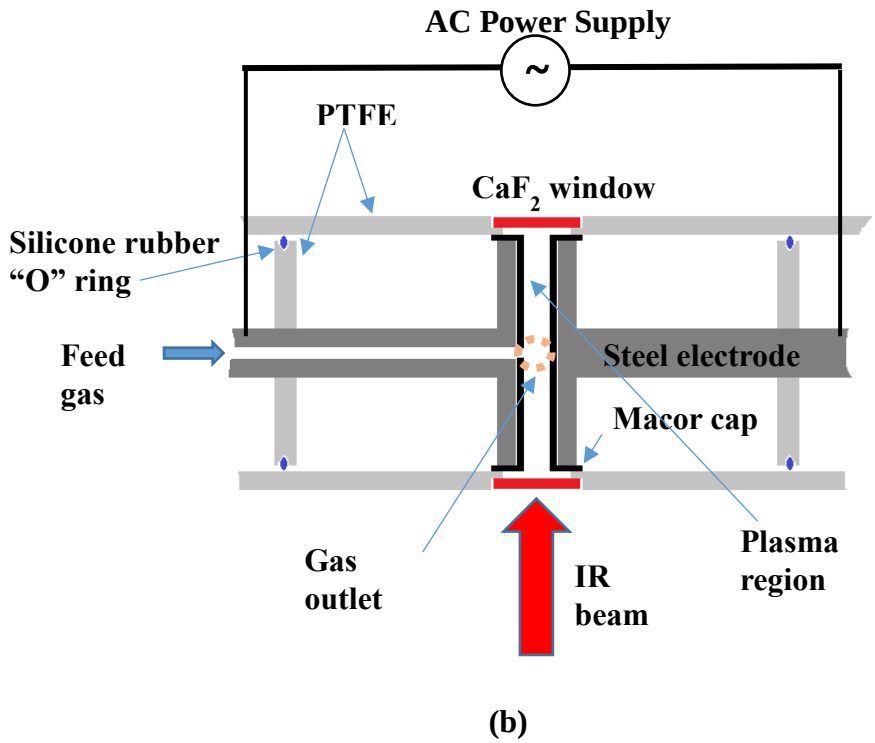

Figure 2.14. (a) A photograph and (b) schematic of the in-situ FTIR NTP transmission cell.

The cell consisted of 15 cm long, cylindrical PolyTetraFluoroEthylene (PTFE) tube with an outer diameter of 6.3 cm and an inner diameter of 2.5 cm. The high voltage electrodes were in the form of two plungers in the PTFE tube so they could be easily taken out of the cell for cleaning and then inserted again, sealing against the inner walls of the cell via PTFE and silicone rubber 'O' rings. One plunger was hollow down its axis (a 5 mm diameter hole) and the feed gas was delivered via this channel and removed via an outlet nozzle in the top of the cell. The electrodes consisted of stainless steel discs (316 S.S.) 2.3 cm in diameter and 2 mm thick, mounted over stainless steel shafts. The electrodes were covered with 5 mm thick and 2.5 cm diameter Macor caps fitted snugly over each stainless steel disc electrode to act as the dielectric, with a hole aligned with the central, gas delivery channel. Macor can be defined as a white, odourless ceramic comprising 55 % Fluorophlogopite mica ($KMg_3(AlSi_3O_{10})(FOH)_2$) and 45 % borosilicate glass. It considered as an excellent dielectric with good thermal stability [1]. Macor might therefore be expected to show some of the catalytic activity of zeolites, however, which are typically comprised of Al and Si are well known to show catalytic activity in thermally driven processes [8].

Two infrared transparent CaF_2 windows (25 mm diameter, 3 mm thick) were glued into the PTFE cell. The distance between the windows (path length) was 5.1 cm. The windows were

positioned such that their centres aligned with the centre of the 5 mm gap between the electrodes as shown in fig. 2.14.

The electrodes were connected to a NeonPro lamp transformer, NP100000-30 which provided an output up to 10 kV at a constant frequency of 24 kHz, see fig. 2.15(a). A voltage controller was used to control the input power to the HV transformers see fig. 2.15(b). The input power to the plasma was monitored using the Gadget 13 A Power Meter; the input powers quoted were those obtained by subtracting the input power observed with plasma from the reading obtained with the system switched on but with no plasma initiated (4 W).

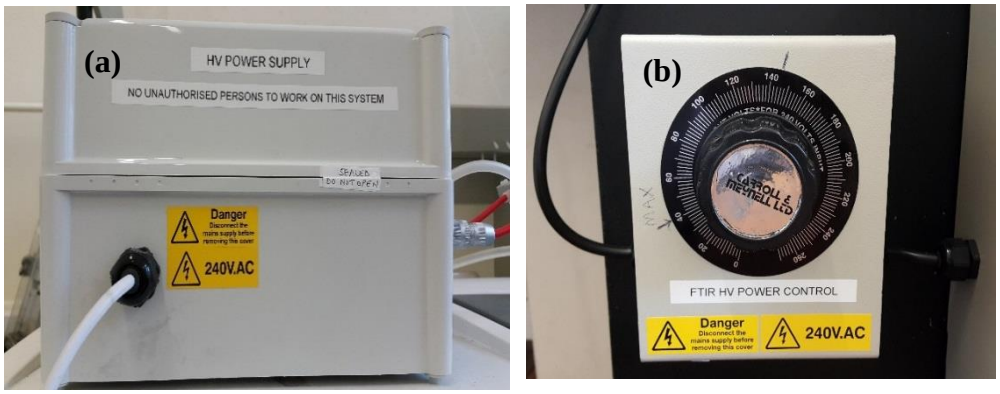

Figure 2.15. Photographs of (a) the HV generator and (b) the voltage controller.

2.7.1. The development of the transmission cell

Initial experiments were carried out using PTFE caps of thickness 3, 5, 7 and 10 mm, see fig. 2.16(a). As can be seen from the figure, the caps had a hole in the centre as inlet and outlet port for the gas used to produce plasma. All caps were tested inside the NTP cell to see if a stable plasma could be produced without arcing.

The 3 and 5 mm thick PTFE caps were susceptible to degradation by the plasma, see fig. 2.16(b); as can be seen from the figure, the caps were damaged during operation due to arcing. Plasma could not be generated using the 7 and 10 mm PTFE caps presumably because they were too thick [9].

The 5 mm thick Macor caps were then fabricated also with a hole in the centre, and modified such that they extended beyond the electrode disc to eliminate any chance of arcing, see figs. 2.16(c) & (d).

The initial design had central channels in both plungers, see fig. 2.16(e) and the next modification step was to employ only one Macor cap with a central channel for the inlet of the feed gas, see fig. 2.16(f), and the cell modified to include an outlet on top as shown in fig. 2.14(a).

Figure 2.16(g) shows a photograph of the stable plasma obtained using the final design of NTP transmission cell. A photograph was taken using a small mirror attached inside the FTIR chamber after opening the front port lid of the chamber. The plasma volume in the transmission cell was 7.4 cm^3 and the residence time at a flow rate of 200 cm^3 min^{-1} was 2.2 seconds.

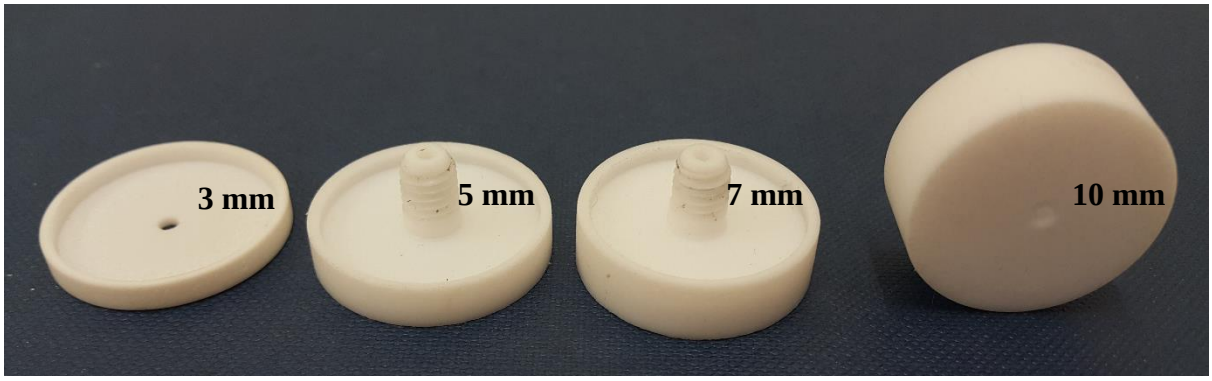

(a)

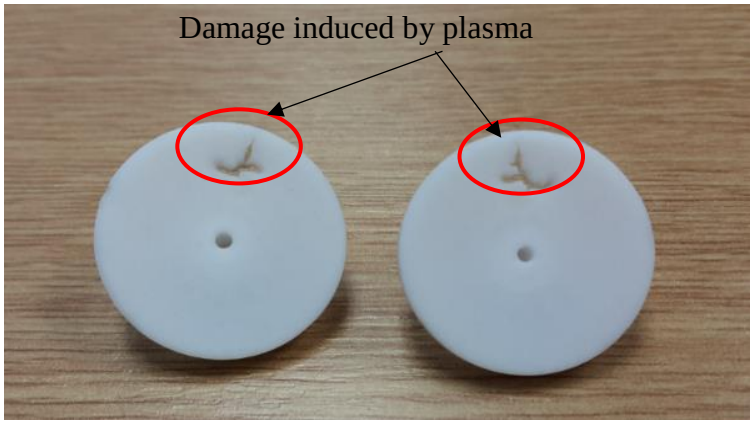

(b)

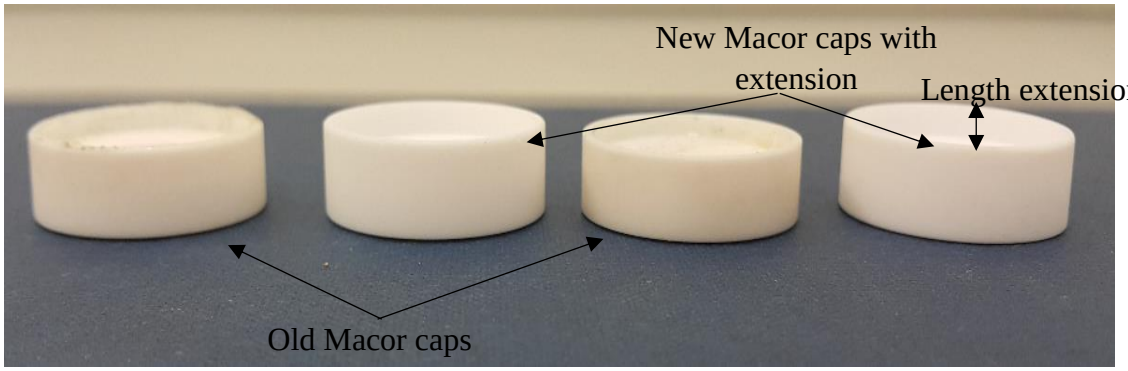

(c)

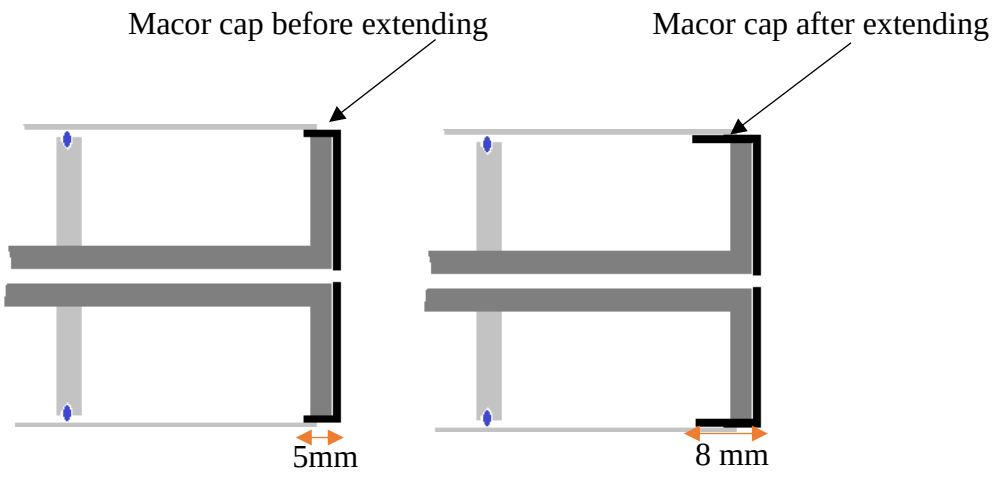
Macor cap before extending
Macor cap after extending
5mm
8 mm

(d)

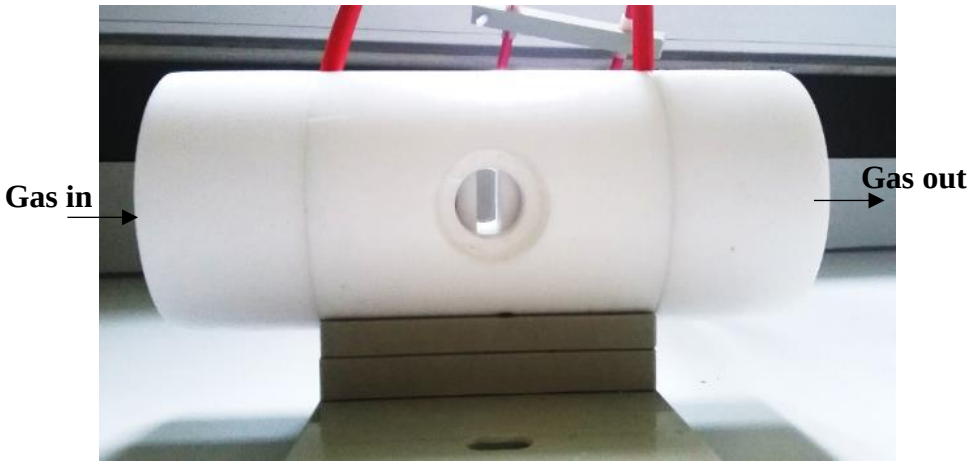
Gas in
Gas out

(e)

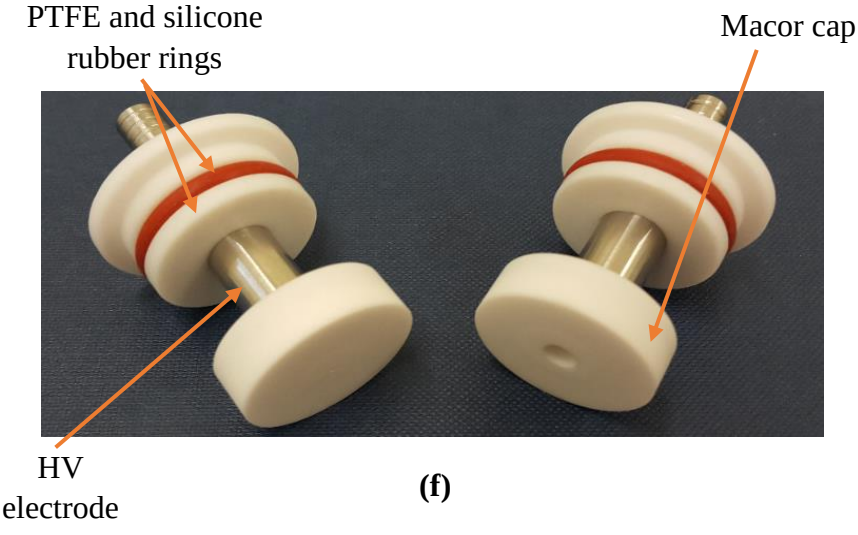
PTFE and silicone rubber rings
Macor cap
HV electrode

(f)

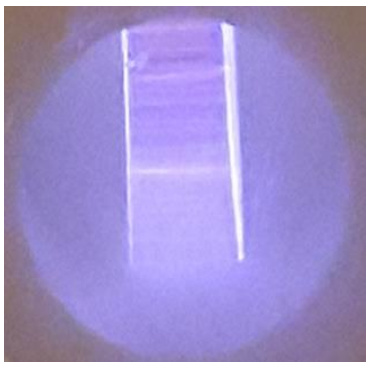

(g)

Figure 2.16. Photographs of: (a) The PTFE caps of different thickness, (b) the damage caused to the PTFE caps during plasma operation, (c) a photograph & (d) schematic of the modification of the Macor cap, (e) the previous design of the in-situ FTIR NTP cell, (f) the 'piston' high voltage electrodes and (g) a stable non-thermal plasma generated between the Macor caps.

2.8. The infrared non-thermal plasma reflectance cell and optical bench

The IR NTP reflectance cell was built in-house and based on the (non-spectroscopic) surface dielectric barrier discharge cell design of Šimek and co-workers [10], see figs. 2.17(a), (b) and 2.18. The cell was rectangular, 12.7 cm x 9.5 cm x 3.5 cm, and fitted with cooling channels and channels for the input and exhaust of the feed gas. A stainless steel shim 2.3 cm x 2.2 cm x 0.07 mm was employed as one electrode, hidden from the IR beam, below which was a Al_2O_3 wafer, 4 cm x 4.9 cm x 0.1 cm and a 3 cm x 3 cm x 0.5 cm Macor plate. The area of Macor and Al_2O_3 wafer was 9 cm^2 and 19.6 cm^2 respectively. The Macor was covered by the second, Ti mesh electrode (50 % open area) and both the Ti mesh and Macor were irradiated by the IR beam via a CaF_2 plate window (25 mm diameter, 2 mm thick). The gap between the Macor and the window was 5 mm.

The same power supply was employed for the reflectance cell as for the transmission cell. In contrast to the transmission cell, which generated a volume discharge [11] between the two Macor caps, the reflectance cell generated a surface discharge across the Macor and Ti mesh [10][11]. The plasma occupied the whole volume between the Macor and window in the reflectance cell, 2 cm^3, and the residence time at a flow rate of 30 cm^3 min^{-1} was 4 seconds.

Figures 2.19(a) and (b) show the in-house built optical bench which consisted of two mirrors at an angle of 57° to the vertical, 45 mm above the floor of the sample compartment and 100 mm apart. The mirrors were positioned such that the angle of incidence on the CaF_2 window was 24° and on 24° on the Macor. In addition, a sheet of cardboard was inserted between the two mirrors to prevent any of the IR beam bypassing the mirrors and reaching the detector.

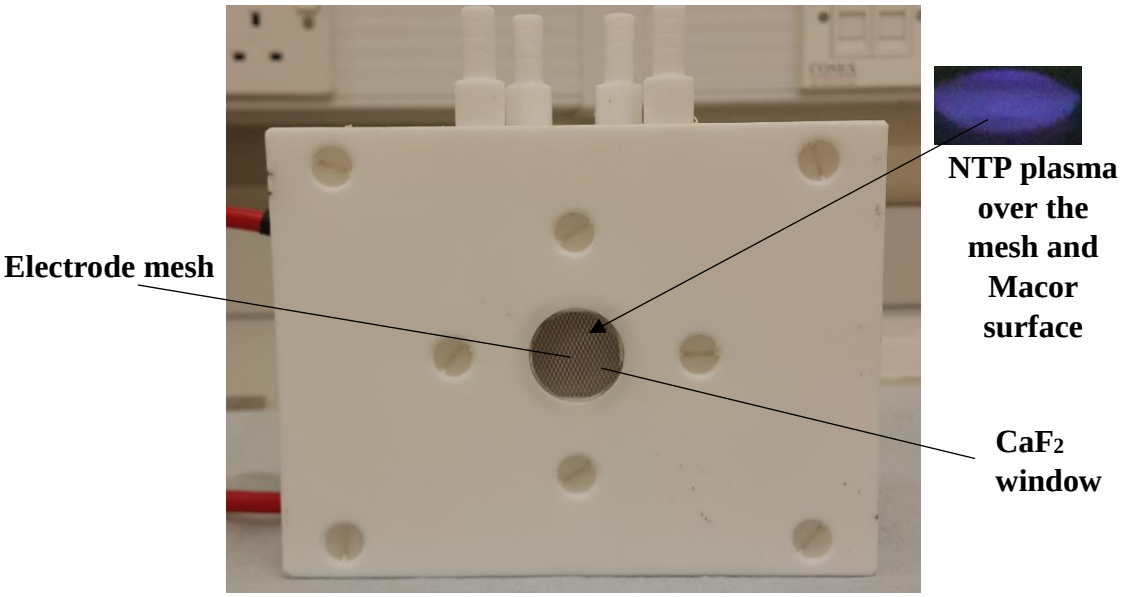

(a)

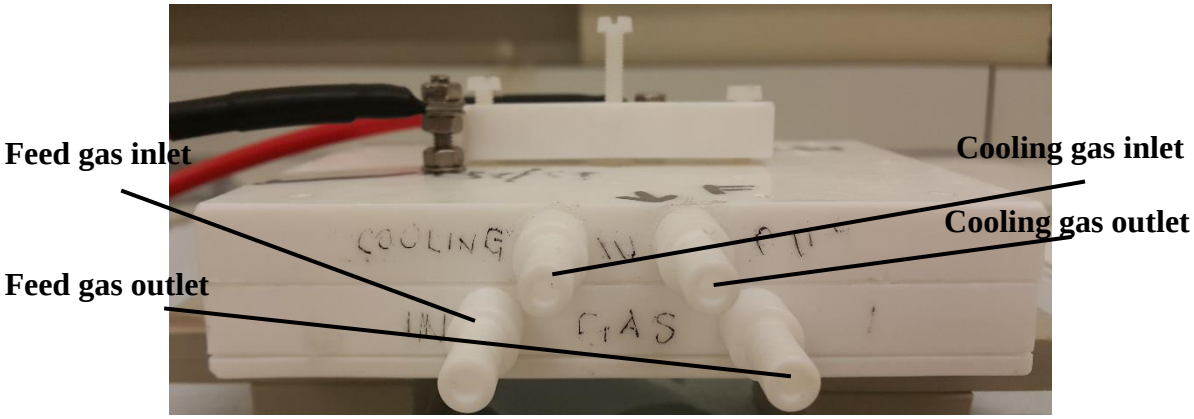

(b)

Figure 2.17. Photographs of (a) reflectance cell and (b) the feed gas and cooling system connections.

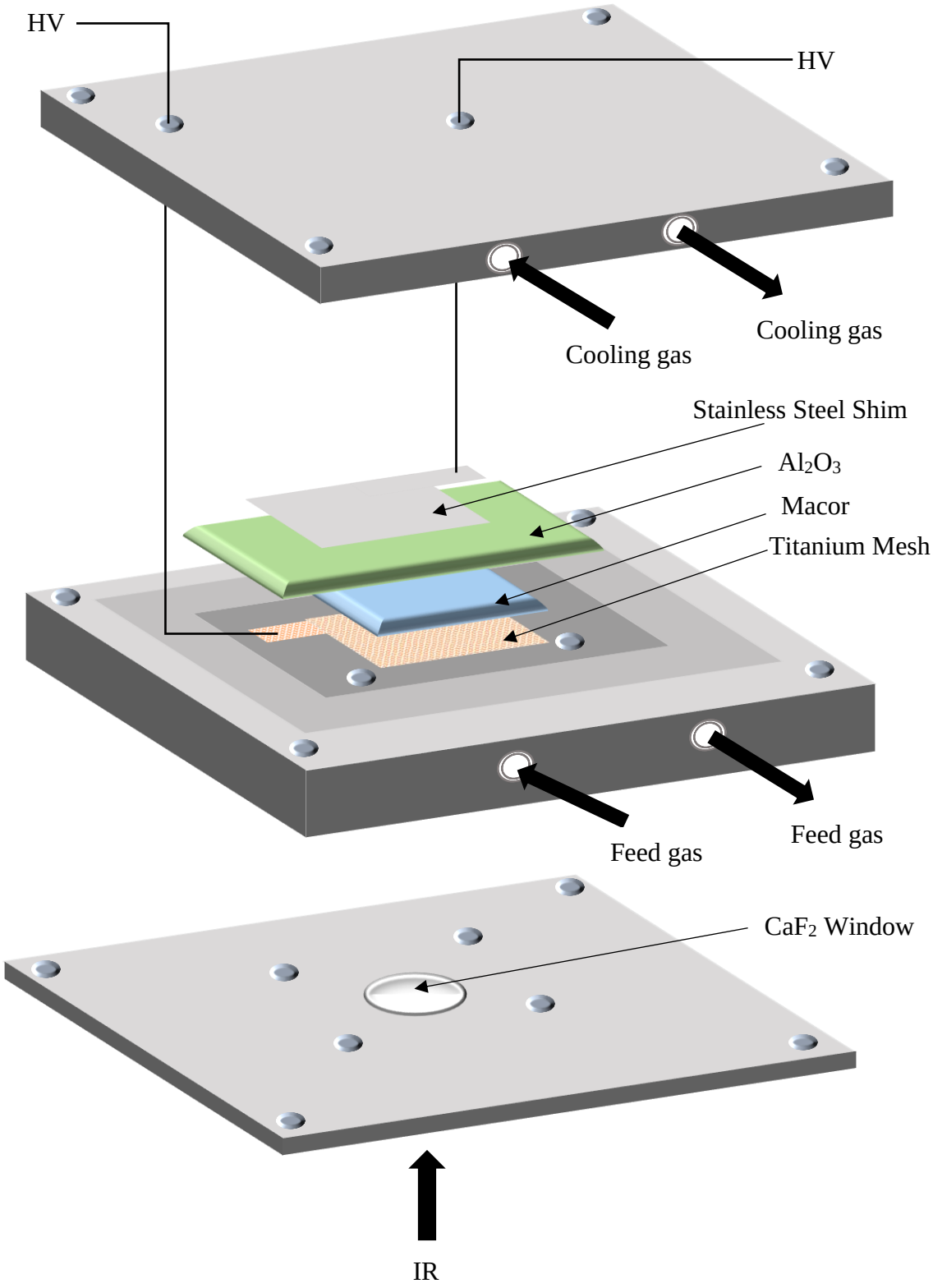

Figure 2.18. Schematic of the IR NTP reflectance cell.

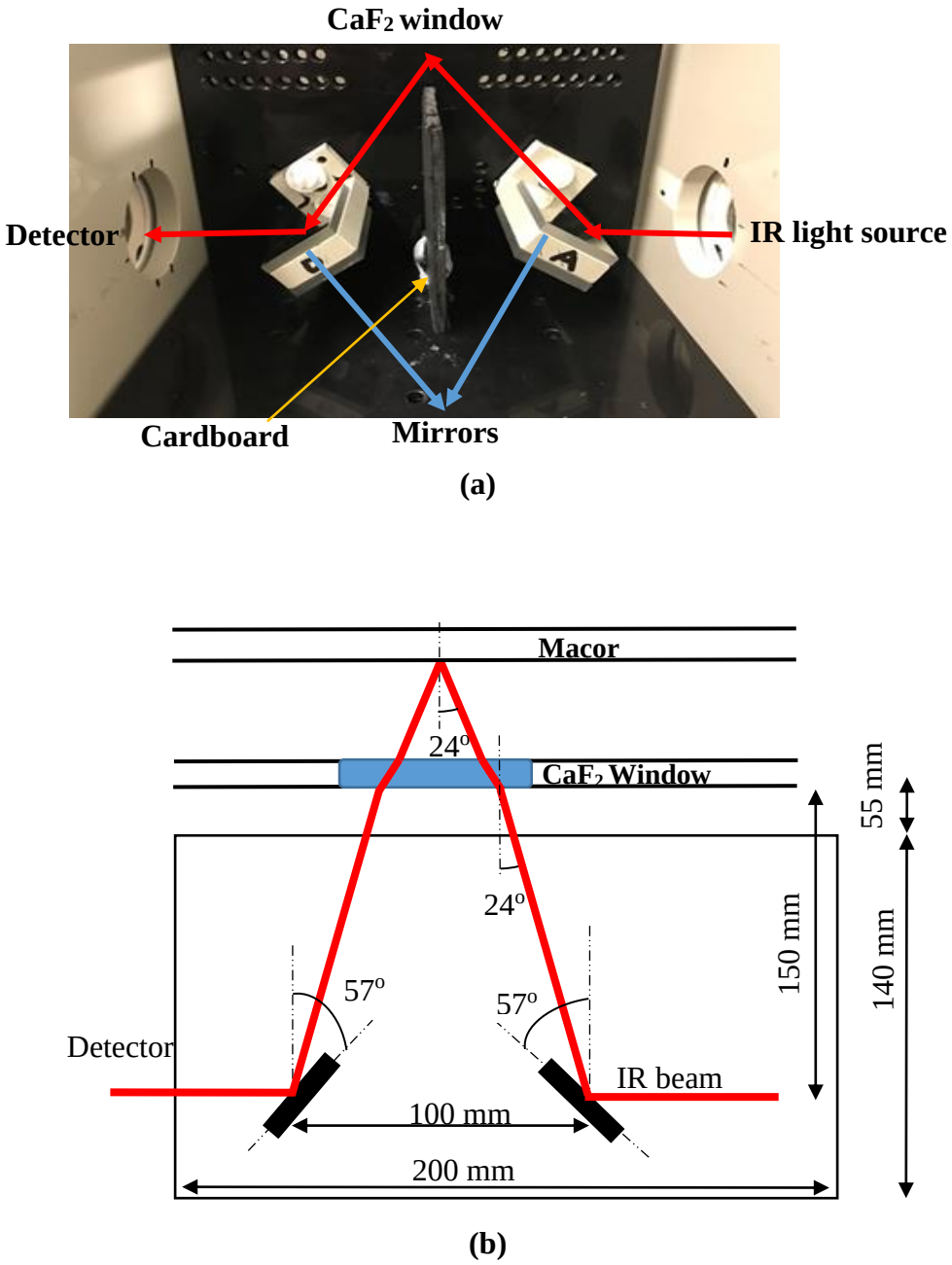

Figure 2.19. (a) A photograph and (b) schematic of the optical bench that used with reflectance cell.

2.8.1. The modification of the reflectance cell and optical bench

Initial experiments were carried out using a ceramic alumina Al_2O_3 layer of the same size as the Macor plate, which was used as an insulator between the two high voltage electrodes to eliminate any chance of arcing that can be generated during the experiment. However, arcing did occur and attacked the Macor and the PTFE of the cell, see figs. 2.20(a) & (b). This led to

a drop in the input power and production of CO_2. In order to prevent this problem, the area of the Al_2O_3 plate was increased to 4 cm x 4.9 cm i.e., larger than the Macor plate.

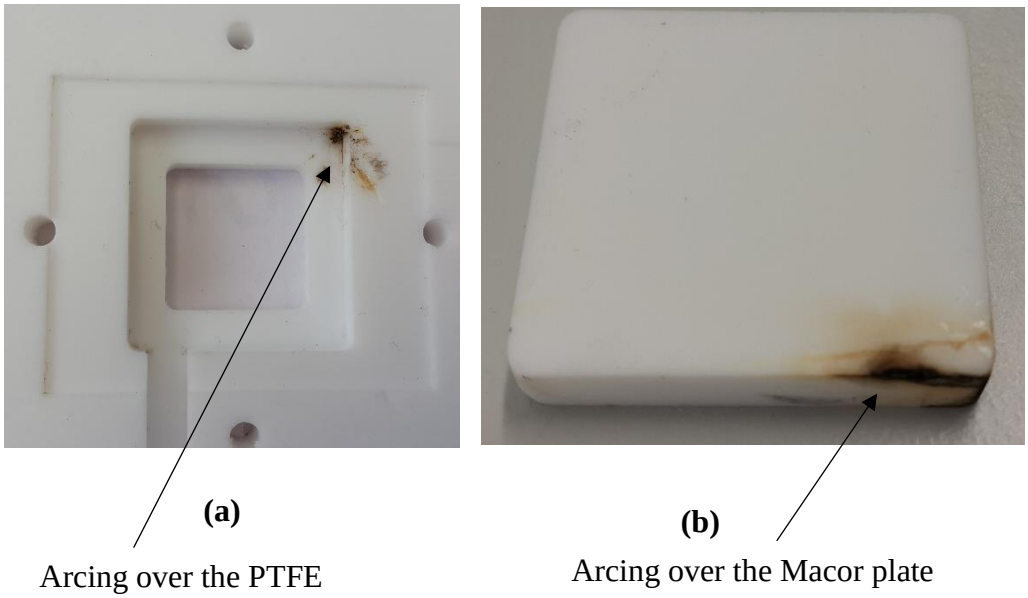

Figure 2.20. Photographs of the result of arcing on the (a) PTFE and (b) Macor plate employed in the reflectance cell.

It was then noticed that, despite feed gases clearly entering the reflectance cell, no gas exhaust was evident in the bubbler. This was due to a large backpressure generated within the cell due to the small size of the outlet holes in the cell. This was corrected by increasing the diameter of the outlets and sealing the cell with silicone glue (Loctite 595, RS components) to prevent any chance of leaking from the edge around the cell surface as shown in figs. 2.21(a) & (b).

Finally, the initial optical bench consisted of 4 mirrors (A, B, C and D) as shown in fig. 2.22, in order to try and ensure a larger angle of incident of the IR beam on the Macor. The positions/angles of the mirrors were obtained via standard geometric calculations and the optics tested using a HeNe laser, see fig. 2.22. Unfortunately, the signal reaching the FTIR detector was too low, partly due to the lower reflectivity of the Macor, see fig. 2.24 and partly due to reflection from the front and back surfaces of the CaF_2 window. Hence, it was decided to employ the 2-mirrors bench shown in figs. 2.19(a) and (b).

As a result, it can be noted that the reflectance cell still very much in development stage with the aim of improving signal-to-noise.

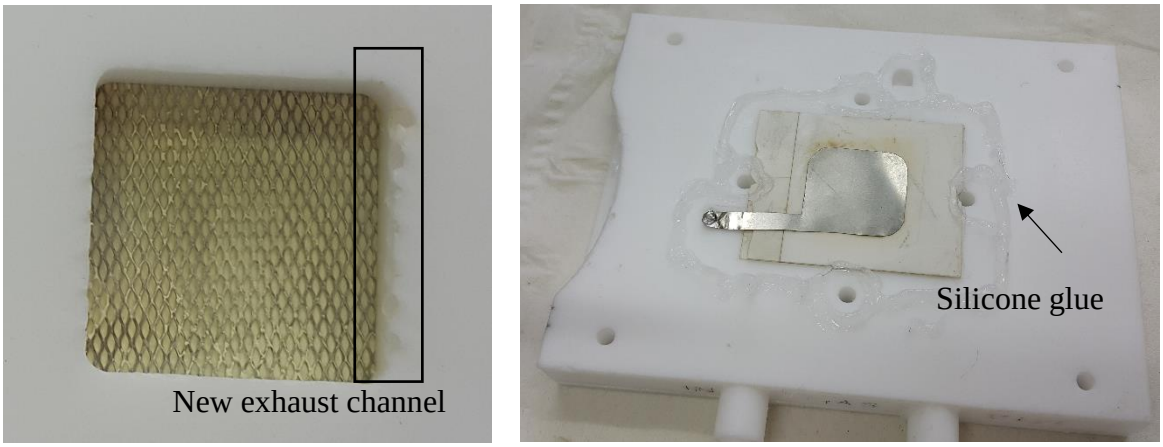

Figure 2.21. Photographs of the modifications of the reflectance cell (a) new holes and (b) gluing the whole cell together.

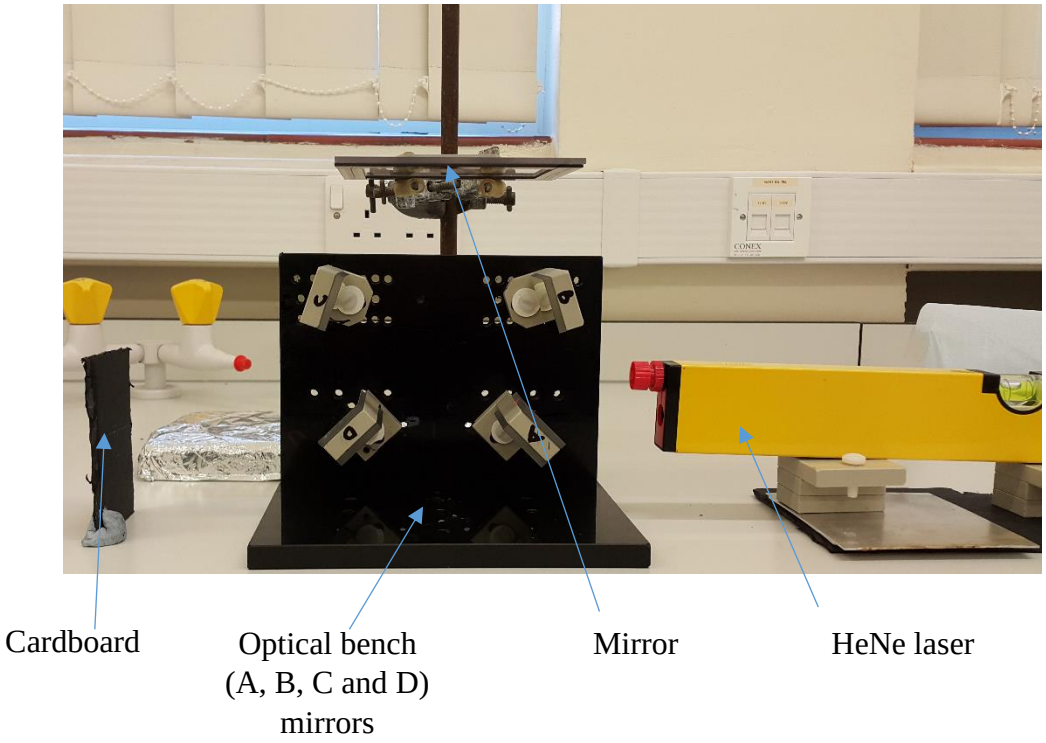

Figure 2.22. A photograph of the original optical bench.

2.9. Experimental procedures for transmission and reflectance cells

The NTP cell was first flushed with N_2 at a flow rate of 200 cm^3 min^{-1} (transmission cell) or 30 cm^3 min^{-1} (reflectance cell) for 120 minutes; when the system was stable, a single beam spectrum was collected (S_R, 100 co-added and averaged scans at 4 cm^{-1} resolution, 100 seconds per scan set). N_2 was then bubbled through the IPA at room temperature and admitted to the cell at a total flow rate of 200 cm^3 min^{-1} (transmission cell) or 30 cm^3 min^{-1} (reflectance cell) and a second single beam spectrum was collected in the absence of plasma. Sample spectra, S_S,

were then taken as a function of time after the high voltage power supply was switched on, and at regular intervals thereafter up to 20 minutes. From the Antoine equation, the partial pressure of IPA at 296K was determined to be around 0.05 bar using the constants A = 4.8610, B = 1357.427 and C = -75.814 so that the concentration in N_2 at 1 bar was around 5% [12]. In addition, there was no difference in the concentration of IPA using different flow rates because the concentration depends on the partial pressure of IPA as a function of temperature. The experiments details are shown in fig. 2.23(a) and the experimental system in fig. 2.23(b).

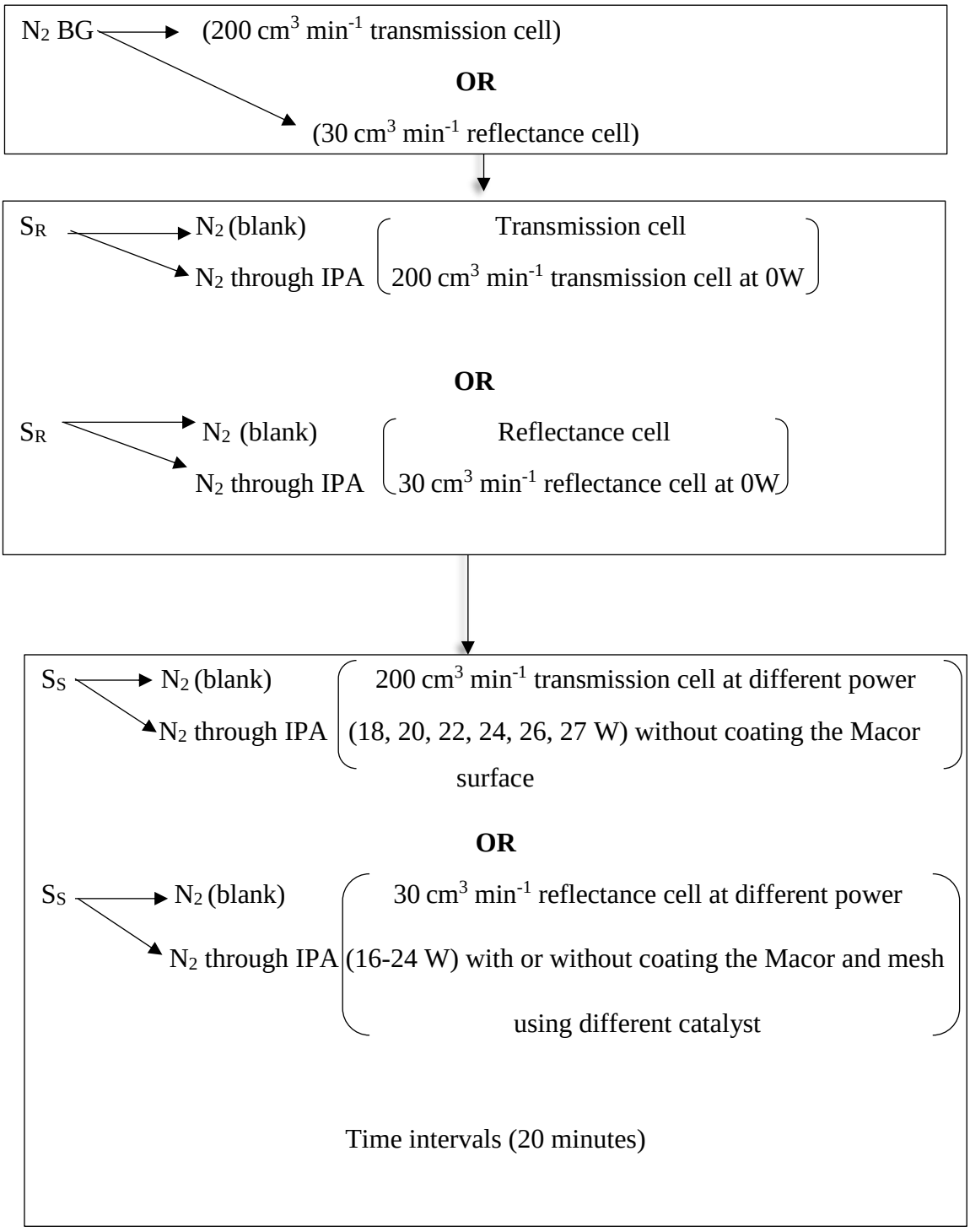

(a)

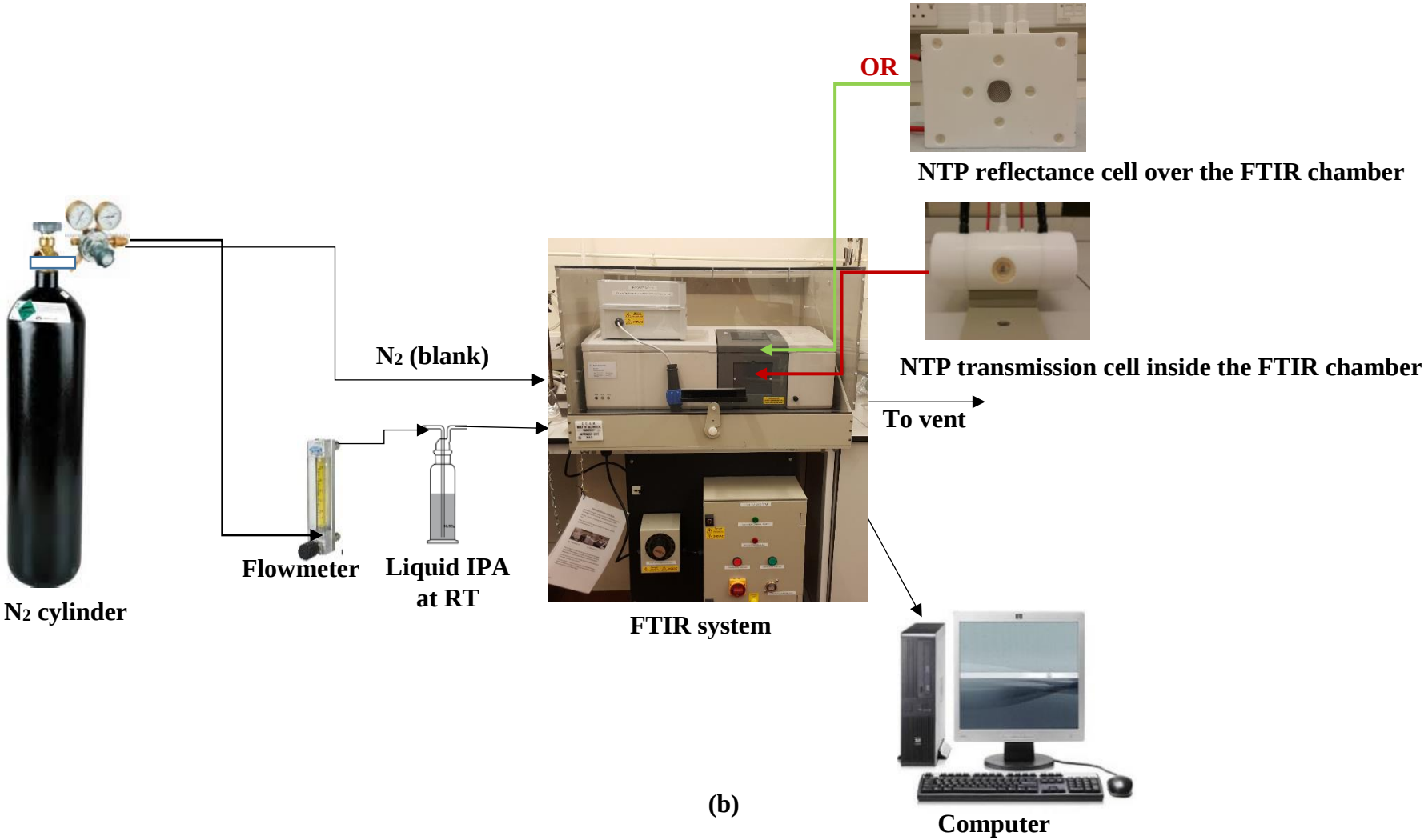

Figure 2.23. (a) Flow chart and (b) schematic diagram of the experimental methods employed using the transmission and reflectance cells. All experiments were carried out using flowing feed gas.

By using the first single beam (of the nitrogen gas with no plasma) as the reference spectrum (S_R) all of the infrared active species present in the plasma were observed; using the second single beam as the reference spectrum resulted in difference spectra, showing only the changes incurred on initiating the plasma.

Figure 2.24(a) shows single beam spectra of the mesh, Macor and window in the reflectance cell. As can be seen, the light intensity reflected from the window was much higher than from the Macor or mesh. This can result in the loss of weaker features: for example fig. 2.24(b) shows spectra collected 10 minutes after initiating the plasma in an experiment employing Macor in the reflectance cell at 24 W and N_2 at a flow rate of 30 cm^3 min^{-1}. As can be seen, correcting for the window has a significant effect upon the spectrum. The features in fig. 2.24(b) are discussed in Chapter 3, section 3.4.1. The uncorrected spectrum was obtained using the beer-lambert law [13]:

$$\text{Absorbance, } A = \log_{10} (S_R/S_S) \quad (2.5)$$

The corrected spectrum was obtained by correcting for the window:

$$\text{Absorbance, } A = \log_{10}[(S_R - S_W)/ (S_S - S_W)] \quad (2.6)$$

where S_W is the spectrum of the window alone.

The data manipulations in equation (2.5) was employed in the experiments employing the transmission cell. These results in difference spectra in which peaks pointing upwards (ie. to + absorbance) represent a gain in absorbing species at S_S with respect to S_R, and peaks pointing down (to – absorbance) represent the loss of absorbing species. The concentrations of some species observed were calculated using the Beer-Lambert law [13]:

$$A = \varepsilon cL \quad (2.7)$$

where: ε is the molar decadic extinction coefficient (M^{-1} cm^{-1}), c = concentration (M), L = optical path length (5.1 cm for transmission cell) or (1 cm for reflectance cell).

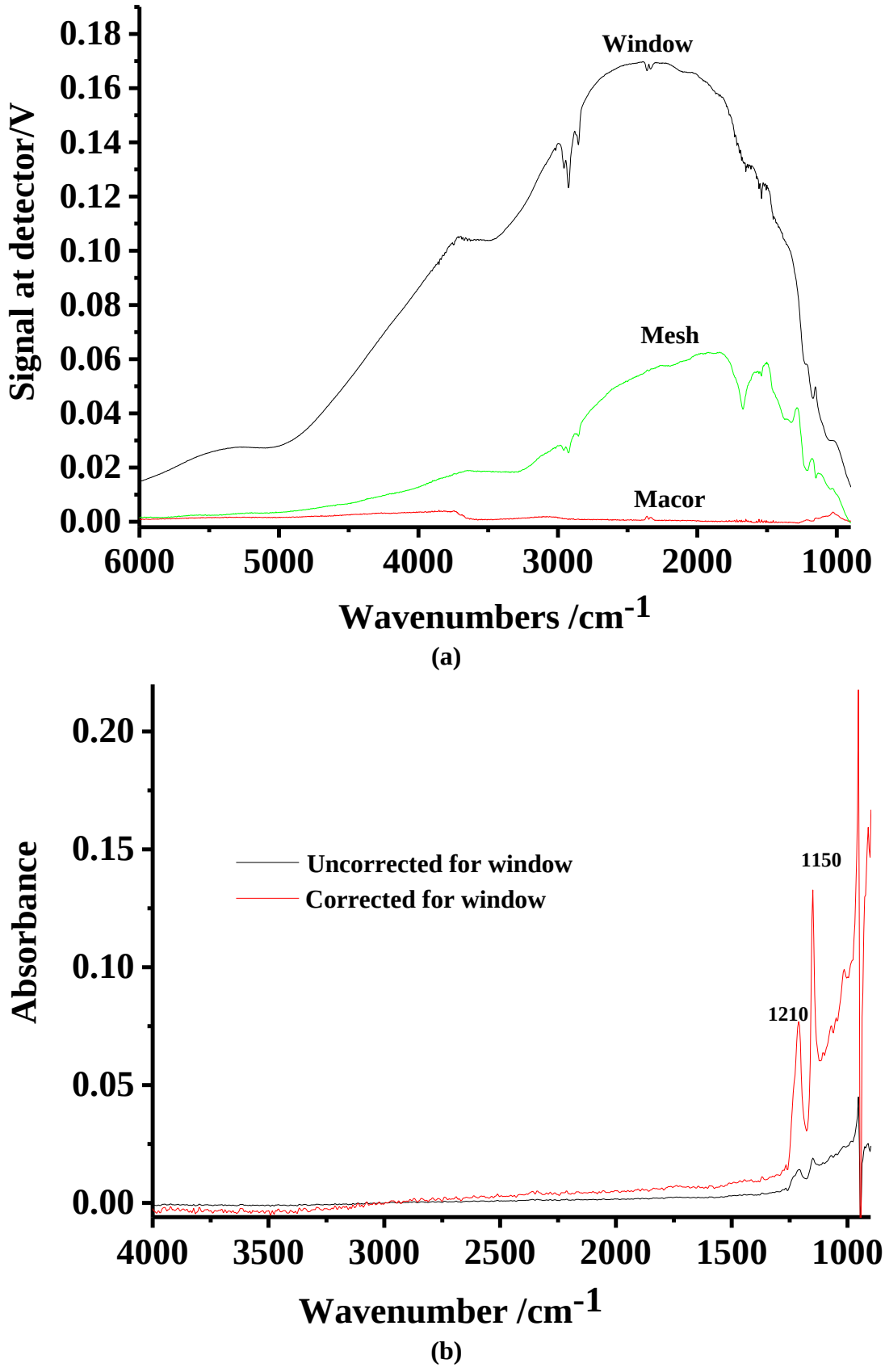

Figure 2.24. Single beam spectra obtained using the reflectance cell: (a) from the Macor, window and mesh layers and (b) reflectance spectra collected 10 minutes after initiating the plasma at 24 W and N_2 at a flow rate of 30 cm^3 min^{-1} before and after corrected for window.

The temperature of the Macor caps of the transmission cell were monitored at an input power of 27 W using a RS-1327 IR Thermometer C infrared thermometer gun in experiments conducted without FTIR data collection (as the cover to the sample compartment had to be removed), and found to increase to ca. 43 °C over 20 minutes. This measurement was repeated with the plasma reflectance cell and the temperatures of the Macor/Ti mesh and window were found to increase to ca. 46 °C over 20 minutes.

2.10. The coating process

In order to study the effect of the catalyst on the decomposition of IPA, three different catalysts solutions were employed (SnO_2 calcined at 400 ºC and 700 ºC, or CeO_2). Thus, 100 mg of the chosen catalyst was suspended in 10 cm^3 ethanol and the sample stirred for 4 hours to produce a thick suspension, see fig. 2.25(a). A few drops of the suspension were then placed on the Ti mesh and Macor of the reflectance cell using a pasteur pipette and the Macor + mesh left in a drying oven for 1 hour for the solvent to evaporate, see fig. 2.25(b). Catalysts could not be employed in the transmission cell due to arcing.

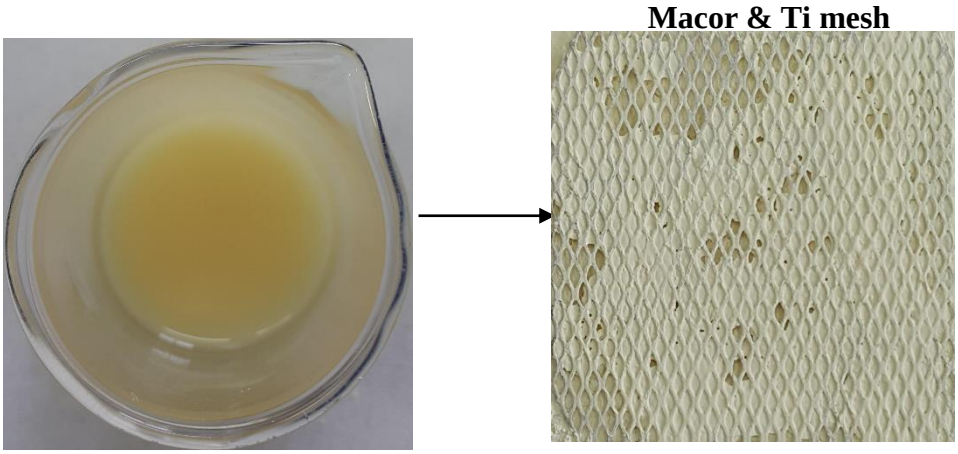

Figure 2.25. Photographs of: (a) the CeO_2 suspension and (b) coating and drying the Macor & Ti mesh in reflectance cell.

2.11. Presslok demountable holder cell

The IR spectra of liquid isopropyl alcohol and isophorone were obtained using a Presslok holder (Thermo Scientific) as shown in figs. 2.26(a) & (b). Assembly of the cell parts was accomplished by compressing the stainless steel layers that separate using a rubber O-ring

barrier to keep the windows safely and to compress the layers together to get the accurate spectrum without any trace of CO_2 or water vapor; ca. 50 µL of the liquid was placed between two 25 mm dia. 2 mm thick CaF_2 windows (Crystran) in the holder.

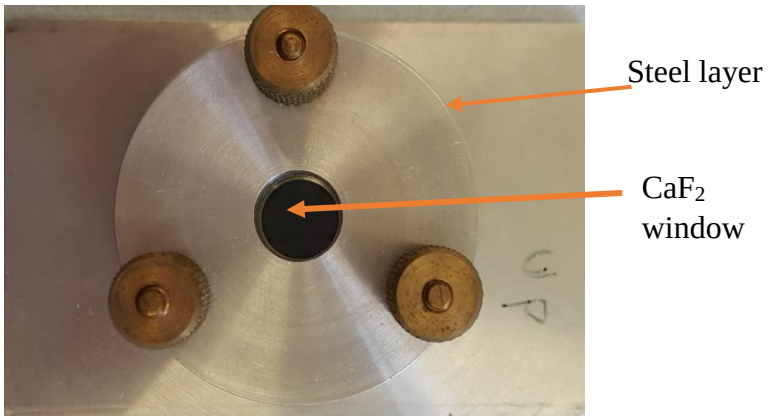

(a)

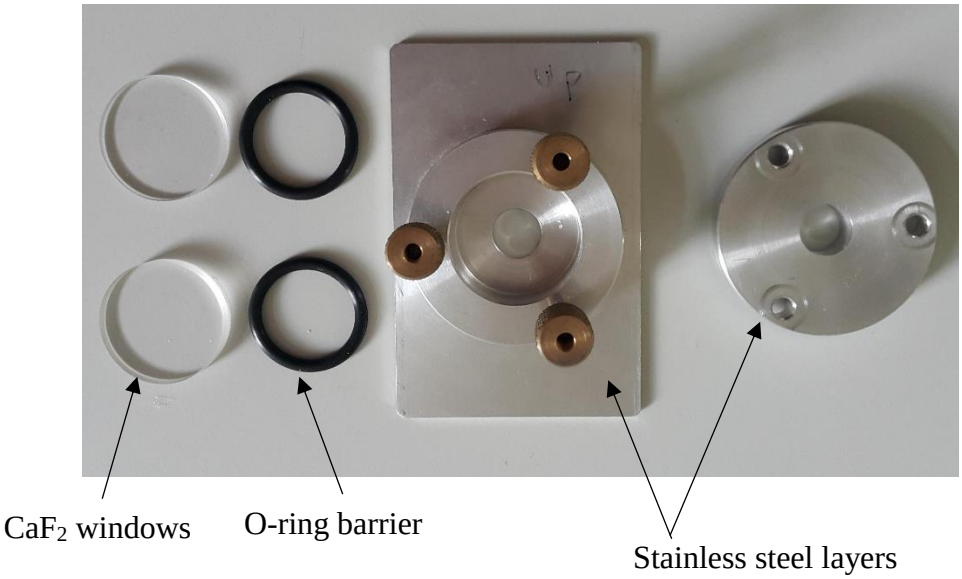

(b)

Figure 2.26. Photographs of the Presslok holder cell (a) the whole cell and (b) cell disassembled.

2.12. References

1. MACOR – Machinable Glass Ceramic Data Sheet [Cited 2016 19 January]. Available from: http://psec.uchicago.edu/ceramics/MACOR%20Data%20Sheet.pdf.

2. Fujihara, S., Maeda, T., Ohgi, H., Hosono, E., Imai, H. and Kim, S.H., 2004. Hydrothermal routes to prepare nanocrystalline mesoporous SnO_2 having high thermal stability. *Langmuir*, *20*(15), pp.6476-6481.
3. Christensen, P.A., Attidekou, P.S., Egdell, R.G., Maneelok, S. and Manning, D.A.C., 2016. An in situ FTIR spectroscopic and thermogravimetric analysis study of the dehydration and dihydroxylation of SnO_2: the contribution of the (100),(110) and (111) facets. *Physical Chemistry Chemical Physics*, *18*(33), pp.22990-22998.
4. Retrieved on 12th Feburary 2013, from website http: //www. engineeringtoolbox.com / boiling-point-water-d_926.html.
5. Waseda, Y., E. Matsubara, and K. Shinoda, *X-Ray diffraction crystallography introduction, examples and solved problems*. 2011, Springer: Berlin,Heidelberg, New York. p. 125.
6. Christensen, P.A. and Jones, S.W.M., 2014. An in situ FTIR study of undoped PolyBenzoImadazole as a function of relative humidity. *Polymer Degradation and Stability*, *105*, pp.211-217.
7. Kubelka, P., *New Contributions to the Optics of Intensely Light-Scattering Materials. Part I.* Journal of the Optical Society of America, 1948. 38(5): p. 448-457.
8. Veerapandian, S.K., Leys, C., De Geyter, N. and Morent, R., 2017. Abatement of VOCs using packed bed non-thermal plasma reactors: a review. *Catalysts*, *7*(4), p.113.
9. Meiners, A., Leck, M. and Abel, B., 2010. Efficiency enhancement of a dielectric barrier plasma discharge by dielectric barrier optimization. *Review of Scientific Instruments*, *81*(11), p.113507.
10. Šimek, M., Pekárek, S. and Prukner, V., 2010. Influence of power modulation on ozone production using an AC surface dielectric barrier discharge in oxygen. *Plasma Chemistry and Plasma Processing*, *30*(5), pp.607-617.
11. Gibalov, V.I. and Pietsch, G.J., 2000. The development of dielectric barrier discharges in gas gaps and on surfaces. *Journal of Physics D: Applied Physics*, *33*(20), p.2618.
12. Biddiscombe, D.P., Collerson, R.R., Handley, R., Herington, E.F.G., Martin, J.F. and Sprake, C.H.S., 1963. 364. Thermodynamic properties of organic oxygen compounds. Part VIII. Purification and vapour pressures of the propyl and butyl alcohols. *Journal of the Chemical Society (Resumed)*, pp.1954-1957.
13. Swinehart, D.F., 1962. The beer-lambert law. *J. Chem. Educ*, *39*(7), p.333.

Chapter 3. An in-situ Fourier Transform InfraRed study of the thermally and plasma driven conversion of isopropyl alcohol at Macor

3.1. Introduction

This chapter reports a study of the Non-Thermal Plasma (NTP) driven conversion of IsoPropyl Alcohol (IPA) at Macor using the plasma transmission and plasma reflectance cells. In addition, for the first time, a direct comparison of the non-thermal plasma and thermally driven processes is presented.

3.2. Infrared studies of the thermally-driven process

3.2.1. Blank experiments

Macor was chosen as the catalyst for the initial studies as it has both a reasonable dielectric constant (ca. 6) and high thermal stability [1]. The Macor was not characterized as it is produced only in pellet form which is extremely hard and hence it has not proved possible to produce contaminant-free powder for, for example, XRD (X-Ray Diffraction) or XPS (X-ray Photoelectron Spectroscopy) by filing etc.

A blank experiment was first carried out using the Specac environmental cell and a Macor disc in pure nitrogen gas in the absence of IPA as a function of temperature from 25 °C to 600 °C.

A typical steady-state single beam spectrum of the Macor disc in nitrogen at flow rate of 200 cm^3 min^{-1} is shown in fig. 3.1. As can be seen from the figure, the spectrum was free from absorptions due to CO_2 and H_2O. The signal at the detector was low due to the poor IR reflectivity of Macor.

Once the reference spectrum was collected, the DRIFTS cell was isolated, i.e. creating a static, nitrogen atmosphere above the Macor, the temperature ramped at 5 °C per minute and sample spectra (S_S) collected at 25 °C (to check the system stability), 50 °C and then every 50 °C up to 600 °C. The results are shown in fig. 3.2. As can be seen from fig. 3.2, there are loss features at 3323, 1477 and 1226 cm^{-1} that increase steadily in intensity as the temperature was increased. Further, there are loss and gain features between ca. 3600 and 3770 cm^{-1}. These bands may be attributed to the surface chemistry of the Macor: however, there are no relevant reports in the

literature on this and attempts to assign the various features in spectrum in fig. 3.2 were without success.

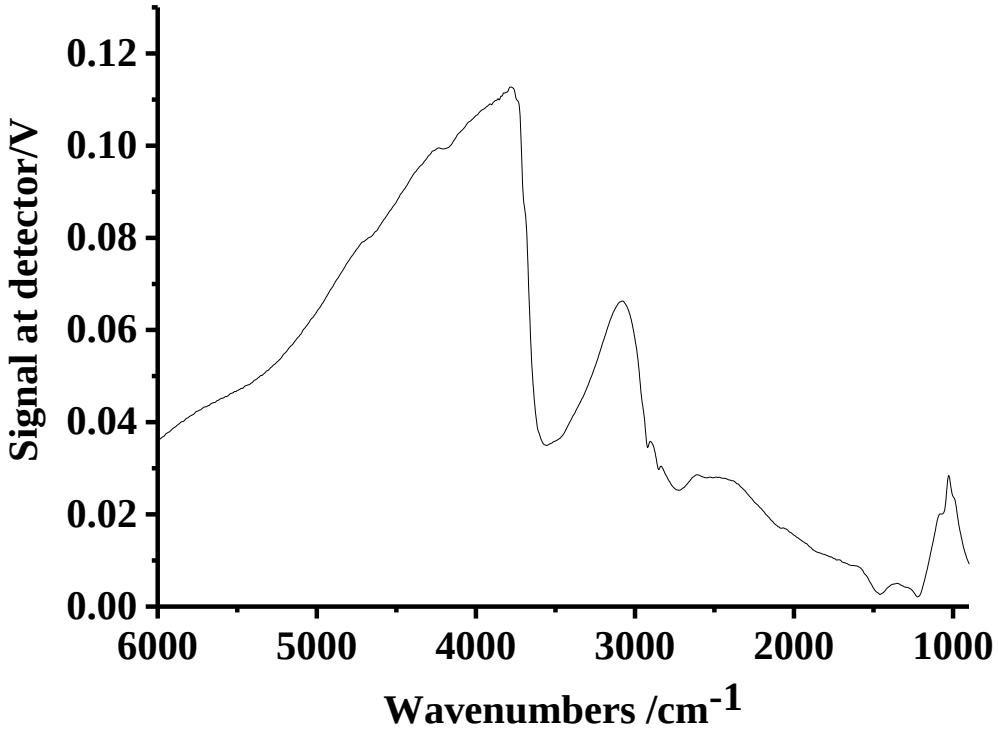

Figure 3.1. A single beam spectrum (100 co-added and averaged scans at 4 cm^{-1} resolution, ca. 120 seconds per scan set) of the Macor disc under nitrogen gas at flow rate of 200 cm^3 min^{-1}.

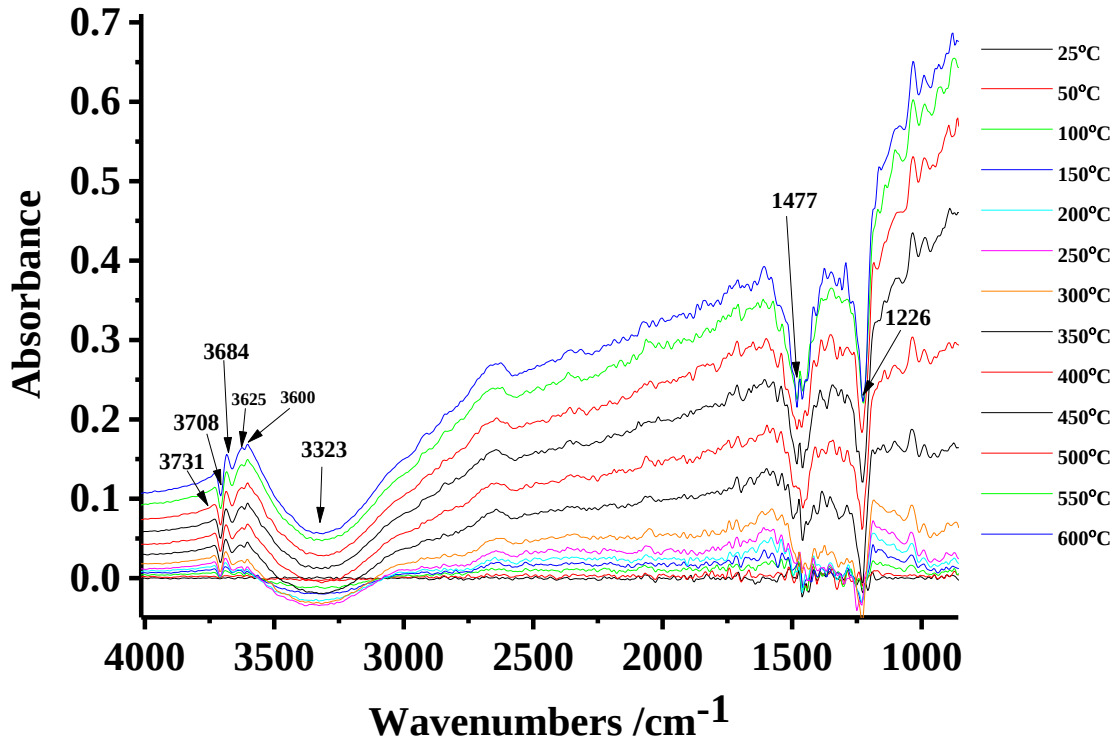

Figure 3.2. FTIR spectra (100 co-added and averaged scans at 4 cm^{-1} resolution, ca. 120 seconds per scan set) collected using the Specac environmental cell and the Macor disc in a static atmosphere of nitrogen gas during an experiment in which the reference spectrum was taken at 25 °C. The temperature was then ramped up at 5 °C min^{-1} and sample spectra collected at 25 °C and 50 °C then every 50 °C to 600 °C.

3.2.2. Experiments using nitrogen and isopropyl alcohol vapour as the feed gas

Figure 3.3 shows a comparison between the typical steady-state single beam spectra of a Macor disc in N_2 and N_2 + IPA vapour at a flow rate of 200 cm^3 min^{-1} in figs 3.1 and 3.3 respectively. As can be seen, there is no significance difference between the spectra apart from the bands at 2976 and 2887 cm^{-1} due to adsorbed IPA [2-8].

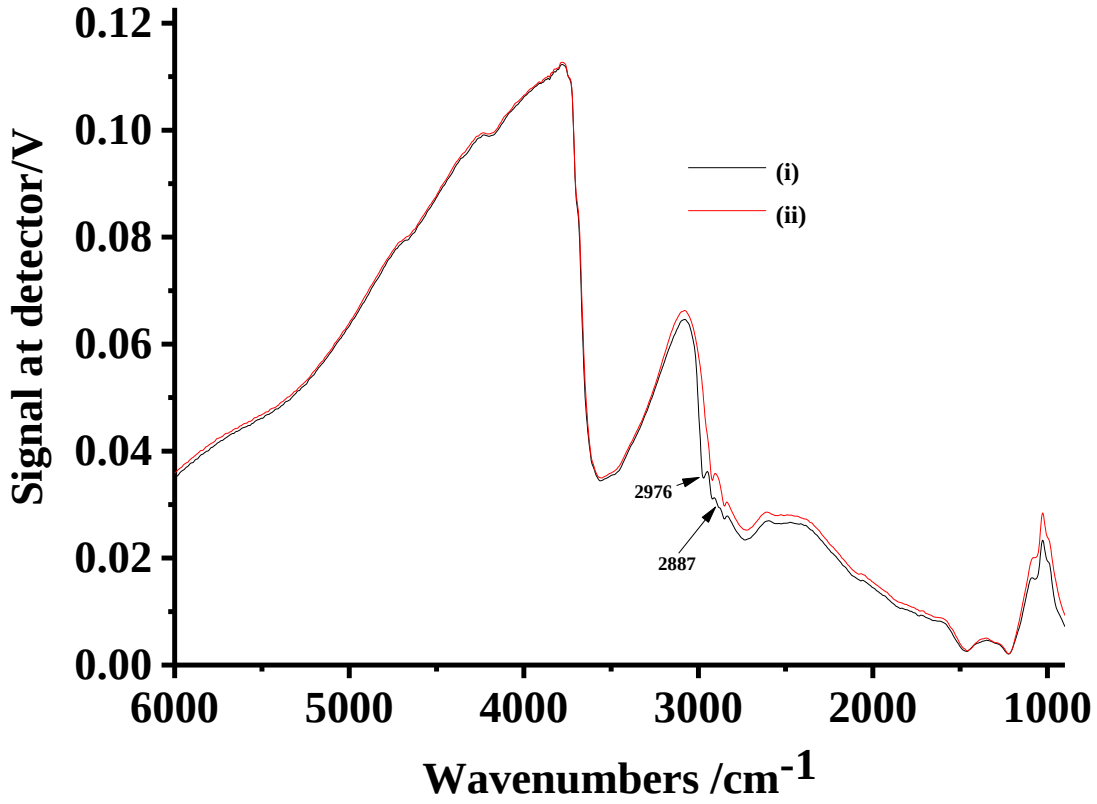

Figure 3.3. Single beam spectra (100 co-added and averaged scans at 4 cm^{-1} resolution, ca. 120 seconds per scan set) of Macor disc under: (i) nitrogen gas and IPA vapour at a flow rate of 200 cm^3 $min^{-1}$and (ii) under nitrogen gas at a flow rate of 200 cm^3 min^{-1}.

Figure 3.4 shows spectra collected during an experiment in which a Macor disc was heated from 25 to 600 °C in a static atmosphere of IPA vapour and nitrogen gas. As above, the reference spectrum (S_R) was collected at 25 °C and the temperature then ramped at 5 °C min^{-1} with sample spectra (S_S) collected at 50 °C and further spectra collected every 50 °C up to 600 °C. For clarity, only the spectra collected every 100 °C are shown.

As can be seen from the figure, there are loss features at 3340, 2976, 2887, 1481, 1232, 1007 and 950 cm^{-1} that increase steadily in intensity as the temperature was increased. In addition, there are loss and gain features between ca. 3600 and 3770 cm^{-1}. The bands between 3600 and

3770 cm^{-1} and loss features at 3340 cm^{-1}, 1481 and 1232 cm^{-1} also appear in the spectra in the absence of IPA (fig. 3.2): hence these bands may be attributed to the surface chemistry of the Macor as mentioned above. The features at 2976, 2887, 1007 and 950 cm^{-1} are due to the loss of adsorbed IPA [2-8]. No obvious product features may be seen in fig. 3.4; and thus it appears that Macor is unreactive with respect to the thermal degradation of IPA.

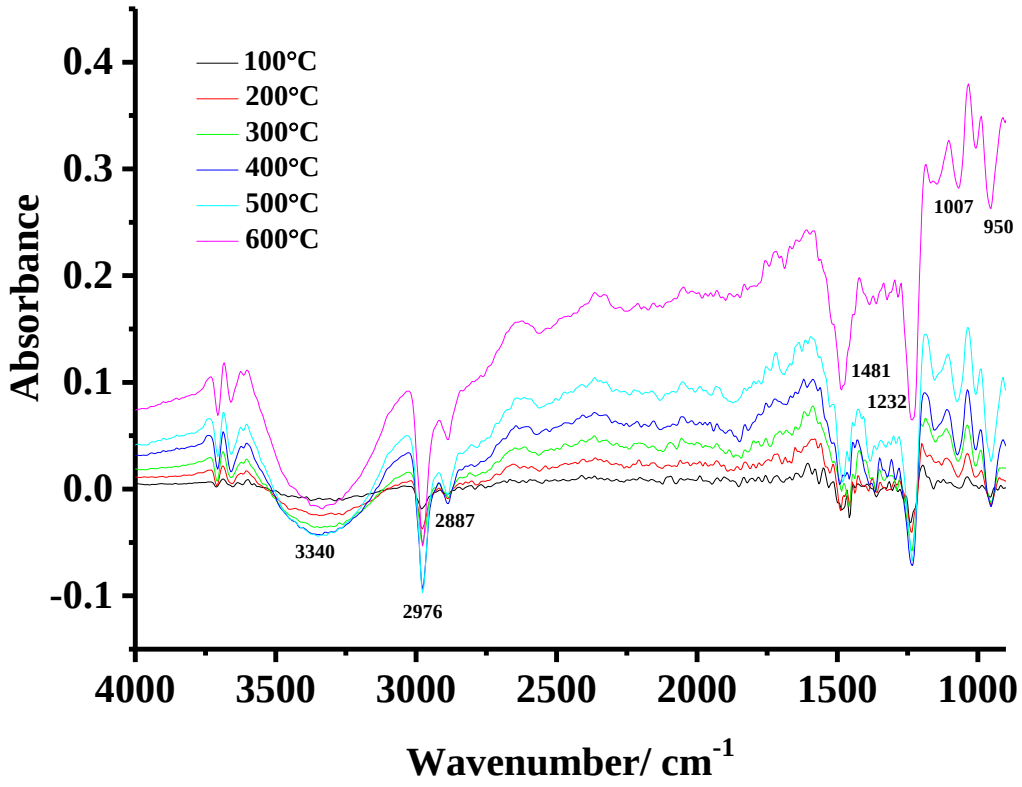

Figure 3.4. FTIR spectra (100 co-added scans and averaged scans at 4 cm^{-1} resolution, ca. 120 seconds per scan set) collected from a 12.5 mm diameter, 2 mm thick Macor disc in a static atmosphere of isopropyl alcohol vapour in nitrogen gas during an experiment in which the reference spectrum was taken at 25 °C; the temperature was then ramped up at 5 °C min^{-1} and sample spectra collected every 50 °C from 50 °C to 600 °C.

Figure 3.5 shows plots of the absorbance at 2000 cm^{-1} in figs. 3.2 and 3.4 vs temperature. As can be seen from figure, there are two distinct regions of behaviour: 25 – 300 ºC (I) and 300 – 600 ºC (II); in region (I), the absorption increases relatively slowly with temperature, followed by a rapid rise in region (II). Similar behaviour was observed in the presence of IPA except that the onset of region (II) was deferred until 450 ºC and the subsequent increase in absorbance less marked. Whilst interesting, the data in fig. 3.5 did not appear to have any relevance to the chemistry of IPA, and hence were not investigated further.

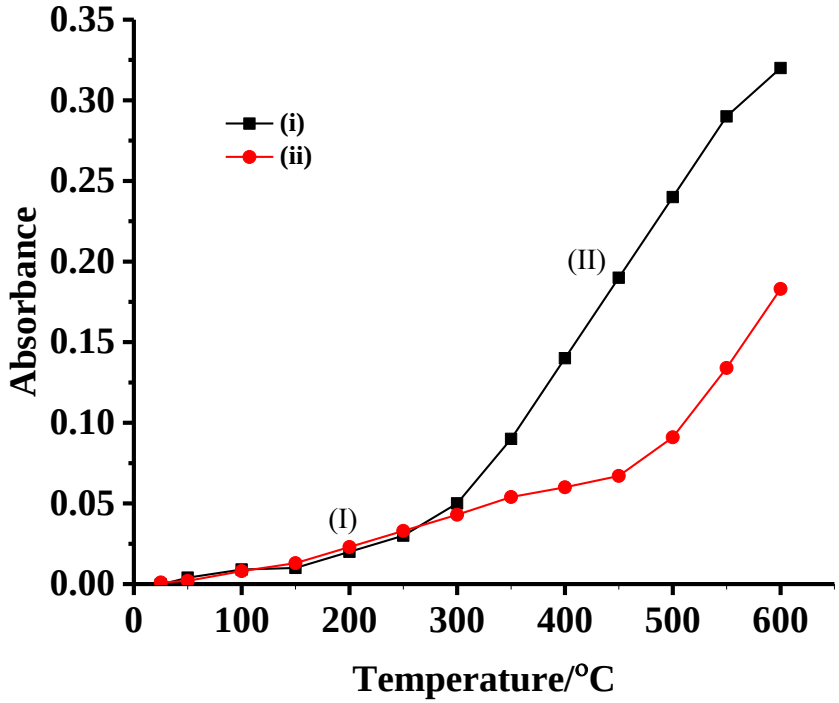

Figure 3.5. Plots of the absorbance at 2000 cm^{-1} in figs. 3.2 and 3.4 using: (i) nitrogen and (ii) nitrogen and IPA vapor.

3.3. Experiments using the plasma transmission cell

3.3.1. Blank experiments

Figure 3.6(a) shows photographs of the plasma region of the transmission cell before and after switching on the power. As can be seen from the figure, a stable purple plasma was generated in the plasma zone after the plasma was initiated, in this case at 20 W.

A typical single beam spectrum of nitrogen at flow rate of 200 cm^3 min^{-1} before plasma was initiated is shown in fig. 3.6(b). As can be seen from the figure, whilst absorptions due to water vapour (i.e. around 3500 and 1640 cm^{-1} [9]) and CO_2 (2360 and 2340 cm^{-1} [10]) were present, they were sufficiently weak to allow experiments to commence.

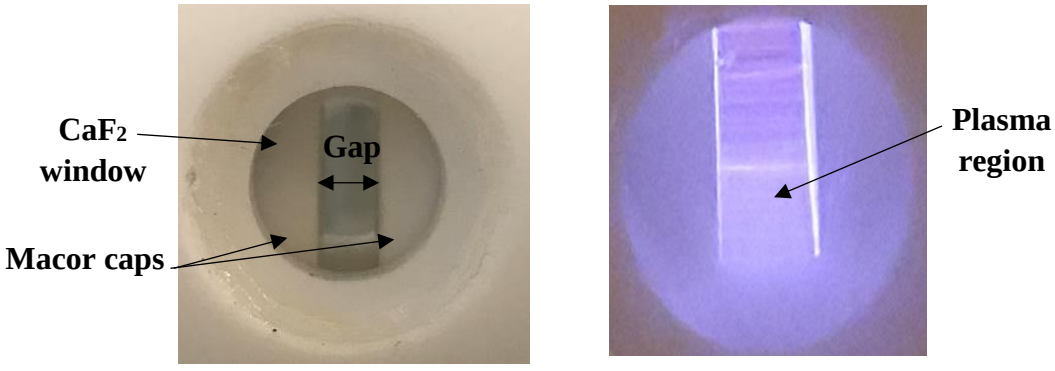

(a)

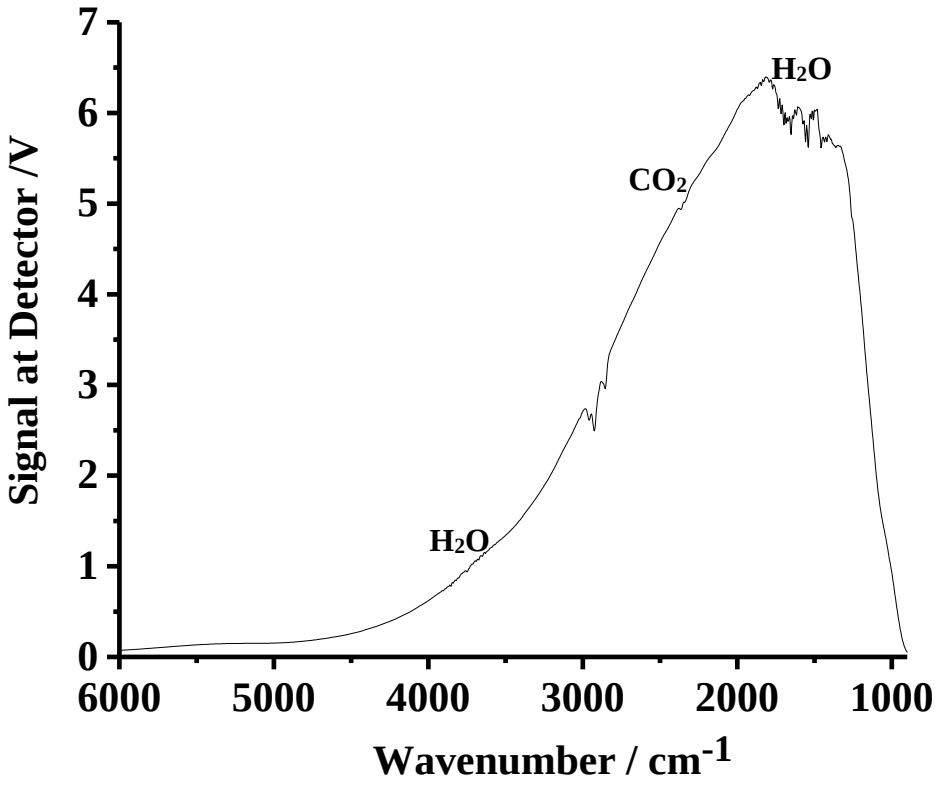

(b)

Figure 3.6. (a) A stable non-thermal plasma generated between the Macor caps in the transmission cell. (b) A single beam spectrum (100 co-added and averaged scans at 8 cm^{-1} resolution, ca. 60 seconds per scanset) collected using the transmission cell and a N_2-feed at of 200 cm^3 min^{-1}.

Figure 3.7 shows spectra collected during an experiment in which N_2 was passed through the transmission cell at flow rate of 200 cm^3 min^{-1} and plasma initiated at an input power of 20 W with spectra collected at regular intervals. The spectra were ratioed to the reference spectrum of N_2 at 25 ºC. As can be seen from the figure, no product absorptions were observed. The bands due to water vapour (I) and CO_2 (II) were caused by small difference in the purge between reference and sample spectra. It is unclear whether the jumps in baseline after 2, 12 and 14 minutes were due to optical effects or electronic interference; however, such jumps only occurred infrequently.

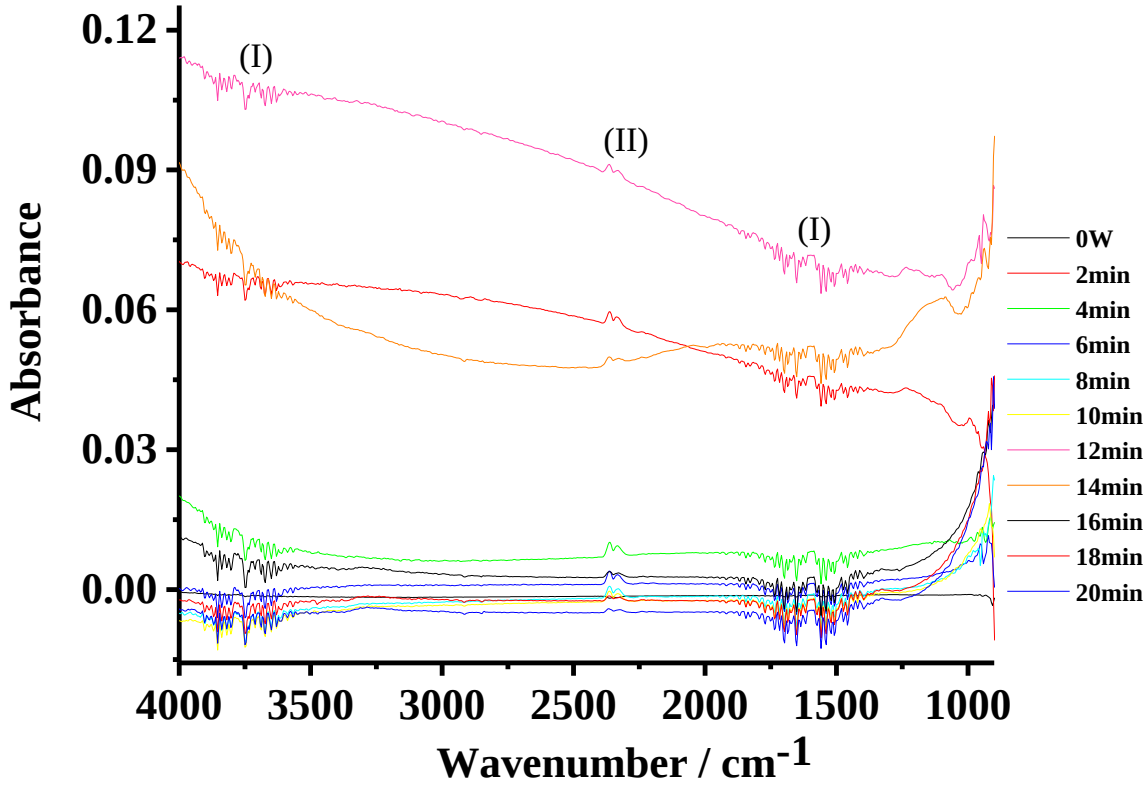

Figure 3.7. In-situ FTIR absorbance spectra of the nitrogen gas-fed plasma (100 co-added and averaged scans at 8 cm^{-1} resolution, ca. 60 seconds per scanset) at 20 W collected as a function of operation. The N_2 was passed through the transmission cell at 298 K at a flow rate of 200 cm^3 min^{-1}. The reference spectrum was collected of N_2 at 25 ºC.

3.3.2. Experiments using nitrogen and isopropyl alcohol

Isopropyl alcohol vapour was delivered to the transmission cell by bubbling nitrogen gas through the alcohol held in a Dreschel bottle at a flow rate of 200 cm^3 min^{-1}. The plasma experiments using N_2 + IPA were carried out at 18, 20, 22, 24, 26 and 27 W (the plasma became unstable at 28 W); and the various product features observed were the same in all the experiments. Typically, the reference spectrum was collected of the flowing N_2 + IPA without plasma, after which the plasma was initiated and sample spectra collected as a function of time.

Figure 3.8 shows a spectrum of gas phase IPA with no plasma; the reference spectrum was collected using pure N_2 at a flow rate of 200 cm^3 min^{-1} at 25 ºC. The assignments of the various features in the spectrum are summarized in table 3.1. There were no bands attributed to liquid phase IPA; the relevance of this is discussed further below.

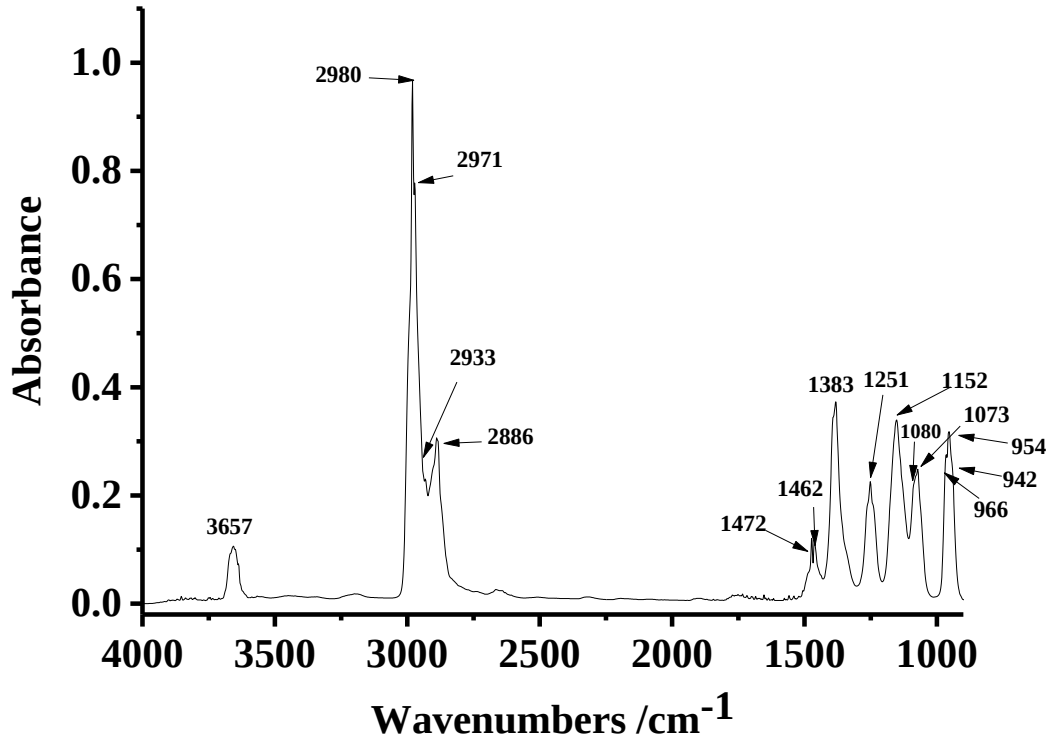

Figure 3.8. In-situ FTIR spectrum of gas phase IPA (100 co-added and averaged scans at 4 cm^{-1} resolution, ca. 100 seconds per scanset). The reference spectrum was collected of N_2 at 25 ºC, the N_2 was then bubbled through pure IPA at 298 K at a flow rate of 200 cm^3 min^{-1}, without plasma and the sample spectrum collected.

3.3.3. The spectra collected at 1 minute

Spectral acquisition commenced 1 minute after initiating the plasma: this period was chosen simply to allow some time for the system to settle, rather than assuming the plasma had reached steady state. Figure 3.9(a) shows the spectra collected after 1 minute during a series of experiments carried out as a function of input power (see the discussion around fig. 3.14 below), the reference spectra in each case being collected of the IPA-containing N_2 gas without plasma. As expected, the figure is dominated by loss features due to gas phase IPA; see fig. 3.10, which compares spectra of liquid and gas phase IPA, and table 3.1 which lists the various features. As can be seen from fig. 3.10, the 3657, the doublet at 1472 and 1462 and the distinctively-shaped band at 1251 cm^{-1} are characteristic of the gas phase IPA, whilst the cluster of bands at 1160, 1130 and 1111 cm^{-1} and single, sharp feature at 952 cm^{-1} are characteristic of the liquid phase IPA. It is clear from fig. 3.9(a) that there is vibrational structure on the high frequency side of the IPA C-H loss features on all the spectra, as well as gain features below ca. 2250 cm^{-1} (arrowed); however, these are obscured by the strong loss features due to gas phase IPA. Hence, in order to highlight any small features, the gas phase IPA spectrum was subtracted from the

spectrum collected at 27 W in fig. 3.9(a), using the 3657 cm^{-1} O-H feature in the gas phase spectrum to determine the scaling factor to ensure annulling of the IPA bands; the result is shown in fig. 3.9(b) and the various features so observed are summarized in table 3.2.

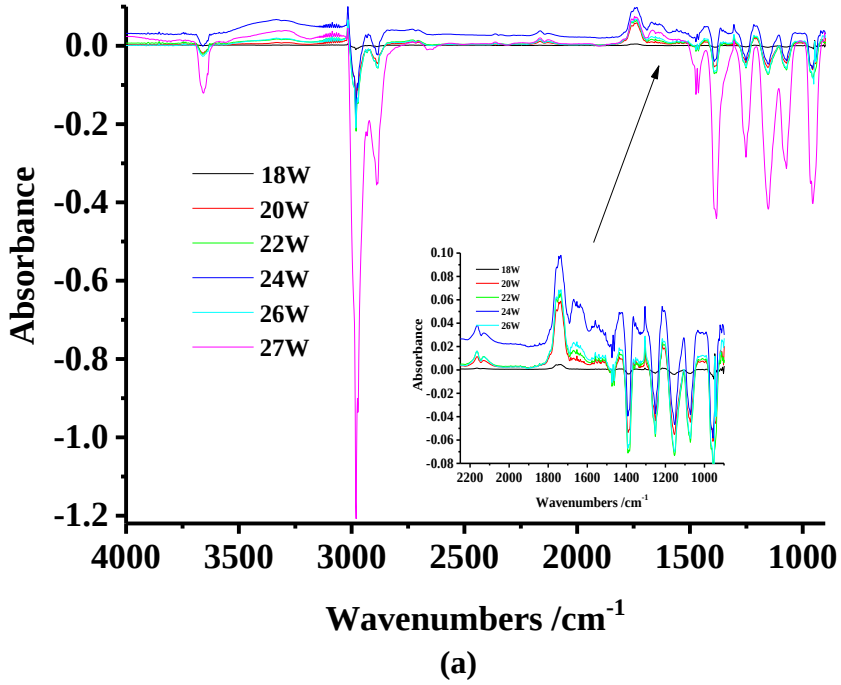

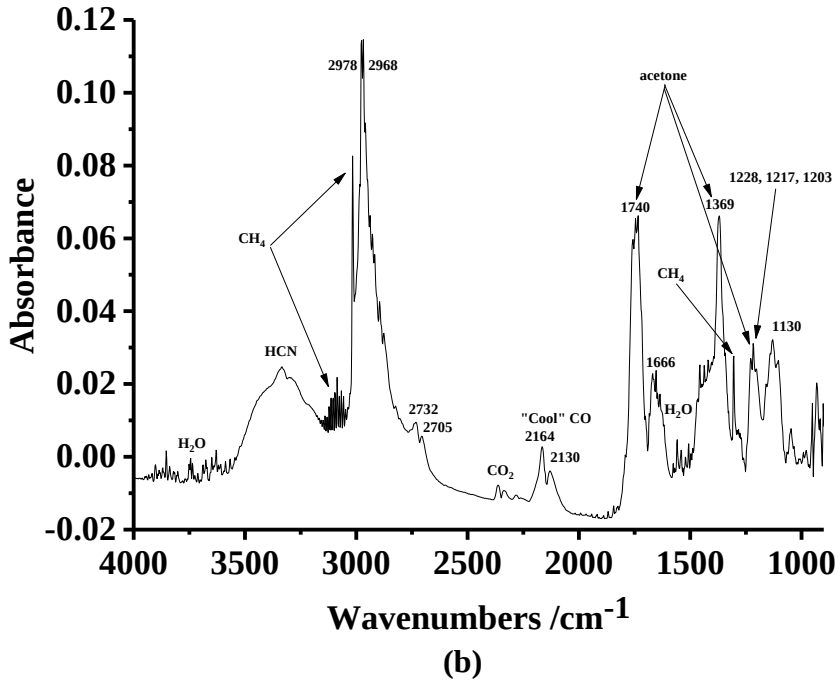

Figure 3.9. (a) FTIR spectra (100 co-added scans and averaged scans at 4 cm^{-1} resolution, ca. 100 seconds per scan set) collected during experiments in which nitrogen gas was passed through isopropyl alcohol at 298 K and atmospheric pressure into the IR plasma transmission cell at a flow rate of 200 cm^3 min^{-1} and a reference spectrum collected. The plasma was then initiated and sample spectra collected as a function of time. The spectra shown were collected after 1 minute at the various input powers shown. The inset shows the spectra below 2200 cm^{-1} without the spectrum taken at 27 W, for clarity. (b) The spectrum collected at an input power of 27 W in (a) with the IPA features annulled, see text for details.

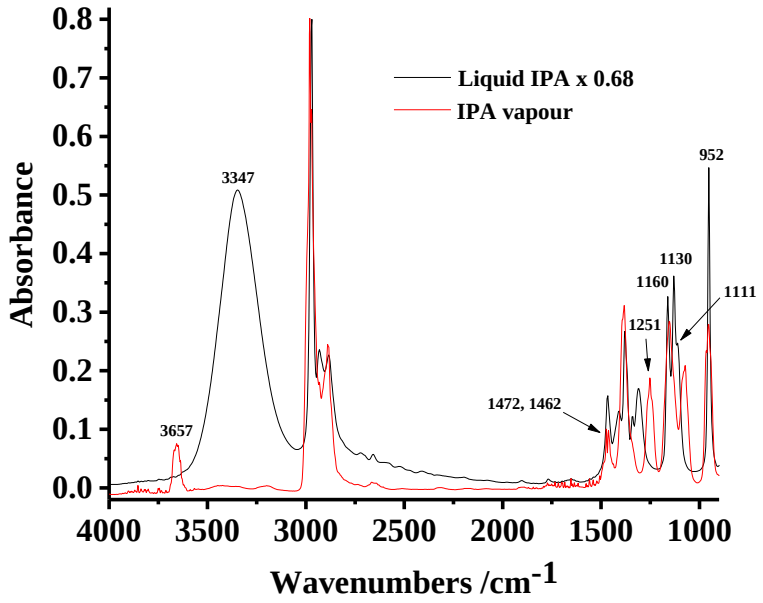

Figure 3.10. Comparison of the spectra of gas phase IPA and an authentic sample of liquid IPA. The former was obtained using the plasma transmission cell see fig. 3.8, and the latter as a thin layer pressed between the CaF_2 windows of a Thermo Scientific Presslok demountable cell holder. The liquid phase spectrum was scaled by a factor of 0.68 to allow comparison.

Gas phase IPA /cm^{-1}	Liquid phase IPA /cm^{-1}	Assignment	Notes
3657	3347	ν_{OH}	ν = stretch bond
2980		ν_{aCH3}	ν_a=asymmetric stretch bond
2971	2971	ν_{aCH3}	ν_a=asymmetric stretch bond
2933	2932	ν_{sCH3}	ν_s= symmetric stretch bond
2900 (sh)			
2886	2883	ν_{CH}	ν = stretch bond
1472	1466	δ_{aCH3}	δ_a= asymmetric deformation bond
1462		δ_{aCH3}	δ_a= asymmetric deformation bond
	1408		
1383	1379	δ_{sCH3}	δ_s = symmetric deformation bond
	1340		
	1310		
1251		δ_{OH}, δ_{CH},	δ = deformation bond
1152	1160	ν_{CC}, ν_{CO}, r_{CH3}	ν =stretch bond, r=deformation
	1130		
	1111		
1080(sh)		ν_{CC}, r_{CH3}	ν =stretch bond, r=deformation
1073		ν_{CC}, r_{CH3}	ν =stretch bond, r=deformation
966		Terminal and bridged C-O str.	
954	952		
942(sh)			

Table 3.1. The IR absorptions of gas and liquid phase isopropyl alcohol [2-4][6-8]11][12], see text for details.

/cm^{-1}	Assignment	Notes
3335 + 3284	ν_{3CH} band of HCN	ν_3=anti symmetric stretch bond
2732 + 2705	?	
2164 + 2130	$\nu_{C=O}$ band of "Cold" CO	ν = stretch bond
1666	$\nu_{C=C}$ band of isophorone	ν = stretch bond
1740	$\nu_{C=O}$ band of acetone	ν = stretch bond
1369	δ_{CH3} band of acetone	δ = deformation bond
1215	ν_{C-C} band of acetone	ν = stretch bond
3086 + 3016	P and Q bands of ν_3 band of CH_4	ν_3 = anti symmetric stretch bond
1305	Q branch of ν_4 band of CH_4	ν_4 = scissoring stretch bond

Table 3.2. The features in fig. 3.9(b). See text for details.

The gain features at 3335 cm^{-1} and 3284 cm^{-1} may be attributed to the P and R branches of HCN [13]: these features were present on all the spectra collected after 1 minute operation. The fine structure centred on 3086 cm^{-1} and the sharp band at 3016 cm^{-1} in fig. 3.9(a) may be unambiguously attributed to the P and Q branches of the ν_3 band of CH_4, and the sharp 1305 cm^{-1} feature to the ν_4 band of CH_4 [14] by comparison with an authentic sample of CH_4 in 13.4 % CH_4+ 10.6 % CO_2 + 76 % N_2, see fig. 3.11; the Q branch in fig. 3.9(b) is distorted by the IPA C-H loss feature.

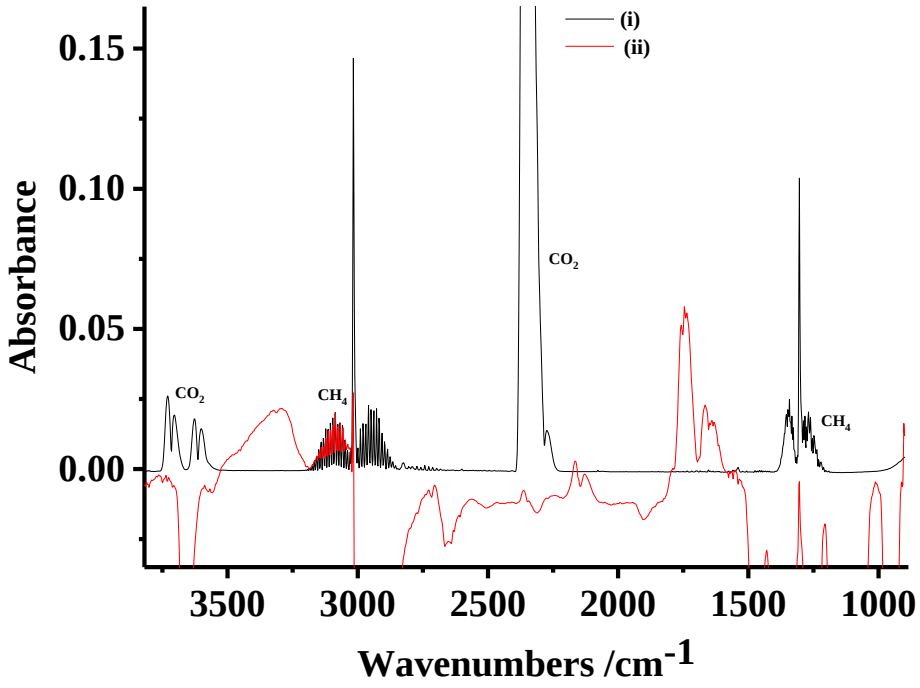

Figure 3.11. The spectrum collected (i) using 13.4 % CH_4+ 10.6 % CO_2 + 76 % N_2 in the plasma transmission cell and that of (ii) collected after 1 min at 27 W in fig. 3.9(a), the spectrum was moved down 0.017 for clarity.

The bands at 1740 cm^{-1}, 1369 and 1215 cm^{-1} may be attributed to gas phase acetone [15] an assignment confirmed by comparison with the IR spectrum of an authentic sample. Thus, figs. 3.12(a) and (b) show the spectrum in fig. 3.9(b) and a spectrum of gas phase acetone obtained by placing ca. 0.1 cm^3 of the liquid in the plasma transmission cell and allowing it to evaporate. As well as the C=O band at 1740 cm^{-1} and the band at 1369 cm^{-1} the features at 1203, 1217 and 1228 cm^{-1} form a highly distinctive group which may be unambiguously assigned to acetone. It is clear from figs. 3.12(a) and (b) that the broad feature around 3347 cm^{-1}, the features at 2968 and 2978 cm^{-1}, the multiple bands around 1130 cm^{-1} and the feature at 1046 cm^{-1} are not due to acetone. With the exception of the 1046 cm^{-1} feature which remains unassigned, these bands may be attributed to liquid IPA condensing on the cell windows, and this is discussed in detail below, as is the origin of the broad feature at ca. 1666 cm^{-1}.

There are at least two possible routes to acetone: the dehydrogenation of IPA over metal and metal oxide catalysis is a well-known endothermic [16] and important reaction requiring temperatures $\geq$ 200 °C catalysed by basic oxides including MgO [16–19]; hence it may be that the acetone is produced in an analogous process involving the removal of dihydrogen from the H of the hydroxyl group and an H atom on the carbon adjacent to the OH moiety. However, such a surface process would be inhibited by the formation of the liquid film, and the data below suggest that the formation of acetone is linked to that of CO and HCN, hence it is more likely that the acetone is produced from an entirely gas-phase process; for example, from mass spectrometry studies of IPA, acetone can be produced by the deprotonation of $C_3H_7O^+$ [20].

It does not seem unreasonable to assign the bands at 2164 and 2130 cm^{-1} in fig. 3.9(b) to the P and R branches of a linear molecule. In addition, the reasonably high frequency of the band centre suggests a light molecule; further the band centre is identical to that of gas phase CO (2145 cm^{-1}), see fig. 3.13 which shows the features in fig. 3.9(b) compared to an authentic sample of CO. The 2164 and 2130 cm^{-1} bands resemble the P and R branches of CO, except with a reduced bandwidth, as would be expected if the molecule was cooled down: for example, Bauerecker et al. [21] observed the rotation-vibration bandwidth of $^{13}C^{16}O$ to be reduced by about 40 % on cooling the gas from 300 K to 45 K, without any change in band centre. From fig. 3.13, the bandwidth is ca. 24 % lower than that of CO at room temperature, and a calculation based on separation of the maxima of the P and R branches [22] suggest a temperature of ca. 115 K, in broad agreement with the work of Bauerecker and co-workers; if the resolution of 4 cm^{-1} is taken into account, this gives a temperature range of 89–143 K. This is a challenging observation as it would be expected that the gas phase molecules in the plasma glow would be

in thermal equilibrium: however, it may simply be the case that the cold CO bands represent the steady state of the species, constantly produced and constantly removed by the gas feed.

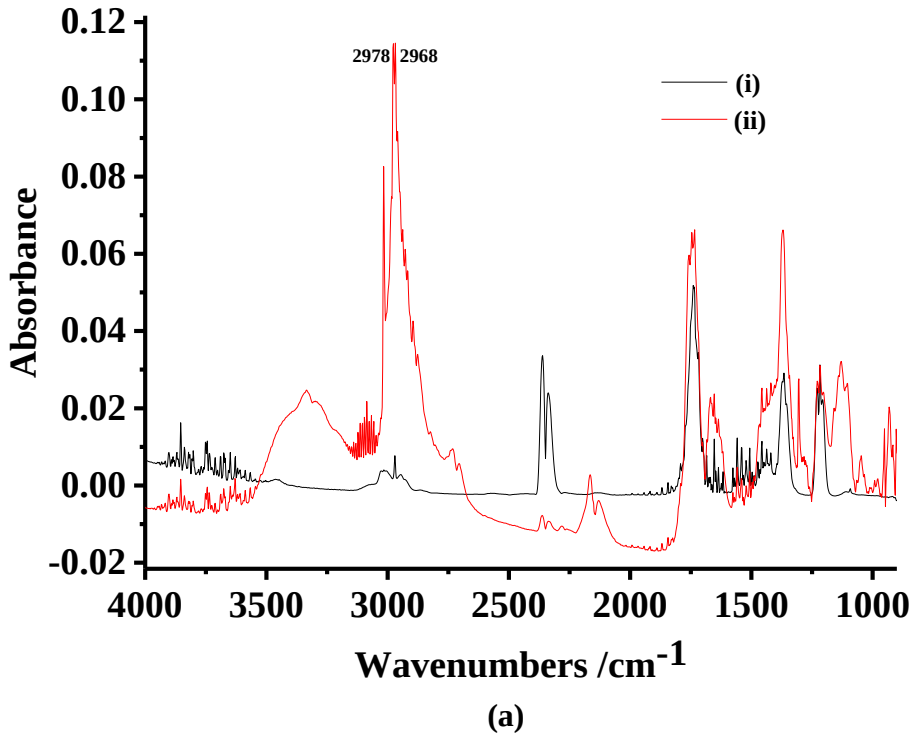

(a)

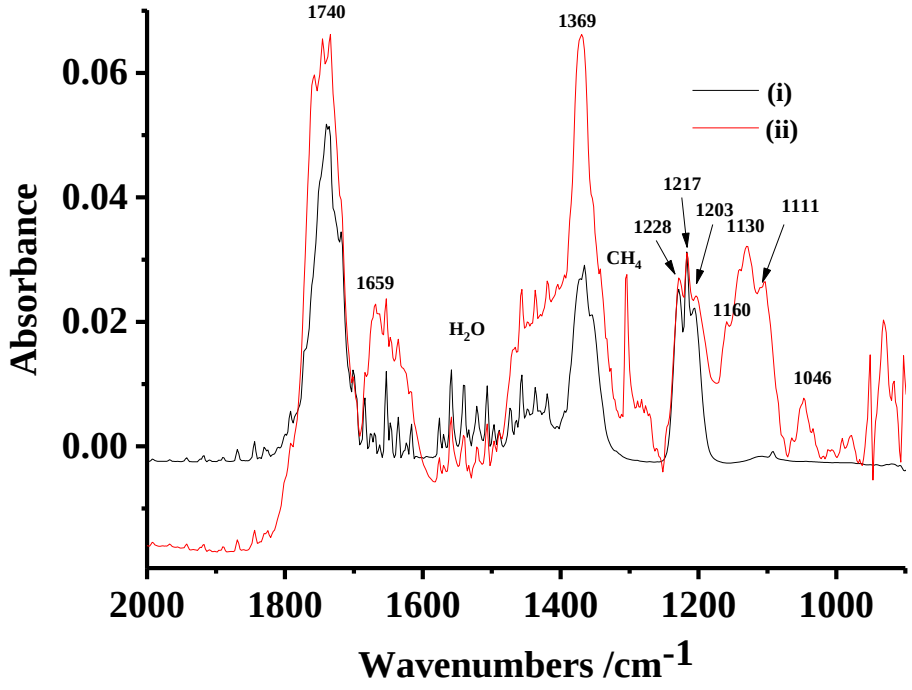

(b)

Figure 3.12. A spectrum of (i) gas phase acetone obtained in the plasma transmission cell and (ii) the spectrum in fig. 3.9(b): (a) full spectral range and (b) 900 – 2000 cm^{-1}. The acetone spectrum was reduced by a factor of 3.9 for comparison.

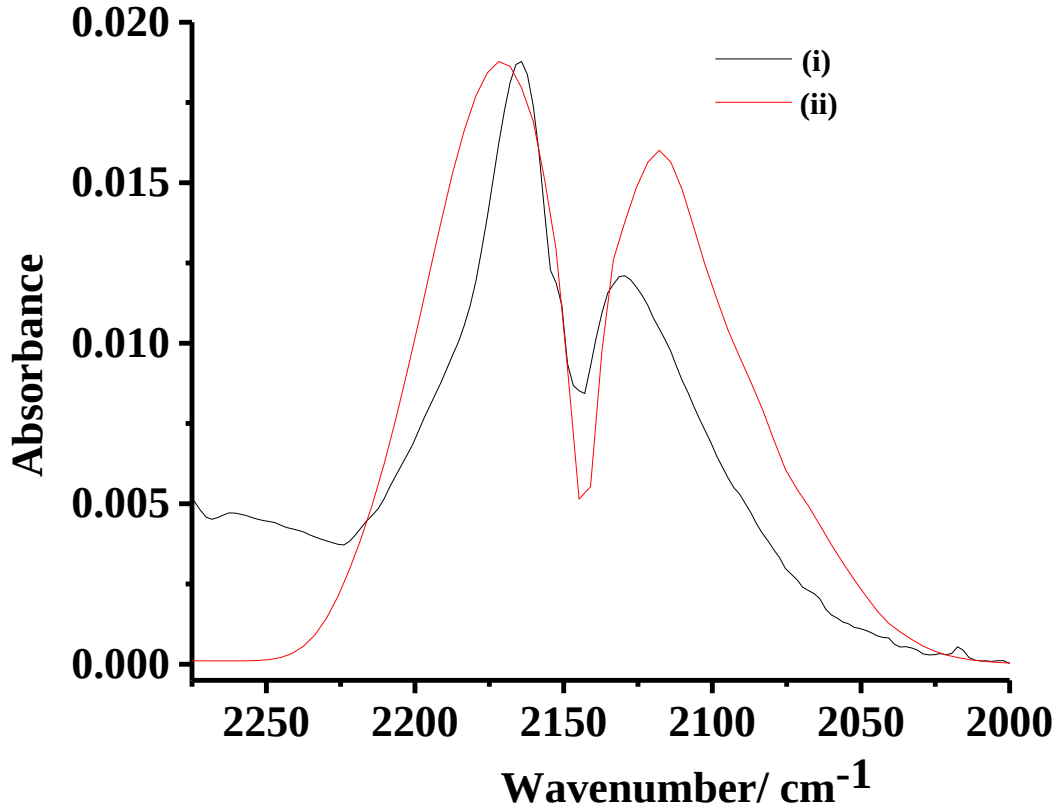

Figure 3.13. (i) The CO spectral region of fig. 3.11 and (ii) that of a spectrum collected of 100 % CO in a 1 cm pathlength transmission cell at 298 K. The spectrum in (ii) has been scaled down by a factor of 15.7.

Figure 3.14 shows typical spectra collected at an input power of 27 W using the spectrum collected without plasma as reference: as can be seen, the CH_4 and CO bands (boxed) are present, and their intensities unchanged throughout the experiment indicating steady-state concentrations: this postulate was supported by the IPA/Ar data discussed below. The HCN features also do not change in intensity with time and hence were annulled when the spectrum collected at 1 minute was subtracted from those collected at longer times (see fig. 3.16) and this is discussed in detail below. It did not prove possible to determine the time dependent behaviour of the acetone due to the overlying strong features.

Figure 3.15(a) shows plots of the partial pressure of methane, and the absorbances of the CO band at 2164 cm^{-1} and the 1740 cm^{-1} acetone band normalised to their maximum values, as a function of input power, measured from the spectra collected after 1 minute and using the spectra collected without plasma as the background. The raw data are presented in fig. 3.15(b). The CH_4 pressure was determined by comparison of the absorbances of the rotational band at 3086 cm^{-1} with the same feature in the spectrum of an authentic sample of 13.4 % CH_4 + 10.6 %

CO_2 + 76 % N_2, see fig. 3.11 and the extinction coefficient of CH_4 was determined from measurements using the pure gas in a 1 cm pathlength cell and is presented in table 3.3 along with that of the 3335 cm^{-1} band of HCN which was estimated from the paper by Choi and Barker [13]. As can be seen, all three species apparently track each other, suggesting they are formed via a common intermediate and/or in the same process, and this postulate was supported by the experiment discussed below in which N_2 was replaced by Ar.

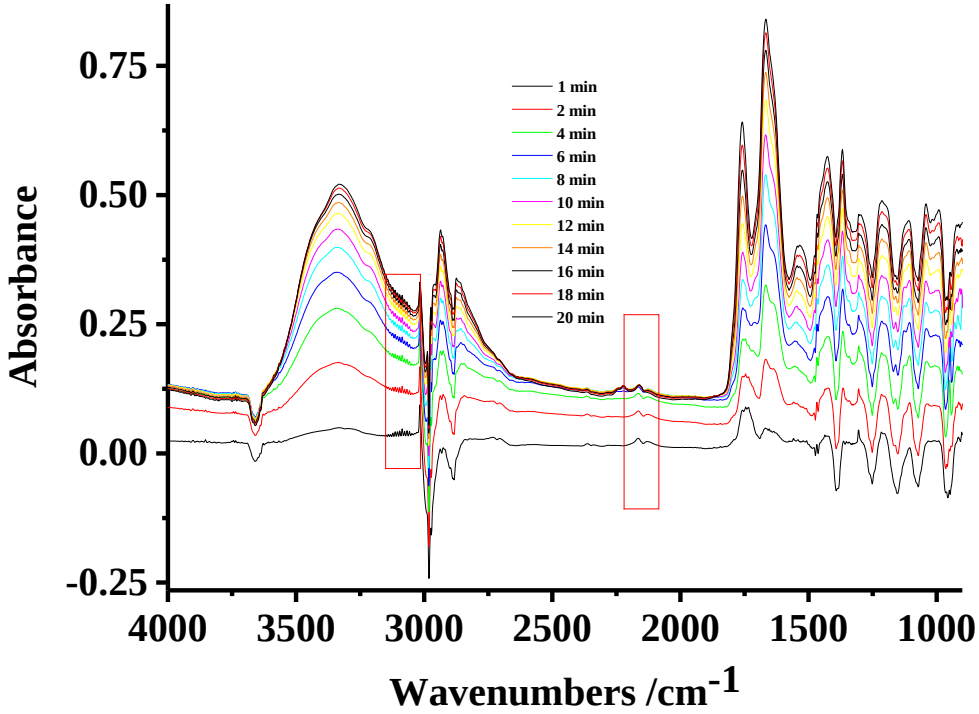

Figure 3.14. In-situ FTIR absorbance spectra (100 co-added scans and averaged scans at 4 cm^{-1} resolution, ca. 100 seconds per scan set) collected during the plasma treatment of IPA at 27 W as a function of plasma operation time. The N_2 gas flow rate was 200 cm^3 min^{-1}, bubbled through a Dreschel bottle of pure IPA at room temperature.

	Peak /cm^{-1}	**ε /M^{-1} cm^{-1}**
CH_4	3086	3.5
	1346	6.4
HCN	3335	2.8 [13]

Table 3.3. The extinction coefficients of various gas phase species.

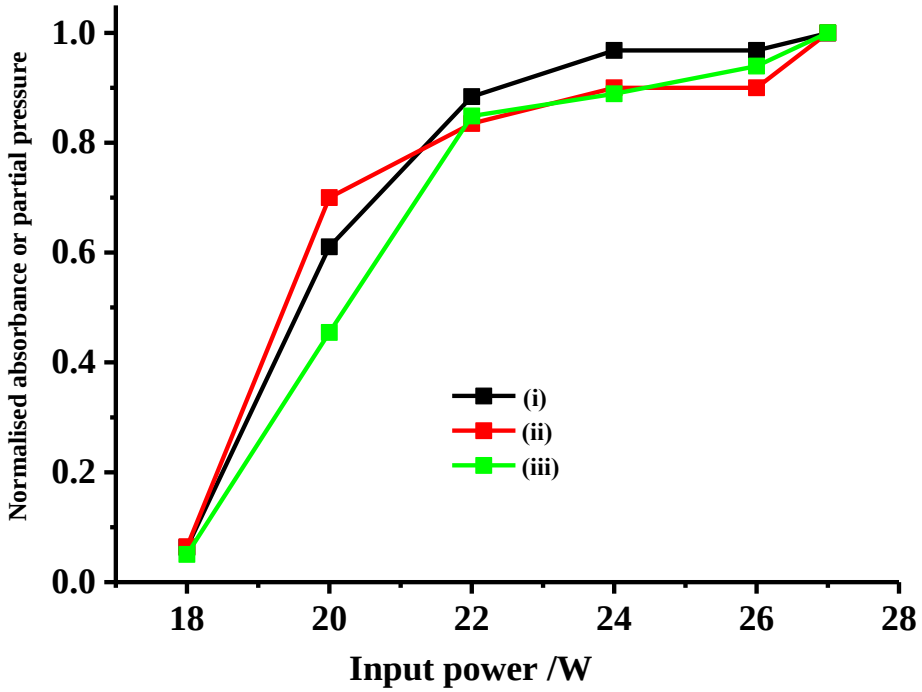

(a)

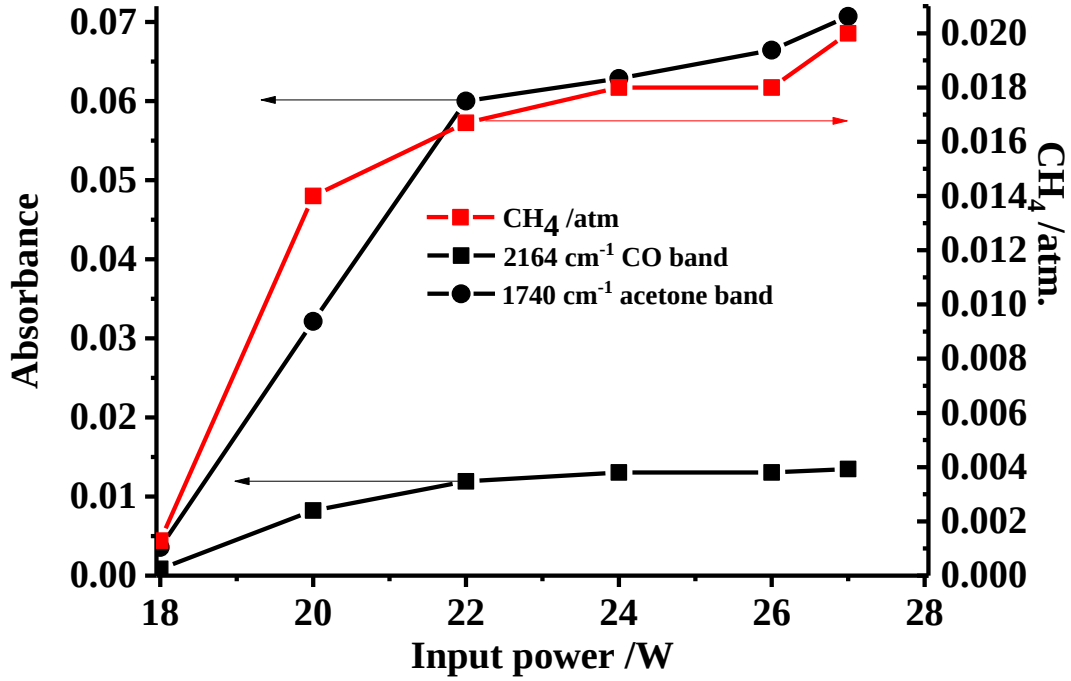

(b)

Figure 3.15. Plots of (i) the absorbance of the 2164 cm^{-1} CO band, (ii) the partial pressure of CH_4 and (iii) the absorbance of the 1740 cm^{-1} acetone band, measured after 1 minute plasma operation as a function of input power from the experiments shown in fig. 3.9(a) normalised to their maximum values and (b) the raw data.

In the plasma transmission cell, the IR beam passed along the surfaces of both the Macor caps, but bands attributable to adsorbed IPA were not observed in any of the spectra recorded using the cell.

3.3.4. The spectra collected at longer times

Figure 3.16 shows the spectrum collected after 1 minute in figs. 3.9(a) and 3.14 subtracted from those taken at longer times in order to remove the loss features due to gas phase IPA; as may be seen from the figure, there is no further reduction in the vapour pressure of the IPA as a function of time once the power to the plasma is switched on. Following the experiment depicted in the figure, a brown oily deposit was observed on the Macor plates and CaF_2 windows, which was also observed in all the plasma experiments using IPA and nitrogen, see fig. 3.17 and the IR spectrum of which corresponded closely to the spectrum collected after 20 minutes in fig. 3.16. As will be discussed further below, this oil appeared to comprise at least two components, A and B. The oil was dissolved in $CDCl_3$ and an attempt was made to analyse it with carbon and proton NMR, but the results were inconclusive.

Figure 3.18(a) shows plots of the key features in fig. 3.16 as a function of time normalized to their maximum values, and fig. 3.18(b) shows the raw data. As can be seen from figs. 3.16 and 3.18, the 1762 and 1536 cm^{-1} bands track each other and may thus be assigned to a single species; it is also clear that the 1666, 1426 and 1370 cm^{-1} features do not belong to the same species as the 1762 and 1536 cm^{-1} bands. Unfortunately, the 1426 and 1370 cm^{-1} bands are in the spectral region where significant overlap of bands from different species may be expected. This challenge is addressed further below.

Close inspection of fig. 3.16 shows the distinctive 1160, 1130 and 1111 cm^{-1} bands attributable to liquid phase IPA, see fig. 3.10, suggesting condensation on the windows and surfaces of the cell as shown in fig. 3.17, which become indistinct in the spectra collected after 8 minutes. These bands do not appear to change in intensity significantly up to 8 minutes, suggesting the thickness of the condensed layer does not change over this timescale. These observations suggest that the spectra in fig. 3.16 could be simplified if divided into two regions, those up to 8 min from which was subtracted the spectrum collected after 1 minute, and the spectrum taken at 8 minutes subtracted from those taken up to 20 minutes. The results are shown in figs. 3.19 and 3.20.

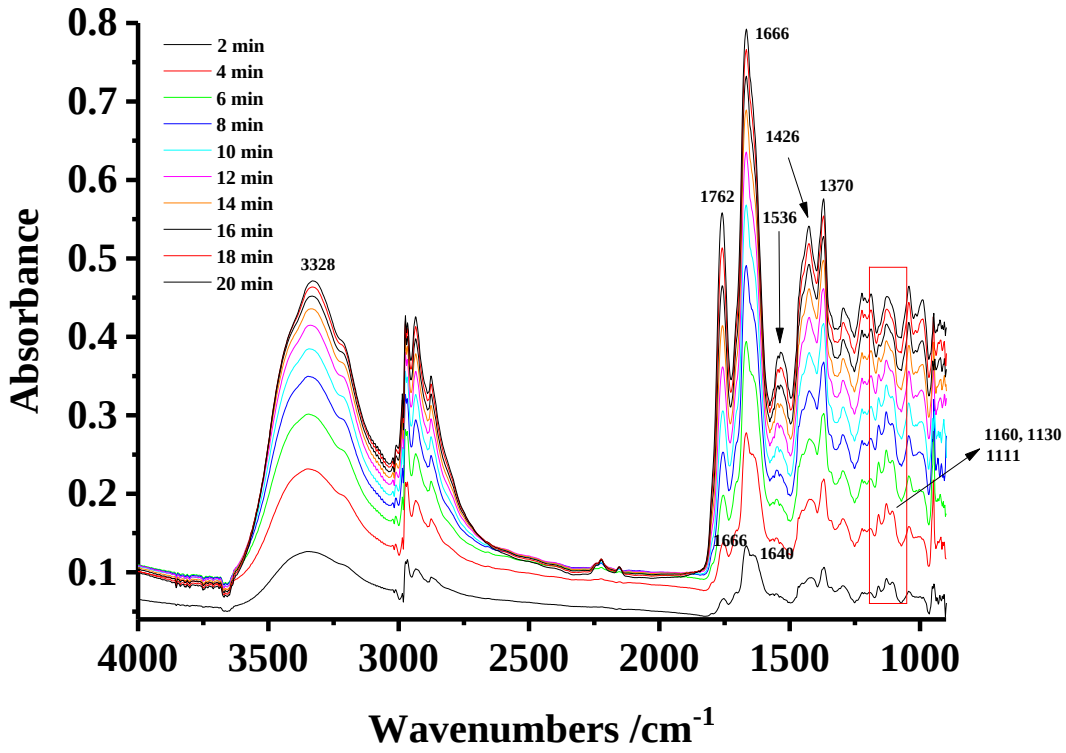

Figure 3.16. The spectra obtained during the experiment carried out at 27 W shown in fig. 3.9(a). The spectra were collected using a gas feed of IPA vapour in N_2. The N_2 was bubbled through pure IPA at 298 K at a flow rate of 200 cm^3 min^{-1}. The reference spectrum was collected under the same conditions, but without plasma. The spectrum collected after 1 minute was subtracted from those taken up to 20 minutes.

(a) **(b)**

Figure 3.17. Photographs of the deposit on the: (a) Macor caps and (b) CaF_2 windows, see text for details.

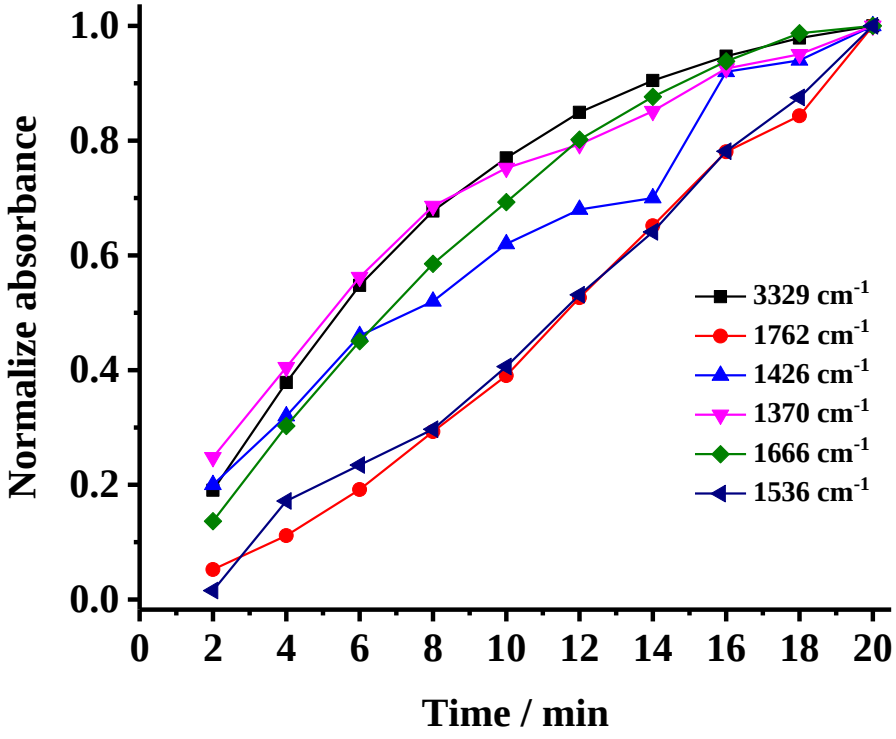

(a)

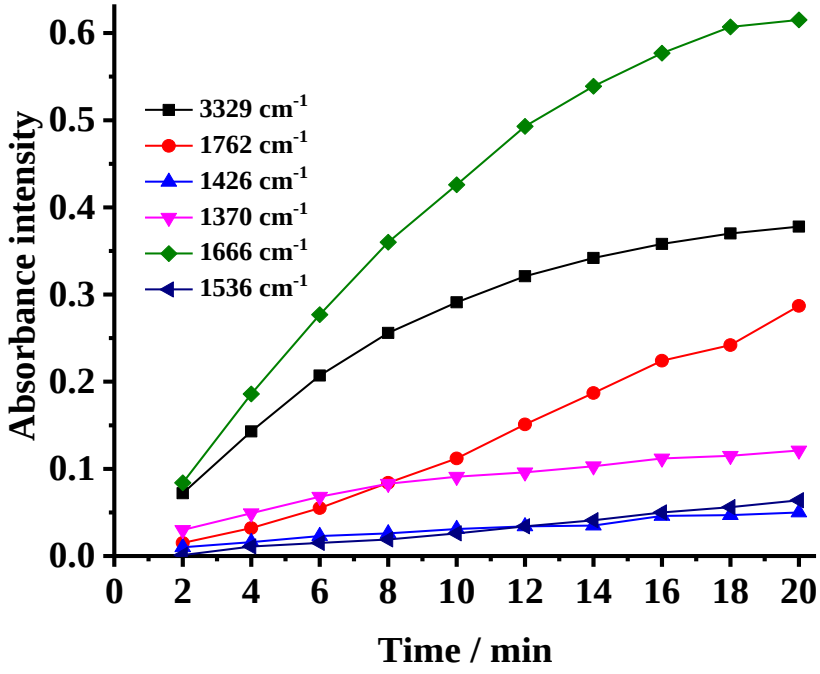

(b)

Figure 3.18. Plots of: (a) the intensities of the key features in fig. 3.16 as a function of time, normalized to their maximum values and (b) the raw data.

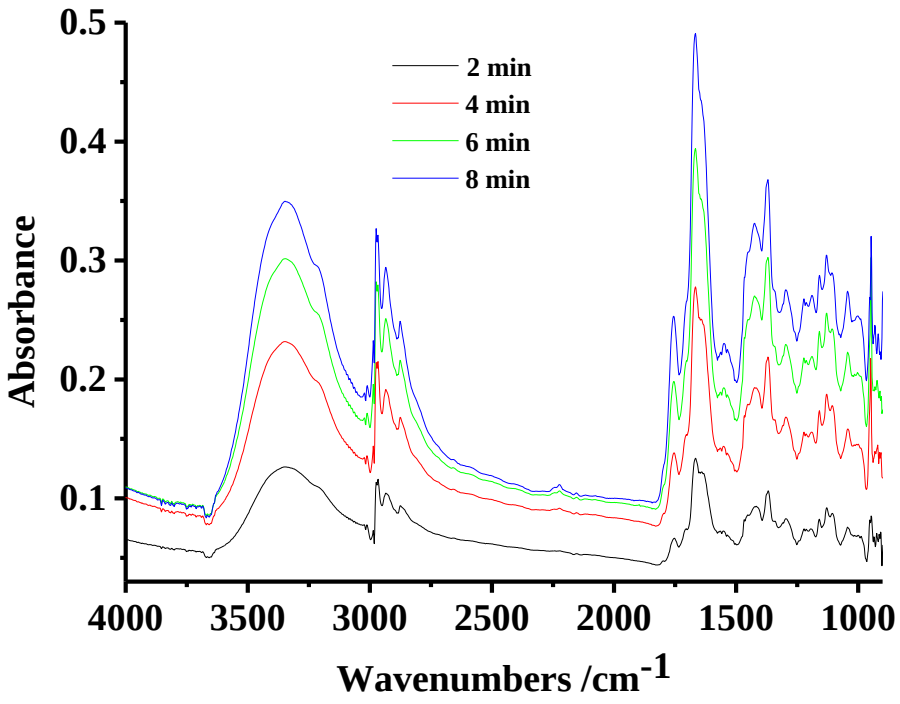

Figure 3.19. The spectrum collected after 1 minute in fig. 3.16 subtracted from those taken up to 8 minutes.

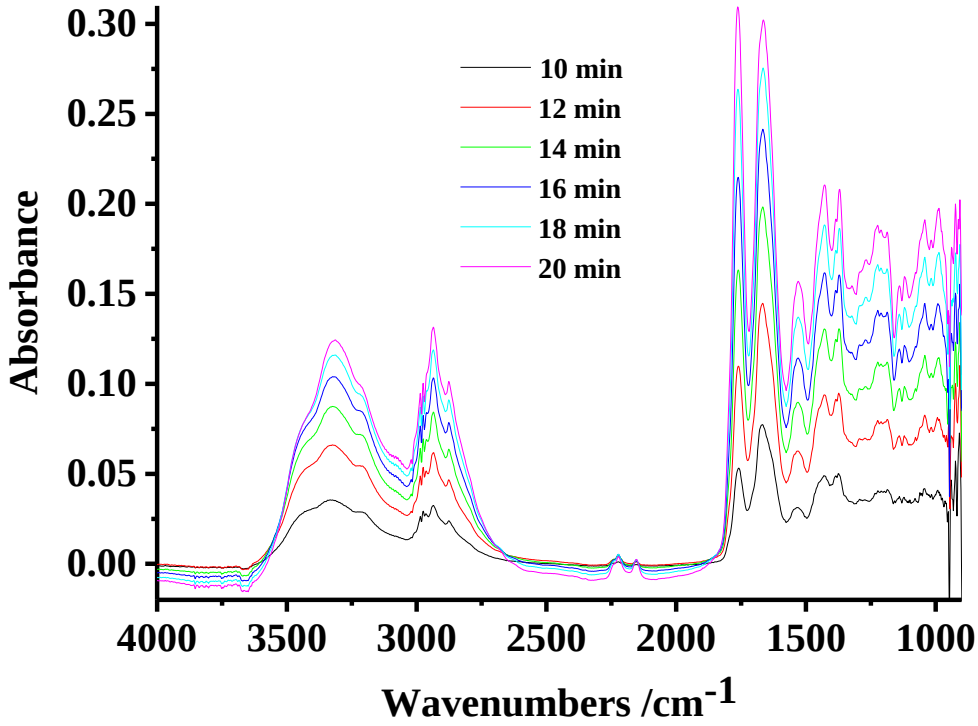

Figure 3.20. The spectrum collected after 8 minutes in fig. 3.16 subtracted from those taken up to 20 minutes.

By comparing the relative intensities of the various features in figs. 3.19 and 3.20 it is clear that there are bands due to at least two different species, some isolated as discussed above, but some clearly overlapping in the spectral region below 1500 cm^{-1}. Figure 3.21 shows the spectra collected at 8 minutes in fig. 3.19 and that at 20 minutes in fig. 3.20 along with the spectrum of liquid IPA in fig. 3.10 scaled such that the 1130 cm^{-1} feature is approximately the same intensity as that in fig. 3.19. It is clear that the peak at 2970 cm^{-1} in figs. 3.19 and 3.21 is due to liquid IPA, that there is a significant contribution from liquid IPA to the broad feature between 2500 and 3700 cm^{-1} in the spectra collected up to 8 minutes and that there are features below 1500 cm^{-1} belonging to both the unidentified species characterized by the strong bands at 1762 and 1666 cm^{-1}. The situation becomes clearer if the spectra collected at 10 min and 20 min in fig. 3.20 are compared, see fig. 3.22; thus the 1762, 1536, 1426 and 1370 cm^{-1} bands belong to one species, species A, and the 1666, 1630(sh), 1430, 1385 and 1373 cm^{-1} features to species B. It is not clear from the various figures what species is responsible for the 3329 cm^{-1} absorption: thus from fig. 3.21 it can be seen that there is an appreciable contribution from the O-H stretch of liquid IPA to the O-H absorption up to 8 minutes, and there are marked differences in the shape of the feature between the two NTP spectra in the figure. Further, it appears from 3.22 that the 2936 and 2876 cm^{-1} C-H bands are common to both species A and B, if in different relative intensities. The various features are summarised in table 3.4. The time-dependent behaviour of the intensities of the 1426 and 1370 cm^{-1} species A bands in fig. 3.18 is clearly distorted by the presence of the underlying 1430, 1385 and 1373 cm^{-1} features of species B as shown in fig. 3.23.

The acetone generated from the IPA may undergo a range of transformations leading to higher molecular species bearing both C=O and –OH groups such as β-hydroxyketones (acid and/or base catalysed Aldol reaction [23]) and diols resulting from Mg catalysed Pinacol coupling [24]. The nature and distribution of the products is dependent upon the catalyst employed as is the extent of similar downstream reactions with additional structural complexity due to facile dehydration of these materials installing random elements of unsaturation. This sequence of events inevitably produces an orange or red polymeric oil as shown in fig. 3.17 [25][26] containing CH_3, C=O, C=C and O-H groups. The number, distribution and nature of these functionalities are a result of both the catalyst and the experimental conditions employed, and the polymers produced are described generically as "polymethylacetylene-like". The C-H asymmetric and symmetric stretches are observed at ca. 2960 and 2865 cm^{-1}, respectively, and the absorptions due to C=O conjugated with the polyene structure appear around 1705 and 1670 cm^{-1}, the latter much stronger than the former. The C=C stretch of the polyene backbone moves

down in frequency as the conjugation increases, see [27] and references therein, and was reported to absorb around 1560 cm^{-1} in the seminal work by Cataldo [25] [26]. If the conjugation between the ketone C=O moieties and the polyene backbone is broken, often by cyclisation and/or the formation of quaternary carbon centres (e.g. geminal CMe_2 groups), the polyene C=C absorption does not shift, but the C=O absorption moves to significantly higher frequencies. Thus it can be suggested that species A is a polymeric product resulting from a cascade of Aldol/Pinacol/dehydration reactions initiated by the formation of acetone. Trinh and Mok [28] investigated the oxidative decomposition of acetone over ZnO and/or MnO_2 catalysts and observed the formation of a brown polymeric deposit on the walls of their reactor. The IR spectrum of this deposit shows similarities to the spectra in fig. 3.16 (see fig. 3.24), and the authors postulated the polymer contained ester groups.

In the thermally-driven Aldol condensation of acetone over alkaline catalysts, as well as polymethylacetylene-like products, isophorone is a common side product (e.g. from cyclisation and subsequent E_{1CB} elimination of water [29]). On the basis of the spectrum as shown in fig. 3.23, product B was identified as isophorone. Interestingly, isophorone is one of the products from the thermal Aldol condensation of acetone at lamellar double hydroxides which, as is the case with Macor, also contain magnesium and aluminium oxides [30].

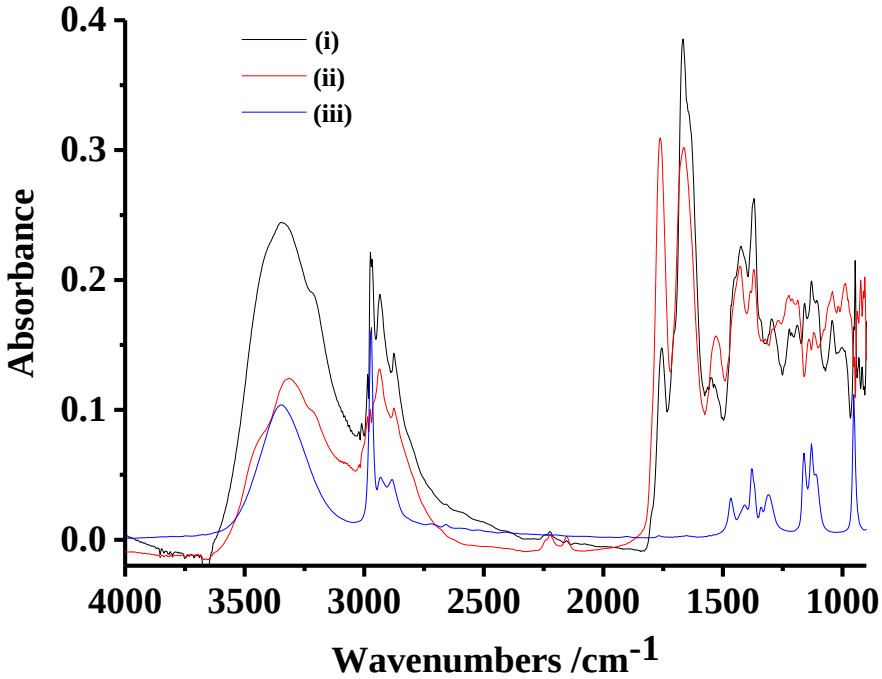

Figure 3.21. A comparison of the spectrum (i) collected after 8 minutes in fig. 3.19, (ii) the spectrum taken after 20 minutes in fig. 3.20, and (iii) the spectrum of liquid IPA in fig. 3.10, the latter reduced by a factor of 7 for clarity. See text for details.

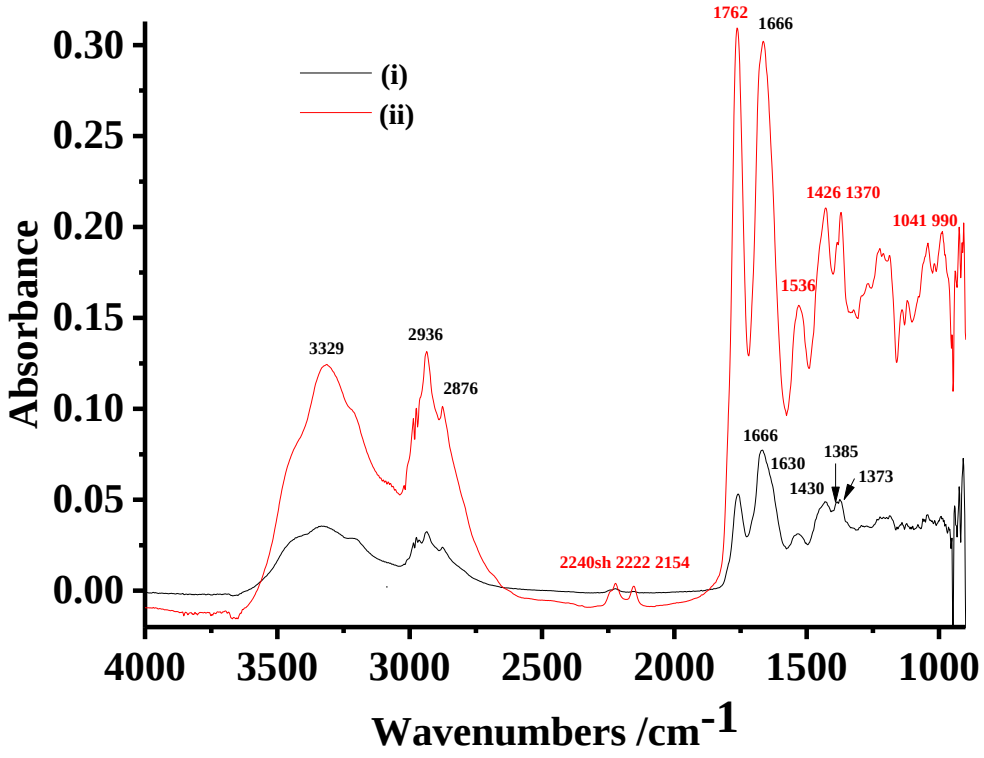

Figure 3.22. The spectra collected after (i) 10 minutes and (i) 20 minutes in fig. 3.20. See text for details.

Product A bands /cm^{-1}	Product B bands /cm^{-1}	Isophorone /cm^{-1}
2936	2936	2957
2876	2876	2869
1762	1666	1668
1536	1630 (sh)	1630
1426	1430	1435
1370	1385	1378
	1373	1367

Table 3.4. The features observed in the spectra in figs. 3.16, 3.19 and 3.20, and the absorptions of isophorone from fig. 3.23.

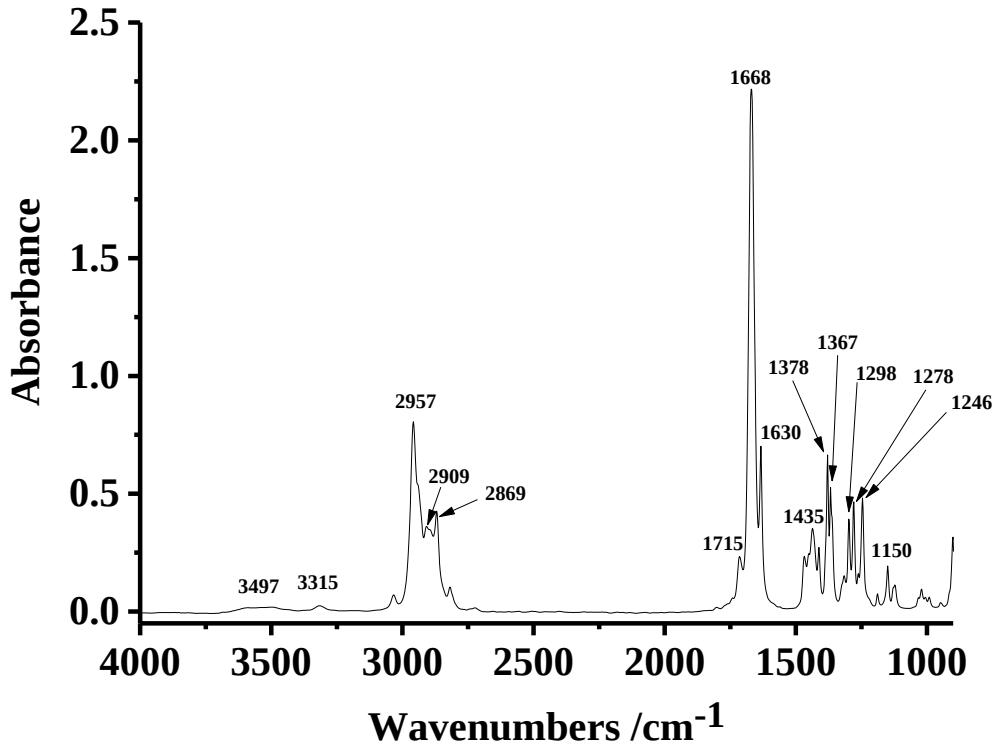

Figure 3.23. IR spectrum of ca. 50 μL isophorone obtained as a thin layer pressed between the CaF_2 windows of a Thermo Scientific Presslok demountable cell holder.

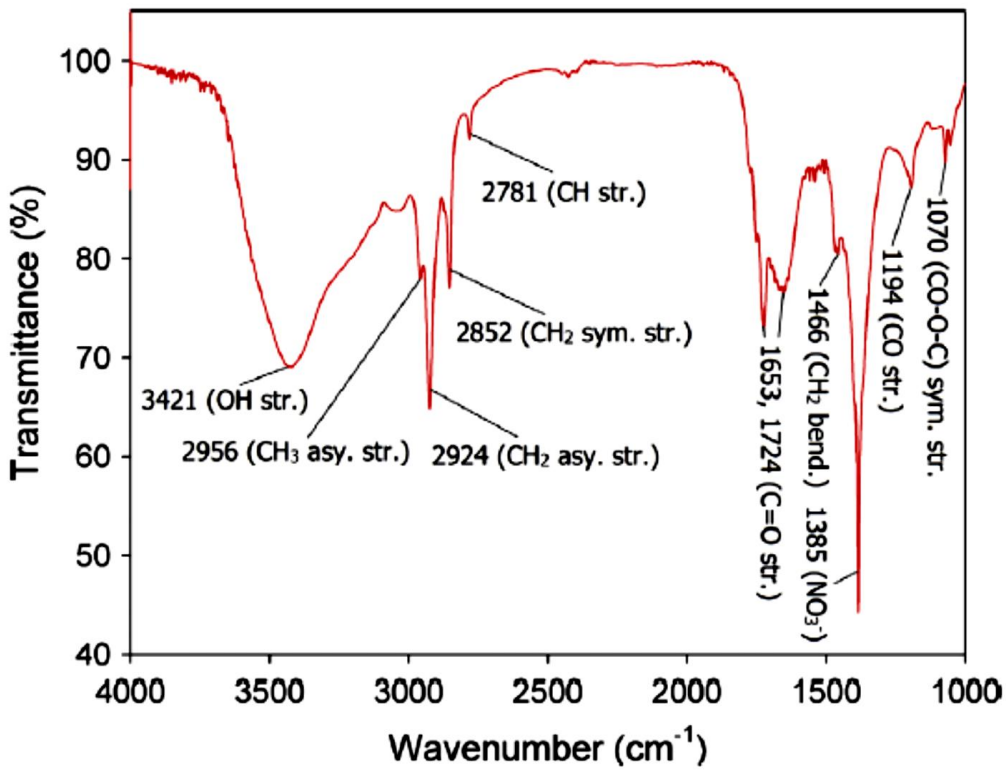

Figure 3.24. FTIR spectrum of the polymer-like deposit collected from the reactor wall in the work by Trinh and Mok [28].

Close inspection of the spectrum collected after 2 minutes in fig. 3.16 shows that the OH band is prominent, as is a clear band at 1640 cm^{-1}. The latter does not track the adjacent 1666 cm^{-1} and becomes overlain by the 1630 cm^{-1} shoulder. The presence of the 1640 cm^{-1} and the broad O-H absorption, along with the sloping absorption that increases at frequencies > 1750 cm^{-1} and the clear, broad absorption underlying the bands below 1750 cm^{-1} suggest the formation of water [31], along with C-OH groups: the former arising from the Aldol condensation reaction.

The production of the gas phase products CO, CH_4 and HCN, and the fact that they fairly rapidly attain a steady-state in the plasma in the flowing feed gas, in conjunction with the separate production of the isophorone and the polymer –containing brown oil which requires a longer time to form, suggests the presence of two separate and parallel reaction pathways. This observation is in accord with the plasma model of Kim et al. [32] in which the active species such as OH radicals occupy a thin layer perhaps 50 μm thick above the catalyst and are available for reaction at the catalyst: above this layer, species produced in the plasma react in the same way as in the absence of catalyst. Thus the gas phase products are produced in the body of the plasma, away from the direct participation of the catalyst, whilst the isophorone and polymer are produced in the plasma adjacent to the catalyst: both possibly require the build-up of intermediates on the Macor, but, as may be seen from the plots in fig. 3.18, the isophorone is produced in a different process to the polymer, and more rapidly.

3.3.5. Experiments using argon and isopropyl alcohol

Figure 3.25(a) shows the spectra obtained in an analogous experiment to that in fig. 3.16 except that the nitrogen feed was replaced by argon. The plasma was initiated at a significantly lower power (8 W in contrast to 18 W using N_2) and the spectra in fig. 3.25(a) were collected at 8 W. The most obvious difference between the two experiments, apart from the expected absence of HCN in fig. 3.25(a), was that no liquid film or isophorone was produced, clearly highlighting the importance of nitrogen gas in their formation. Cold CO, at 136 K (allowing for the resolution gives a temperature range of 108–167 K) was also produced. Figure 3.25(b) shows the spectrum collected after 1 minute in fig. 3.25(a) with the IPA bands annulled by subtraction, using the O-H stretch at 3657 cm^{-1} to determine the scaling factor. The acetone bands are clear, as are the CO_2, cold CO and methane absorptions. In addition to the bands stated above, there are features at 3315 and 3263 cm^{-1} in figs. 3.25(a) and (b) which may be attributed to the C-H stretch of

acetylene [33]. Along with the inhibition of the film formation, the production of acetylene strongly suggests the existence of a modified mechanism on employing argon.

Figure 3.26 shows plots of the various features in fig. 3.25(a) as a function of time. As was stated above, it is clear that (1) the methane, cold CO, CO_2 and acetone essentially show steady state concentrations (as was noted above), whereas the acetylene in the plasma glow steadily increases, and (2) all the species clearly track each other, suggesting they arise from the same or linked process(es). From the figure, the steady state partial pressure of methane was ca. 12 mBar, i. e. not insignificant. The oscillating nature of the plots in fig. 3.26 are fascinating, but their interpretation requires further study.

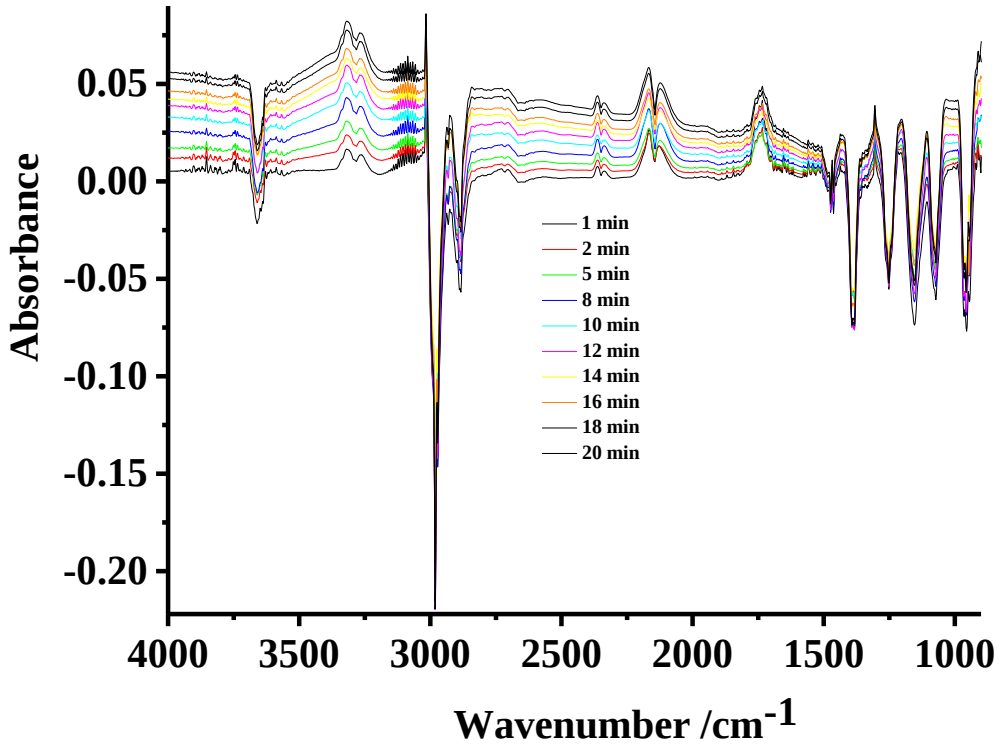

(a)

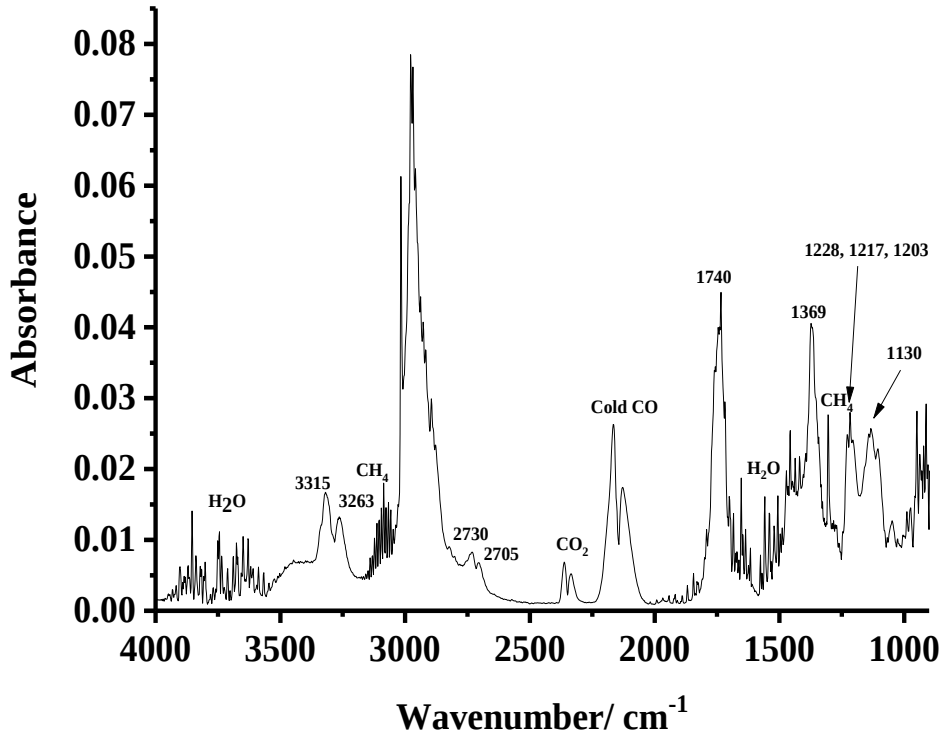

(b)

Figure 3.25. (a) The spectra collected in an analogous experiment to that in fig.3.16, except that the feed gas was argon and the input power 8 W. (b) The spectrum collected after 1 minute in fig. 3.25(a), the gas phase IPA bands were annulled using the spectrum of pure IPA, and employing the O-H stretch of the IPA at 3657 cm^{-1} to determine the subtraction factor.

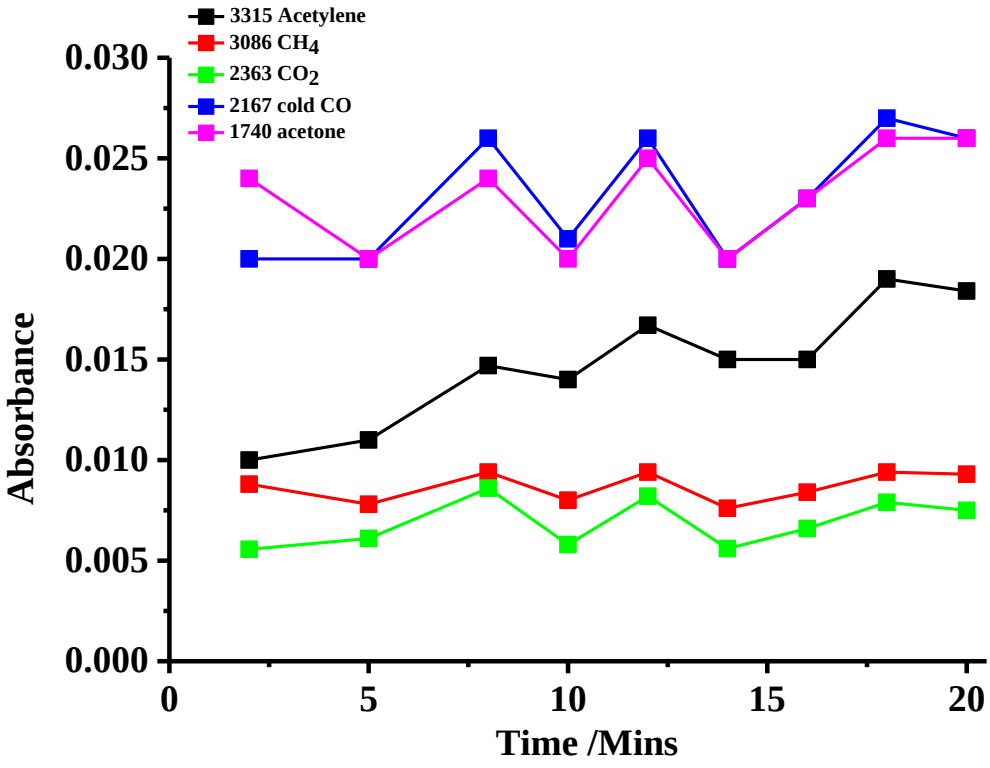

Figure 3.26. Plots of the intensities of the various features in fig. 3.25(a) as a function of time.

3.3.6. The proposed mechanism

First, it will be useful to review the key facts arising from the data discussed above:

- It is clear that cold CO, CH_4, HCN and acetone are produced in the plasma glow in the first minute.
- From fig. 3.14 and numerous repeats, it is clear that CH_4 and cold CO (at least) are produced for the full 20 minutes, ie the formation of the liquid has no effect, therefore their formation must take place entirely in the gas phase.
- It is clear from figs 3.15 and 3.26 that CO, CH_4, HCN and acetone track each other exactly suggesting some commonality.
- Replacing N_2 by Ar not only removes HCN but results in the formation of acetylene.

The production of cold C=O suggests the presence of a "loose" or "late" transition state and hence the possible presence of a roaming mechanism. The roaming mechanism was first proposed by van Zee et al [34] in a seminal paper on the photolysis of formaldehyde to CO and H_2: in essence the standard, tight transition state route produced rotationally hot CO whilst the loose transition state resulted in rotationally cold CO because of rotational deactivation. During the photolysis of acetaldehyde, the formation of a loose transition state allows a roaming mechanism that results in CH_4 and cold CO [35-37], and work by the Klippenstein group [38][39] shows the same is true for thermal decomposition of CH_3CHO at T > 1000 K, more details are explained in Chapter 5.

It is not unreasonable to postulate acetaldehyde as an intermediate: it is difficult to identify from IR spectra in the presence of acetone as it usually appears as a shoulder on the lower frequency of the acetone 1740 cm^{-1} C=O stretch. Further, in our case, it may be present at low steady state concentrations. If acetaldehyde is the key intermediate then the following mechanism would explain the observed data. As per the model proposed by Kim and co-workers [32], there are two reaction zones, the Macor/plasma interface and the bulk plasma, the chemistry in the latter wholly uninfluenced by the Macor. In the bulk of the plasma, the formation of both acetaldehyde and acetone takes place via electron impact:

$$CH_3CHOHCH_3 + e^- \rightarrow CH_3CHO + CH_4 \qquad (3.1)$$

$$CH_3CHOHCH_3 + e^- \rightarrow C_3H_7O^+ + H^+ + 2e^- \qquad (3.2)$$

$$C_3H_7O^+ \rightarrow CH_3COCH_3 + H^+ \quad (3.3)$$

Other decomposition mechanisms are also possible such as reaction with excited metastable N_2 (e.g. $A^3\sum_u^+$) and atomic nitrogen such as in the following reaction:

$$CH_3CHOHCH_3 + N \rightarrow C_3H_7 + HNO \quad (3.4)$$

Acetone does not react further: in contrast, acetaldehyde does reacts further, either by electron impact or photoexcitation: nitrogen-fed non-thermal plasmas show significant emission [40] around the λ_{max} for the dissociation of acetaldehyde of 308 nm [35]:

$$CH_3CHO + e^- \rightarrow [CH_3\text{----}CHO]^{\ddagger} + e^- \text{ (Loose TS)} \quad (3.5)$$

$$CH_3CHO + h\nu \rightarrow [CH_3\text{----}CHO]^{\ddagger} \text{ (Loose TS)} \quad (3.6)$$

$$[CH_3\text{----}CHO]^{\ddagger} \rightarrow CH_4 + CO\text{(cold)} \text{ (Roaming)} \quad (3.7)$$

$$\{[CH_3\text{----}CHO]^{\ddagger} \rightarrow CH_3 + CHO \quad (3.8)$$

In the absence of the liquid film, i.e. with the Macor surface accessible, acetaldehyde is dehydrated to acetylene, catalysed by aluminium/magnesium oxide sites [41] on the Macor:

$$CH_3CHO \rightarrow HC{\equiv}CH + H_2O \quad (3.9)$$

3.4. The experiments using the plasma reflectance cell

3.4.1. Blank experiments

Figures 3.27(a) and (b) shows spectra collected at an input power of 24 W as a function of time using the reflectance cell with Macor and Ti mesh exposed to the IR beam and a nitrogen-fed plasma. The spectra were collected every 2 minutes after turning on the plasma but only a selection are shown, for clarity. The spectra below were all corrected for the window absorption. As can be seen from the figures, the spectra are featureless apart from a sharp, intense feature at 1150 cm^{-1} and a weaker and broader band at 1210 cm^{-1}, both of which grow with time.

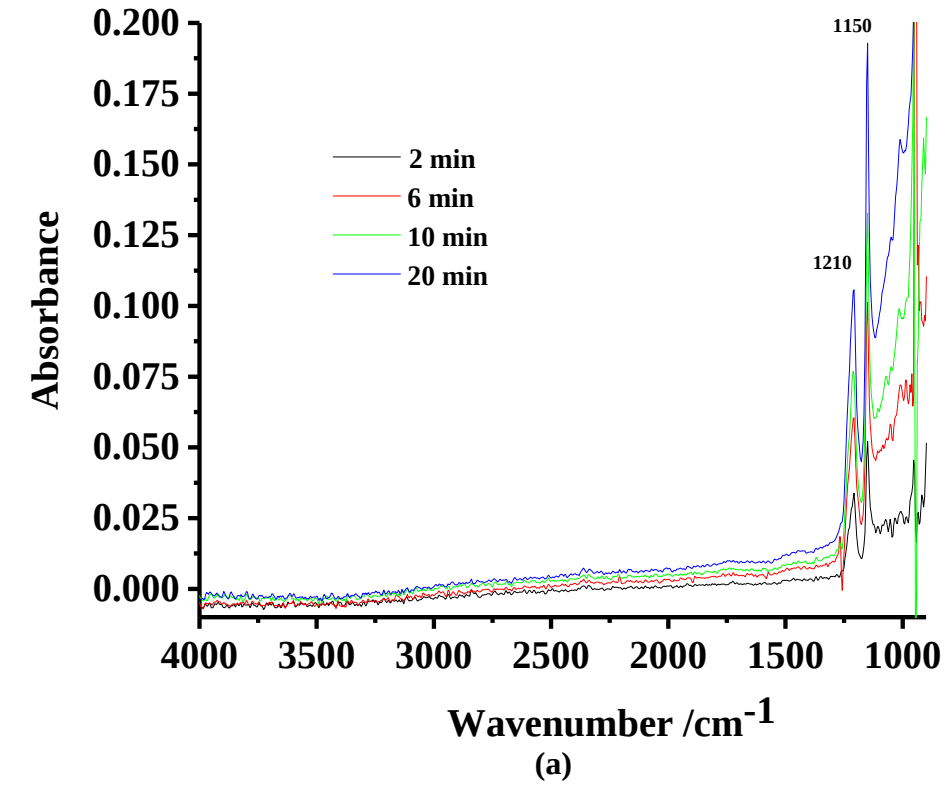

(a)

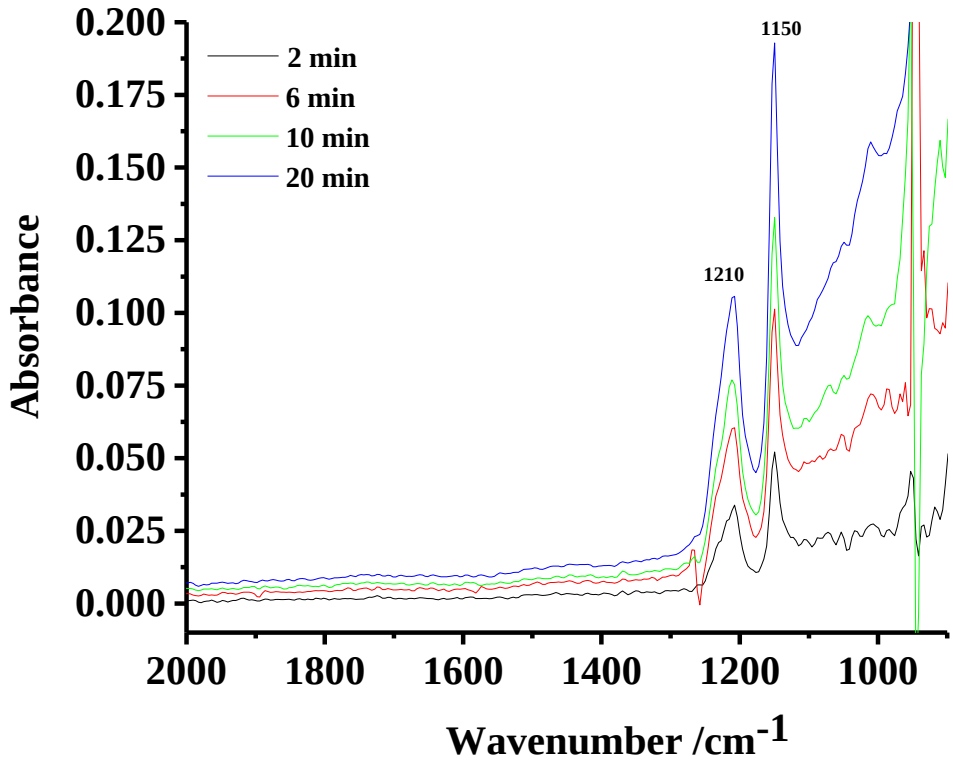

(b)

Figure 3.27. In situ FTIR spectra (8 cm^{-1} resolution, 100 co-added and averaged scans, 60 seconds per scanset) collected using the plasma reflectance cell with Macor+Ti mesh at the times shown on the figure at an input power of 24 W using nitrogen as the feed gas. The spectrum collected immediately before the plasma was initiated was employed as the reference and the spectra were corrected for the CaF_2 window reflection. (a) full spectra range and (b) 900-2000 cm^{-1}.

Figure 3.28 shows plots of the intensities of the 1150 and 1210 cm^{-1} features as a function of time during the experiment shown in fig. 3.27(a) and after the plasma was switched off. As can be seen, the features track each other, although not exactly, and it is not clear from this and other such experiments that they are due to the same species. However, both are induced by the plasma and relax slowly, over many minutes, when the plasma was switched off.

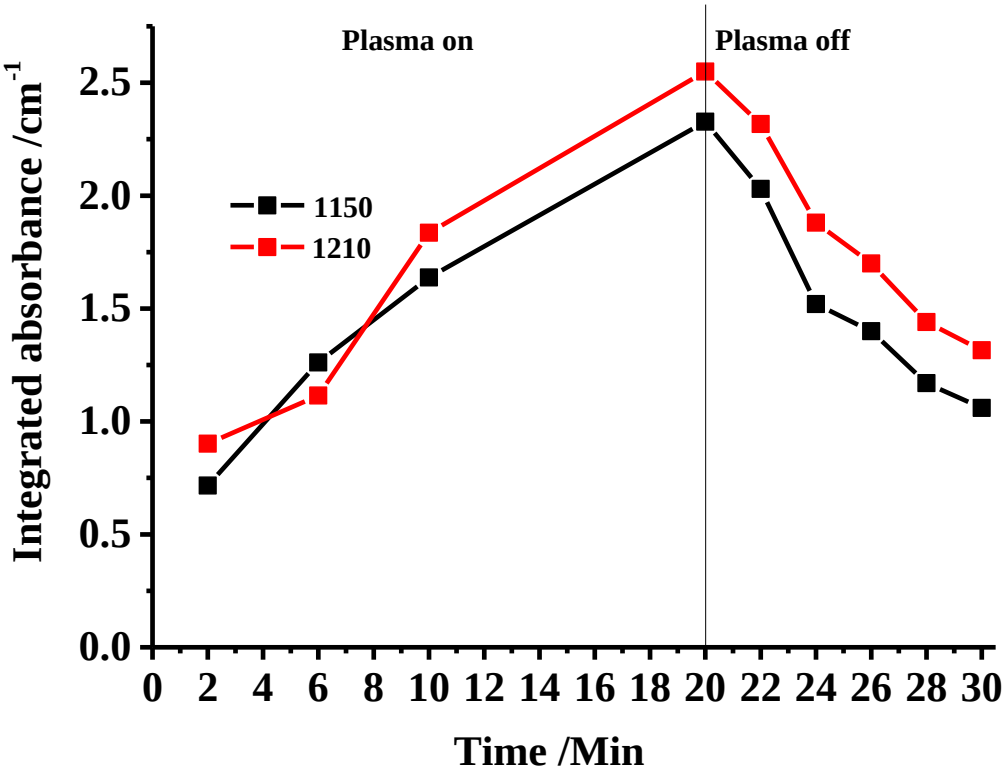

Figure 3.28. Plots of the 1150 and 1210 cm^{-1} features in fig. 3.27 showing the decrease in these bands when the plasma was switched off.

Figure 3.29 shows plots of the integrated absorptions of the two bands obtained from analogous experiments to that in fig. 3.27(a) as a function of input power from the spectra taken after 20 minutes operation: clearly, the features also increase in intensity with input power, but not in a linear fashion. The spectral ranges over which the 1150 & 1210 cm^{-1} bands were integrated between 1114 to 1174 cm^{-1} and 1175 to 1252 cm^{-1}, respectively.

The 1150 and 1210 cm^{-1} bands can only be due to changes at the surface of the Ti mesh or Macor, due to the chemical simplicity of the system. The Transverse Optical (TO) and Longitudinal Optical (LO) absorptions of silica absorb in the region 1000 – 1250 cm^{-1} [42] with frequencies and relative intensities that vary with the thickness of the film and the stress within

the film, and hence the 1150 and 1210 cm^{-1} may be due to Si-O in the Macor. However, these features were also observed in experiments using the reflectance cell in which the Macor was completely coated with CeO_2 or SnO_2 but the Ti mesh was still exposed, as discussed further in Chapters 4 and 5, suggesting the bands were due to Ti-O type species: but, according to the literature, such species are reported as absorbing at frequencies < 1000 cm^{-1} [43][44].

Whilst very interesting, it is not clear that the species responsible for the 1150 and 1210 cm^{-1} features participate in the reduction of IPA and hence are not relevant to the aim of this project. Further work is in progress to elucidate this chemistry.

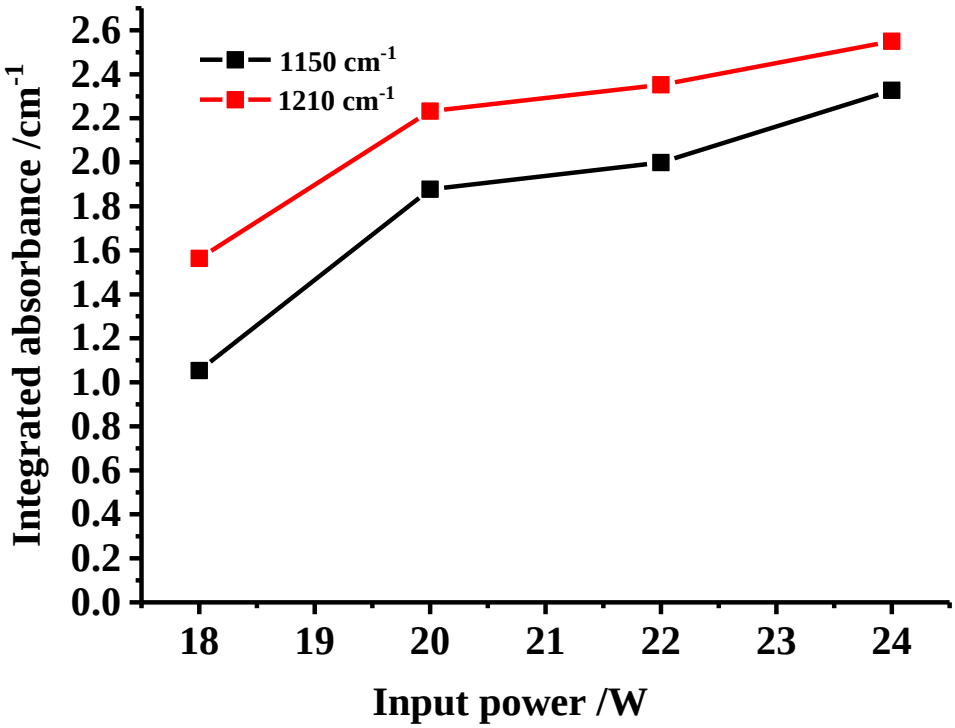

Figure 3.29. Plots of the integrated absorptions of the 1150 and 1210 cm^{-1} bands after 20 minutes operation as a function of input power from the experiment in fig. 3.27 and analogous experiments.

3.4.2. Experiments using nitrogen and isopropyl alcohol

The non-thermal plasma driven reaction of IPA in dinitrogen at Macor + Ti mesh was investigated using the plasma reflectance cell. Figure 3.30 shows the evolution of the IR spectra of gas phase IPA as a function of treatment time at 16 W, the IR spectra were collected after subtraction of the contribution of the IPA gas phase spectrum before turning on the power. CO, HCN and CH_4 were not detected, possibly because the pathlength of the reflectance cell was ca.

5 × lower than that of the transmission cell. However, a liquid film was produced and the IR bands observed below 2000 cm^{-1} were very similar to those seen using the transmission cell. Figure 3.31 shows spectra of the liquid films remaining in the plasma transmission and reflectance cells after the experiments shown in figs. 3.14 and 3.29. The spectra differ only in the relative amounts of isophorone (intense signature band at 1666 cm^{-1}) and polymethylacetylene-like species (intense signature band at 1762 cm^{-1}). Figures 3.32(a)-(c) show photographs of the liquid deposit in the reflectance cell.

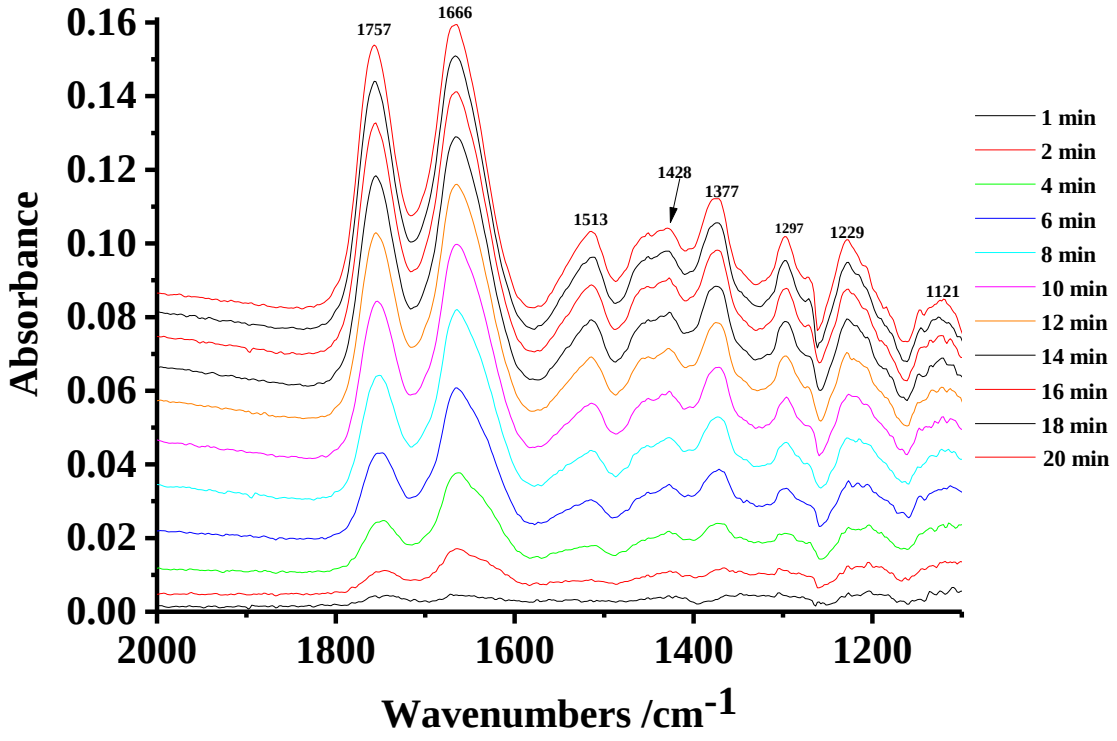

Figure 3.30. In-situ FTIR absorbance spectra of IPA dissociation at 16 W (100 co-added and averaged scans at 4 cm^{-1} resolution, ca. 100 seconds per scanset) collected as a function of plasma operation time using a gas feed of IPA vapour in N_2. The N_2 was bubbled through pure IPA at 298 K at a flow rate of 30 cm^3 min^{-1}. The reference spectrum was collected under the same conditions, but without plasma.

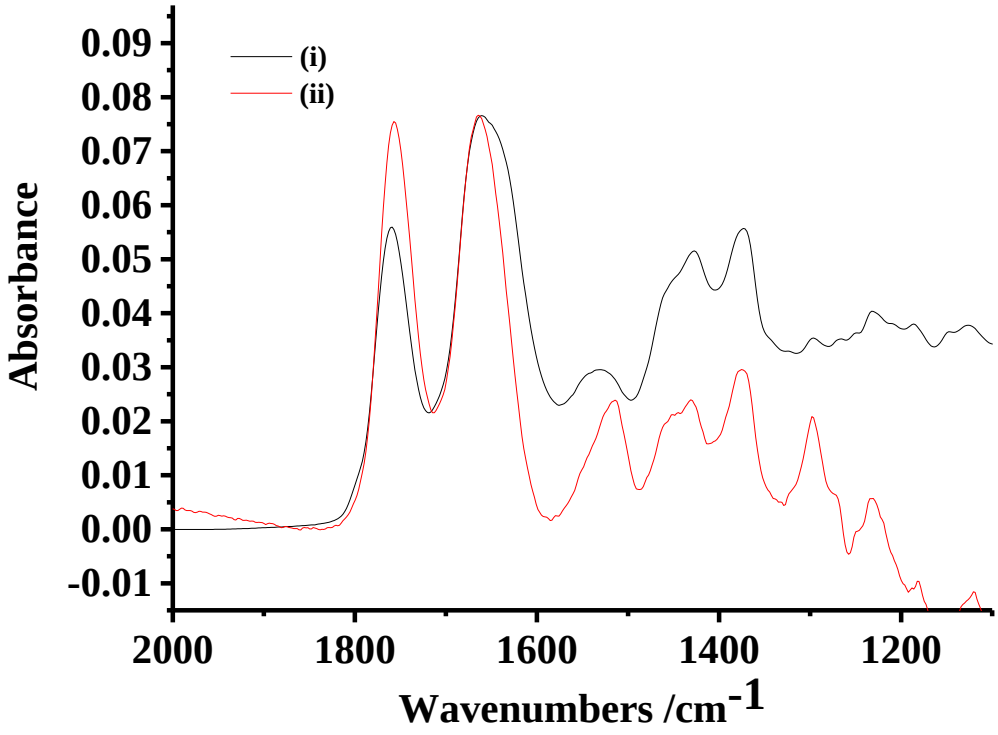

Figure 3.31. Spectra of the liquid films remaining on (i) the windows of the plasma transmission cell and (ii) the windows and Ti/Macor of the plasma reflectance cell after operation for 20 minutes at 27 W and 16 W using N_2/IPA as the feed, respectively, for 20 minutes.

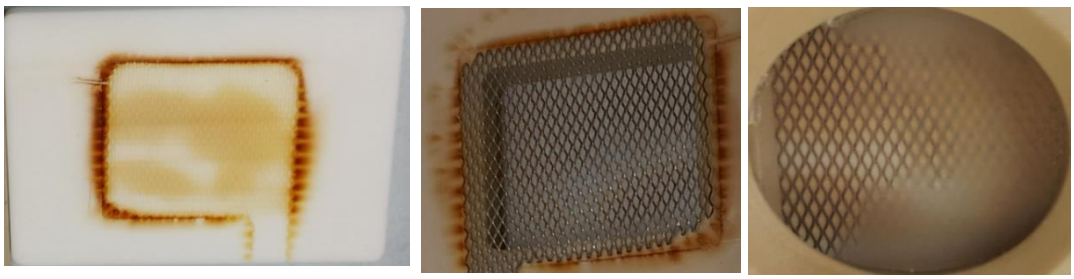

(a) **(b)** **(c)**

Figure 3.32. Photographs of the deposit on the: (a) Macor, (b) Ti mesh and (c) CaF_2 window, see text for details.

3.4.3. Experiment using argon

Figure 3.33 shows the spectra obtained in an analogous experiment to that in fig. 3.27(a) except using a feed gas of 100 % Ar and an input power of 7 W (when Argon was employed in the feed, it was found that plasma was initiated and sustained at lower input power than when using N_2, and the maximum power that could be employed was also lower). None of the products

features seen with N_2 were observed. However, the 1150 and 1210 cm^{-1} features are clearly visible, growing with time.

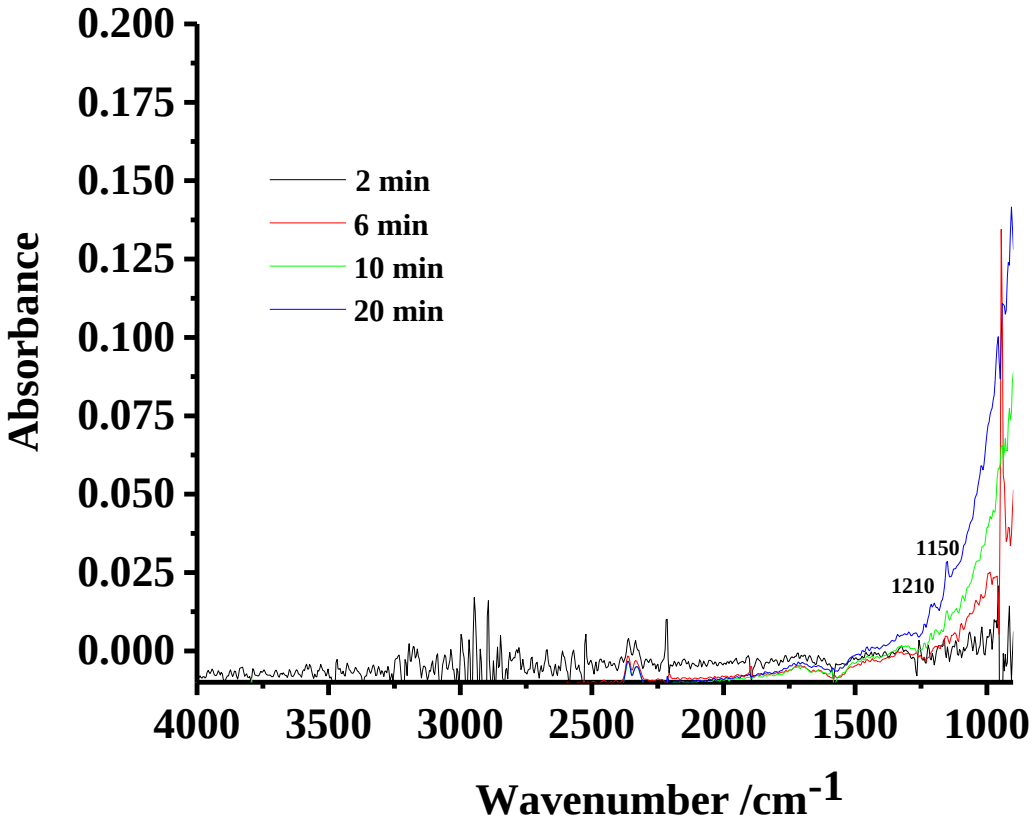

Figure 3.33. The spectra collected in an analogous experiment to that in fig. 3.27(a), except that the feed gas was argon and the input power 7 W.

3.5. Conclusion

Macor does not catalyse any reaction of isopropyl alcohol in dinitrogen at temperatures up to 600 °C. In contrast, it has a very significant effect upon the analogous plasma-driven process. In N_2 + IPA fed non-thermal plasma, two reaction zones are established: one at the Macor/plasma interface where the Macor catalyses the formation of a brown oil containing a polymethylacetylene-like polymer also (probably) bearing nitrogen containing functionality, and isophorone [25][26]. This oil eventually blocks the Macor surface preventing further reactions of this nature. The second zone is in the bulk of the plasma, remote from the Macor. In this zone, CO at a rotational temperature << 200 K and CH_4, HCN and acetone are also produced. Electron impact of the IPA results in acetone and probably acetaldehyde production: the former does not react further. In contrast, the acetaldehyde is excited to form a loose transition state via electron impact or photo-excitation from the plasma emission: this results in

the dissociation of the acetaldehyde to CH_4 and cold CO via a roaming reaction. Replacing the dinitrogen by argon completely inhibits the formation of the oil, leaving the Macor surface clear, and this now catalyses the formation of acetylene in the plasma transmission cell.

3.6. References

1. MACOR – Machinable Glass Ceramic Data Sheet [Cited 2016 19 January]. Available from: http://psec.uchicago.edu/ceramics/MACOR%20Data%20Sheet.pdf.
2. Xu, W., Raftery, D. and Francisco, J.S., 2003. Effect of irradiation sources and oxygen concentration on the photocatalytic oxidation of 2-propanol and acetone studied by in situ FTIR. *The Journal of Physical Chemistry B*, *107*(19), pp.4537-4544.
3. Miyata, H., Wakamiya, M. and Kubokawa, Y., 1974. Infrared studies of interaction of oxygen with 2-propanol and acetone adsorbed on MgO and NiO. *Journal of Catalysis*, *34*(1), pp.117-123.
4. Rossi, P.F., Busca, G., Lorenzelli, V., Saur, O. and Lavalley, J.C., 1987. Microcalorimetric and FT-IR spectroscopic study of the adsorption of isopropyl alcohol and hexafluoroisopropyl alcohol on titanium dioxide. Langmuir, 3(1), pp.52 - 58.
5. Arsac, F., Bianchi, D., Chovelon, J.M., Ferronato, C. and Herrmann, J.M., 2006. Experimental Microkinetic Approach of the Photocatalytic Oxidation of Isopropyl Alcohol on TiO_2. Part 1. Surface Elementary Steps Involving Gaseous and Adsorbed C_3H_xO Species. The Journal of Physical Chemistry A, 110(12), pp.4202 - 4212.
6. Rivallan, M., Fourré, E., Aiello, S., Tatibouët, J.M. and Thibault-Starzyk, F., 2012. Insights into the Mechanisms of Isopropanol Conversion on γ-Al_2O_3 by Dielectric Barrier Discharge. *Plasma Processes and Polymers*, *9*(9), pp.850-854.
7. Rodrigues, A., Tatibouët, J.M. and Fourré, E., 2016. Operando DRIFT Spectroscopy Characterization of Intermediate Species on Catalysts Surface in VOC Removal from Air by Non-thermal Plasma Assisted Catalysis. *Plasma Chemistry and Plasma Processing*, *36*(4), pp.901-915.
8. Mehrotra, R.C. and Batwara, J.M., 1970. Preparation and some reactions of alkoxides of gadolinium and erbium. *Inorganic Chemistry*, *9*(11), pp.2505-2510.
9. Armaroli, T., Bécue, T. and Gautier, S., 2004. Diffuse reflection infrared spectroscopy (DRIFTS): Application to the in situ analysis of catalysts. *Oil & Gas Science and Technology*, *59*(2), pp.215-237.
10. Herzberg, G. "Molecular spectra and molecular structure. Vol. 2: Infrared and Raman spectra of polyatomic molecules", Van Nostrand, Reinhold, New York, 1945.

11. Koga, O., Onishi, T. and Tamaru, K., 1980. Adsorption and decomposition of isopropyl alcohol over zinc oxide. Infrared and kinetic study. *Journal of the Chemical Society, Faraday Transactions 1: Physical Chemistry in Condensed Phases*, *76*, pp.19-29.
12. Hussein, G.A., Sheppard, N., Zaki, M.I. and Fahim, R.B., 1989. Infrared spectroscopic studies of the reactions of alcohols over group IVB metal oxide catalysts. Part 1.—Propan-2-ol over TiO_2, ZrO_2 and HfO_2. *Journal of the Chemical Society, Faraday Transactions 1: Physical Chemistry in Condensed Phases*, *85*(7), pp.1723-1741.
13. Choi, K. N. and Barker, E. F., 1932 Infrared Absorption Spectrum of Hydrogen Cyanide, *Phys. Rev*., 42(6), p.777.
14. Herzberg, G. "Infrared and Raman Spectra of Polyatomic Molecules"; D. Van Nostrand Company: New York, 1945, pp 306 – 307.
15. Dellepiane, G. and Overend, J., 1966. Vibrational spectra and assignment of acetone, ααα acetone-d3 and acetone-d6. *Spectrochimica Acta*, *22*(4), pp.593-614.
16. Luyben, W.L., 2010. Design and control of the acetone process via dehydrogenation of 2-propanol. *Industrial & Engineering Chemistry Research*, *50*(3), pp.1206-1218.
17. Rioux, R.M. and Vannice, M.A., 2003. Hydrogenation/dehydrogenation reactions: isopropanol dehydrogenation over copper catalysts. *Journal of Catalysis*, *216*(1), pp.362-376.
18. Said, A.E.A.A., El-Wahab, M.M.A. and Goda, M.N., 2016. Selective synthesis of acetone from isopropyl alcohol over active and stable CuO–NiO nanocomposites at relatively low-temperature. *Egyptian Journal of Basic and Applied Sciences*, *3*(4), pp.357-365.
19. Halawy, S.A., Mohamed, M.A. and El-Hafez, S.F.A., 1994. Dehydrogenation of isopropyl alcohol over CoNi/Mg oxide catalysts. *Journal of Molecular Catalysis*, *94*(2), pp.191-201.
20. Tsang, C.W. and Harrison, A.G., 1971. Concerning the structure and fragmentation of $[C_3H_7O]^+$ ions derived from alcohols. *Journal of Mass Spectrometry*, *5*(7), pp.877-884.
21. Bauerecker, S., Taraschewski, M., Weitkamp, C. and Cammenga, H.K., 2001. Liquid-helium temperature long-path infrared spectroscopy of molecular clusters and supercooled molecules. *Review of Scientific Instruments*, *72*(10), pp.3946-3955.
22. Herzberg, G. "Molecular Spectra and Molecular Structure: I Spectra of Diatomic Molecules", 2nd Edn., Van Nostrand, New York, 1950, p126 – 127.
23. Laue, T. and Plagens, A., "Named organic reactions", John Wiley & Sons, 2005.
24. Rojas, C.M., "Molecular Rearrangements in Organic Synthesis", John Wiley & Sons, 2015.

25. Cataldo, F., 1996. Synthesis of ketonic resins from self-polymerization of acetone, 1. Action of protic and lewis acids on acetone. *Macromolecular Materials and Engineering*, *236*(1), pp.1-19.
26. Cataldo, F., 1996. Synthesis of ketonic resins from self-polymerization of acetone, 2. Action of bases on acetone and the synthesis of halogenated and diels-alder adducts. *Macromolecular Materials and Engineering*, *236*(1), pp.21-33.
27. Peluso, A., Seel, M. and Ladik, J., 1985. The infrared and Raman spectrum of trans-polyacetylene: A self-consistent-field study. *Solid State Communications*, *53*(10), pp.893-896.
28. Trinh, H.Q. and Mok, Y.S., 2014. Plasma-catalytic oxidation of acetone in annular porous monolithic ceramic-supported catalysts. *Chemical Engineering Journal*, *251*, pp.199-206.
29. Cockerill, A.F., 1973. Elimination reactions. *In Comprehensive chemical kinetics. Elsevier*, *9*, pp. 163-372.
30. Manriquez, M.E., Hernández-Cortez, J.G., Wang, J.A., Chen, L.F., Zuñiga-Moreno, A. and Gómez, R., 2015. Synthesis of transition metal doped lamellar double hydroxides as base catalysts for acetone aldol condensation. *Applied Clay Science*, *118*, pp.188-194.
31. Giguère, P.A. and Harvey, K.B., 1956. On the infrared absorption of water and heavy water in condensed states. *Canadian Journal of Chemistry*, *34*(6), pp.798-808.
32. Kim, H.H., Teramoto, Y., Negishi, N. and Ogata, A., 2015. A multidisciplinary approach to understand the interactions of nonthermal plasma and catalyst: a review. *Catalysis Today*, *256*, pp.13-22.
33. Stein, S. E. "Infrared Spectra", NIST Chemistry WebBook, in NIST Standard Reference Database Number 69, Eds. P.J. Linstrom and W.G. Mallard, National Institute of Standards and Technology, Gaithersburg MD, 8860, http://webbook.nist.gov, (retrieved 24 October 2017).
34. van Zee, R.D., Foltz, M.F. and Moore, C.B., 1993. Evidence for a second molecular channel in the fragmentation of formaldehyde. *The Journal of Chemical Physics*, *99*(3), pp.1664-1673.
35. Heazlewood, B.R., Jordan, M.J., Kable, S.H., Selby, T.M., Osborn, D.L., Shepler, B.C., Braams, B.J. and Bowman, J.M., 2008. Roaming is the dominant mechanism for molecular products in acetaldehyde photodissociation. *Proceedings of the National Academy of Sciences*, *105*(35), pp.12719-12724.
36. Bowman, J.M., 2006. Skirting the transition state, a new paradigm in reaction rate theory. *Proceedings of the National Academy of Sciences*, *103*(44), pp.16061-16062.

37. Houston, P.L. and Kable, S.H., 2006. Photodissociation of acetaldehyde as a second example of the roaming mechanism. *Proceedings of the National Academy of Sciences*, *103*(44), pp.16079-16082.
38. Sivaramakrishnan, R., Michael, J.V. and Klippenstein, S.J., 2009. Direct observation of roaming radicals in the thermal decomposition of acetaldehyde. *The Journal of Physical Chemistry A*, *114*(2), pp.755-764.
39. Harding, L.B., Georgievskii, Y. and Klippenstein, S.J., 2009. Roaming radical kinetics in the decomposition of acetaldehyde. *The Journal of Physical Chemistry A*, *114*(2), pp.765-777.
40. Xiao, D., Cheng, C., Shen, J., Lan, Y., Xie, H., Shu, X., Meng, Y., Li, J. and Chu, P.K., 2014. Characteristics of atmospheric-pressure non-thermal N_2 and N_2/O_2 gas mixture plasma jet. *Journal of Applied Physics*, *115*(3), p.033303.
41. Everett, C., 2004. *Acetaldehyde dehydration to produce ethyne*. U.S. Patent Application 10/673,946.
42. Moreno, J.A., Garrido, B., Samitier, J. and Morante, J.R., 1997. Analysis of geometrical effects on the behavior of transverse and longitudinal modes of amorphous silicon compounds. *Journal of applied physics*, *81*(4), pp.1933-1942.
43. Zeitler, V.A. and Brown, C.A., 1957. The infrared spectra of some Ti-O-Si, Ti-O-Ti and Si-O-Si compounds. *The Journal of Physical Chemistry*, *61*(9), pp.1174-1177.
44. Adamczyk, A. and Długoń, E., 2012. The FTIR studies of gels and thin films of Al_2O_3–TiO_2 and Al_2O_3–TiO_2–SiO_2 systems. *Spectrochimica Acta Part A: Molecular and Biomolecular Spectroscopy*, *89*, pp.11-17.

Chapter 4. An in-situ Fourier Transform InfraRed study of the thermally and plasma driven conversion of isopropyl alcohol over tin oxide

4.1. Introduction

This chapter reports the application of in-situ reflectance Fourier Transform Infrared spectroscopy to the study of the thermally and plasma driven reaction of IsoPropyl Alcohol (IPA) at SnO_2 coated Macor/Ti mesh using Fourier Transform Infrared spectroscopy.

4.2. The characterization of tin oxide nanopowders

4.2.1. Physical properties of SnO_2 nanopowders

Tin dioxide is a white powder that is insoluble in water [1-6]. Figures 4.1(a)-(c) show photographs of the SnO_2 samples, uncalcined and calcined at 400 and 700 °C respectively. As can be seen from the figures, the samples show various colours: thus, the uncalcined sample was white, the sample calcined 400 °C was pale yellow and the sample calcined at 700 °C was yellow. It has been reported in the literature that undoped SnO_2 is white [1][2][7][8]; however, there are a few factors that effect the colour of undoped SnO_2 such as ageing time [4] or sintering at high temperature [2]. Hall et al. [2] found that the colour of SnO_2 could be changed from white to yellow as a function of increasing temperature and particle size.

(a) **(b)** **(c)**

Figure 4.1. Photographs of the SnO_2 nanopowders prepared using the hydrothermal process at 180 ^oC: (a) as prepared, and calcined at (b) 400 ^oC & (c) 700 ^oC.

4.2.2. X-ray diffraction results

X-ray diffraction studies were carried on the SnO_2 samples calcined at different temperatures in order to check the sample purity and to determine the average particle size via Scherrer's equation [9].

Figure 4.2 shows the XRD patterns of the dried nanopowders calcined at 400 and 700 °C respectively. The diffraction patterns of the two samples calcined at 400 and 700 °C agreed with that of the single phase of the crystal system type tetragonal SnO_2 (tin oxide); Cassiterite, syn; 01-077-0447 which was obtained from the ICDD database. The most intense lines at 2Θ=26.5º, 33.8º, 37.9º and 51.8º were present in both samples, and were in agreement with the literature [1][7][10-14]. In addition, from fig. 4.2 it was clear that these samples were pure as there were no reflection peaks due to any impurities. It is clear from the figure that the Full Width at Half Maximum (FWHM) of the peaks decreases with increasing calcination temperature showing that the particle size increased from 6.09 nm to 17.06 nm as the calcination temperature was increased. The average particle size was calculated from the peaks at 2Θ=26.5º, 33.8º, 37.9º and 51.8º using Scherrer's equation as discussed in Chapter 2. This was in agreement with literature studies on SnO_2 nanopowders prepared by the hydrothermal process [1][10][11][14]; thus, Sakai et al. [11] studied the effect of temperature on particle size and found that the particle size of SnO_2 increased from 5 nm to 14 nm when the calcination temperature increased from 100 °C to 900 °C. The same behavior was observed by Fujihara and co-workers [1].

Nanoparticulate SnO_2 was chosen as a catalyst for two reasons: (1) SnO_2 is widely used as a catalyst in alcohol sensors [15] and (2) FTIR data on the heating of SnO_2 nanopowder in air as a function of temperature were already available [16]. In addition, there is a wealth of IR data in the literature on the interaction of IPA with oxide surfaces under thermal conditions, see for example [17-24]. Moreover, due to their specific properties such as high surface area and small particle size, which are different from their corresponding bulk state, nanomaterials in general have attracted great interest in the past few years [25]. Consequently, SnO_2 nanopowders find potential wide application in, for example, solid state gas sensors, transparent conductors, rechargeable Li batteries and optical electronic devices [4][5]. These applications depend on properties of SnO_2 such as the energy gap (E_g= 3.64 eV at 330 K, see [4][5] and references therein). SnO_2 is a semiconductor due to the presence of oxygen vacancies [25].

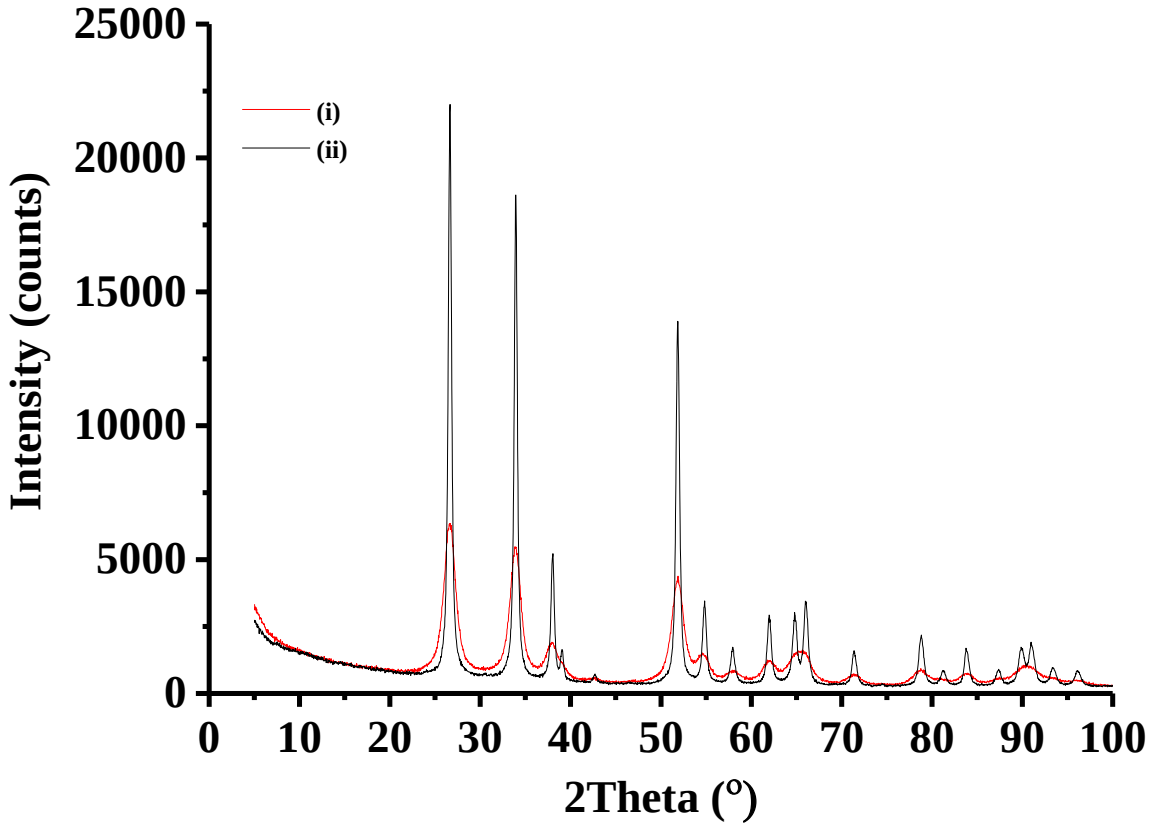

Figure 4.2. The XRD patterns of the SnO_2 nanopowders prepared by hydrothermal process calcined at: (i) 400 °C and (ii) 700 °C.

4.3. Infrared studies of the thermally-driven process

4.3.1. Blank experiments

Figure 4.3 shows the background spectra collected from KBr powder and the SnO_2 powder calcined at 400 °C. The powders were dispersed in KBr and the spectra obtained under nitrogen at a flow rate of 200 cm^3 min^{-1} and 25 °C. In both spectra, the fine structure around 1629 cm^{-1} and 3400 cm^{-1} are due to water vapour, and the peaks around 2900 cm^{-1} to the plastic coating on the beamsplitter. The peaks at 1260, 1616 cm^{-1} and the sharp bands between 3400 and 3600 cm^{-1} were due to Sn-OH groups that are not hydrogen bonded, ie. are isolated [16]. The broad feature between 2500 & 4000 cm^{-1} may be attributed to adsorbed water and adsorbed hydrogen-bonded OH groups [16]. The analogous spectrum of the SnO_2 calcined at 700 °C showed essentially the same features, but the bands due to adsorbed water and OH were reduced, see fig. 4.4.

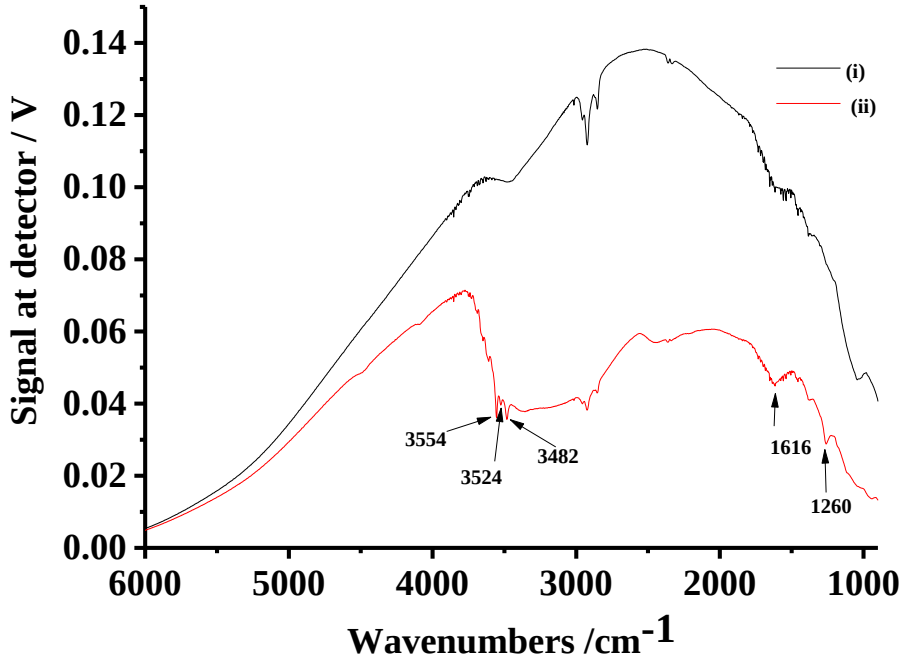

Figure 4.3. Single beam spectra (100 co-added and averaged scans at 4 cm^{-1} resolution, ca. 120 seconds per scan set) of: (i) KBr and (ii) SnO_2 calcined at 400 ºC diluted in KBr (20 mg SnO_2 + 80 mg KBr), under nitrogen gas at a flow rate of 200 cm^3 min^{-1}.

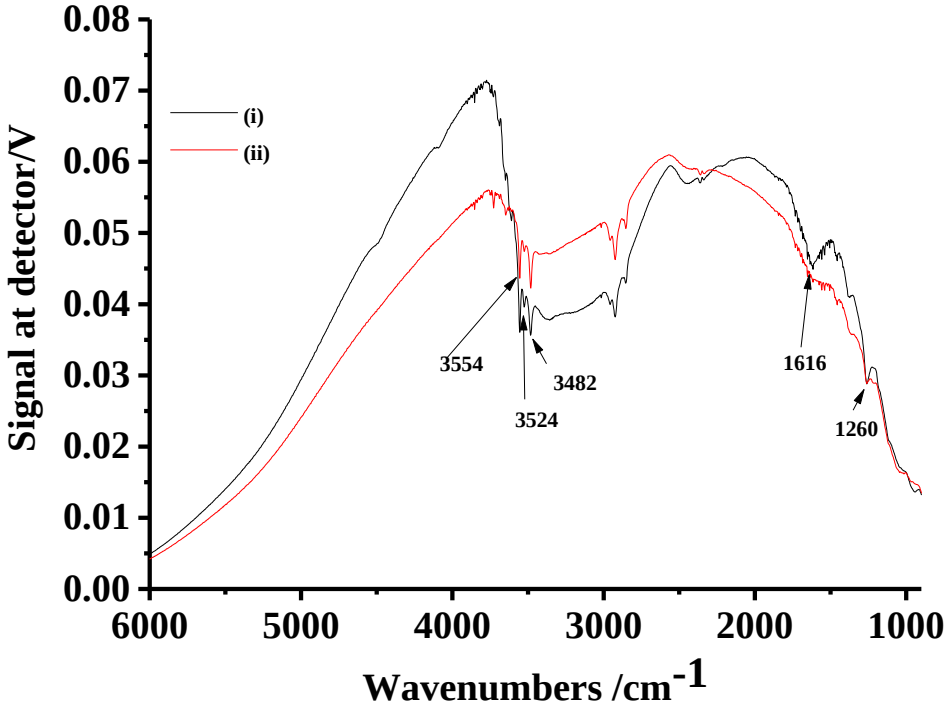

Figure 4.4. Comparison between the single beam spectra (100 co-added and averaged scans at 4 cm^{-1} resolution, ca. 120 seconds per scan set) of SnO_2 calcined at: (i) 400 ºC and (ii) 700 ºC, diluted in KBr (20 mg SnO_2 + 80 mg KBr), under nitrogen gas at a flow rate of 200 cm^3 min^{-1}.

Figures 4.5(a) & (b) show spectra collected from the SnO_2 sample calcined at 400 °C and diluted in KBr as a function of temperature in a static nitrogen atmosphere. The reference spectrum employed in this case was acquired using pure KBr at 25 °C under nitrogen gas at a flow rate of 200 cm^3 min^{-1}; thus, the spectra are "absolute" spectra of the SnO_2 as the KBr gives a featureless IR response. As can be seen from the figure, there is a significant decrease in the intensity of the broad band between 2500 cm^{-1} and 3800 cm^{-1} as of the temperature is increased, suggesting the loss of adsorbed water from the sample surface, in agreement with the literature [26][27].

Figure 4.6 shows the spectra obtained in an analogous experiment to that in fig. 4.5 except that the SnO_2 calcined at 400 ºC was replaced by SnO_2 calcined at 700 ºC. It can be seen that the intensities of all the features decreased compared to the experiment in fig. 4.5. In addition, the feature at 1629 cm^{-1} was absent from fig. 4.6 as would be expected if the assignment to physisorbed water is correct.

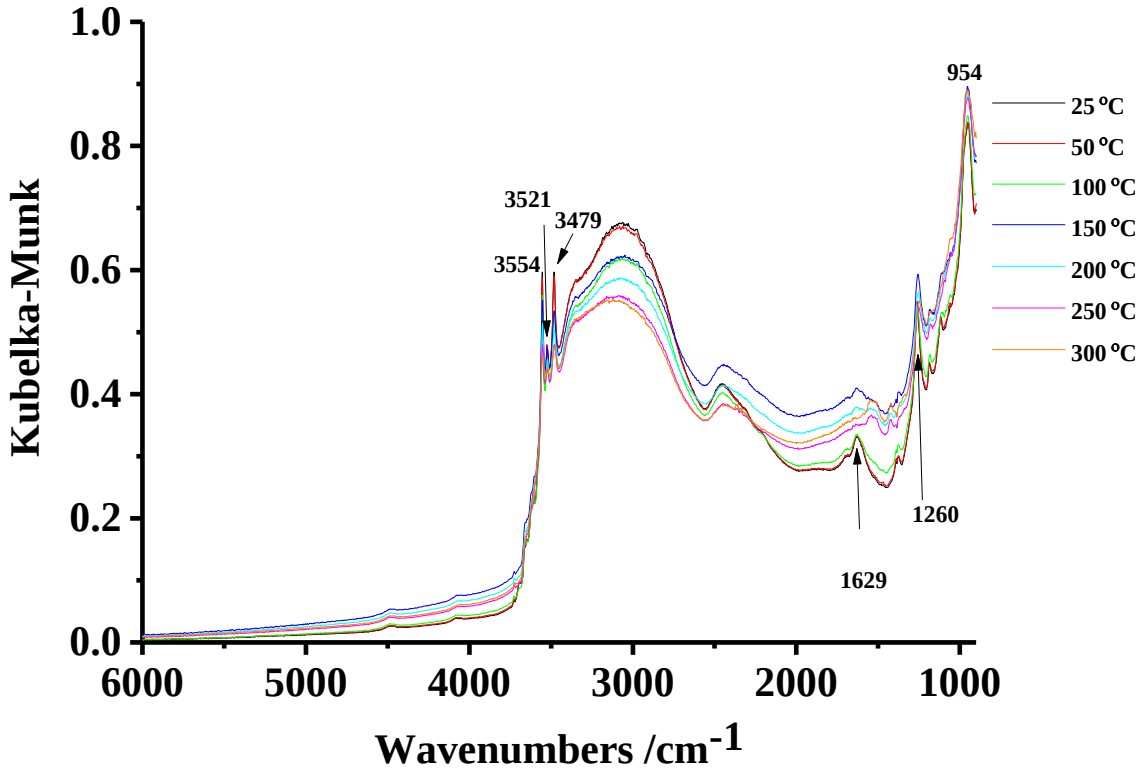

(a)

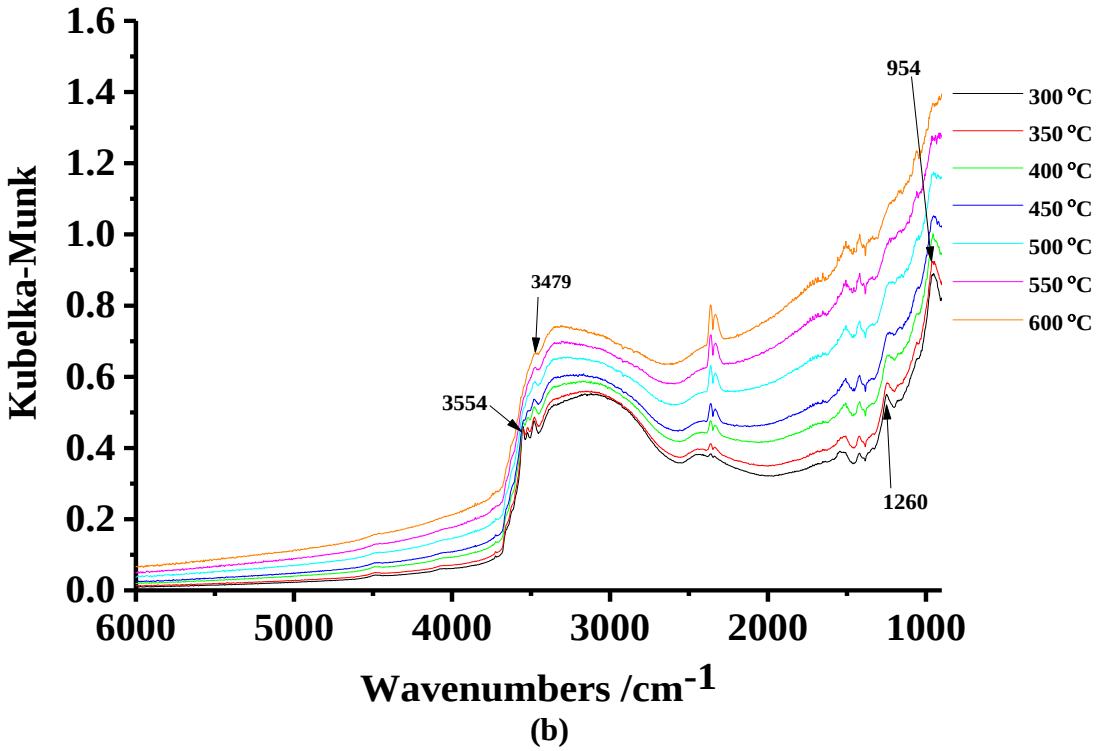

Figure 4.5. In-situ FTIR spectra (100 co-added scans and averaged scans at 4 cm^{-1} resolution, ca. 120 seconds per scanset) collected using the environmental chamber during an experiment in which a spectrum was collected at 25 ºC and the temperature ramped at 5 ºC min^{-1} and further spectra taken at the temperatures shown: (a) 25 ºC - 300 ºC and (b) 300 ºC – 600 ºC. The sample was 20 mg SnO_2 calcined at 400 ºC + 80 mg KBr in a static atmosphere of dinitrogen. The reference spectrum was collected in dinitrogen using pure KBr.

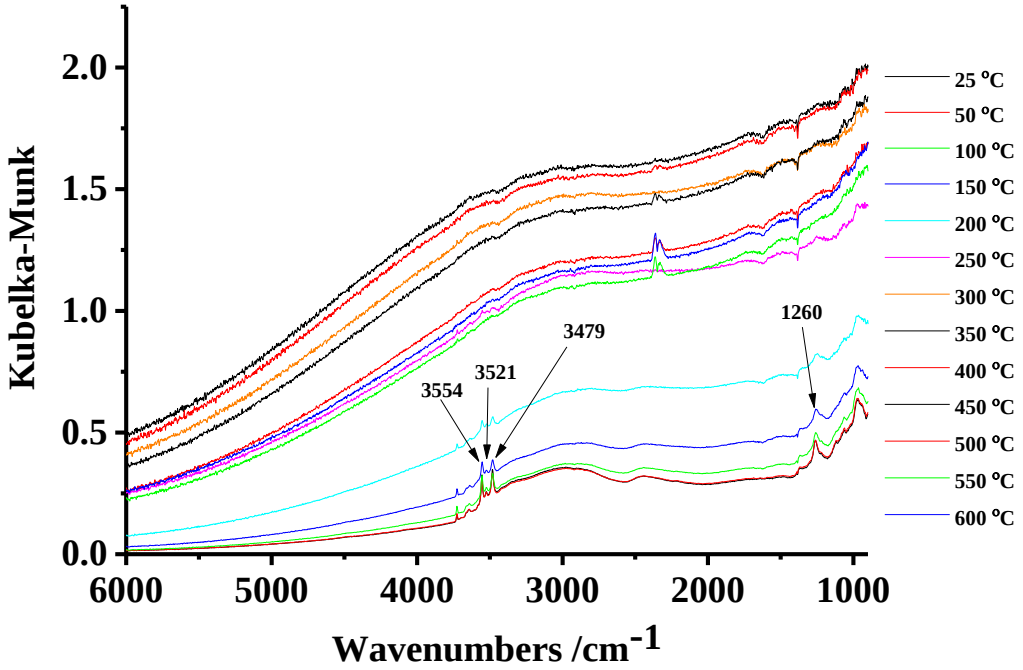

Figure 4.6. The spectra collected in an analogous experiment to that in fig.4.5, except that the SnO_2 sample used was calcined at 700 °C.

Figure 4.7 shows plots of the KM at 2000 cm^{-1} in figs. 4.5 and 4.6 vs temperature for both SnO_2 samples calcined at 400 and 700 °C, respectively. As can be seen from the figure, in the spectra of the sample calcined at 400 °C, the absorption at 2000 cm^{-1} increase slightly up to 150 °C before decreasing to 250 °C. Thereafter, the absorption steadily increases in temperature. In contrast, the corresponding plot for the sample calcined at 700 °C increases slightly up to 100 °C and then more significantly up to 350 °C after which it decreases to 550 °C, and then shows a small increase at 600 °C. Comparing with the KM plot at 2000 cm^{-1} vs temperature for SnO_2 sample heating under static air condition [16], it was in complete contrast with fig. 4.7. Further investigation is required to explain the data in fig. 4.7, but they may be attributed to the relative amounts of oxygen vacancies.

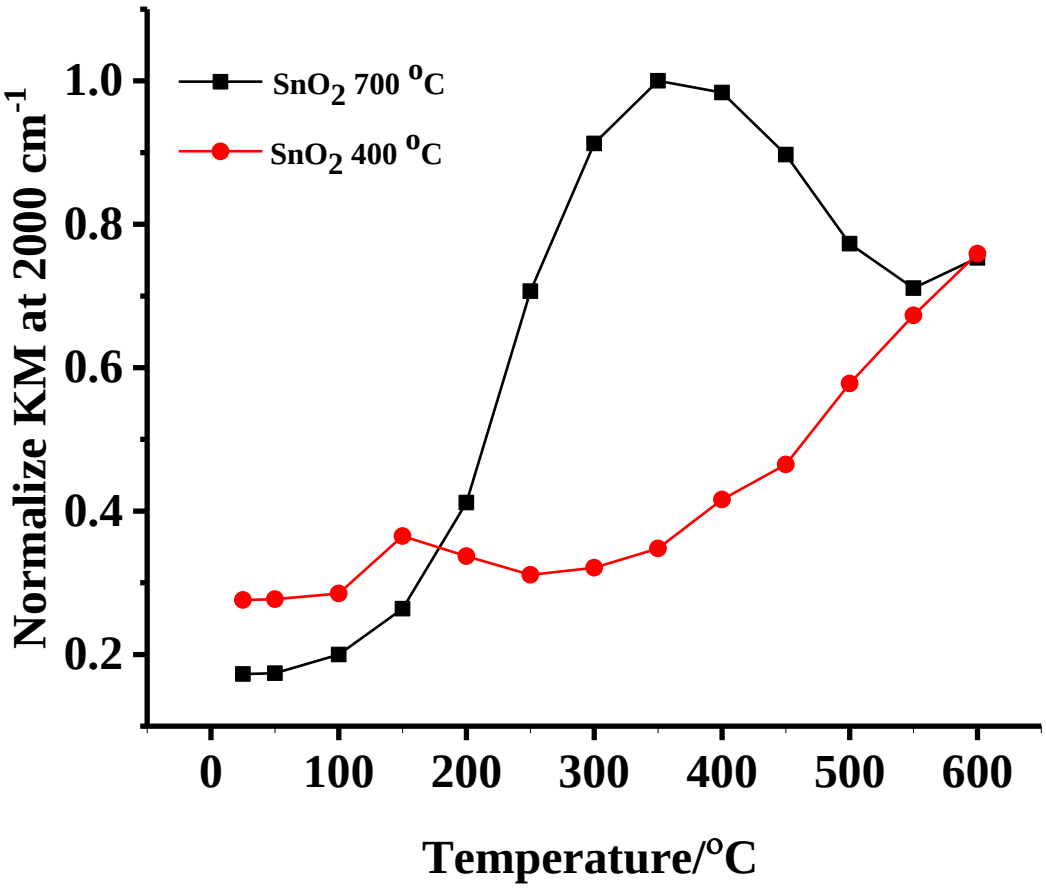

Figure 4.7. Plots of the KM intensity at 2000 cm^{-1} in figs. 4.5 & 4.6.

4.3.2. Experiments using N_2 and IPA vapour as the feed gas

Isopropyl alcohol vapour was delivered to the chamber of the DRIFTS cell by bubbling nitrogen gas through the alcohol held in a Dreschel bottle. When a 12.5 mm diameter, 2 mm thick Macor

disc was exposed to an atmosphere of IPA+N_2 in the environmental chamber and heated to 600 °C, no reaction was observed to take place as stated in Chapter 3.

In contrast to the results observed with Macor, SnO_2 clearly had an effect on the reaction of IPA. Thus, fig, 4.8 shows spectra collected from the SnO_2 powder sample calcined at 400 ºC in a static atmosphere of N_2 and IPA vapour as a function of temperature using KBr as the reference spectrum; thus, the spectra are "absolute" spectra of the SnO_2. As may be seen, there are marked differences in the spectra collected at temperatures > 100 ºC compared to those taken in the absence of IPA [16]. Further, the spectra in fig. 4.8 collected at temperatures > 150 ºC show significant differences compared to those taken at T ≤ 150 ºC, and these will be discussed in detail below; first, however, the electronic absorption apparent in the spectra will be discussed.

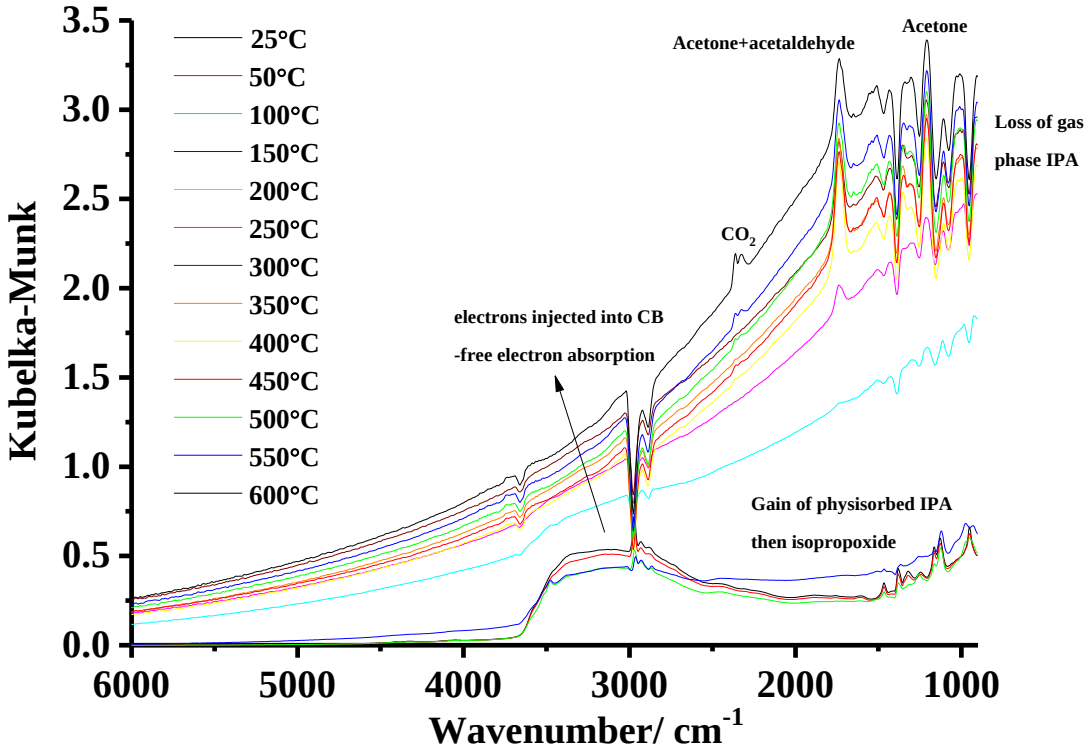

Figure 4.8. In-situ FTIR spectra (100 co-added scans and averaged scans at 4 cm^{-1} resolution, ca. 120 seconds per scanset) collected using the environmental chamber during an experiment in which a spectrum was collected at 25 ºC and the temperature ramped at 5 ºC min^{-1} and further spectra taken at the temperatures shown. The sample was 20 mg SnO_2 powder calcined at 400 ºC + 80 mg KBr in a static atmosphere of isopropyl alcohol/dinitrogen. The reference spectrum was collected in dinitrogen + IPA using pure KBr.

Christensen and co-workers [16] reported in-situ FTIR studies on the heating of a SnO_2 nanopowder prepared in the same way as the sample employed in this work. When the SnO_2 was heated in air in the absence of IPA, the same curving baseline was observed as in fig. 4.8 and this was attributed to absorption by free electrons present in the conduction band of the SnO_2 which had been promoted from oxygen vacancy levels [28] within 0.2 eV of the conduction band edge. Such absorptions generally exhibit a zero energy onset [29] and follow a $1/\nu^n$ power law (n = 2 – 3) [30][31]. The free electron absorption did not change on heating the sample: however, broad absorptions attributable to transitions from the oxygen vacancy levels ([32], and references therein) which were present at 25 °C were lost on heating. The spectra in fig. 4.8 are in complete contrast to those observed in the absence of IPA: thus, whilst the free electron absorption does not change up to 100 °C, at temperatures above this, see fig. 4.9 which shows a plot of the Kubelka-Munk function at 2000 cm^{-1} as a function of temperature, the absorption increases in intensity. In addition, there is no evidence for the broad absorptions due to transitions from the oxygen vacancy states.

From fig. 4.9, it is clear that the number of free electrons is varying as the temperature is increased, but not in a homologous fashion and there are four clear regions: 25 – 100 ºC (I); 100 – 300 ºC (II); 300 – 400 ºC (III) and 400 – 600 ºC (IV). In region (I) there is very little change in the electronic absorption, but a clear increase with temperature in region (II) followed by a fall in region (III) and a less steep increase in region (IV). At temperatures > 150 ºC, the water and other surface features on the SnO_2 are lost as the free electron absorption increases, suggesting that the increasing electronic conductivity of the SnO_2 may be causing an increasing fraction of the refracted IR light to be fully absorbed with the consequent loss of information on surface species. In order to illustrate the reproducibility of the infrared data discussed in this work, fig. 4.10 shows normalized plots of the Kubelka-Munk function at 2000 cm^{-1} from three separate experiments covering a 20 month period: as can be seen, the general trend is reproducible when allowances are made for variations in sample mass, packing etc. Furthermore, the various features due to the physisorbed and chemisorbed IPA intermediates and products were all reproducible (compare, for example, figs. 4.9 and 4.16).

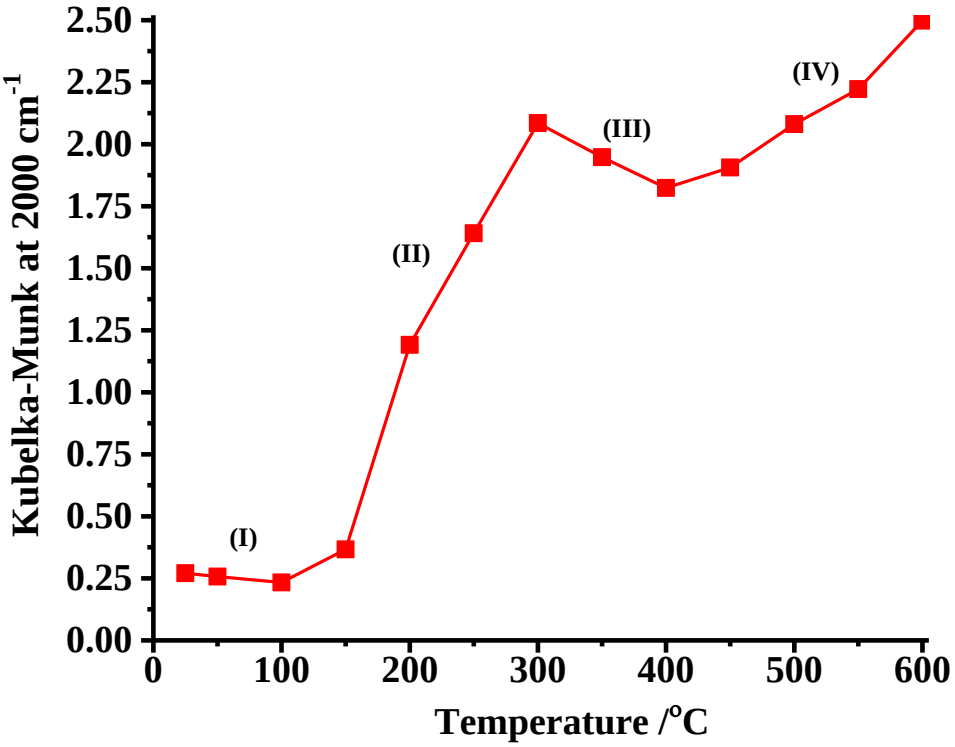

Figure 4.9. Plots of the Kubelka-Munk function at 2000 cm^{-1} with respect to temperature from the experiment in fig. 4.8.

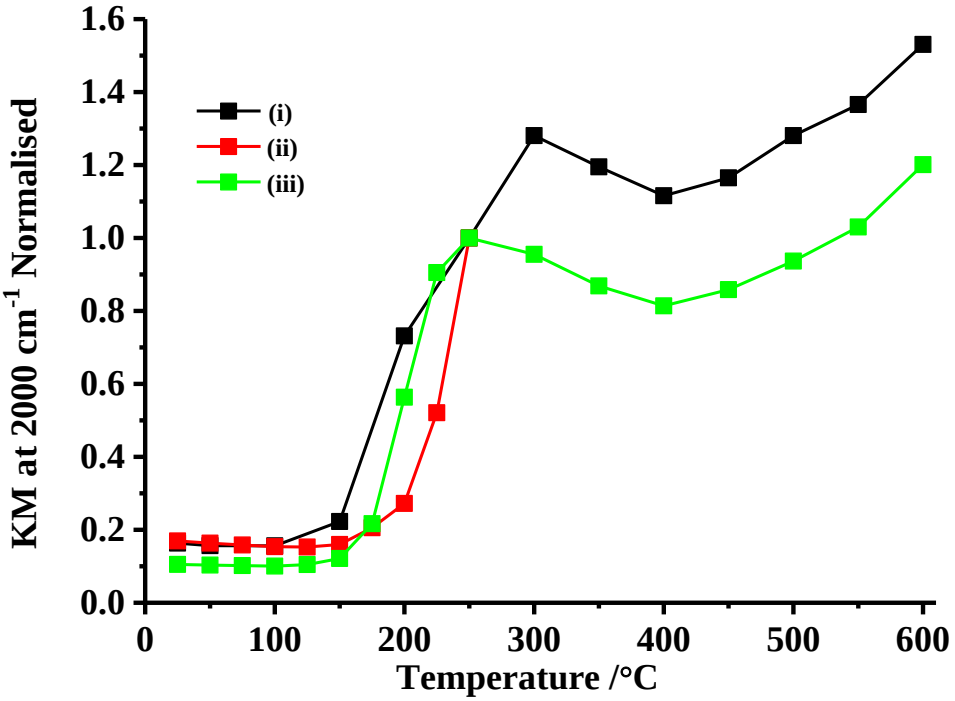

Figure 4.10. The plots in (i) fig. 4.9 and (ii) fig. 4.16, and (iii) the analogous plot from a repeat of the experiment in fig. 4.9 carried out 20 months later. The experiment shown in fig. 4.16 was carried out 3 months after that in fig. 4.9. In each case, the plots were normalized to the maximum value of the Kubelka-Munk function at 2000 cm^{-1} and 250 °C to facilitate comparison.

Figure 4.11 shows the spectra collected at 200, 250, 400 and 600 °C in fig. 4.8 with those taken at 200, 250 and 400 °C enhanced by a factor of 2.1, 1.5 and 1.4, respectively, in order to match their Kubelka-Munk functions at 2000 cm^{-1} with that of the spectrum taken at 600 °C. As can be seen from the figure, allowing for the broad loss features from 3500 to 2000 cm^{-1} due to dehydroxylation of the SnO_2 [16], and some variation in the baseline below 1500 cm^{-1} at 600 °C, the free electron absorption is clearly unchanged in form as the temperature increases: i.e. it simply increases in intensity.

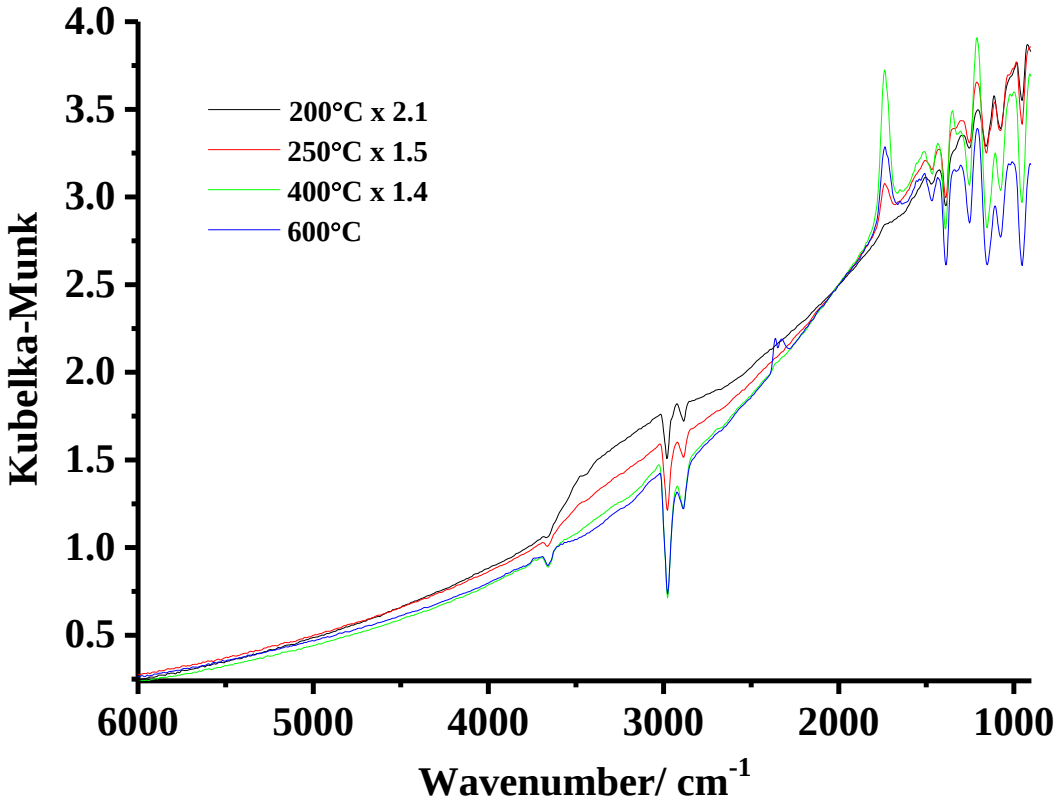

Figure 4.11. The spectra collected at 200, 250, 400 and 600 °C in fig. 4.8, with those taken at 200, 250 and 400 °C enhanced by a factor of 2.1, 1.5 and 1.4, respectively, in order to match their Kubelka-Munk functions at 2000 cm^{-1} with that of the spectrum taken at 600 °C.

As was stated above, an increase in the intensity of the free electron absorption as the temperature was increased was not observed in the absence of IPA [16], suggesting that, at temperatures ≥ 100 ºC, electron injection into the conduction band of the SnO_2 from the IPA is taking place, with a hiatus between 300 and 400 ºC. The electron injection is likely to be from newly-created oxygen vacancies, caused by oxidation of the IPA. In support of this postulate, the colour of the nanoparticulate SnO_2 sample was pure white before the experiment in fig. 4.8, see fig. 4.12(a), and was perceptibly darkened after the experiment; see fig. 4.12(b).

(a) **(b)**

Figure 4.12. Photographs of the SnO_2 powder employed in the experiment in fig. 4.8 (a) before and (b) after the experiment.

Figure 4.13 shows the spectra collected up to 100 °C in fig. 4.8 over the spectral range 900 – 1700 cm^{-1}: as can be seen, there appears to be very little change in the various absorptions at 50 °C compared to 25 °C, but a significant change at 100 °C, supporting the possible role of electron injection into the conduction band of the SnO_2 initiating reaction.

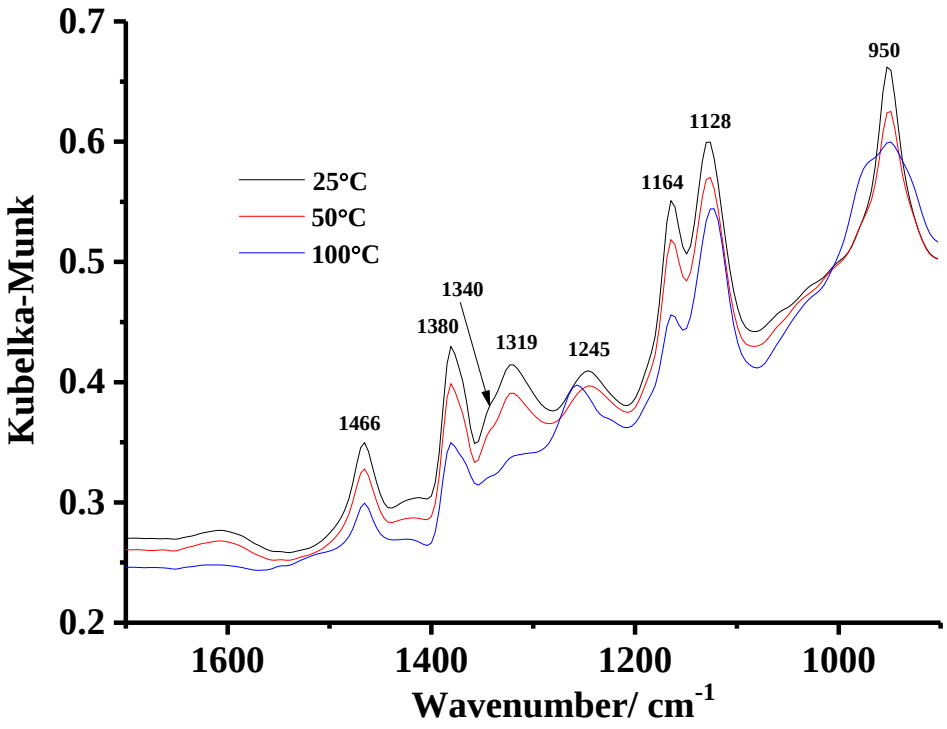

Figure 4.13. The spectra collected up to 100 °C in fig. 4.8 over the spectral range 900 – 1700 cm^{-1}.

Figure 4.14 shows the spectrum collected at 25 ºC in fig. 4.8. As can be seen from figs. 4.13 and 4.14, there are a number of sharp features superimposed upon the sloping baseline and the

broad water absorptions, and these are summarized in table 4.1. It is generally accepted that IPA can absorb on oxide surfaces in up to three forms [18-20][33-35]: broadly these are: (I) IPA structure unpurturbed and weakly adsorbed, (II) structure unpurturbed and strongly adsorbed and (III) chemisorbed as the isopropoxide, and the IR bands so observed, along with their assignments, are given in table 4.1, along with the features observed in the spectrum of liquid IPA (measured in a Presslok holder between two CaF_2 plates) and in the spectrum of $ThOCH(CH_3)_2$ as an example of an alkoxide [36].

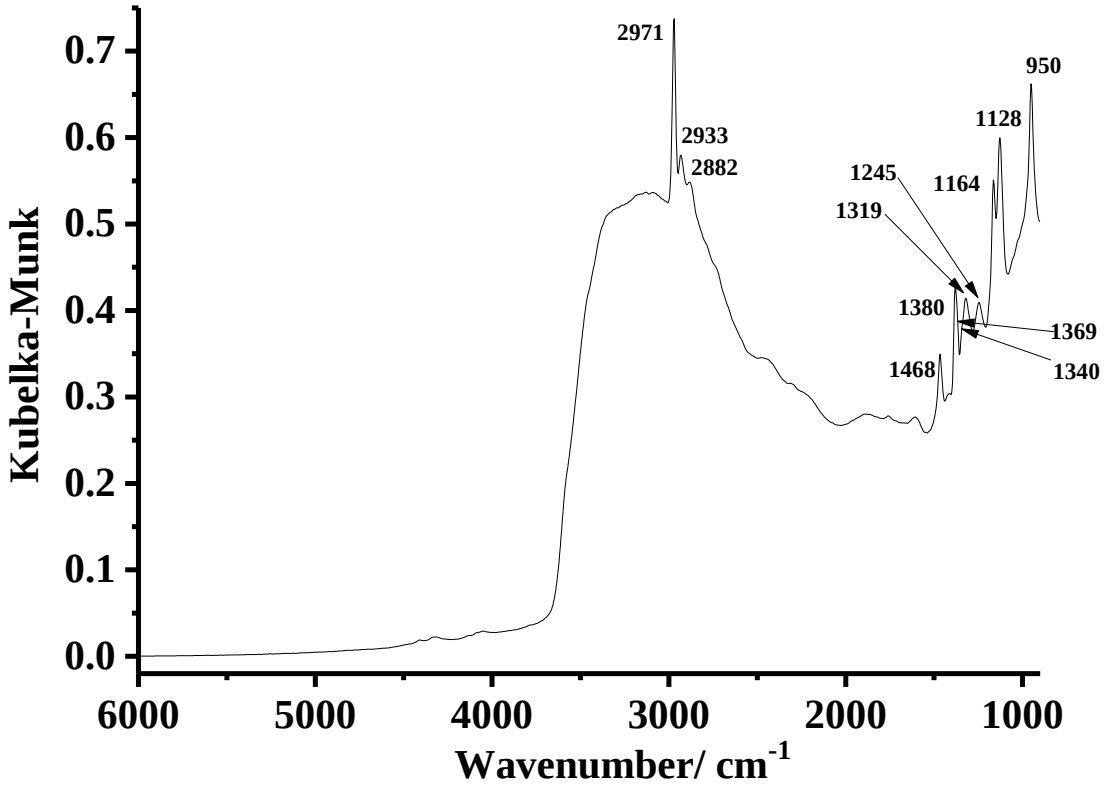

Figure 4.14. The spectrum collected at 25 °C in fig. 4.8.

Figures 4.15(a) & (b) compares the spectra of the liquid IPA and IPA vapour measured in a 5.1 cm pathlength transmission cell. Note that the assignments by Xu et al. [20] do not agree with those generally presented in the literature, and that it is not clear whether Rivallan et al. [33] attribute all the bands observed with adsorbed IPA to the isopropoxide, $AlOCH(CH_3)_2$, or just the 1166 and 1132 cm^{-1} features.

It is clear from table 4.1 that the IR absorptions of the various forms of adsorbed IPA are very similar, and hence it is not surprising that the assignments of these features causes confusion.

Resini and co-workers [23] and Xu et al. [20] follow Rossi et al. [18] in discriminating between IPA adsorbed as the unperturbed molecule (weakly physisorbed with O-H bond intact, type (I), or strongly physisorbed, type (II), in table 4.1) and as the isopropoxide chemisorbed via a metal-oxygen bond (type (III) in table 4.1) via the presence of absence of a broad band between 1200 and 1400 cm^{-1} attributable to the OH deformation (δ_{OH}), which appears around 1250 cm^{-1} in the gas phase spectrum but is absent from the liquid phase spectrum (see fig. 4.15). Rossi et al. [18] state that this band is present in the spectrum of "monomeric" IPA in CCl_4, which suggests that it disappears, or moves and is concealed under another band, if any hydrogen bonding is present. If this band is present, this is generally taken as evidence that all the features are attributable to type (I) or (II) adsorption, if the other features are present but it is absent, this is taken as evidence for chemisorption. At first sight, on this basis, the features in fig. 4.14 may be attributed to types (I) and/or (II) physisorbed IPA.

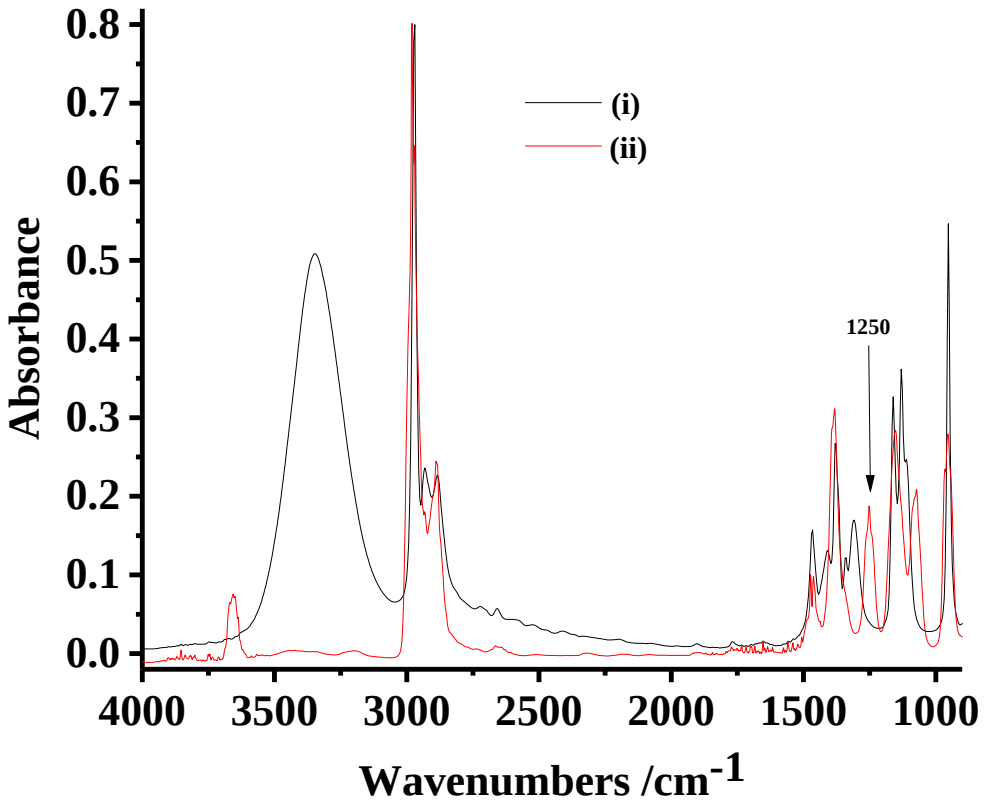

(a)

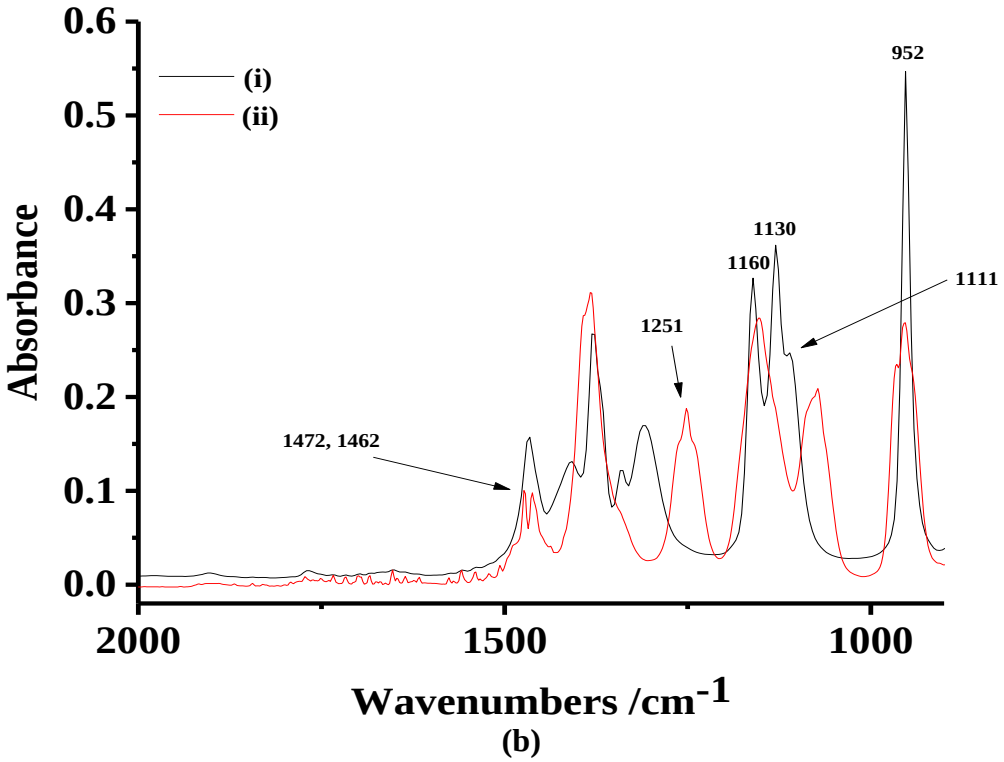

Figure 4.15. FTIR spectrum of isopropyl alcohol: (i) 50 μL of the alcohol was sandwiched between two 2 mm thick CaF_2 plates. The spectrum has been scaled by a factor of 0.68 for clarity. (ii) FTIR spectrum of isopropyl alcohol vapour in a 5.1 cm pathlength transmission cell: (a) full spectral range and (b) 900 – 2000 cm^{-1}. (a) full spectral range and (b) 900 – 2000 cm^{-1}.

In order to check the reproducibility of the data in fig. 4.8, and to obtain more spectra, the experiment in fig. 4.8 was repeated up to 250 ºC, with spectra collected every 25 ºC, and the results are presented in figs. 4.16(a)-(c). Only the spectra collected up to the onset of the change in the free electron absorption are presented, for clarity.

Figures 4.16(b) and (c) show the spectra in fig. 4.16(a) except over restricted spectral ranges, and fig. 4.17 the spectrum collected at 150 ºC in fig. 4.16(a). It is clear from the figures that the peaks at 2971, 2933 and 2882 cm^{-1} decrease in intensity, and are replaced by bands at 2962, 2930 and 2866 cm^{-1}, although the 2971 cm^{-1} band is still present at 150 ºC (see below). In the lower frequency region, the 1466 cm^{-1} feature decreases in intensity but is not lost by 150 ºC, the 1383, 1340 and 1322 cm^{-1} features are lost, whilst the 1369 and 1245 and 1128 cm^{-1} bands decrease in intensity and shift slightly in position. The 950 cm^{-1} band decreases and bands grow-in on either side at 975 and 926 cm^{-1}, whilst the 1165 cm^{-1} band decreases in intensity but does not disappear. Thus, at first sight, fig. 4.17 appears to show the spectrum of a single adsorbed

species produced by the transformation of the physisorbed IPA; however, the behaviour of the 1369, 1245, 1165 and 1128 cm^{-1} bands suggests that the situation is not quite so simple. This becomes clearer if the spectra obtained at 175 and 200 ºC are also considered, see fig. 4.18, which shows these spectra with their baselines offset down to overlie the spectrum taken at 150 ºC.

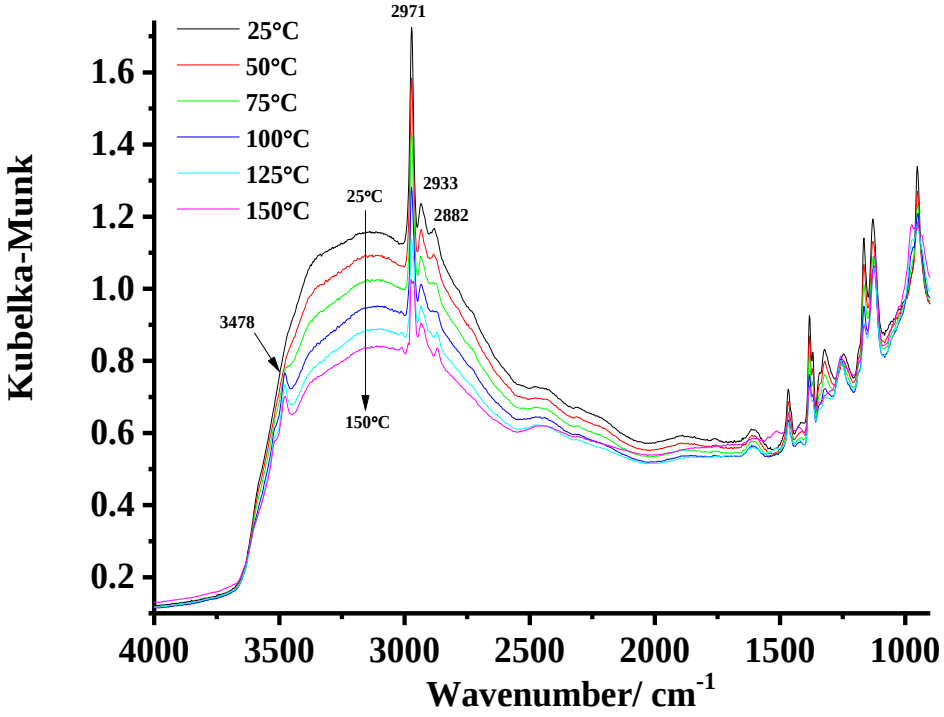

(a)

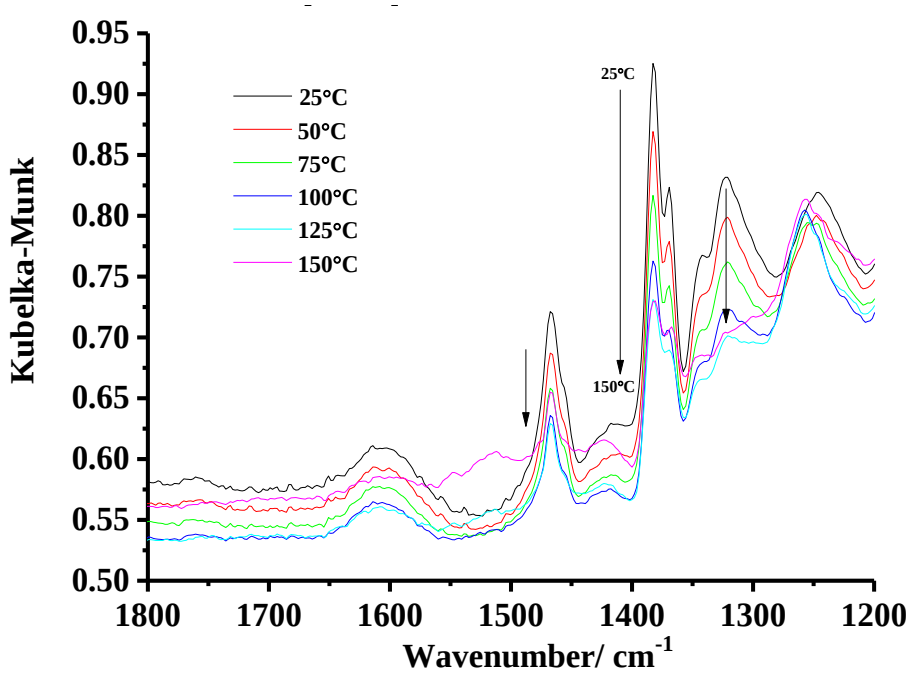

(b)

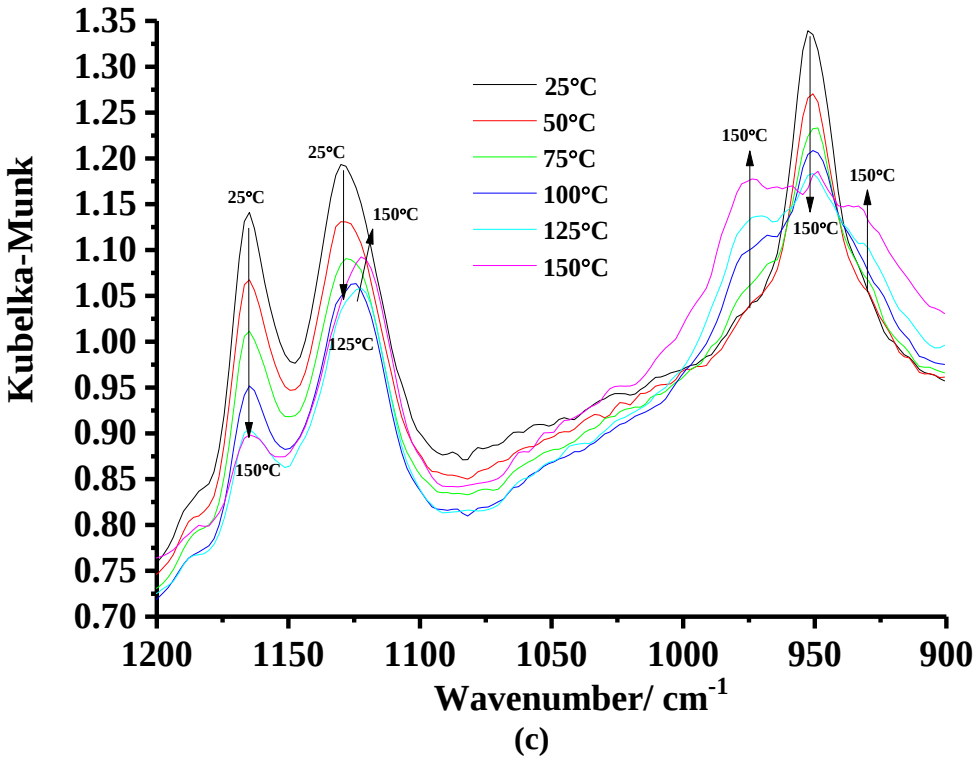

Figure 4.16. A repeat of the experiment in fig. 4.8 up to 250 ºC, with spectra collected every 25 ºC: (a) full spectral range, (b) 1200 to 1700 cm^{-1} and (c) 900 to 1200 cm^{-1}.

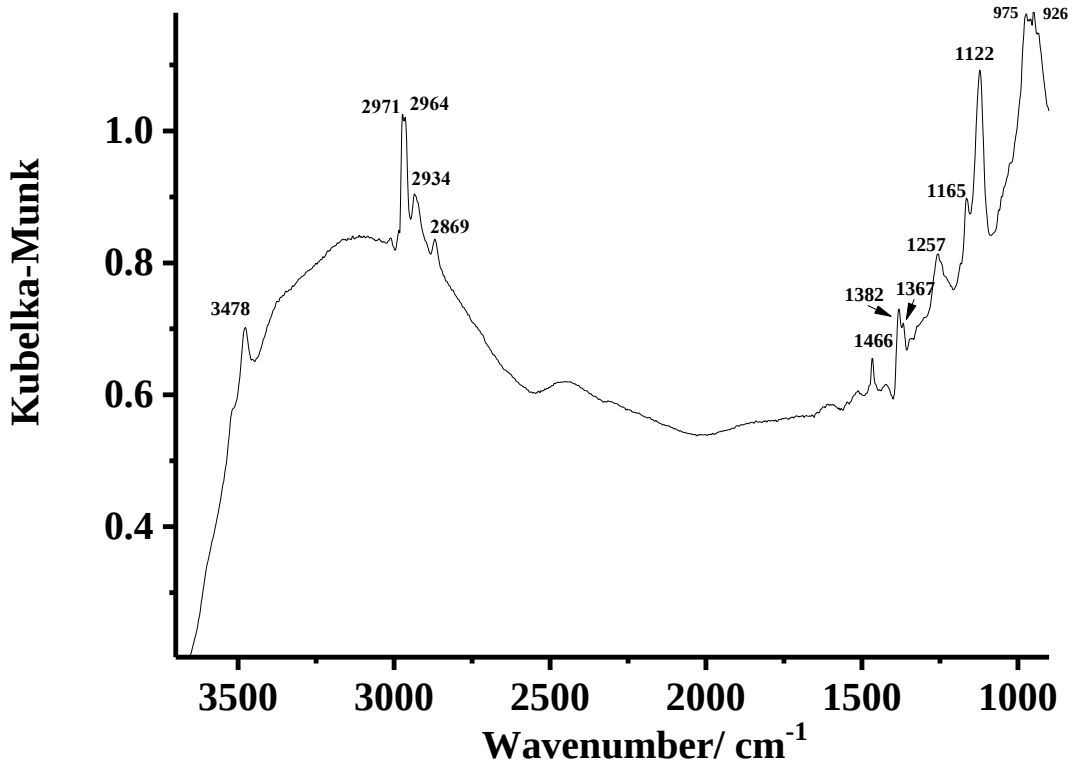

Figure 4.17. The spectrum collected at 150 ºC in fig. 4.16(a).

Figure 4.19 shows the original spectra. From fig. 4.18 it can be seen that the 2971 cm^{-1} feature disappears as the temperature is increased to 200 ºC (leaving the 2964, 2934 and 2869 cm^{-1} bands) as do all the absorptions below 1600 cm^{-1} apart from the 1118 cm^{-1}, 975 and 926 cm^{-1} features. Mehrotra and Batwara [36] and Zaki and Shepherd [37] attribute multiple bands around 950 cm^{-1} to isopropoxide species. Further, the spectrum attributed by Resini and co-workers [23] to adsorbed isopropoxide is identical to that in fig. 4.17, and is characterised by significantly lower C-H band intensities (in contrast to the intensities of these features in the spectra of the physisorbed IPA, see fig. 4.8, and the spectra of liquid and vapour-phase IPA, see fig. 4.15), with the intensity of the 2964 cm^{-1} feature comparable to that of the 1122 cm^{-1} band. Thus it appears that desorption of IPA gives gas phase IPA (the ν_{OH} band slightly shifted compared to the physisorbed molecule), only those bands that have frequencies sufficiently different to those of the adsorbed species appearing in the difference spectra, leaving absorptions due to the isopropoxide species.

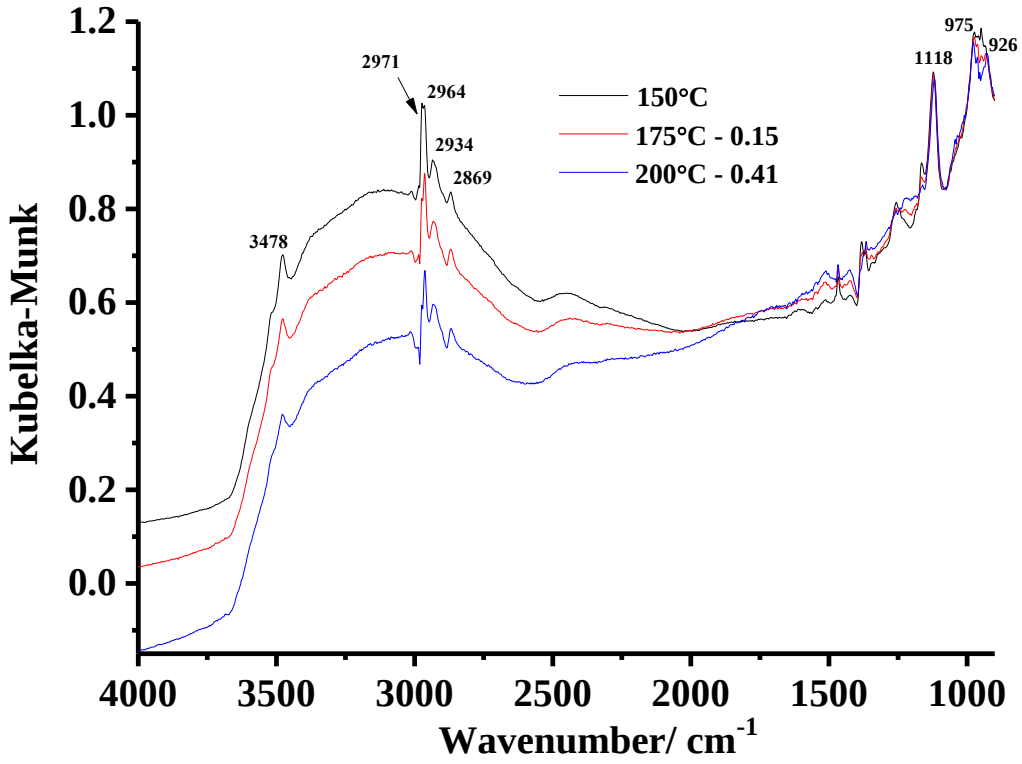

Figure 4.18. The spectra obtained at 175 and 200 ºC in fig. 4.16(a). The baselines of the spectra were offset down to overlie the spectrum taken at 150 ºC.

$IPA_{(l)}$* /cm^{-1}	**$IPA_{(ads)}$* /cm^{-1}**	[35]	[33]	[32] (I)	[32] (II)	[32] (III)	[19] (III)	[30] (I) or (II)	[30] (III)	[18] (II)	[18] (III)	**Assignment**
2971	2971			2973	2968	2972				2973		ν_{aCH3}[32]
2933	2933			2938	2930	2936				2936		ν_{sCH3}[32]
2882	2882			2870	2938	2872				2872		ν_{C-H}[32]
		1615										
1466	1468	1460s	1464	1472 1462	1468 1458	1466 1454		1468		1465		δ_{aCH3}[30][32] δ_{aCH3}[32]
1408				1400	1390							$\delta_{CH,}$ δ_{OH}[31]
1378	1380	1380s		1382	1386	1382					1386	δ_{sCH3}[32] Gem dimethyl[35]
1369sh	1369		1368	1364	1365	1369	1362	1380				δ_{sCH3}[30][32] ν_{C-O}[19]
1340	1340	1340m		1345	1345	1342		1340				γ_{CH}[30][32]
1310	1319	1315m		1310	1292					1293		δ_{OH}, δ_{CH}[32]
	1245									1252		δ_{OH} physisorbed and gas -phase IPA[18]
1160	1164	1165s	1172	1172	1169	1165	1166		1166		1168	$\nu_{CC,}$ ν_{CO}, r_{CH3}[32] ν_{CC},ν_{CO}[30] δ_{aCH3}[19]
1139	1128		1134	1167		1148	1124		1132		1131	$\nu_{CC,}$ ν_{CO}, $_{CH3}$[32] ν_{sCH3}[19] ν_{CC}[30]
1111												
		1008m										Terminal and bridged C-O str.[35]
		975m										Terminal and bridged C-O str.[35]
952	950	965 m										Terminal and bridged C-O str.[35]

*Table 4.1. Literature assignments of the IR bands in the spectra of IPA adsorbed on oxides, and in the IR spectrum of $Th^{**}OCH(CH_3)_2$ [36]. * refers to liquid and adsorbed IPA obtained from this work and ** refers to Thorium.*

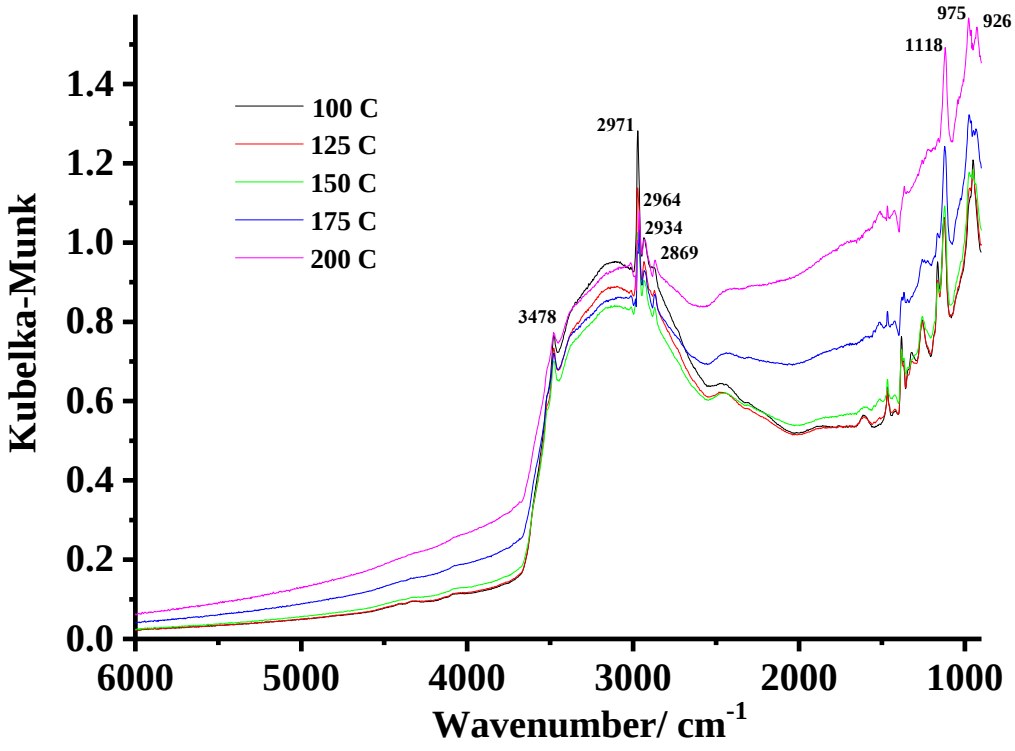

Figure 4.19. The spectra in the experiment shown in fig. 4.16(a) collected between 100 and 200 °C.

Ever since the pioneering studies of, for example, Greenler [38] it has been generally accepted that alcohols adsorb on metal oxides to give a mixture of physisorbed (unperturbed) alcohols (corresponding to types (I) and (II) above) and alkoxide species (type (III) above). In fact, three forms of physisorbed states have been postulated [22] i.e. with the hydrogen atom of the O-H group interacting with the oxygen atom of an M-OH group, that bridging two metal ions and directly with the metal ion of a Lewis acid cationic site. Two of these presumably correspond to types (I) and (II) above. At temperatures > 50 °C, the physisorbed IPA (types (I) and (II)) is converted to the alkoxide form, bonded through oxygen to the surface.

Again, two types of alkoxides are believed to exist: bonded to a single oxygen atom and bonded to a bridging oxygen atom, giving peaks at 1170 cm^{-1} and 1130 cm^{-1}, respectively [22]; changes in the relative intensities of these features reflecting changes in the relative surface occupancy by these species. In the nomenclature above, these are designated as types (IIIa) and (IIIb). Thus, it does not seem unreasonable to postulate that the spectra in figs. 4.16(a)-(c) show, as well as the desorption of IPA, the conversion of types (I) and (II) physisorbed IPA to types (IIIa) and (IIIb) chemisorbed propoxide species, with the latter form predominating. This, in turn,

suggests the presence of bridging O atoms, which is not unreasonable given that the calcination temperature employed (400 °C) is sufficient to effect some dehydroxylation of the surface [16]. Hence the type (II) physisorbed IPA may also be the form interacting with bridging oxygen atoms.

Figure 4.18 suggests that, apart from the changes due to dehydroxylation, and a continuing loss of type (I) and/or (II) IPA (eg. see the decrease in the intensity of 950 cm^{-1} band), little change apparently occurs between 150 °C and 200 °C. However, figs. 4.9 and 4.20 show that large changes do occur in the free electron absorption and in the fingerprint region of the spectra. Figure 4.20 shows the spectrum collected at 100 °C in the experiment in figs. 4.16(a)–(c) subtracted from those taken up to 200 °C. Loss features due to the remaining adsorbed IPA present at 100 °C are clearly visible and increase with increasing temperature, as are the increase in the free electron absorption and broad loss features due to the dehydroxylation of the surface. The only clear gain feature is a band with a maximum at ca. 1512 cm^{-1}: there may be other gain features but these are obscured by the IPA loss bands. Both in terms of the frequency of this band and a likely mechanism, a reasonable assignment of the 1512 cm^{-1} feature is to the C=C stretch of adsorbed enolate [21], bound side-on via coordination to the double bond and formed from the isoproxide [21]:

$$M\text{-}OH + (CH_3)_2CHOH \rightarrow M\text{-}O\text{-}CH(CH_3)_2 + H_2O \quad (4.1)$$

$$M\text{-}O\text{-}CH(CH_3)_2 + M \rightarrow CH_3C(OH)=CH_2\text{---}M + M\text{-}H \quad (4.2)$$

$$M\text{-}H + M\text{-}H \rightarrow 2M + H_2 \quad (4.3)$$

There are no clearly identifiable product features in fig. 4.20, suggesting that the enolate builds up on the surface at temperatures from 100 to 200 °C. From figs. 4.16(a), 4.18 and 4.19 it can be seen that a band attributable to an isolated OH stretch at 3478 cm^{-1} [16] appears at temperatures > 75 ºC, *eg* as the desorption of IPA commences. This suggests, on the basis of previous work in Newcastle [16] that the IPA is physisorbed via hydrogen bonding and that desorption of the alcohol from the surface frees up or reveals the SnOH groups previously hydrogen bonded. This can be more clearly seen by subtracting the spectrum collected at 25 ºC in fig. 4.8 from those taken up to 150 ºC, in order to remove the effect of the free electron absorption, and the resultant spectra are shown in fig. 4.21. In contrast to the results observed during the heating of the fully hydrated SnO_2 in air [16] the spectra do not show the loss of various forms of adsorbed water, presumably because the water was replaced by the adsorbed

IPA, the loss features of which are clearly increasing in intensity as the temperature was increased in fig. 4.21.

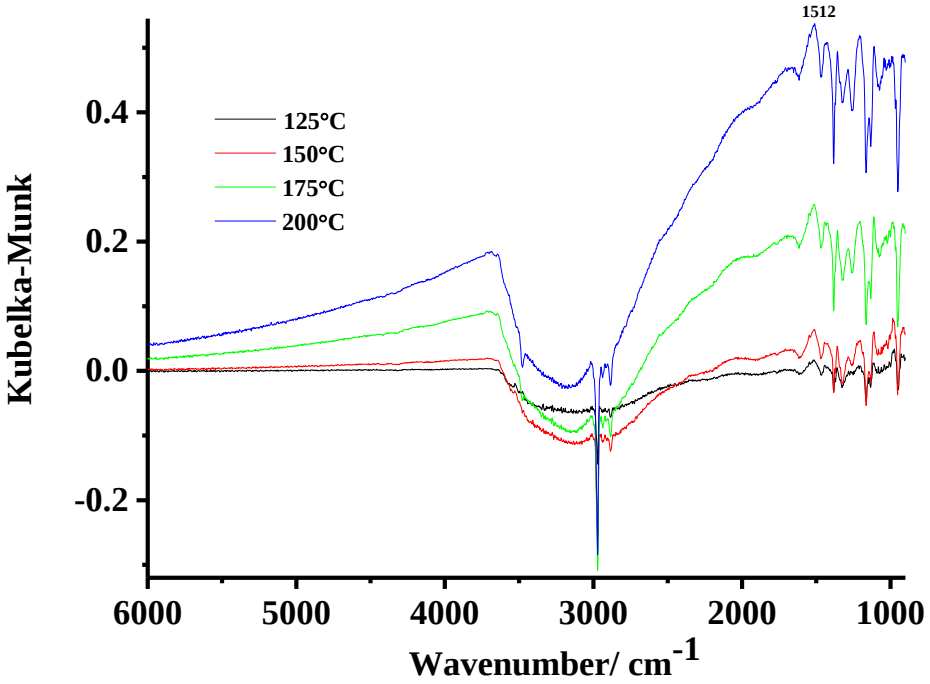

Figure 4.20. The spectra collected in the experiment in fig. 4.16 from 125 to 200 ºC. The spectrum taken at 100 ºC was subtracted from all the spectra shown.

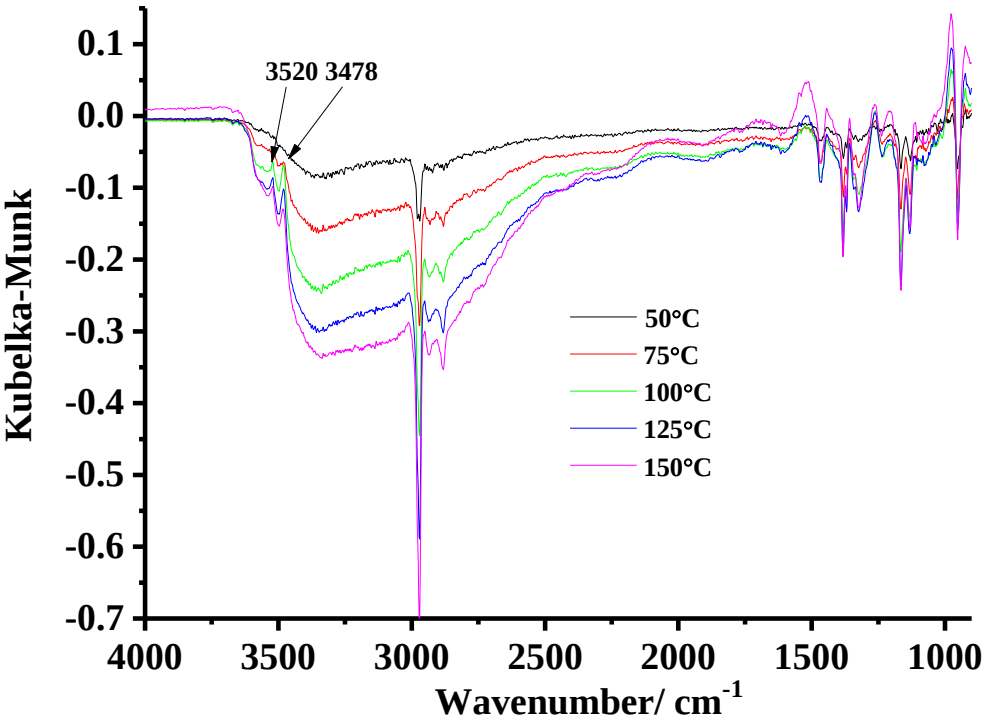

Figure 4.21. The spectra in fig. 4.8 collected at different temperature. The reference spectrum was collected at 25 °C.

The broad loss between 4000 and 1500 cm^{-1} is due to the loss of hydrogen bonding between the SnOH groups on the surface and adsorbed IPA, resulting in the appearance of the two bands due to isolated SnOH stretches at 3520 and 3478 cm^{-1} as the IPA is removed. This may be interpreted in terms of the model of the surface SnOH groups proposed by Morishige and co-workers [39] and Morimoto *et al*. [40][41]. These authors consider the OH species on the three main low index surfaces of SnO_2, namely (100), (110) and (111). The fully hydroxylated (100) surface contains OH groups in which the H atoms are sunk somewhat into the hollow sites between the oxygen atoms. Hence, the OH groups on this surface would not be expected to form hydrogen bonds to any significant extent with physisorbed IPA molecules. In contrast, the OH groups of the (110) plane point outwards perpendicularly from the surface and hence would be expected to form hydrogen bonds with physisorbed IPA. The (111) surface is slightly more complicated, but the OH groups again point outwards and hence could also form hydrogen bonds with physisorbed IPA.

Thus, loss of water from the (100) facets does not "release" SnOH groups from hydrogen bonding, hence there is no gain of absorption due to isolated OH, whereas loss of water from the (111) and (110) facets results in the gain in intensity of the bands at 3520 cm^{-1} and 3478 cm^{-1} due to appearance of isolated SnOH groups. Although there is no direct evidence for two forms of physisorbed IPA (type (I) and (II)), it does not seem unreasonable to postulate that type (I) IPA was adsorbed on the (100) facets, and type (II) on the (110) and (111) facets.

Figure 4.22(a) shows plots of the intensities of the various features in fig. 4.8 as a function of temperature, normalised to their maximum values, and fig. 4.22(b) shows the raw data. Figure 4.23 shows selected spectra from fig. 4.8: as can be seen from the figure, loss features appear at 1469, 1390, 1252*, 1153*, 1076 and 952 cm^{-1} at 200 °C and increase steadily in intensity up to 600 °C. Gain features appear at 1738 cm^{-1}, 1715 cm^{-1}(sh) and ca. 1207 cm^{-1} (the frequencies of the features marked with * in the figure are difficult to determine accurately due to the bands pointing in the opposite direction distorting the peak position) but only at temperatures > 200 °C . The figure supports the difference in the temperature-dependent behaviour of the 1738 cm^{-1} gain feature and the various loss features. The loss features may be attributed to gas phase isopropyl alcohol, see table 4.1 and [42]: clearly the reactant is lost steadily at all temperatures > 150 °C.

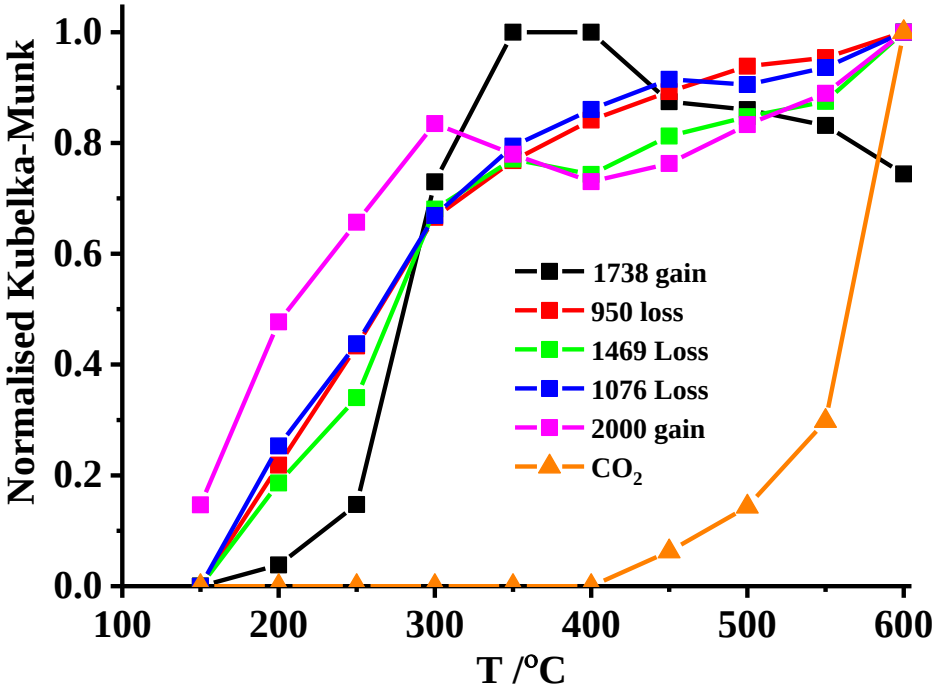

(a)

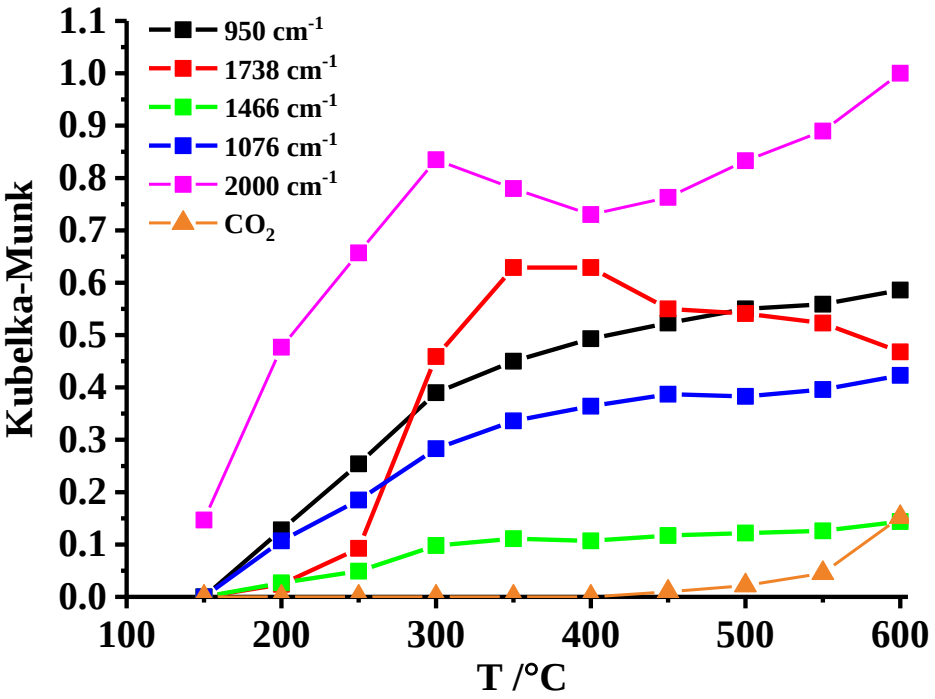

(b)

Figure 4.22. Plots of the Kubelka-Munk intensities of the various features in fig. 4.8 as a function of temperature: (a) normalized to their maximum values using N_2 and IPA vapour as a feed gas and (b) the raw data.

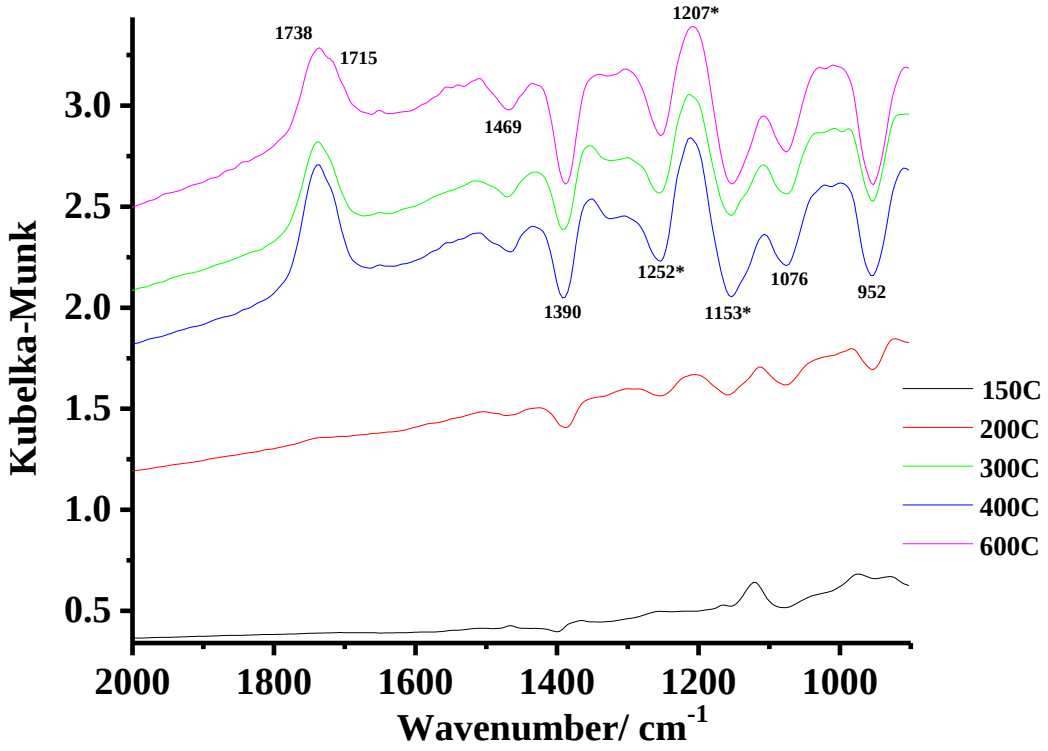

Figure 4.23. Selected FTIR spectra from fig. 4.8.

Figure 4.24 shows the spectrum taken at 100 °C in fig. 4.8 subtracted from those collected from 150 to 300 °C. Additional loss features at 2974 and 2887 cm^{-1} due to the gas phase IPA may clearly be seen in the figure. Subtracting the spectrum collected at 100 °C brings out gain features with bands at ca. 1354, 1212 and 1104 cm^{-1} as well as 1738 cm^{-1} and the shoulder at 1715 cm^{-1}. The shoulder at 1715 cm^{-1} may be attributed to acetaldehyde [42] and the remaining gain features to gas phase acetone [43]. Region (II) shows a significant increase in free electron density in the semiconductor, consistent with the oxidation of the adsorbed species from IPA to acetone. Thus, in region (II), at T > 150 °C, the adsorbed enolate is oxidised to acetone:

$$CH_3C(OH)=CH_2\text{---}M + (CH_3)_2CHOH + M \rightarrow M\text{-}O\text{-}CH(CH_3)_2 + (CH_3)_2C=O + M\text{-}H \quad (4.4)$$

presumably as the temperature is sufficient to overcome the activation barrier. In region (III), 300 – 400 °C, it is not clear why the free electron absorption decreases and the gas phase acetone concentration remains steady.

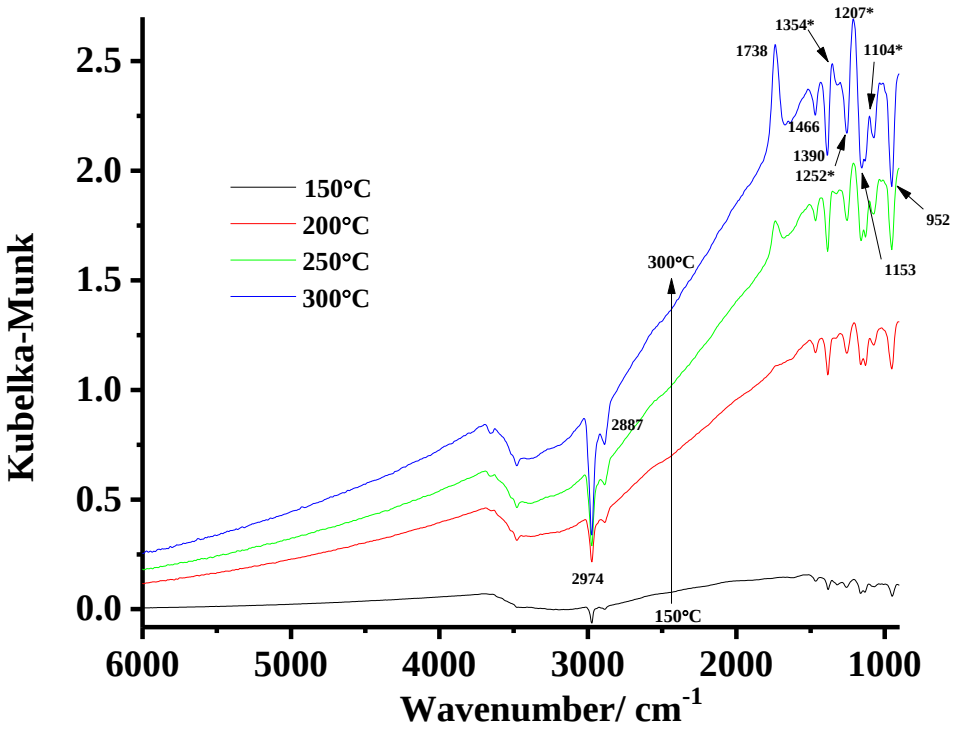

Figure 4.24. The spectra collected in the experiment in fig. 4.8 collected between 150 and 300 ºC, with that taken at 100 ºC subtracted.

Figure 4.25 shows the spectrum collected at 400 °C in fig. 4.8 subtracted from those taken up to 600 °C. The spectra show the gain of free electrons in the conduction band of the SnO_2 and the concomitant oxidation of the acetone to CO_2 (2362 and 2330 cm^{-1} [44]). The acetone loss features < 1400 cm^{-1} are clear due to the absence of gain features. From fig. 4.8, it can be see that a significant amount of acetone was still present over this temperature range, along with the weaker CO_2 gain features, showing that the conversion of acetone and acetaldehyde to CO_2 was by no means complete.

In order to check the effects of the calcination temperature on the thermal reaction of IPA, the SnO_2 sample calcined at 700 °C was employed in DRIFTS cell. The experiment in fig. 4.8 was repeated up to 600 ºC with spectra collected every 25 ºC up to 250 ºC and every 50 ºC up to 600 ºC, the reference spectrum was taken using KBr at 25 ºC in N_2 + IPA and the results are presented in fig. 4.26.

In terms of the vibrational bands, as can be seen from the figure, the behavior was similar to that observed in fig. 4.8, i.e. acetone, acetaldehyde and CO_2 were generated products. In addition, physisorbed IPA and then isopropoxide were observed up to 150 ºC. At temperature > 150 ºC, loss features due to gas phase IPA were observed.

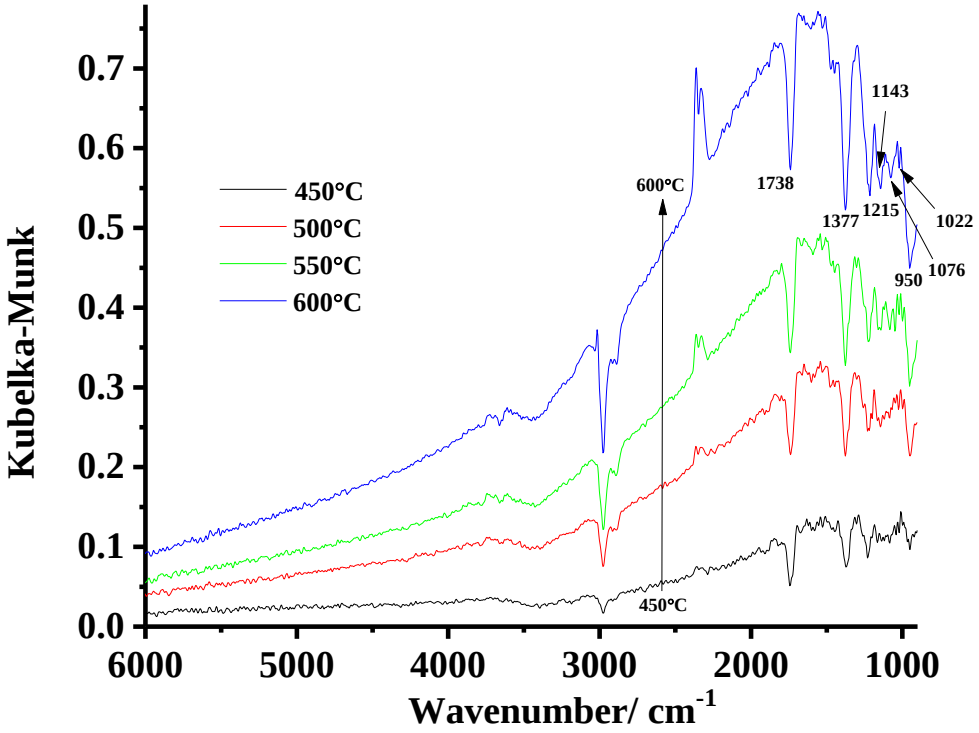

Figure 4.25. The spectra collected in the experiment in fig. 4.8 collected between 450 and 600 ºC, with that taken at 400 ºC subtracted.

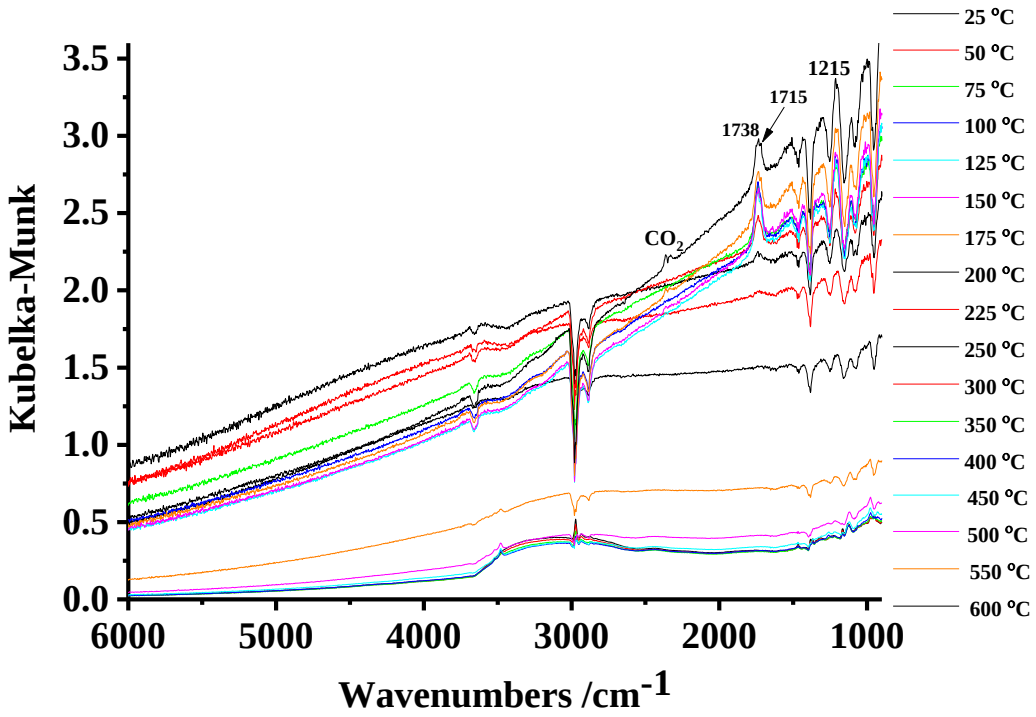

Figure 4.26. The spectra obtained in an analogous experiment to that in fig. 4.8 except that the spectra were collected every 25 ºC up to 250 ºC and every 50 ºC up to 600 ºC using the SnO_2 sample calcined at 700 ºC.

The experiments in figs. 4.8 and 4.26 were repeated using the same samples, see figs 4.27(a) & (b) in order to determine if the changes in sample colour observed on heating in IPA were reflected in changes in activity towards the oxidation of IPA. For clarity, only selected spectra are shown. In terms of the products produced on heating the samples eg. acetone, acetaldehyde and CO_2, as can be seen from the figures, the samples were clearly still active. However, a comparision of fig. 4.8 and 4.27(a), and 4.26 and 4.27(b) shows clearly that there were significant changes in the temperature dependences of the electronic absorptions, most particularly for the sample calcined at 400 °C, see figs 4.28(a) & (b). Figure 4.28(a) shows the plots of the intensity of the Kubelka-Munk function at 2000 cm^{-1} normalized to their maximum values as a function of temperature for the fresh and used SnO_2 samples at different calcined temperatures (see figs. 4.8, 4.26 and 4.27); the raw data is shown in fig. 4.28(b). Despite the different structures of the electronic absorption between the spectra of SnO_2 samples calcined at 400 ºC and 700 ºC, it is interesting to note that the temperature dependences of the absorption at 2000 cm^{-1} were essentially the same, with the magnitude simply being lower for the SnO_2 sample calcined at 700 ºC. In general, the KM function was increased as a function of temperature for both the new and used SnO_2 sample calcined at 700 ºC and for the new SnO_2 sample calcined at 400 ºC, without an obvious change in the activity and selectivity between the new and the used powder samples. In contrast, different behavior was obtained using the used SnO_2 sample calcined at 400 ºC and further investigation is required to explain the data in fig. 4.28, but they may be attributed to the reduction of the isolated OH groups on the catalyst surface which enhance an increase in the number of cross-links and that lead to a stronger adsorption of IPA with the catalyst surface. Hence, the electron absorption was increased after 250 ºC and the IPA start decompose and convert to other products.

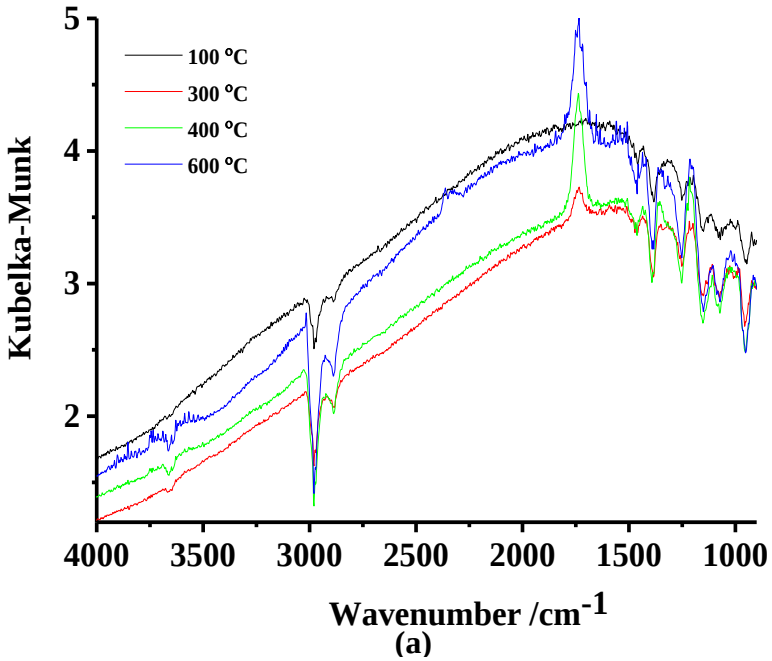

(a)

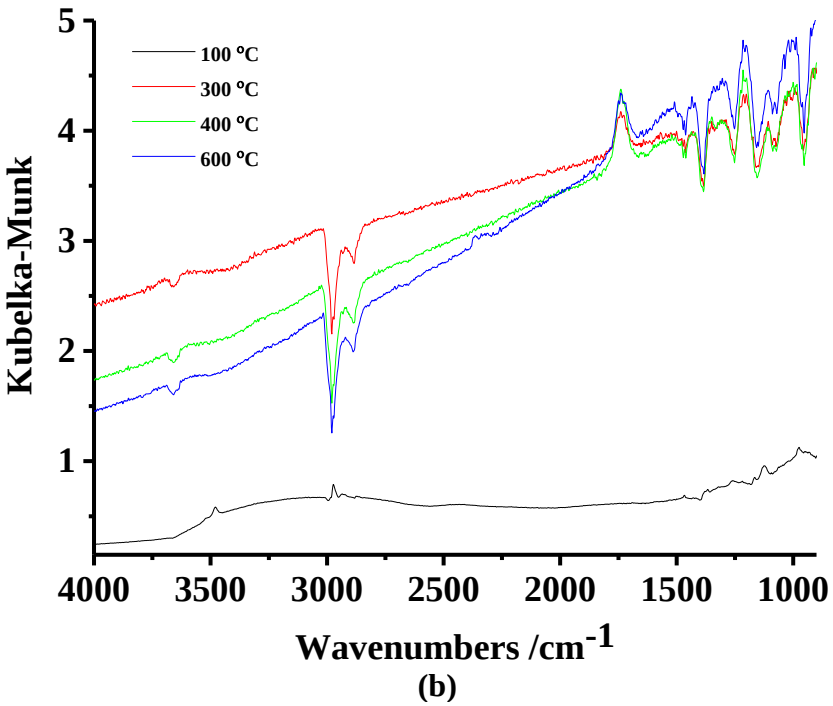

Figure 4.27. (a) The spectra collected when an analogous experiment to that in fig.4.8 was repeated using the same sample of SnO_2 calcined at 400 ºC and (b) the spectra collected in when analogous experiment to that in fig.4.26 was repeated using the same sample of SnO_2 calcined at 700 ºC.

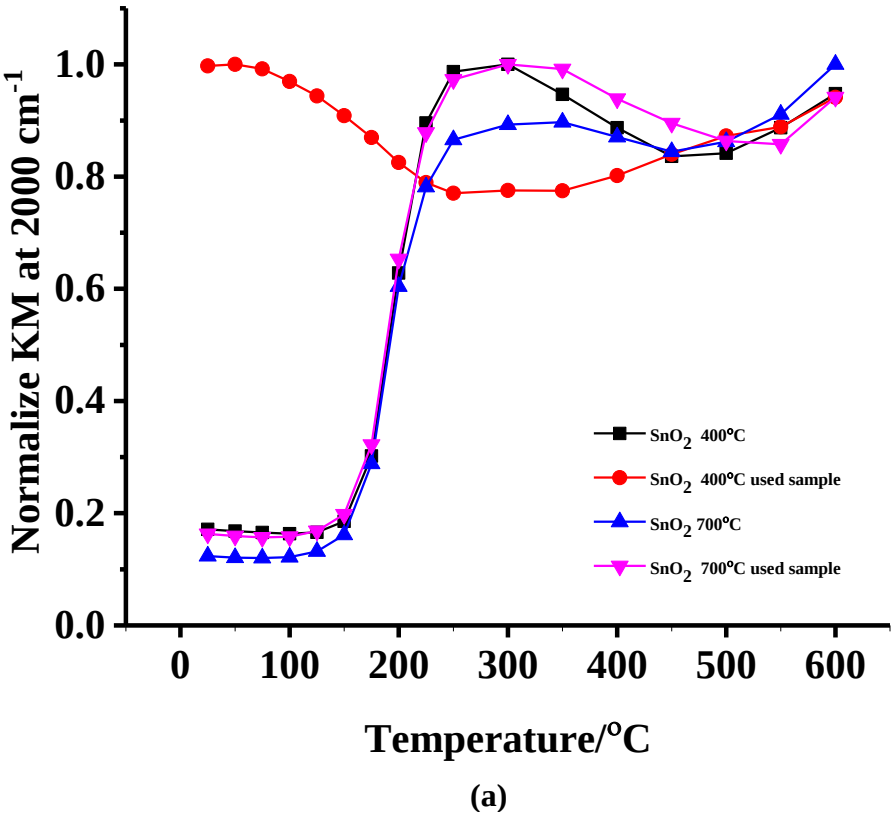

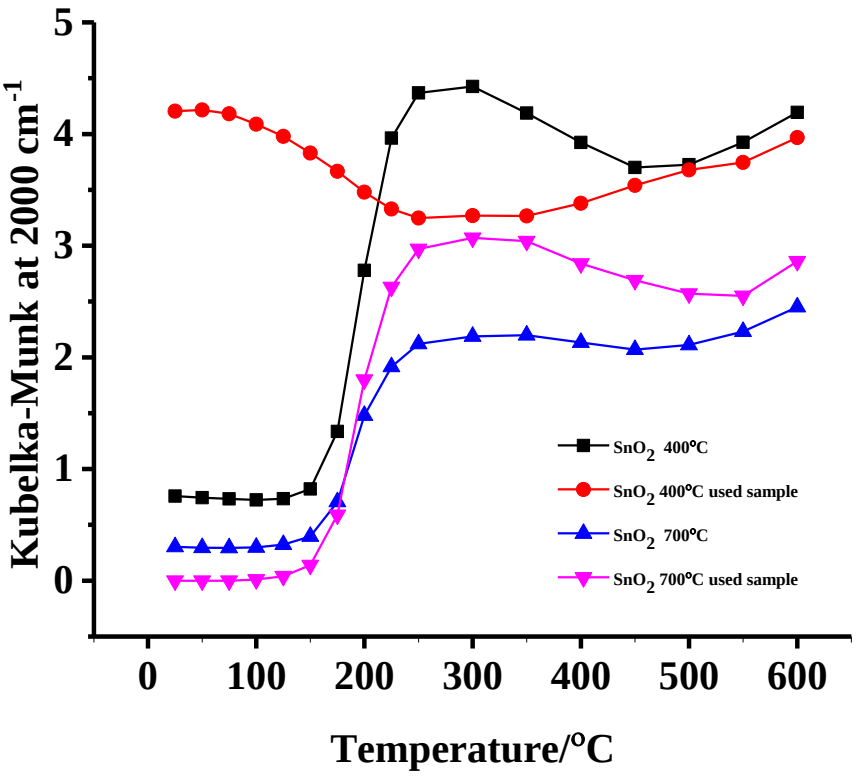

(b)

Figure 4.28. Plots of the KM intensities at 2000 cm^{-1} for the spectra of the new and used SnO_2 samples as shown in figs. 4.8, 4.26 & 4.27 as a function of temperature: (a) normalized to their maximum values and (b) the raw data, see text for details.

The intensity of the acetone absorption at 1738 cm^{-1} was chosen to prove the effect of re-heating the samples, and fig. 4.29(a) shows plots of the KM intensities of the acetone features at 1738 cm^{-1} normalized to their maximum values as a function of temperature for the new and used SnO_2 samples measured from the spectra in figs. 4.8, 3.26 and 4.27, and the raw data are shown in fig. 4.29(b). As can be seen from figs. 4.29(a) & (b), re-heating the SnO_2 sample calcined at 700 ºC in IPA actually enhances its activity towards the production of acetone. In contrast, re-heating the SnO_2 sample calcined at 400 ºC does not markedly increase the maximum amount of acetone produced, but does result in a more sustained production at the higher temperatures. In generally, the activities of the new and used SnO_2 samples calcined at 400 ºC were higher than those observed using the new and used SnO_2 samples calcined at 700 ºC. Re-heating samples can enhance the dehydroxylation the oxide surface and this may have improved the surface reactivity of the catalyst. As a result, it would be also expected that the number of Lewis and Bronsted sites on the surface would be increased in the used samples so the production of acetone increased. However, increasing the calcination temperature may be led to

agglomeration the sample and hence increased the particle size and decreased surface area leading to decreased IPA conversion to acetone comparing to the sample calcined at 400 ºC [37].

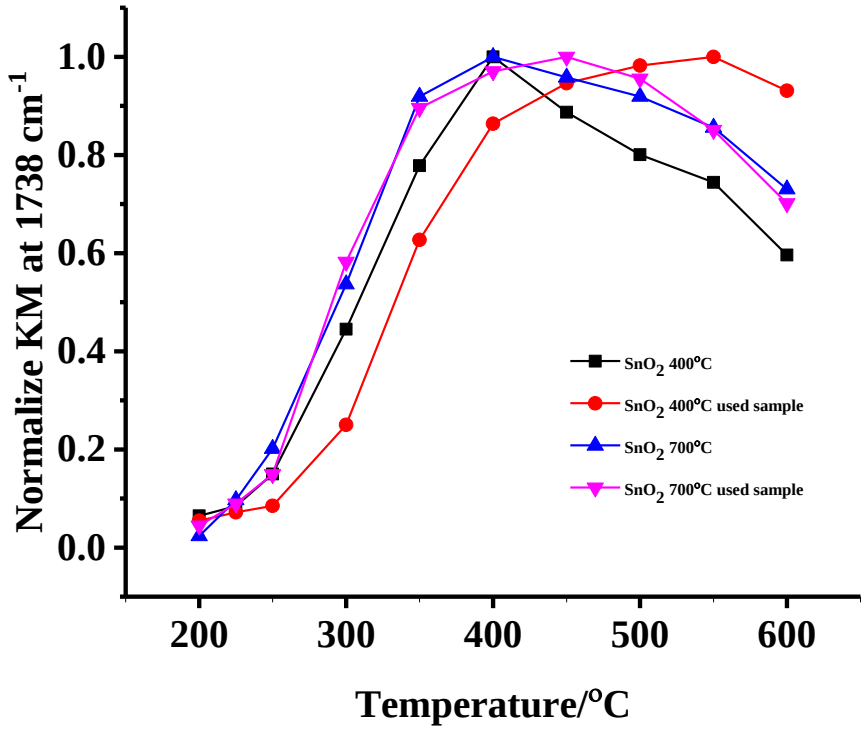

(a)

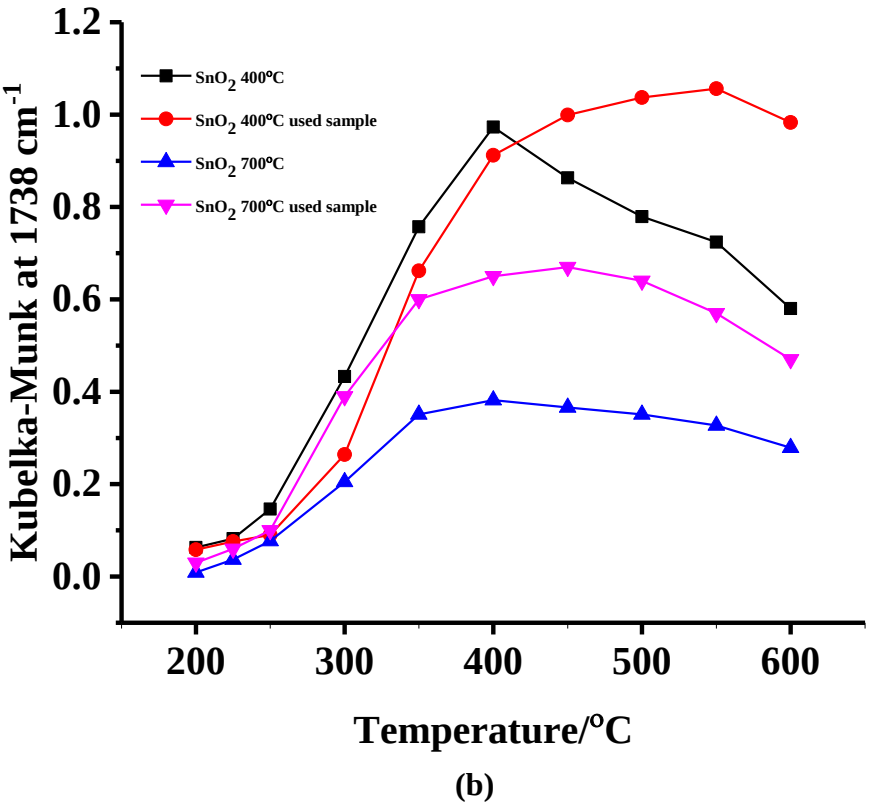

(b)

Figure 4.29. Plots of the KM intensities at 1738 cm^{-1} for fresh and used SnO_2 samples in figs. 4.8, 4.26 & 4.27 as a function of temperature: (a) normalized to their maximum valuse under a static condition of N_2 and IPA vapour as a feed gas and (b) the raw data.

4.4. The plasma experiments using the reflectance cell

4.4.1. Blank experiments

In general, powder catalysts could only be employed in the reflectance cell as coating catalyst powder onto the Macor caps of the transmission cell caused arcing, as shown in fig. 4.30.

(a) **(b)**

Figure 4.30. Photographs of the Macor caps in the NTP transmission cell (a) with and (b) without coating with SnO_2 nanopowder.

The non-thermal plasma – driven reaction of dinitrogen at Macor in reflectance cell was reported in Chapter 3. No obvious products were observed in the plasma but two bands at 1210 and 1150 cm^{-1} were observed due to optical modes of SiO_2 or possibly to Ti-O vibrations.

The preparation of the SnO_2 coated Macor/Ti mesh was discussed in section 2.10 in Chapter 2. In the plasma reflectance experiments using the SnO_2 coatings, the reference spectra were taken with a pure N_2 feed at 30 cm^3 min^{-1}, after which the plasma was initiated at an input power of 20 W and further spectra collected as a function of time up to 20 minutes as shown in fig. 4.31(a). For clarity, only the spectra collected after 2, 6, 10 and 20 minutes are presented in the figure. As may be seen from the figure, the spectra are featureless apart from the two strong bands at 1210 cm^{-1} (broad) and 1150 cm^{-1}, that increase in intensity steadily with time. Figure 4.31(b) shows the spectra obtained in an analogous experiment to that in fig. 4.31(a) except that the coating suspension was prepared using SnO_2 nanopowders calcined at 700 ºC and the plasma initiated at 20 W.

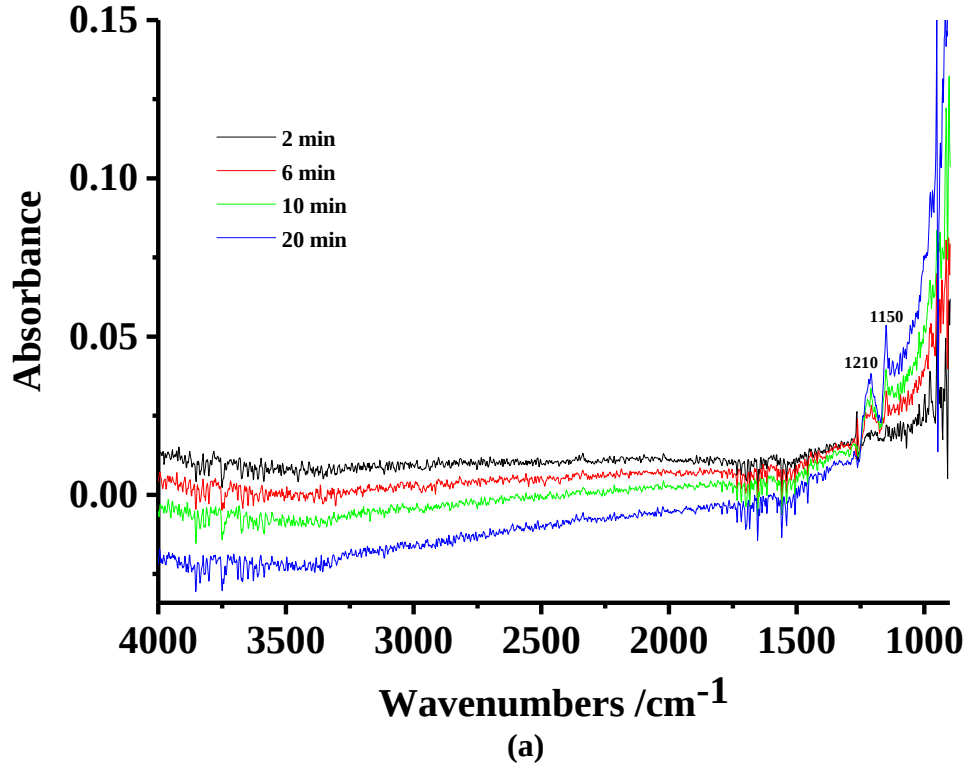

(a)

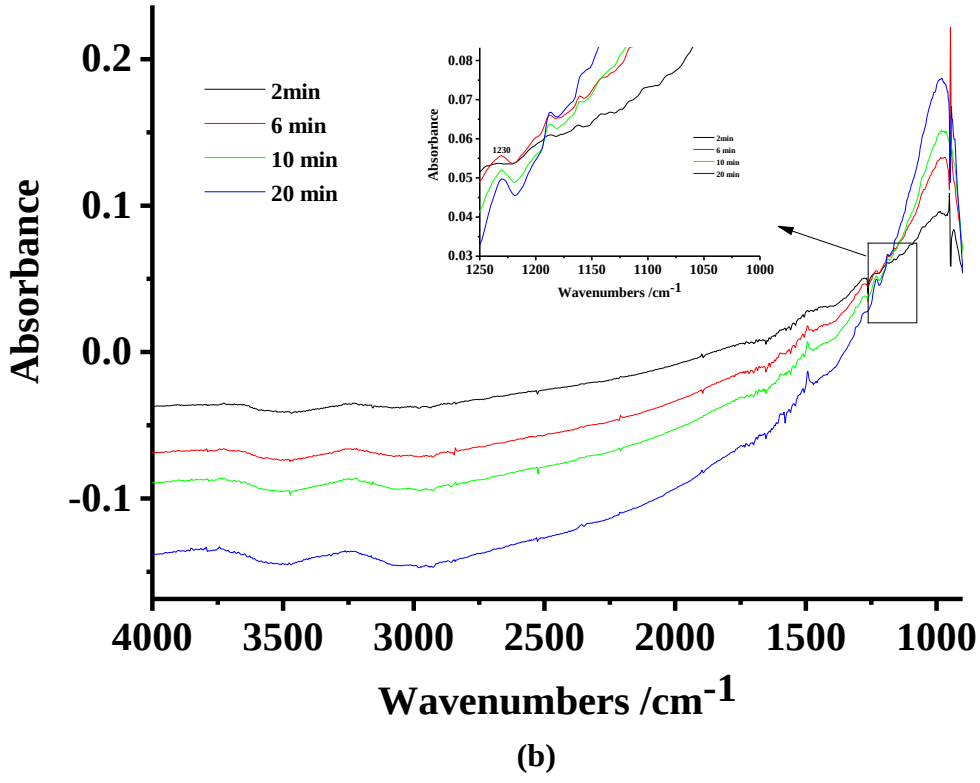

(b)

Figure 4.31. (a) In situ FTIR spectra (4 cm^{-1} resolution, 100 co-added and averaged scans, 100 seconds per scanset) collected using the plasma reflectance cell at the times shown on the figure at an input power of 20 W using nitrogen as the feed gas and the SnO_2 calcined at 400 ºC coating on the Macor/Ti mesh. (b) The spectra collected in an analogous experiment to that in fig. 4.31(a), except that the coating employed the SnO_2 calcined at 700 ºC. The spectra collected immediately before the plasma was initiated was employed as the reference spectra and the spectra were corrected for the CaF_2 window reflection.

4.4.2. Experiments using N_2 and IPA vapour as the feed gas

The non-thermal plasma –driven reaction of IPA in dinitrogen at Macor using the transmission cell was discussed in Chapter 3. In brief, two sets of products were observed: gas phase reaction, with no influence of the Macor, results in the fragmentation of the IPA to produce methane and CO, the latter a temperature << 200 K, as well as the production of acetone and HCN. These species rapidly attained steady-state concentrations in the plasma which remained largely unchanged with time. In contrast, reaction at the Macor resulted in the condensation of the acetone to form a polymethylacetylene-like liquid that also contained isophorone. Figure 4.32 shows spectra of the reflectance cell after operation for 20 minutes at 20 W and 16 W with and without a coating of SnO_2 calcined at 400 ºC. It can be seen that no deposit was formed using SnO_2, even at the higher input power employed than in the absence of the SnO_2 (20 W off 16 W). This strongly suggests that the Macor was acting as a catalyst and this activity was inhibited on coating with SnO_2.

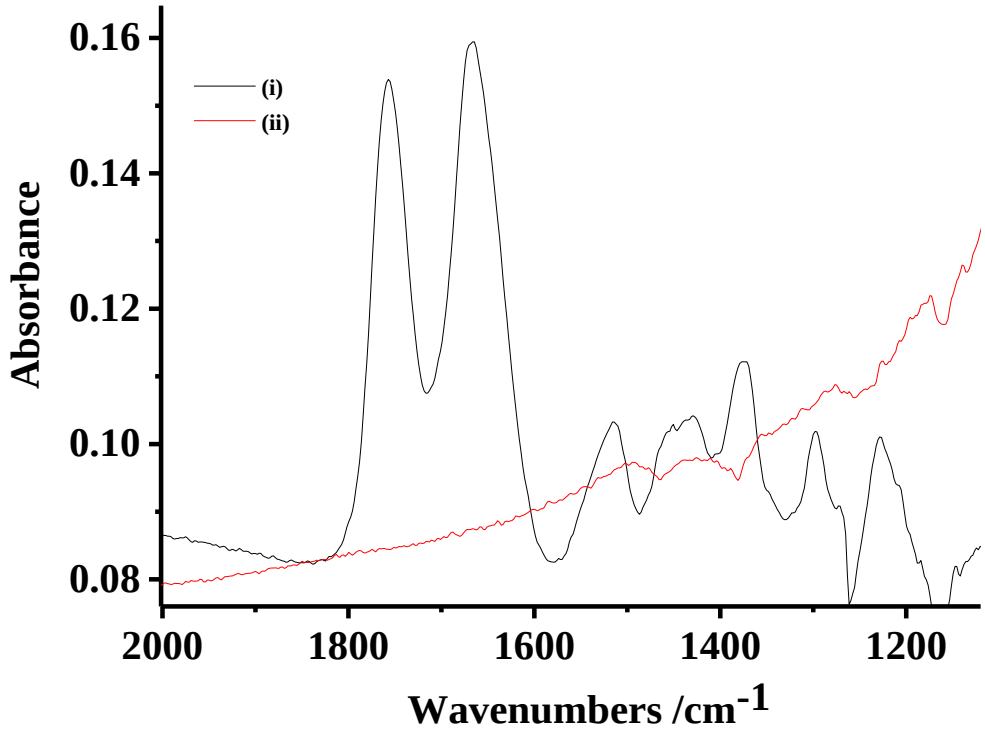

Figure 4.32. Spectra of the reflectance cell after operation for 20 minutes using N_2/IPA as the feed (i) without coating with SnO_2 and (ii) with coating at 16 W and 20 W, respectively.

4.5. Conclusions

Using in-situ FTIR spectroscopy it was shown that non-thermal plasma does not drive any reaction of isopropyl alcohol at SnO_2-coated Macor: however, IPA does react at SnO_2 in the analogous thermally-driven process. This is in complete contrast to the analogous processes at uncoated Macor, where IPA is inactive in the thermally-driven process but undergoes a variety of reactions in the non-thermal plasma, catalysed by the Macor. Thus, the common practice of the selection of catalysts for plasma-driven processes based on those materials active in the analogous thermally-driven systems is of limited validity.

FTIR spectroscopy allowed the detailed unpicking of the mechanism of the oxidation of IPA at SnO_2, including the role played by the semiconducting nature of the oxide. Thus, at 25 ºC, the IPA is physisorbed on the surface of the oxide to produce two adsorbates: on increasing the temperature above 50 ºC, the physisorbed IPA partially desorbs, releasing previously hydrogen-bonded SnOH groups, and partially converts to two forms of chemisorbed isopropoxide. At temperatures between ca. 100 and 200 ºC, the isopropoxide species are converted to adsorbed enolate, bound end-on through the C=C bond. At temperatures > 150 ºC, the adsorbed enolate is oxidised to acetone and acetaldehyde via electron injection into the conduction band of the SnO_2. At temperatures > 400 ºC, the acetone and acetaldehyde are oxidised further, again via electron injection, to CO_2.

4.6. References

1. Fujihara, S., Maeda, T., Ohgi, H., Hosono, E., Imai, H. and Kim, S.H., 2004. Hydrothermal routes to prepare nanocrystalline mesoporous SnO_2 having high thermal stability. *Langmuir*, *20*(15), pp.6476-6481.
2. Hall, D.L., Wang, A.A., Joy, K.T., Miller, T.A. and Wooldridge, M.S., 2004. Combustion synthesis and characterization of nanocrystalline tin and tin oxide (SnOx, x= 0–2) particles. *Journal of the American Ceramic Society*, *87*(11), pp.2033-2041.
3. Lu, C.H. and Wen, M.C., 2008. Synthesis of nanosized TiO_2 powders via a hydrothermal microemulsion process. *Journal of Alloys and Compounds*, *448*(1-2), pp.153-158.
4. Masuda, Y., 2012. Crystal growth of tin oxide nano-sheets in aqueous solutions and time variation of N_2 adsorption characteristics. *Progress in Crystal Growth and Characterization of Materials*, *58*(2-3), pp.106-120.

5. Patil, G.E., Kajale, D.D., Gaikwad, V.B. and Jain, G.H., 2012. Preparation and characterization of SnO_2 nanoparticles by hydrothermal route. *International Nano Letters*, *2*(1), p.17.
6. Song, K.C. and Kang, Y., 2000. Preparation of high surface area tin oxide powders by a homogeneous precipitation method. *Materials Letters*, *42*(5), pp.283-289.
7. Susana, M.M., Oana, S., Stefania, Z. and Maria, Z., 2011. Advanced SnO_2-Based Ceramics: Synthesis, Structure, Properties. In *Advances in Ceramics-Synthesis and Characterization, Processing and Specific Applications*. InTech. 101-126.
8. Rockenberger, J., Zum Felde, U., Tischer, M., Tröger, L., Haase, M. and Weller, H., 2000. Near edge X-ray absorption fine structure measurements (XANES) and extended X-ray absorption fine structure measurements (EXAFS) of the valence state and coordination of antimony in doped nanocrystalline SnO_2. *The Journal of Chemical Physics*, *112*(9), pp.4296-4304.
9. Waseda, Y., E. Matsubara, and K. Shinoda, *X-Ray diffraction crystallography introduction, examples and solved problems*. 2011, Springer: Berlin,Heidelberg, New York. p. 125.
10. Tan, L., Wang, L. and Wang, Y., 2011. Hydrothermal synthesis of SnO_2 nanostructures with different morphologies and their optical properties. *Journal of Nanomaterials*, *2011*, p.10.
11. Sakai, G., Miura, N. and Yamazoe, N., 2000. Preparation of stabilized nanosized tin oxide particles by hydrothermal treatment. *Journal of the American Ceramic Society*, *83*(12), pp.2983-2987.
12. Bagheri-Mohagheghi, M.M., Shahtahmasebi, N., Alinejad, M.R., Youssefi, A. and Shokooh-Saremi, M., 2008. The effect of the post-annealing temperature on the nano-structure and energy band gap of SnO_2 semiconducting oxide nano-particles synthesized by polymerizing–complexing sol–gel method. *Physica B: Condensed Matter*, *403*(13-16), pp.2431-2437.
13. Hirano, M., Dozono, H. and Kono, T., 2011. Hydrothermal synthesis and properties of solid solutions and composite nanoparticles in the TiO_2–SnO_2 system. *Materials Research Bulletin*, *46*(9), pp.1384-1390.
14. Wang, Y.X., Sun, J., Fan, X. and Yu, X., 2011. A CTAB-assisted hydrothermal and solvothermal synthesis of ZnO nanopowders. *Ceramics International*, *37*(8), pp.3431-3436.
15. Chiu, H.C. and Yeh, C.S., 2007. Hydrothermal synthesis of SnO_2 nanoparticles and their gas-sensing of alcohol. *The Journal of Physical Chemistry C*, *111*(20), pp.7256-7259.

16. Christensen, P.A., Attidekou, P.S., Egdell, R.G., Maneelok, S. and Manning, D.A.C., 2016. An in situ FTIR spectroscopic and thermogravimetric analysis study of the dehydration and dihydroxylation of SnO_2: the contribution of the (100),(110) and (111) facets. *Physical Chemistry Chemical Physics*, *18*(33), pp.22990-22998.
17. Xu, H., Wakamiya, M. and Kubokawa, Y., 1974. Infrared studies of interaction of oxygen with 2-propanol and acetone adsorbed on MgO and NiO. *Journal of Catalysis*, *34*(1), pp.117-123.
18. Rossi, P.F., Busca, G., Lorenzelli, V., Saur, O. and Lavalley, J.C., 1987. Microcalorimetric and FT-IR spectroscopic study of the adsorption of isopropyl alcohol and hexafluoroisopropyl alcohol on titanium dioxide. *Langmuir*, *3*(1), pp.52 - 58.
19. Arsac, F., Bianchi, D., Chovelon, J.M., Ferronato, C. and Herrmann, J.M., 2006. Experimental Microkinetic Approach of the Photocatalytic Oxidation of Isopropyl Alcohol on TiO_2. Part 1. Surface Elementary Steps Involving Gaseous and Adsorbed C_3HxO Species. *The Journal of Physical Chemistry A*, *110*(12), pp.4202 - 4212.
20. Xu, W., Raftery, D. and Francisco, J.S., 2003. Effect of irradiation sources and oxygen concentration on the photocatalytic oxidation of 2-propanol and acetone studied by in situ FTIR. *The Journal of Physical Chemistry B*, *107*(19), pp.4537 - 4544.
21. Koga, O., Onishi, T. and Tamaru, K., 1980. Adsorption and decomposition of isopropyl alcohol over zinc oxide. Infrared and kinetic study. *Journal of the Chemical Society, Faraday Transactions 1: Physical Chemistry in Condensed Phases*, *76*, pp.19-29.
22. Hussein, G.A., Sheppard, N., Zaki, M.I. and Fahim, R.B., 1989. Infrared spectroscopic studies of the reactions of alcohols over group IVB metal oxide catalysts. Part 1.—Propan-2-ol over TiO_2, ZrO_2 and HfO_2. *Journal of the Chemical Society, Faraday Transactions 1: Physical Chemistry in Condensed Phases*, *85*(7), pp.1723-1741.
23. Resini, C., Montanari, T., Busca, G., Jehng, J.M. and Wachs, I.E., 2005. Comparison of alcohol and alkane oxidative dehydrogenation reactions over supported vanadium oxide catalysts: in situ infrared, Raman and UV–vis spectroscopic studies of surface alkoxide intermediates and of their surface chemistry. *Catalysis Today*, *99*(1), pp.105-114.
24. Fuente, S.A., Ferretti, C.A., Domancich, N.F., Díez, V.K., Apesteguía, C.R., Di Cosimo, J.I., Ferullo, R.M. and Castellani, N.J., 2015. Adsorption of 2-propanol on MgO surface: A combined experimental and theoretical study. *Applied Surface Science*, *327*, pp.268-276.
25. Teterycz, H., Klimkiewicz, R. and Łaniecki, M., 2004. Study on physico-chemical properties of tin dioxide based gas sensitive materials used in condensation reactions of n-butanol. *Applied Catalysis A: General*, *274*(1-2), pp.49-60.

26. Rahmelow, K.I.M. and Hubner, W., 1997. Infrared spectroscopy in aqueous solution: Difficulties and accuracy of water subtraction. *Applied Spectroscopy*, *51*(2), pp.160-170.
27. Harrison, P.G. and Willett, M.J., 1989. Tin oxide surfaces. Part 20.—Electrical properties of tin (IV) oxide gel: nature of the surface species controlling the electrical conductance in air as a function of temperature. *Journal of the Chemical Society, Faraday Transactions 1: Physical Chemistry in Condensed Phases*, *85*(8), pp.1921-1932.
28. Maier, J. and Göpel, W., 1988. Investigations of the bulk defect chemistry of polycrystalline tin (IV) oxide. *Journal of solid state chemistry*, *72*(2), pp.293-302.
29. Nütz, T., Felde, U.Z. and Haase, M., 1999. Wet-chemical synthesis of doped nanoparticles: blue-colored colloids of n-doped SnO_2: Sb. *The Journal of chemical physics*, *110*(24), pp.12142-12150.
30. Panayotov, D.A., Burrows, S.P. and Morris, J.R., 2012. Infrared spectroscopic studies of conduction band and trapped electrons in UV-photoexcited, H-atom n-doped, and thermally reduced TiO_2. *The Journal of Physical Chemistry C*, *116*(7), pp.4535-4544.
31. Summitt, R. and Borrelli, N.F., 1965. Infrared absorption in single crystal stannic oxide. *Journal of Physics and Chemistry of Solids*, *26*(5), pp.921-925.
32. Ghiotti, G., Chiorino, A., Martinelli, G. and Carotta, M.C., 1995. Moisture effects on pure and Pd-doped SnO_2 thick films analysed by FTIR spectroscopy and conductance measurements. *Sensors and Actuators B: Chemical*, *25*(1-3), pp.520-524.
33. Rivallan, M., Fourré, E., Aiello, S., Tatibouët, J.M. and Thibault-Starzyk, F., 2012. Insights into the Mechanisms of Isopropanol Conversion on γ-Al_2O_3 by Dielectric Barrier Discharge. *Plasma Processes and Polymers*, *9*(9), pp.850-854.
34. Rodrigues, A., Tatibouët, J.M. and Fourré, E., 2016. Operando DRIFT spectroscopy characterization of intermediate species on catalysts surface in VOC removal from air by non-thermal plasma assisted catalysis. *Plasma Chemistry and Plasma Processing*, *36*(4), pp.901-915.
35. Miyata, H., Wakamiya, M. and Kubokawa, Y., 1974. Infrared studies of interaction of oxygen with 2-propanol and acetone adsorbed on MgO and NiO. *Journal of Catalysis*, *34*(1), pp.117-123.
36. Mehrotra, R.C. and Batwara, J.M., 1970. Preparation and some reactions of alkoxides of gadolinium and erbium. *Inorganic Chemistry*, *9*(11), pp.2505-2510.
37. Zaki, M.I. and Sheppard, N., 1983. An infrared spectroscopic study of the adsorption and mechanism of surface reactions of 2-propanol on ceria. *Journal of Catalysis*, *80*(1), pp.114-122.

38. Greenler, R.G., 1962. Infrared study of the adsorption of methanol and ethanol on aluminum oxide. *The Journal of Chemical Physics*, *37*(9), pp.2094-2100.
39. Morishige, K., Kittaka, S. and Morimoto, T., 1980. The thermal desorption of surface hydroxyls on tin (IV) oxide. *Bulletin of the Chemical Society of Japan*, *53*(8), pp.2128-2132.
40. Morimoto, T., Yokota, Y. and Kittaka, S., 1978. Adsorption anomaly in the system tin (IV) oxide-water. *The Journal of Physical Chemistry*, *82*(18), pp.1996-1999.
41. Morimoto, T., Kiriki, M., Kittaka, S., Kadota, T. and Nagao, M., 1979. Differential heat of chemisorption. 3. Chemisorption of water on tin (IV) oxide. *Journal of Physical Chemistry*, *83*(21), pp.2768-2770.
42. Stein, S. E., "Infrared Spectra", NIST Chemistry WebBook, in NIST Standard Reference Database Number 69, Eds. P.J. Linstrom and W.G. Mallard, National Institute of Standards and Technology, Gaithersburg MD, 20899, http://webbook.nist.gov, (retrieved November 15 2017).
43. Hasan, M.A., Zaki, M.I. and Pasupulety, L., 2003. Oxide-catalyzed conversion of acetic acid into acetone: an FTIR spectroscopic investigation. *Applied Catalysis A: General*, *243*(1), pp.81-92.
44. Martin, P.E. and Barker, E.F., 1932. The infrared absorption spectrum of carbon dioxide. *Physical Review*, *41*(3), p.291.

Chapter 5. An in-situ Fourier Transform InfraRed study of the thermally and plasma driven of isopropyl alcohol conversion over cerium oxide

5.1. Introduction

This chapter reports the application of in-situ reflectance Fourier Transform Infrared spectroscopy to the study of the thermally and plasma driven reaction of IsoPropyl Alcohol (IPA) at CeO_2 coated Macor/Ti mesh using Fourier Transform Infrared spectroscopy.

5.2. XRD data of CeO_2 nanopowders

A typical X-ray diffraction pattern of the CeO_2 nanopowder employed in the work described in this chapter is shown in figs 5.1(a) and (b). The lines at 2Θ=28.5º, 33.07º, 47.5º and 56.3º are consistent with the single phase of the crystal system type cubic CeO_2 (cerium oxide); cerianite, syn; 04-005-4553 which was obtained from the ICDD database and in agreement with the literature [1-4]. No peaks attributable to other phases were observed. The average particle size was found to be ca. 47 nm, calculated from the peaks at 2Θ=28.5º, 33.07º, 47.5º and 56.3º using Scherrer's equation as discussed in Chapter 2.

Cerium oxide was chosen as the third catalyst for study because of its well-known catalytic activity with respect to the dehydration and dehydrogenation of IPA [5][6]. Further, it has a high dielectric constant ε_r = 24.5 [7] and is relatively thermally stable [5][6]. CeO_2 also finds application as an electrolyte in Solid Oxide Fuel Cells (SOFCs) [8] and in electrochemical sensors [1].

5.3. Infrared studies of the thermally-driven process

5.3.1. Ceria in a nitrogen flow (Sample A) from 25 °C to 600 °C

It is well-known that CeO_2 adsorbs CO_2 from the air to form adsorbed carbonates and bicarbonate [9], and hence it was decided to investigate the effect of pre-heating CeO_2 on the presence of such adsorbed species and hence the conversion of IPA. Further, as DRIFTS spectroscopy generally requires the dilution of the sample with an inert diluent, in this case KBr, it was also decided to check that this material was actually inert by studying pure CeO_2.

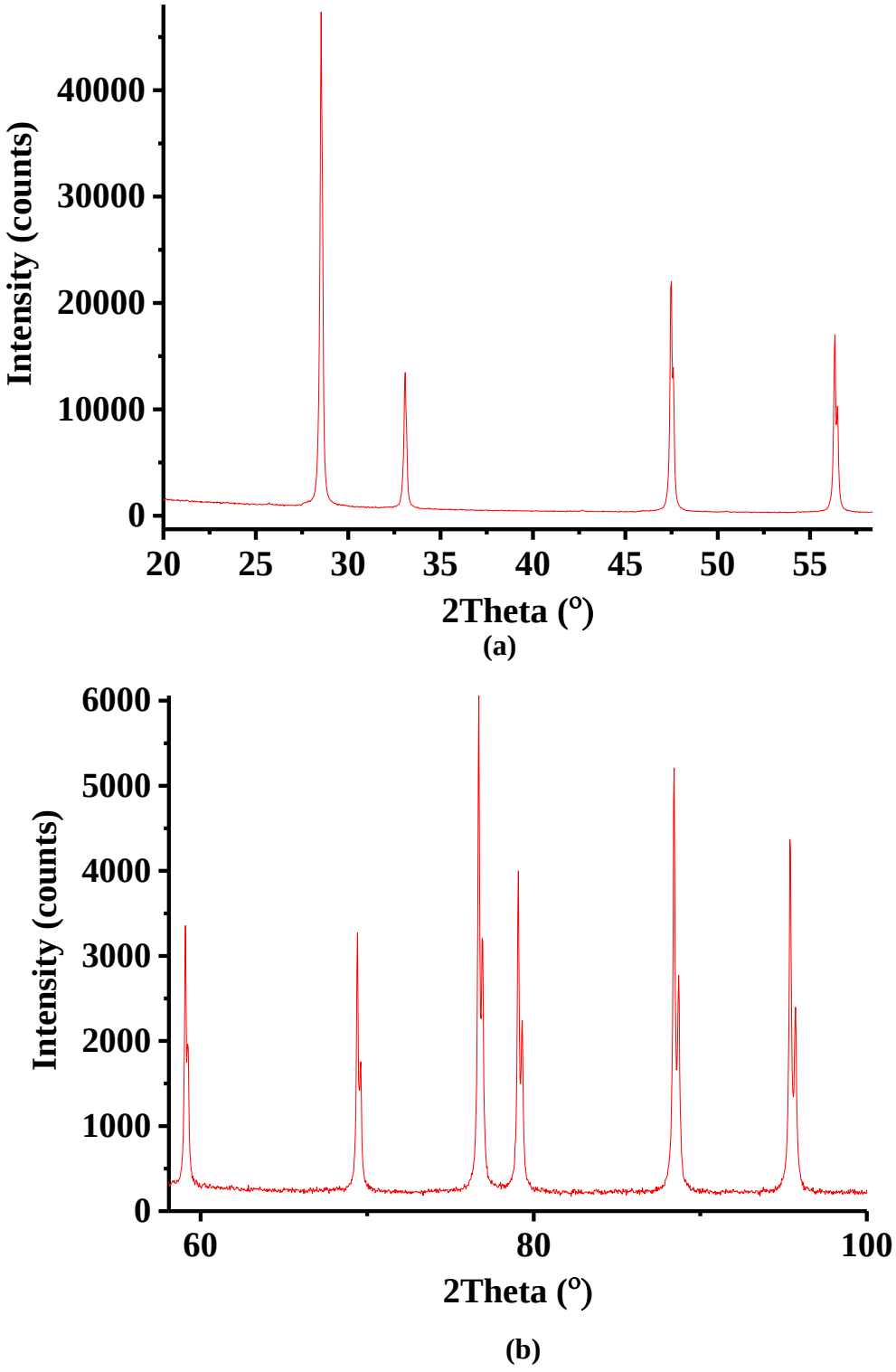

Figure 5.1. A typical XRD pattern of the CeO_2 nanopowder samples employed in this work showing 2Θ = (a) 20 to 58° and (b) 58 to 100°.

Thus, four samples of CeO_2 from the same batch were employed: for three of the samples, 20 mg of sample was mixed with 80 mg of spectroscopic grade KBr and FTIR spectra collected as described below in a pure N_2 atmosphere: this sample is referred to as A. Sample B was also

mixed with KBr as for sample A and spectra collected in a N_2+IPA atmosphere (sample B1), the experiment was then repeated using the same sample, now designated as B2, on the following day. Sample C was employed as follows: the sample was heated in flowing N_2 at a rate of 5 ºC per minute up to 600 ºC and held at this temperature for 2 hours before being allowed to cool in flowing nitrogen for 3 days. The sample was then heated in N_2+IPA and spectra collected as described below (sample C1). The reflectance accessory was then flushed with nitrogen and the sample left under flowing nitrogen overnight. The previous day's experiment was then repeated using N_2+IPA (sample C2). The experiments utilising sample D were an exact repeat of those using sample C except pure CeO_2 was employed. Table 5.1 summarizes the composition of the various samples and the experimental parameters employed.

Exp.	Sample	Comp.[a]	Pretreatment	Atmosphere	Comments
1	A	M	None	N_2	
2	B1	M	None	N_2 + IPA	After experiment, sample left overnight in N_2
3	B2	M	None	N_2 + IPA	Repeat of exp. 2 using the same sample
4	C1	M	Heated in flowing N_2 to 600˚C, held for 2 hours then cooled in flowing N_2 for 3 days	N_2 + IPA	After experiment, left overnight in flowing N_2
5	C2	M	None	N_2 + IPA	Repeat of exp. 4 using the same sample
6	D1	P	Heated in flowing N_2 to 600˚C, held for 2 hours then cooled in flowing N_2 for 3 days	N_2 + IPA	After experiment, left overnight in flowing N_2
7	D2	P	None	N_2 + IPA	Repeat of exp. 6 using the same sample

[a] *M = 20 mg CeO_2+80 mg KBr, P = pure CeO_2.*

Table 5.1. The samples and experimental conditions employed in the thermal FTIR experiments.

For clarity, only the spectra from samples A, B1 and D2 are generally presented below as they exemplify the trends observed. The experiments spanned 12 months and, as can be seen, the various trends observed were reproducible.

Spectra were recorded in reflectance mode: thus a reference spectrum (S_R, 100 co-added scans and averaged scans at 4 cm^{-1} resolution, ca. 2 minutes per scanset) was collected from a pure KBr sample at 25 °C. The KBr was then replaced with 20 mg CeO_2 + 80 mg KBr or 100 mg CeO_2 and a second reference spectrum (S_R, 100 co-added and averaged scans at 4 cm^{-1} resolution, ca. 2 minutes per scanset) taken under the same conditions. The chamber was then isolated from the gas flow and a sample spectrum Ss (S_S, 100 co-added and averaged scans at 4 cm^{-1} resolution, ca. 2 minutes per scanset) collected at 25 ºC. The temperature of the sample was then increased at 5 °C min^{-1} and a further sample spectrum collected at 50 ºC, after which spectra S_S were collected every 50 ºC up to 600 ºC. The spectra were manipulated as:

$$\text{Reflectance } R_T = (S_S/S_R) \qquad (5.1)$$

This method was chosen rather than the Kubelka-Munk manipulation as it was found that the latter gave erroneous results with some samples, in agreement with the literature [10]. Spectra produced according to the manipulation shown in equation (5.1) have bands pointing up ($R_T > 1$) due to the loss of absorbing species in S_S with respect to S_R, and peaks pointing down (to $R_T < 1$) due to the gain of absorbing species. This is of course the opposite of that described above for the absorbance difference spectra. In order to remove unchanging absorptions, spectra were subtracted from each other with appropriate subtraction factors as specified.

In order to establish the identity of the surface species before IPA was added, thermal ramps in nitrogen were first analysed. Figure 5.2(a) shows the spectrum collected at 25 °C during an experiment in which the temperature of sample A was ramped from 25 °C to 600 °C and spectra collected at regular intervals (referenced to pure KBr) in a static N_2 atmosphere, and fig. 5.2(b) shows all the spectra from the experiment. As can be seen from the figures, the spectra are dominated by strong absorptions due to hydrogen-bonded Ce-OH groups (2250 – 4000 cm^{-1} [5]) and various forms of adsorbed carbonate (900 – 1750 cm^{-1} [6][11-13]). In addition, the sharp feature at 3690 cm^{-1} in fig. 5.2(a) may be attributed to isolated OH [5] i.e. Ce-OH groups not hydrogen bonded. The band at 2340 cm^{-1} in figs. 5.2(a) and (b) may be attributed to the asymmetric stretch of physisorbed CO_2 [14][15]: interestingly, the band was present even up to 600 °C, see fig. 5.2(b). This was unexpected, and may indicate that the CO_2 was present in

interstitial voids in the CeO_2 [16], see discussion below. Figure 5.2(c) compares the spectra collected at 25 °C and 200 °C in fig. 5.2(b) over the spectral region in which the physisorbed CO_2 occurs: both spectra were offset to $R_T = 1$ at 2150 cm^{-1}, and the spectrum collected at 25 °C enhanced by a factor of 1.3 to facilitate comparison. The asymmetric shape of the bands suggests the CO_2 is physisorbed on a number of different sites [17]: the band maxima of the two features were the same and, as expected, the band at 200 °C was broader than that at 25 °C suggesting some rotational excitation. The small changes in band shape on heating may suggest some redistribution among surface sites.

The adsorption of CO_2 on CeO_2 has been well-studied, and a summary of the assignments of various features observed in the IR studies is presented in table 5.2. In terms of the temperature at which the various forms of carbonate desorb or convert, Slostowski et. al. [17] divides the adsorbates into weakly adsorbed (hydrogen carbonate and bridged) which can be removed at room temperature by flowing nitrogen over the sample, and strongly adsorbed (bidentate, monodentate and polydentate) which require a temperature of up to 500 °C to remove them from the surface.

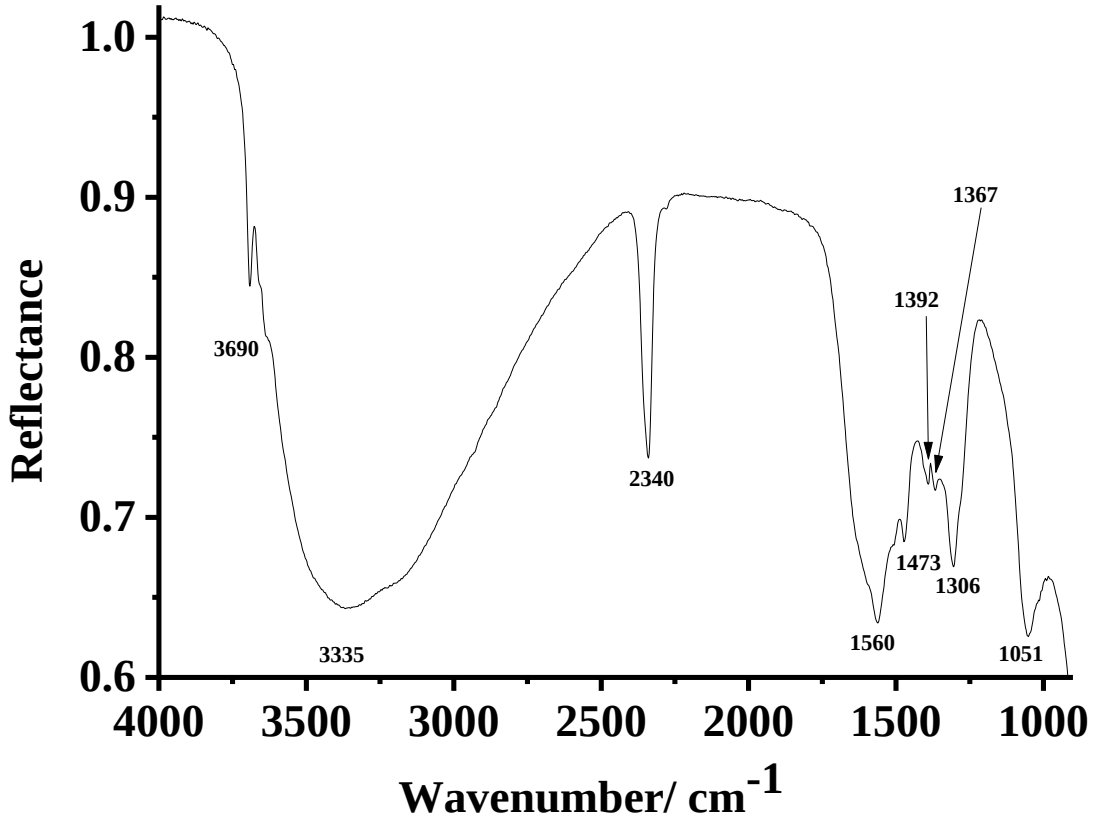

(a)

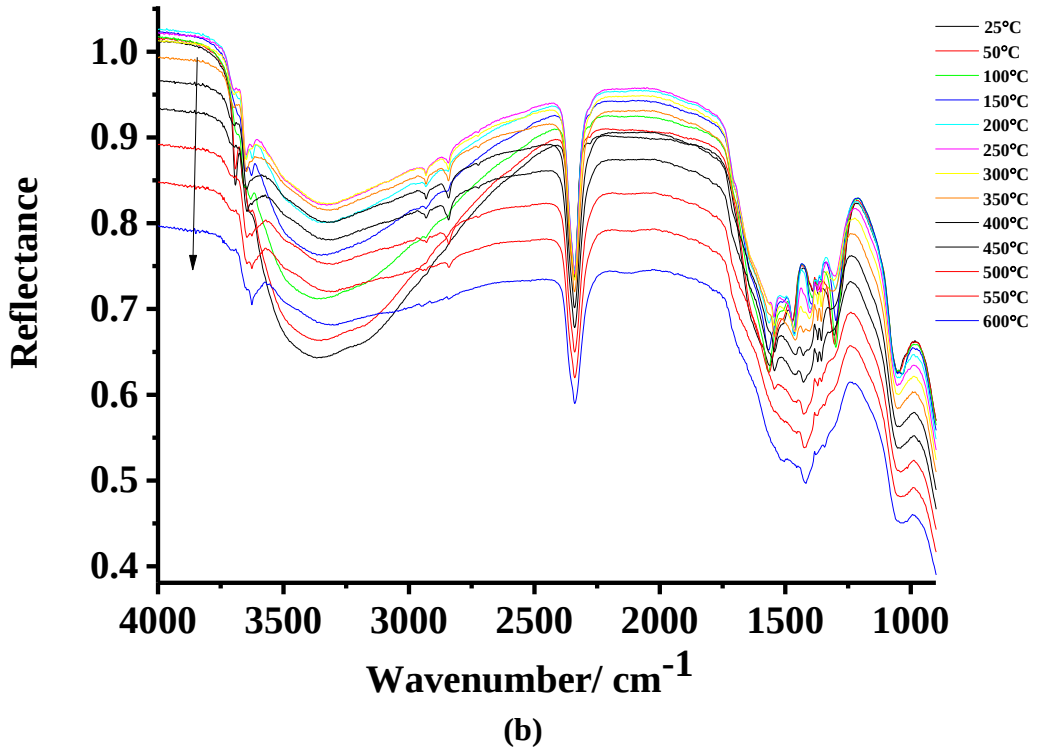

(b)

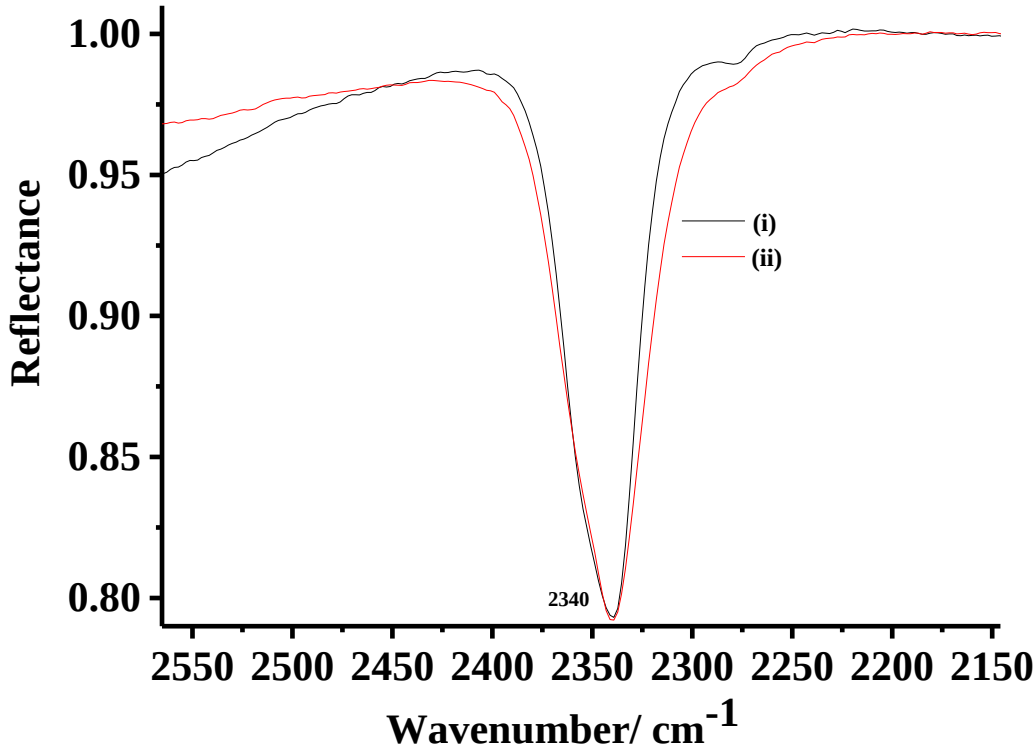

(c)

Figure 5.2. Spectra (4 cm^{-1} resolution, 100 co-added and averaged scans, 120 second per scanset) collected as a function of temperature during an experiment in which the temperature of 20 mg CeO_2 + 80 mg KBr was ramped from 25 °C to 600 °C in a static N_2 atmosphere: the spectrum collected at 25 °C using KBr in the same atmosphere was employed as the reference. (a) The spectrum taken at 25 °C, (b) all the spectra collected during the experiment and (c) the spectra taken at (i) 25 °C and (ii) 200 °C showing the CO_2 asymmetric stretch region: the spectrum in (i) was scaled up by 1.3 and the latter spectrum (ii) was moved up 0.004 to aid comparison. Both spectra were offset to 1 for comparison.

Adsorbed species		[13]	[6]		[12]	[11]
Bicarbonate	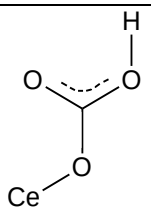	1600 1398 1215	I 3617 1599 1413 1218 1025 823	II 3617 1613 1391 1218 1045 823	 1404 1217	1670 – 1695 1310 – 1338 650 – 970
Monodentate	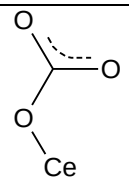	 1465 1353	1504 1351		1507	 1454 1348 1062 854
Bridged	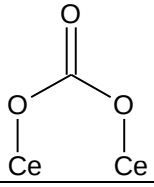	 1651 1242	1736 1135			1728 1396 1219 1132
Bidentate	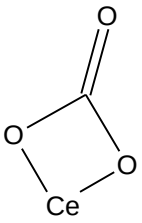	1580 1292	1567 1289 1014 856		1570 1287 1011 856	1562 1286 1028 854
Polydentate	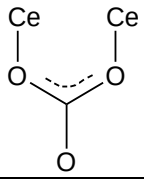	- -	1462 1353 1066 854		1476 1367	

Table 5.2. Assignments of the various carbonaceous species from the adsorption of CO_2 on CeO_2.

Yoshikawa and co-workers [18] present a somewhat more detailed and different picture: with a temperature of 200 °C required for desorption of bicarbonate, 300 °C for monodentate and bidentate carbonate and 450 °C for the polydentate form. Intuitively, however, it may be expected that those forms of carbonate with multiple metal-oxygen bonds (eg. bridged, bidentate and polydentate) would be more strongly bonded to the surface than monodentate carbonate and bicarbonate.

Figure 5.3(a) shows the change in mass during a TGA experiment as discussed in Chapter 2, in which a sample of pure CeO_2 was heated in nitrogen to 600 °C, allowed to cool and the change in its mass recorded as a function of temperature. This was repeated a further two times during

the same experiments. Figure 5.3(b) shows the m/z = 18, 32 and 44 responses recorded during the first heating of the sample along with the change in mass (note scaling factors). As can be seen from the figures, the sample loses mass over the full temperature range, but most particularly between 25 and 150 °C and 300 and 400 °C; there is also a steady evolution of O_2 over the full range, and of water up to ca. 400 °C.

CO_2 was evolved in two distinct regions, 75 – 150 °C and 300 – 400 °C, the latter in broad agreement with the postulated existence of adsorbed carbonaceous species having various thermal stabilities [17][18]. Figure 5.3(c) shows the mass change and the m/z = 18, 32 and 44 responses recorded during the second heating of the sample (run 2) in fig. 5.3(a): the responses are very similar to those observed during run 1, suggesting that, on being stored overnight in air, CO_2 and water re-adsorbed onto the sample surface. Figure 5.3(d) shows the mass change and the m/z = 18, 32 and 44 responses recorded during run 3 after storing in nitrogen overnight: as may be seen from the figure, whilst there is no evolution of O_2 or CO_2, dehydration and/or dehydroxylation of the sample still took place [19], although with about 60 % the amount of evolved H_2O. This is associated with a very small mass loss of 0.05 % compared with 0.15 % for the previous two runs.

Figures 5.4(a) – (d) show the spectra in fig. 5.2(b) presented as difference spectra reflecting, in broad terms, the temperature ranges identified in the TGA experiment: thus fig. 5.4(a) shows the spectrum collected at 25 °C subtracted from those taken at 50 and 100 °C, fig. 5.4(b) the spectrum taken at 100 °C subtracted from those up to 250 °C, fig. 5.4(c) the spectrum collected at 250 °C subtracted from the 350 and 400 °C spectra and (d) the spectrum taken at 400 °C subtracted from those collected up to 600 °C.

From figs. 5.4(a) – (d) it can be seen that there is a broad loss extending from ca. 2250 to 3750 cm^{-1} accompanied by a band at ca. 1642 cm^{-1}: by analogy to SnO_2 [19], this may be attributed to the loss of hydrogen-bonded Ce-OH groups via the dehydration and possibly dehydroxylation of the CeO_2. There are also the loss and gain of sharp features above 3500 cm^{-1} due to the redistribution/loss of isolated Ce-OH groups [11].

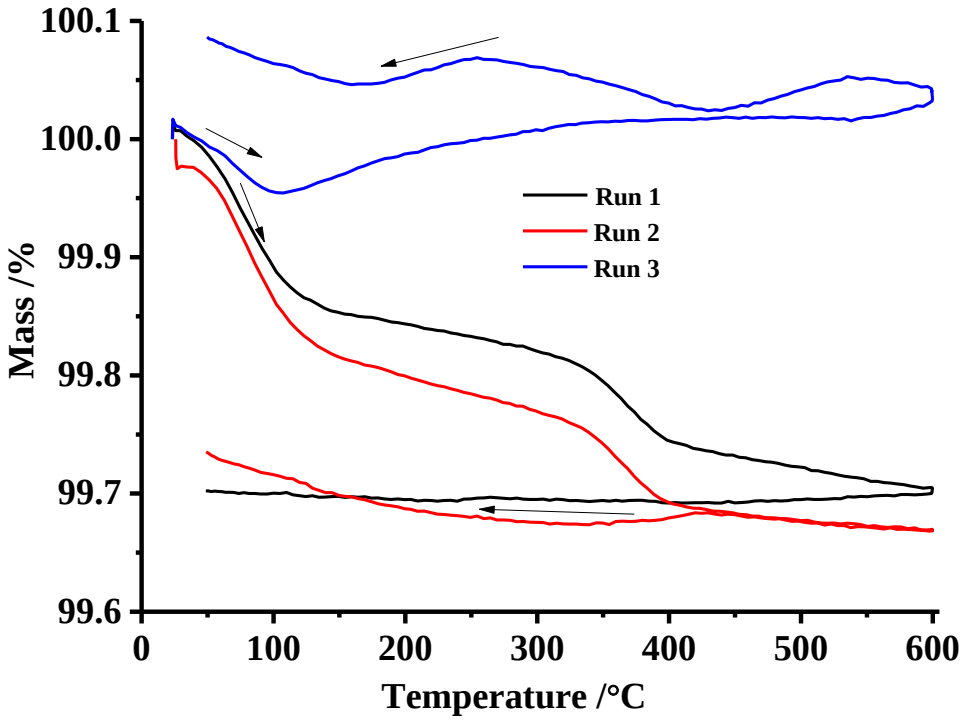
100.1
100.0
99.9
99.8
99.7
99.6
Mass /%
0
100
200
300
400
500
600
Temperature /°C
Run 1
Run 2
Run 3

(a)

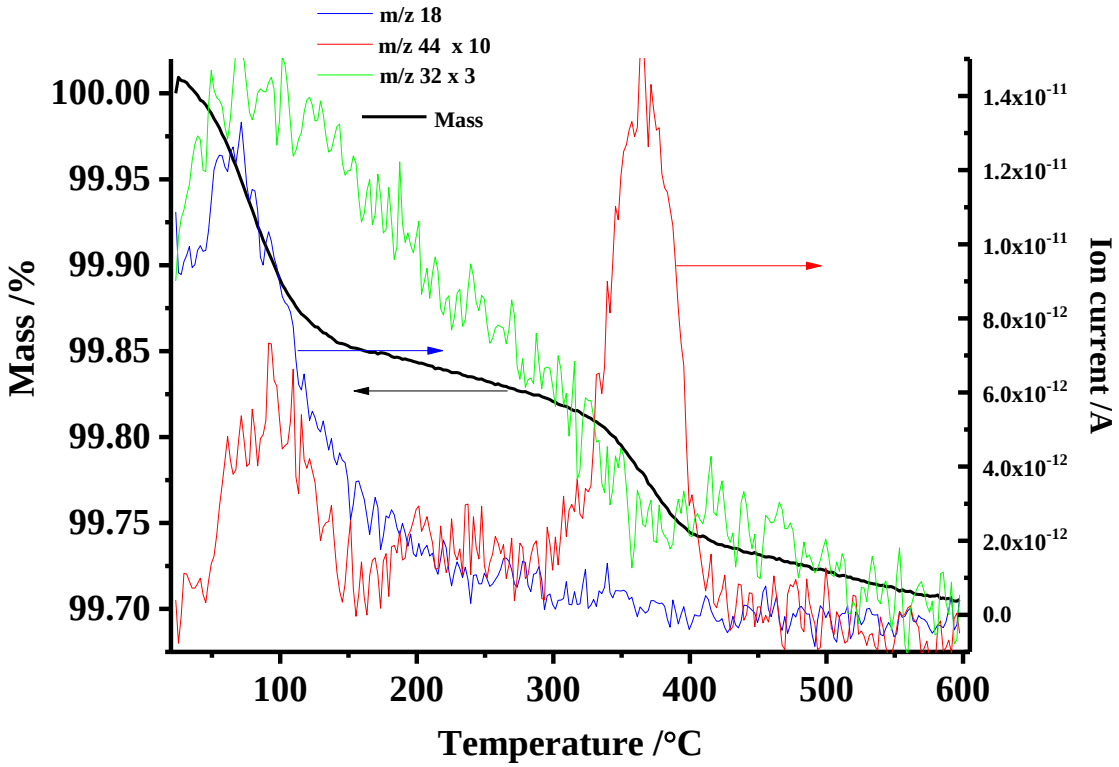
m/z 18
m/z 44 x 10
m/z 32 x 3
Mass
100.00
99.95
99.90
99.85
99.80
99.75
99.70
Mass /%
100
200
300
400
500
600
Temperature /°C
1.4x10-11
1.2x10-11
1.0x10-11
8.0x10-12
6.0x10-12
4.0x10-12
2.0x10-12
0.0
Ion current /A

(b)

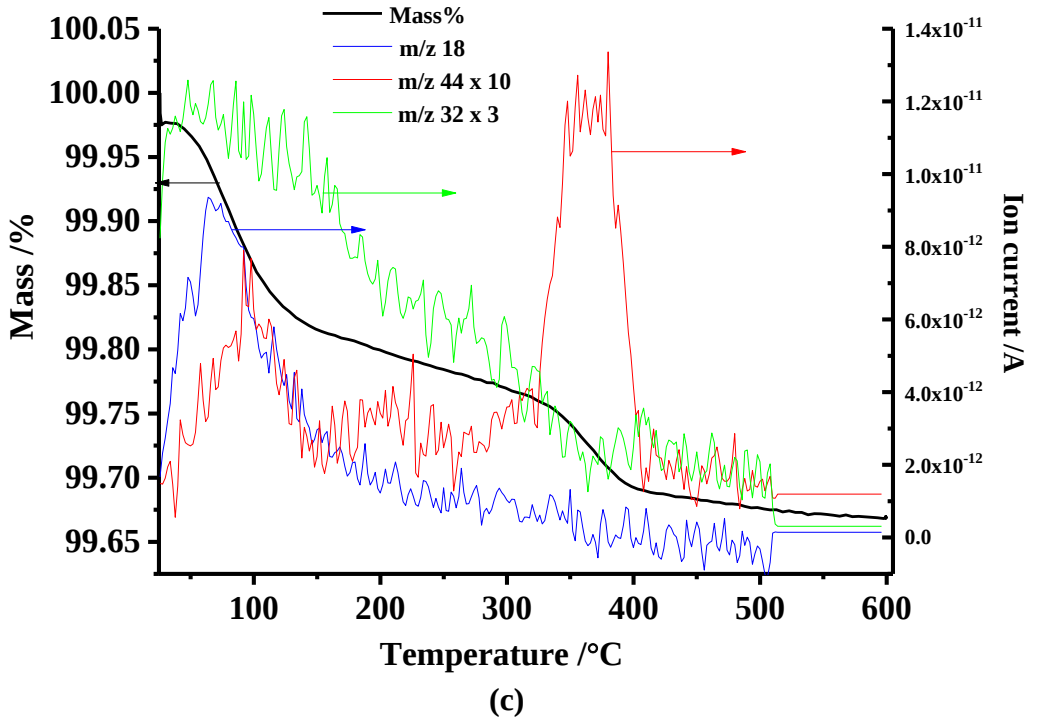

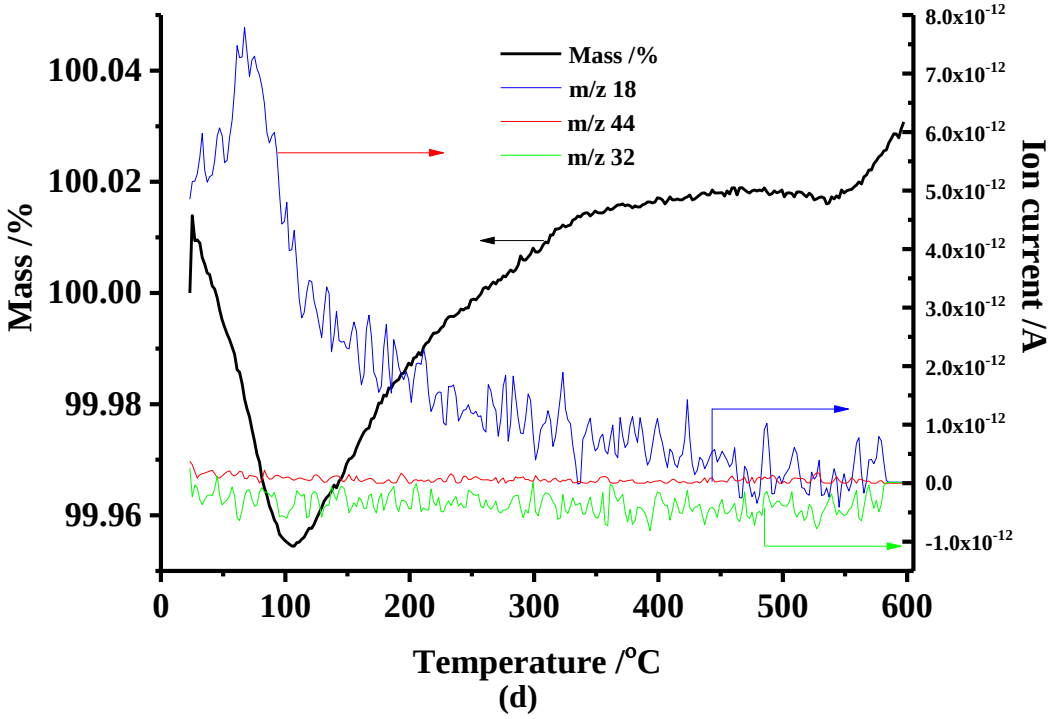

Figure 5.3. (a) The thermogravimetric response of 55.5 mg of CeO_2, heated in 40 cm^3 min^{-1} flowing nitrogen 5 °C min^{-1} from room temperature to 600 °C (Run 1). The sample was held at 600 °C for 10 minutes and then cooled at 5 °C min^{-1} to room temperature. (b) & (c) The m/z = 18, 32 and 44 responses recorded during the first and second heating cycles (Runs 1 and 2, respectively) of the sample in (a): the m/z = 32 responses were enhanced by a factor of 3 and the m/z = 44 responses by a factor of 10. (d) The m/z = 18, 32 and 44 responses recorded during the third heating of the sample in (a), Run 3. Run 1 was carried out on day 1 and the sample left in air overnight. Run 2 was carried out on day 2 and the sample left in flowing nitrogen overnight and run 3 carried out the following day. The ion current plots were offset to facilitate comparison.

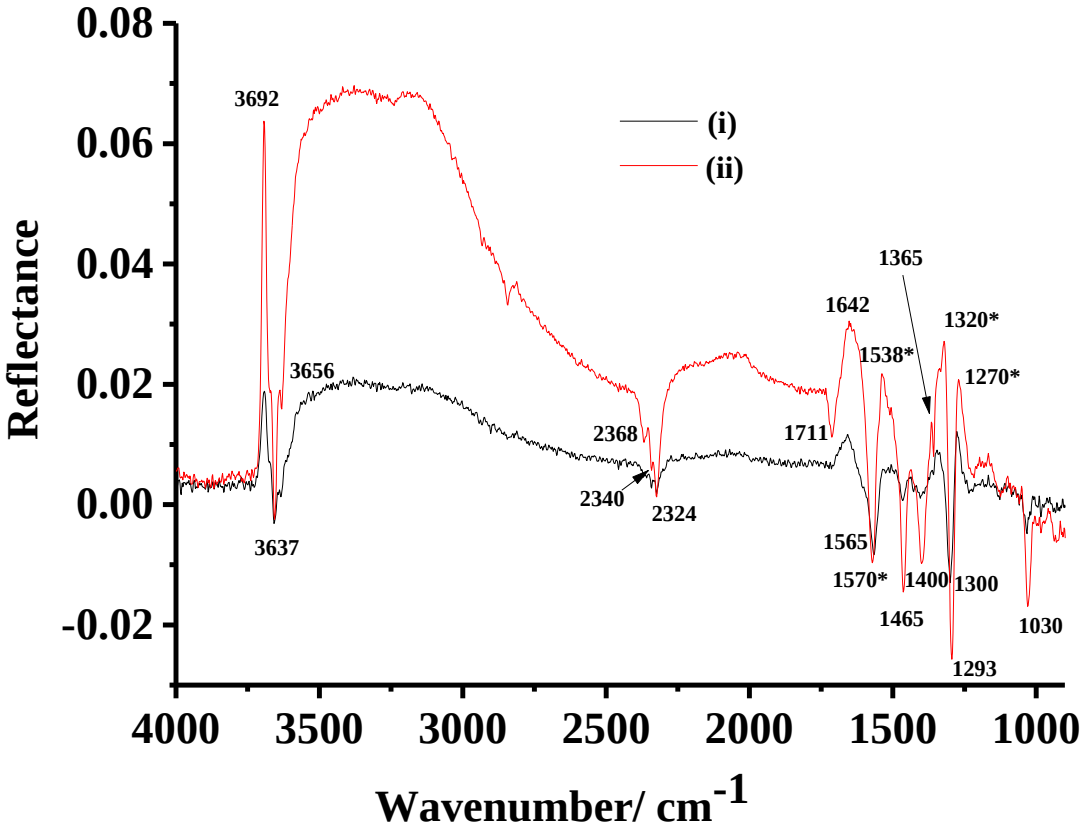
0.08
0.06
0.04
0.02
0.00
-0.02
Reflectance
(i)
(ii)
3692
3656
3637
2368
2340
2324
1711
1642
1365
1538*
1320*
1270*
1565
1570*
1400
1300
1465
1030
1293
4000
3500
3000
2500
2000
1500
1000
Wavenumber/ cm-1

(a)

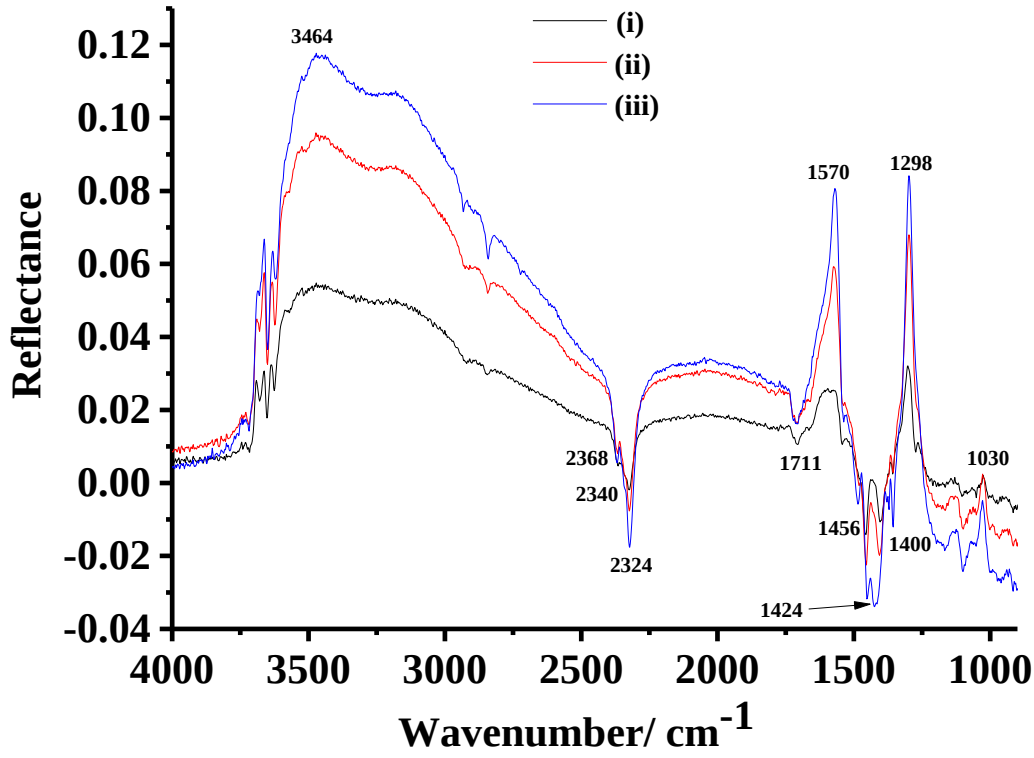
0.12
0.10
0.08
0.06
0.04
0.02
0.00
-0.02
-0.04
Reflectance
(i)
(ii)
(iii)
3464
2368
2340
2324
1711
1570
1298
1030
1456
1400
1424
4000
3500
3000
2500
2000
1500
1000
Wavenumber/ cm-1

(b)

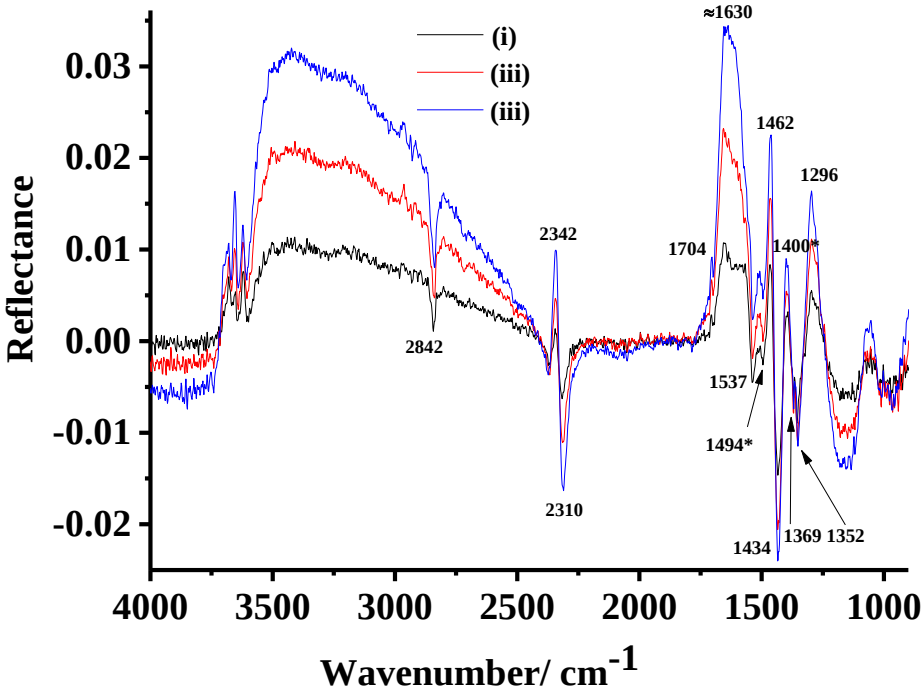

(c)

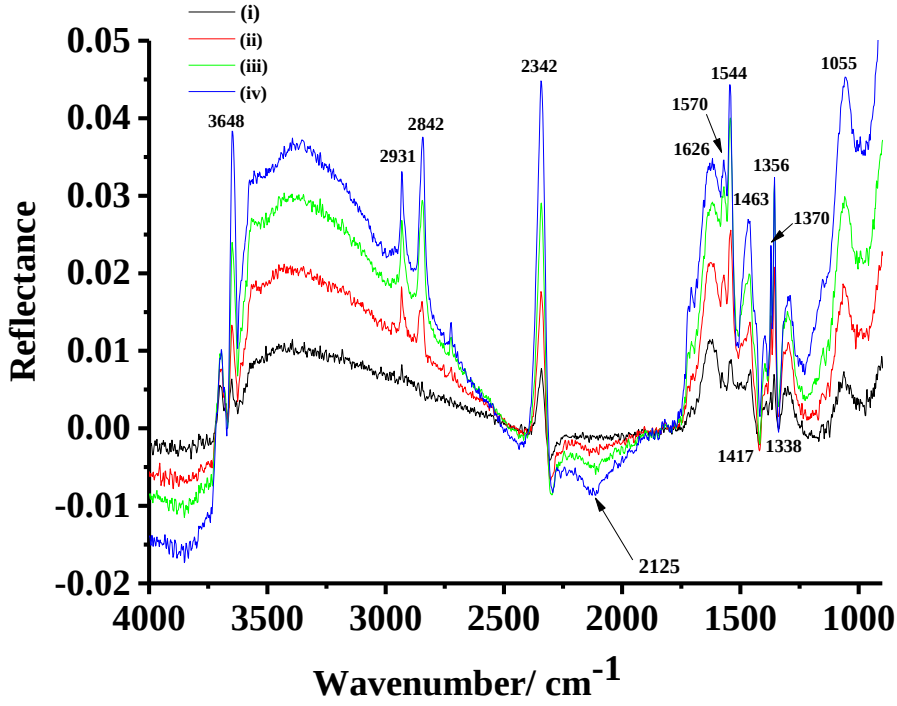

(d)

Figure 5.4. The spectra in fig. 5.2(b) with: (a) the spectrum taken at 25 °C subtracted from those collected at (i) 50 and (ii) 100 °C; (b) the spectrum taken at 100 °C subtracted from those collected at (i) 150, (ii) 200 and (iii) 250 °C; (c) the spectrum taken at 250 °C subtracted from those collected at (i) 300, (ii) 350 and (iii) 400 °C, the spectra were moved up by 0.009, 0.025 and 0.050, respectively and (d) the spectrum taken at 400 °C subtracted from those collected up to 600 °C: the spectra collected at (i) 450, (ii) 500, (iii) 550 and (iv) 600 °C were moved up by 0.030, 0.069, 0.110 and 0.155, respectively. Species gains are negative, losses positive in these difference reflectance spectra.

In figs. 5.4(a) and (b) there are gain features in the region of the band due to physisorbed CO_2: the absence of corresponding loss features in the same region suggest that there is a conversion of adsorbed carbonate/ bicarbonate species to CO_2 and that these molecules are distributed across different sites. It may also be the case that some of the adsorbed carbonates, e.g. bicarbonates [17], are desorbing as CO_2.

Due to its relatively high frequency, the 1711 cm^{-1} gain feature in figs. 5.4(a) and (b) is most likely due to bridged carbonate (see table 5.2). The peaks at 1570 and 1298 cm^{-1} in the same figures (the 1298 cm^{-1} feature appears at 1293 cm^{-1} in fig. 5.4(a) due to distortion by the loss features either side) may be attributed to bidentate carbonate [6][11 – 13]: they are gained up to 100 °C and then lost between 100 and 250 °C.

Over the temperature range between 300 and 400 °C, the physisorbed CO_2 band is bipolar, suggesting the transfer of more loosely bound CO_2 to sites where the CO_2 is more strongly adsorbed. At higher temperatures, there is a marked loss of physisorbed CO_2 (also clear in fig. 5.2(c)) presumably due to diffusion out of the voids and desorption into the gas phase: the amount of CO_2 involved is too low for the corresponding gain features due to gas phase CO_2 to be observed.

The gain feature at ca. 2125 cm^{-1} in fig. 5.4(d) has been attributed to CO adsorbed at Ce^{3+} sites: however, this absorption has also been observed at reduced CeO_2 produced in the absence of carbonaceous impurities etc and hence was assigned instead to the $^2F_{5/2} \rightarrow {}^2F_{7/2}$ electronic transition of Ce^{3+} ions. This transition is strictly forbidden, but becomes partially allowed by crystal field effects involving surrounding O vacancies [20]: for example, it has been postulated that two Ce^{3+} species are associated with an O vacancy surrounded by large interstitial voids [16].

Overall, from figs. 5.4(a) to (d) it is clear that heating the CeO_2 causes a redistribution of the surface carbonate/bicarbonate species, with some apparently diffusing into the voids. Comparing the low intensities of the various features below 1800 cm^{-1} in figs. 5.4(a) – (d) to those in the spectra in fig. 5.2(b), however, shows that the amount of adsorbed species is small. Further, given the very wide variation in the band assignments in table 5.2, it is also clear that assigning the various features below 1800 cm^{-1} in any detail to specific forms of adsorbed carbonate or bicarbonate could be of limited validity. Hence, in the discussion below, figs.

5.4(a) – (b) are employed primarily to identify bands associated only with adsorbed carbonate and, more particularly, not associated with the reaction of IPA at the CeO_2.

5.3.2. All samples: 100 °C

Figures 5.5(a) – (d) show the spectra collected using sample A at 100, 250, 400 and 600 °C in figs. 5.4(a) – (d) along with the spectra collected in analogous experiments using samples B1 and D2. Sample A is representative of unpretreated CeO_2 heated in N_2, sample B1 of unpretreated CeO_2 heated in N_2 and IPA, and sample D2 of CeO_2 that has been pretreated by heating several times (from the data obtained using all samples, the KBr employed as a diluent appears to have no effect) in N_2 and IPA.

From the 100° – 25 °C spectra in fig. 5.5(a) it can be seen that there are marked differences between the spectra collected from sample A (N_2 only) and B1 (N_2 + IPA) on the one hand, and sample D2 (N_2 +IPA) on the other. Thus, B1 shows the same interchange of adsorbed carbonaceous species as sample A, except with some reduction in intensity of these species (this can be most clearly seen by comparing the 1293 and 1460 cm^{-1} gain features in the spectra of samples A and B1) whilst the intensities of the band at 1711 cm^{-1} due to the formation of bridging carbonate are approximately the same.

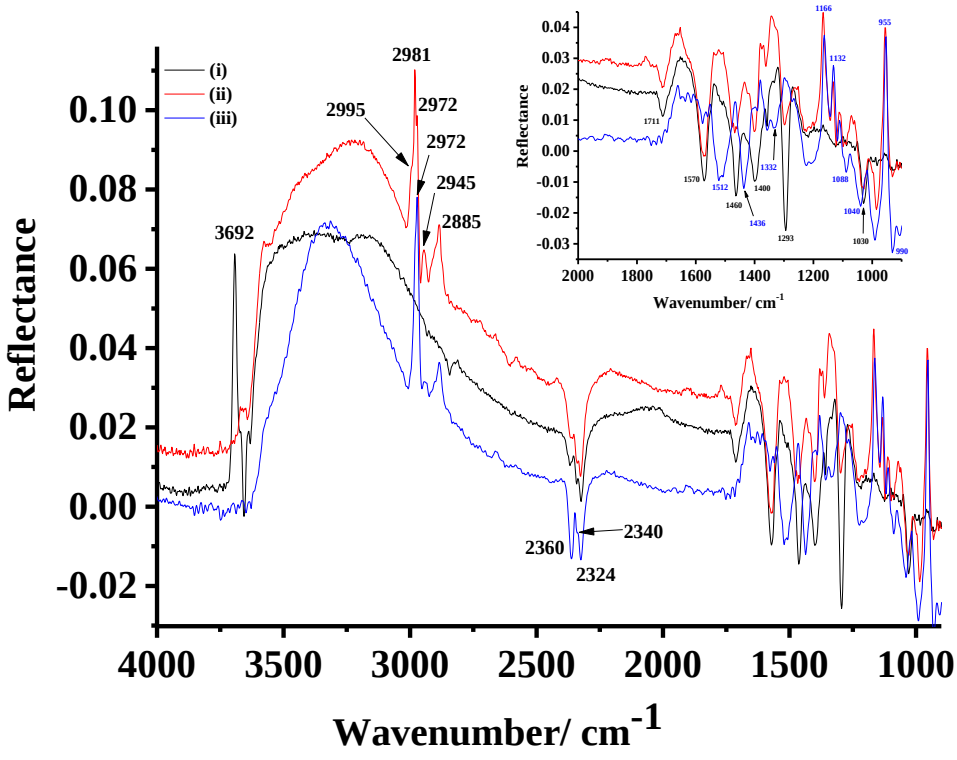

(a)

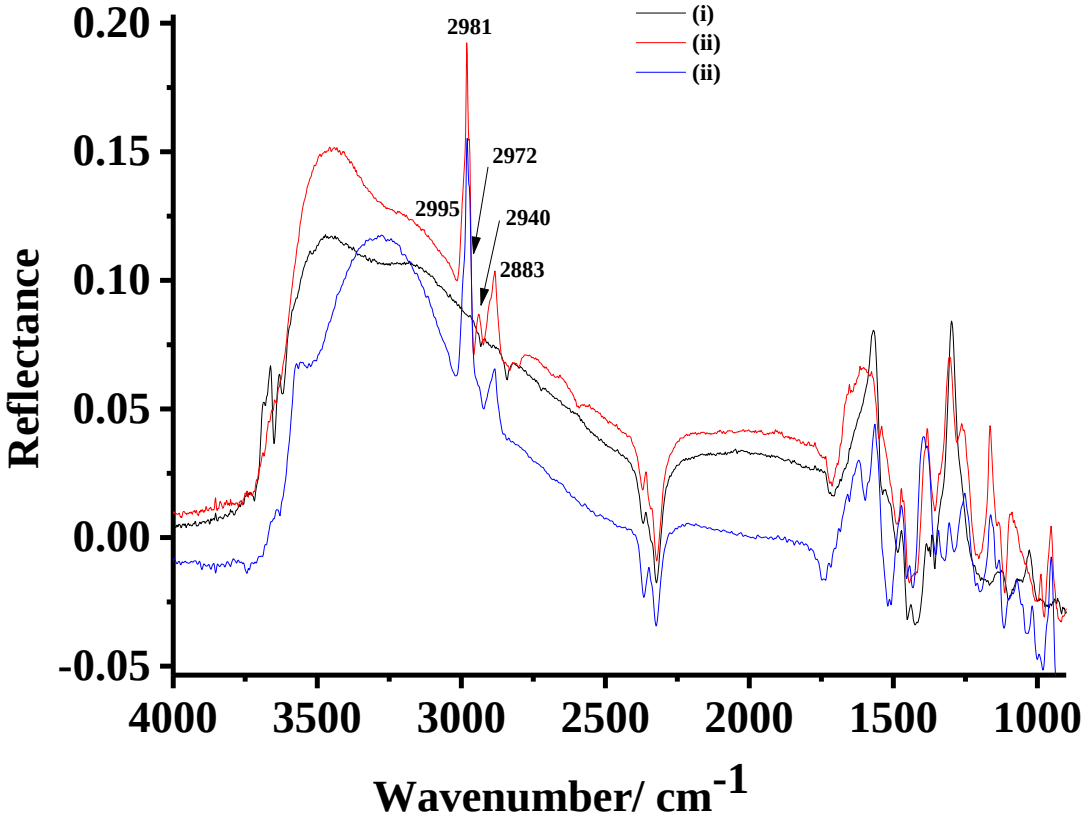
(i)
(ii)
(ii)
2981
2972
2995
2940
2883
Reflectance
Wavenumber/ cm-1

(b)

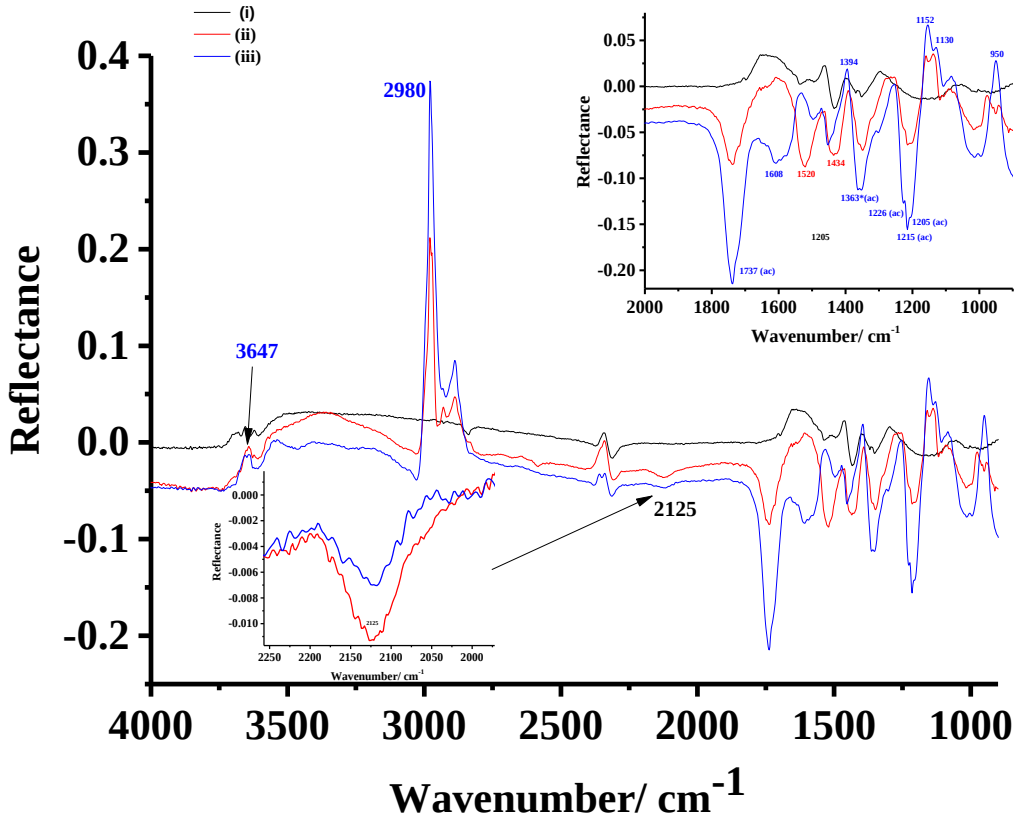
(i)
(ii)
(iii)
2980
3647
2125
Reflectance
Wavenumber/ cm-1
1152
1130
950
1394
1608
1520
1434
1363*(ac)
1226 (ac)
1205 (ac)
1205
1215 (ac)
1737 (ac)

(c)

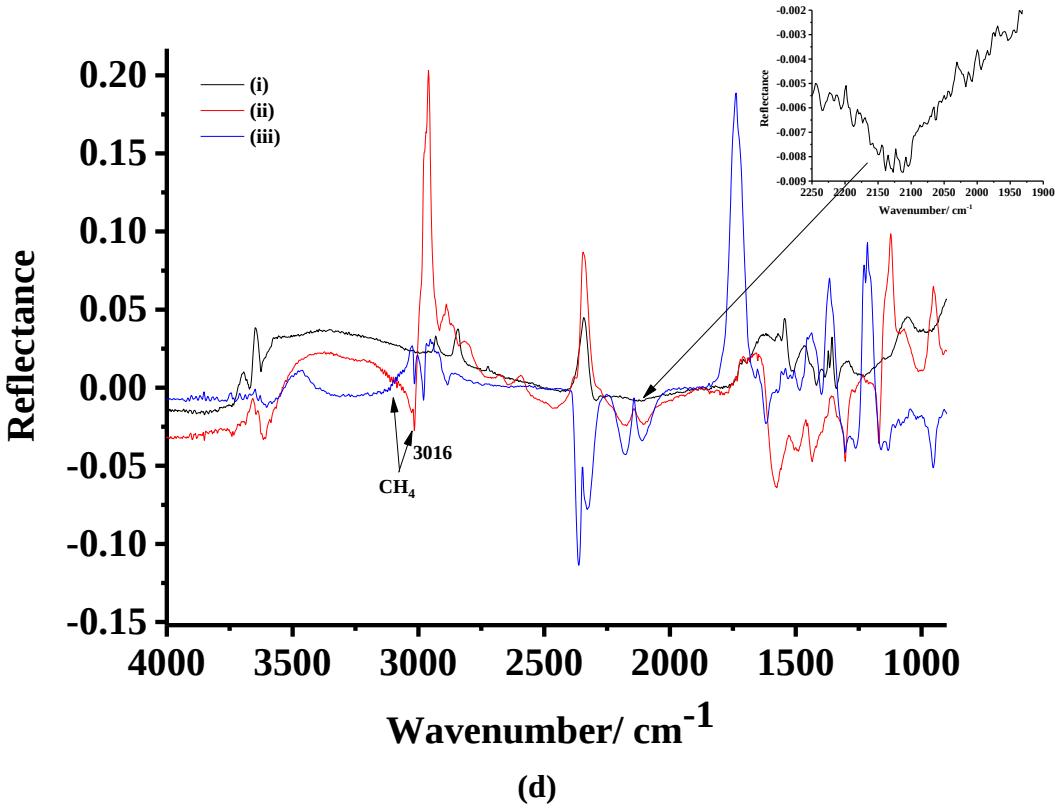

Figure 5.5. The spectra in figs. 5.4(a) – (d) collected at 100 °C, 250°C, 400 °C and 600 °C using: (i) sample A with spectra collected in analogous experiments using samples (ii) B1 and (iii) D2. (a) The spectra collected at 25 °C subtracted from those taken at 100 °C, (b) 250 °C – 100 °C, (c) 400 °C – 250 °C and (d) 600 °C – 400 °C.

These carbonaceous bands are absent from the spectrum of sample D2, suggesting that the previous heat treatments had reduced or removed the adsorbed carbonaceous materials. The previous heat treatment of sample D2 also resulted in marked differences between the samples in the O-H absorption region: the broad absorption between ca. 2250 and 3750 cm^{-1} due to the loss of hydrogen-bonded O-H from sample B1 is comparable in width to the analogous feature of sample A, whilst this feature in the spectrum of sample D2 is significantly narrower, presumably to the dehydroxylation of the surface following the previous heat treatments.

The loss of physisorbed IPA from samples B1 and D2 may be seen by the features at 1166, 1132 and 1111 cm^{-1} which appear in the spectra of liquid IPA as discussed in Chapter 3, section 3.3.3 except that in the liquid phase spectrum the 1166 cm^{-1} band is less intense than the 1132 cm^{-1} feature. It has been reported that the adsorption of IPA at dehydroxylated CeO_2 results in isopropoxide species on the surface and this could account for the clear differences between the spectra of samples B1 and D2 in the C-H region [21].

The multiple peaks in the region of the CO_2 fundamental absorption between 2250 and 2400 cm^{-1} in the spectra of samples A and B1 suggest the gain of physisorbed CO_2 on various sites, presumably due to conversion from adsorbed carbonate and diffusion into the voids. Sample D2 shows a marked difference in that the prominent 2360 cm^{-1} band and the shoulder at 2340 cm^{-1} may be attributed to gas phase CO_2: this is unlikely to be due to the chemical reaction of IPA at the CeO_2 as the temperature at which adsorbed IPA undergoes decomposition has been reported to be 190 °C [22] and hence is most likely to be due to desorption of adsorbed bicarbonate.

It is clear that the features at 930, 990, 1040, 1088, 1332, 1436 and 1512 cm^{-1} in the spectrum of sample D2 are not observed in the spectra of samples A and B1, suggesting they are only produced at the dehydroxylated/decarbonated surface; however, as was stated above, actual conversion of IPA would not be expected until temperatures ca. 190 °C [22], suggesting these features may simply be due to additional adsorbed carbonate species.

5.3.3. All samples: 250 °C

From fig. 5.5(b) it can be seen that, again, samples A and B1 show very similar responses over the spectral range between 2250 and 3750 cm^{-1} and the CO_2 absorption region. In the former region, the spectrum of sample D2 is markedly different, clearly showing a much narrower band due to the loss of hydrogen-bonded Ce-OH species. Again, the presence of the prominent 2360 cm^{-1} CO_2 band suggests the desorption as well as re-arrangement of adsorbed carbonate at the surface on heating. As at 100 °C, there is the gain of bridged carbonate at 1711 cm^{-1}on heating samples A and B1, which is absent from the spectrum of D2. The peak at ca. 1737 cm^{-1} in the spectrum of sample D2 may be attributed to the formation of acetone (see discussion below), in agreement with Kulkarni and Wachs [22]. The shoulder to the low frequency side of the 1737 cm^{-1} feature may be attributed to acetaldehyde: this species is difficult to identify from infrared spectra, but often appears as a shoulder on the acetone C=O band as discussed in Chapter 3.

5.3.4. All samples: 400 °C

Figure 5.5(c) compares the spectra collected at 400 °C with the corresponding spectra taken at 250 °C subtracted. The features at 1737 cm^{-1}, 1363 and 1226, 1215 and 1205 cm^{-1} may be unambiguously attributed to the gain of gas-phase acetone; in the gas-phase spectrum of an authentic sample of acetone as discussed in Chapter 3 section 3.3.3, there are bands at 1371,

1365 and 1355 cm^{-1}, in fig. 5.5(c), however, these features are somewhat distorted by the loss feature near 1394 cm^{-1} due to IPA. The loss features at 3647, 2980, 1152, 1130 and 950 cm^{-1} are also due to gas-phase IPA (as mentioned in Chapters 3 & 4).

It can be seen in fig. 5.5(c) that the 2125 cm^{-1} band is present in the spectra of both samples B1 and D2, and (as was discussed above) appearing in the spectrum of sample A in nitrogen at 450 °C, supporting it is assignment to an electronic band rather than CO adsorbed on Ce^{3+}.

5.3.5. All samples: 600 °C

There are marked differences between the spectra in fig. 5.5(d). Thus, there is a gain of methane in the spectra of samples B1 and D2, as shown by the fine structure between 3000 and 3300 due to the P-branch, and a sharp band at 3016 cm^{-1} due to the Q branch, of the C-H asymmetric stretch as well as the characteristic P and R branches of gas phase CO centred at 2143 cm^{-1} [23]. The methane appears at temperatures > 500 °C at sample B1 and > 450 °C at D2. The separation of the maxima of the P and R branches of the CO [24] in the 600 °C spectrum of sample D2 in fig. 5.5(d) suggests a temperature of the CO of 147 °C [24], more details are mentioned in Chapter 3: fig. 5.6 shows the CO region of the spectra collected at temperatures > 300°C in the experiment depicted in figs. 5.5(a) – (d) using sample D2 with the spectrum collected at 300°C (where no CO is apparent) subtracted. Also shown on the figure is the spectrum of CO at 600°C produced using Spectralcalc by Prof. Philip Martin, School of Chemical Engineering and Analytical Science, the University of Manchester. Thus it appears that reaction of IPA at CeO_2 at temperatures above 400°C produced methane and cold CO, and this is discussed further below.

Samples A and B1 both show the loss of a broad peak due to physisorbed CO_2 at 2345 cm^{-1} in fig. 5.5(d), whilst sample D2 shows the clear gain of gas phase CO_2. Sample D2 also shows clear loss features due to gas-phase acetone. The absence of any features due to acetone in the spectrum of sample B1 and the strong loss features in the spectrum of sample D2 may be explained in terms of fig. 5.7(a) which shows plots of the intensities of the acetone band at 1737 cm^{-1} observed during the experiments employing samples B1, C2, D1 and D2 as a function of temperature between 200 and 600 °C. In each case, the spectra collected at 200 °C (immediately prior to the onset of acetone formation) were subtracted from those taken at the higher temperatures. From the figure it can be seen that the intensities of the acetone band are

approximately equal at 400 °C and 600 °C, with the result that when the former was subtracted from the latter, as in fig 5.5(d), the peak was annulled.

As would be expected, no acetone was observed in the absence of IPA. From fig. 5.7(a) it can be seen that, in all cases, the formation of acetone rises to a maximum around 400 – 450 °C before declining. The presence of the maximum may reflect further oxidation of the acetone and/or the complete consumption of the reactant IPA: this is discussed further below. The temperature at which the formation of acetone commences clearly requires active sites to be freed up by pre-heating, as it decreases in the order D2 < C2 < D1 < B1. The temperature of the maximum also appears to reflect this. As would be expected, more acetone is produced from the pure CeO_2 than the mixture with KBr. The spectra shown in figs. 5.5(a) – (d) were used to obtain the plots in figs. 5.7(a) – (d).

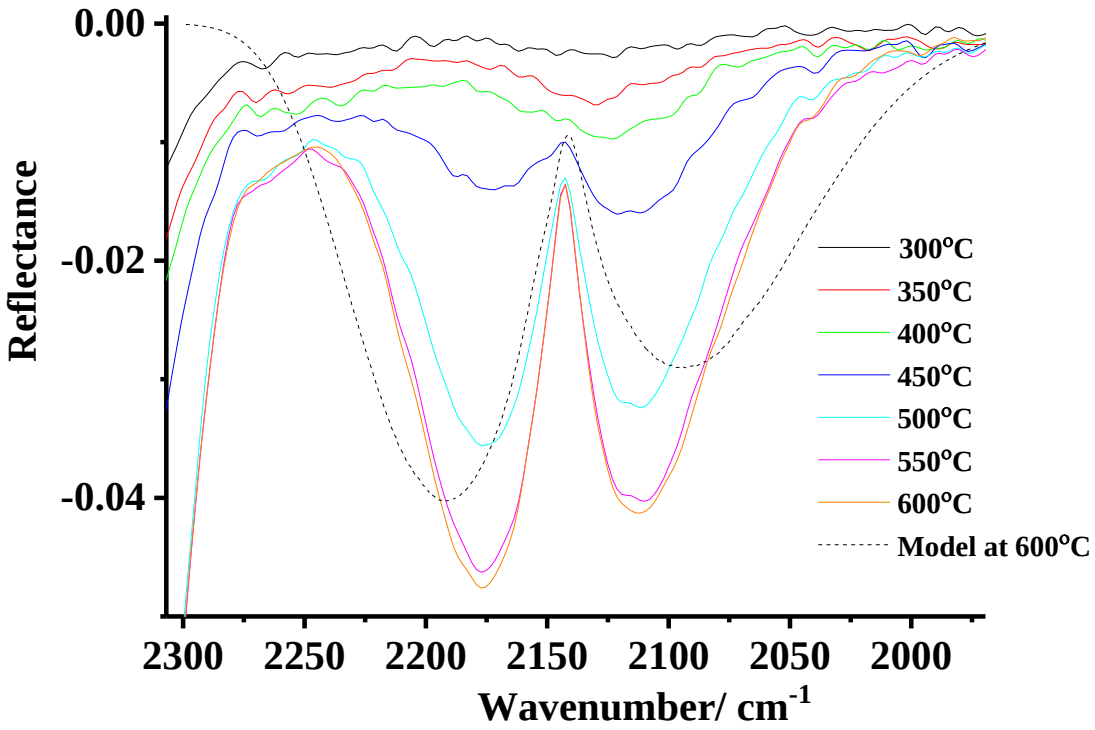

Figure 5.6. Spectra showing the CO spectral region collected at temperatures > 300 °C from sample D2 during the experiment depicted in figs. 5.5(a) – (d) with the spectrum collected at 300 °C subtracted. The separation of the P and R branch maxima modelled using Spectralcalc on the basis of a temperature of 600 °C is also shown.

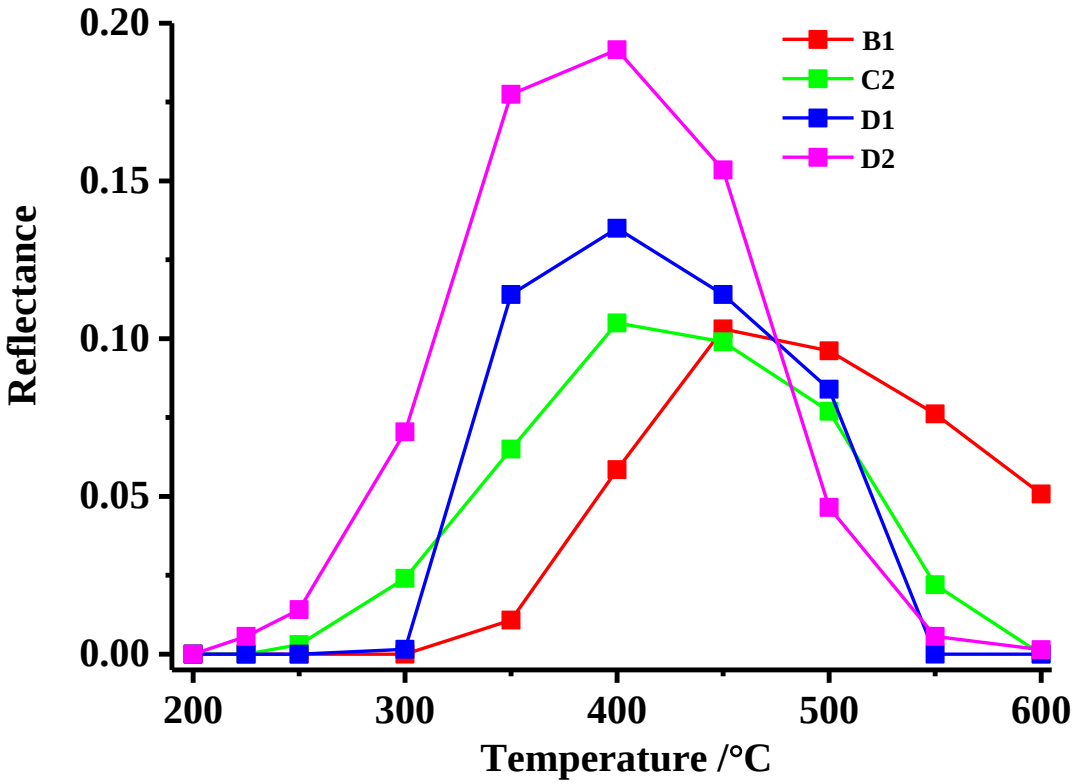
0.20
0.15
0.10
0.05
0.00
Reflectance
200
300
400
500
600
Temperature /°C
B1
C2
D1
D2

(a)

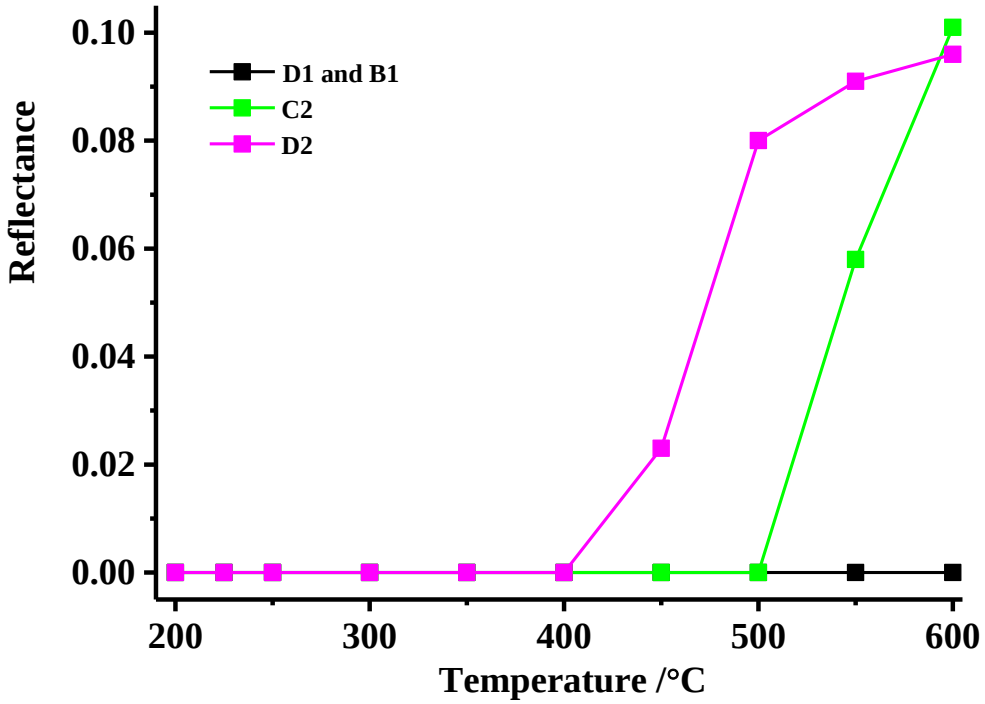
0.10
0.08
0.06
0.04
0.02
0.00
Reflectance
200
300
400
500
600
Temperature /°C
D1 and B1
C2
D2

(b)

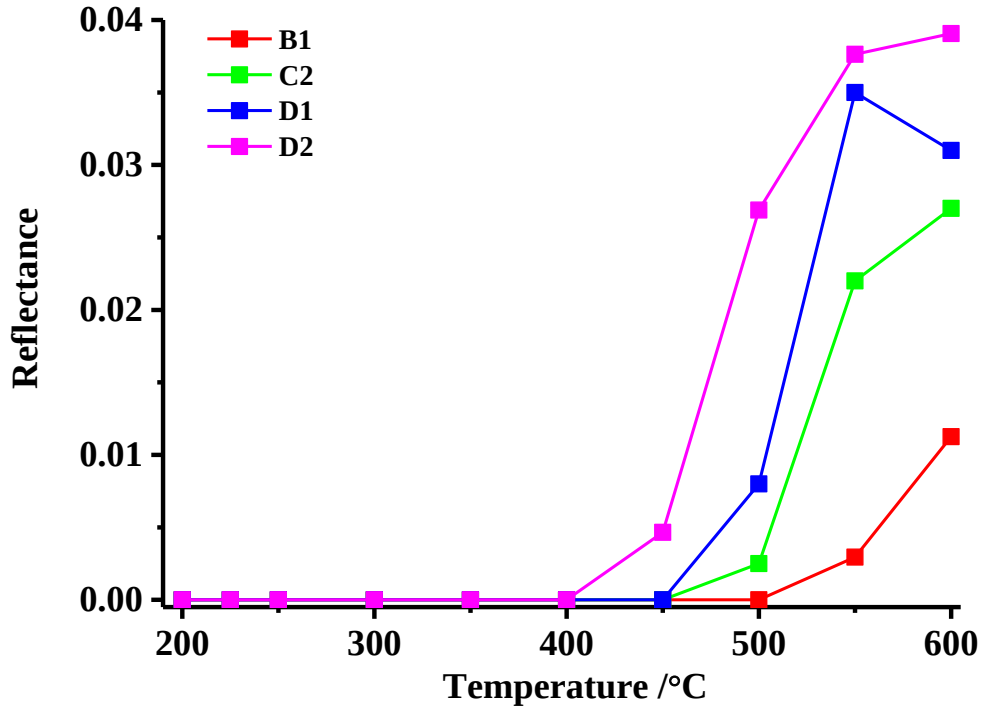

(c)

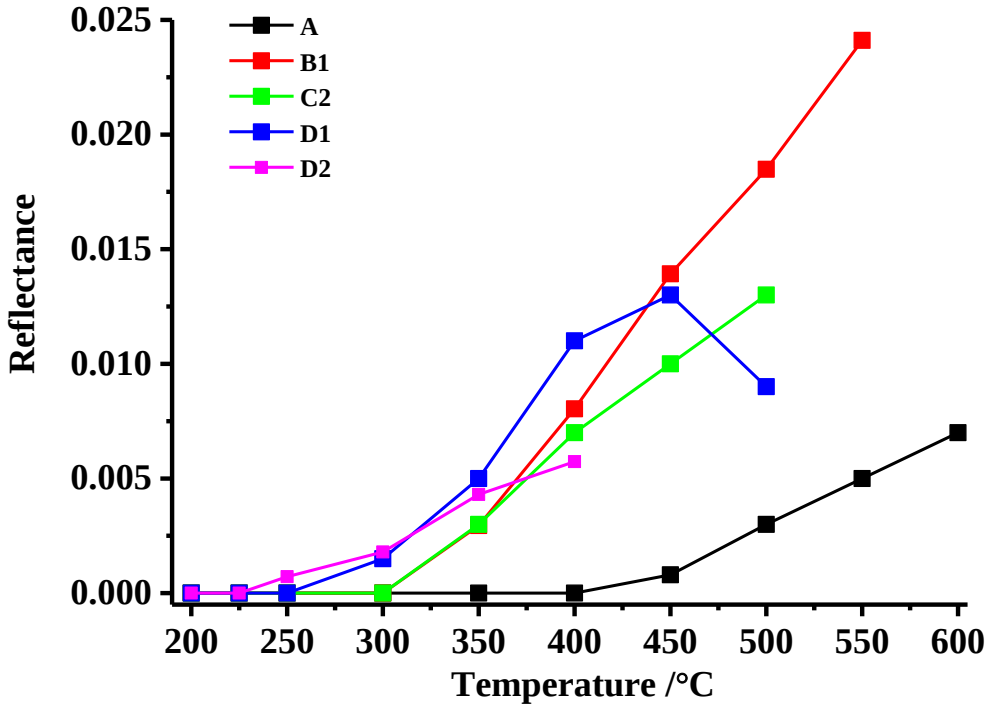

(d)

Figure 5.7. Plots of the intensities of the various features from the analogous experiments to that shown in fig. 5.2(b) using samples B1, C2, D1 and D2 as a function of temperature between 250 and 600 °C. In each case, the spectra collected at 200 °C were subtracted from those at higher temperature. (a) 1737 cm^{-1} band of acetone, (b) the 2362 cm^{-1} gas phase CO_2 feature, (c) the 2177 cm^{-1} band of gas phase CO and (d) the 2125 cm^{-1} band due to Ce^{3+}.

Figure 5.7(b) shows analogous plots for the gas phase CO_2 band at 2362 cm^{-1}. CO_2 is not apparent in the spectra of samples A, B1 or D1, only in the highly pretreated samples C2 and D2, suggesting that at active sites on the CeO_2 must be freed from adsorbed carbonate for CO_2 to be produced. The onset for CO_2 formation at the pure CeO_2 sample was 400 °C; lower than at the CeO_2+KBr, although the intensities of the 2362 cm^{-1} features at 600 °C were the same.

Figure 5.7(c) shows plots of the 2177 cm^{-1} gas phase CO feature as a function of temperature for samples B1, C2, D1 and D2. As with acetone, no gas phase CO was produced in the absence of IPA. Again, from the plots, it can be seen that increasing heat treatment resulted in increased production of CO and a decrease in the onset temperature. The production of CO by heating IPA at CeO_2 has not, to our knowledge, been reported previously and may be evidence of a roaming mechanism [25-31], see discussion in Chapter 3.

Roaming mechanisms include pathways that bypass the conventional saddlepoint transition state of a particular reaction [26][27][29]. Roaming dynamics are not restricted to small molecules such as formaldehyde or to hydrogen atoms as the roaming species [24]. Whilst transition state theory is still robust, it is becoming increasingly apparent that roaming mechanisms may be more widespread that at first thought [26][27] and represent a significant challenge to the current paradigm. The definitions of "loose" or "tight" transition state can be very simply explained in terms of the Eyring equation [32]:

$$k = (k_B T/h).\exp(\Delta S^{\neq}/R).\exp(-\Delta H^{\neq}/RT) \quad (5.2)$$

where $\Delta S^{\neq}$ is the entropy change associated with the formation of the transition state, and $\Delta H^{\neq}$ the corresponding enthalpy change or activation energy. In a loose transition state, there are more degrees of freedom than in the reactants or, in other words, the transition state provides more energy levels that can be occupied at the specified temperature, corresponding to a positive change in entropy between the ground state of the reactants and the transition state; while the interaction of the transition state with the surface is relatively weak compared to that of the ground state. Conversely, a negative $\Delta S^{\neq}$ corresponds to a tight transition state where the rotation, vibration and/or translational modes are more restricted and the interaction of transition state and surface is quite strong. Where $\Delta S^{\neq} = 0$, $A = k_B T/h$.

It was reported in Chapter 3 the formation of methane and cold CO in a gas phase process from IPA in a non-thermal plasma above Macor and postulated a roaming mechanism. It may thus be the case that the current work is an example of an analogous thermal process, this time taking place at the surface of the CeO_2. Further work is required to investigate this postulate.

Figure 5.7(d) shows plots of the 2125 cm^{-1} band due to Ce^{3+} sites. It is clear that reduction of the Ce^{4+} takes place both in the presence and absence of IPA, but is significantly enhanced under the latter conditions.

Figures 5.8(a) – (d) show the intensities of the various features in the plots in figs. 5.7(a) – (d) normalised to their maximum values and plotted according to sample in order to interrogate any relationships between the various species. However, there are no obvious relationships between the various species produced during the oxidation of IPA apart from the fact that CO_2 is produced as acetone is consumed, as may be expected. The Ce^{3+} $^2F_{5/2} \rightarrow {}^2F_{7/2}$ electronic transition may show a relationship to the acetone feature in figs. 5.8(c) and (d), but this is less clear in figs. 5.8(a) and (b): and such a relationship seems unlikely in view of the fact that the 2125 cm^{-1} feature is also seen during the heating of sample A in N_2 albeit at a much lower intensity, see fig. 5.7(d).

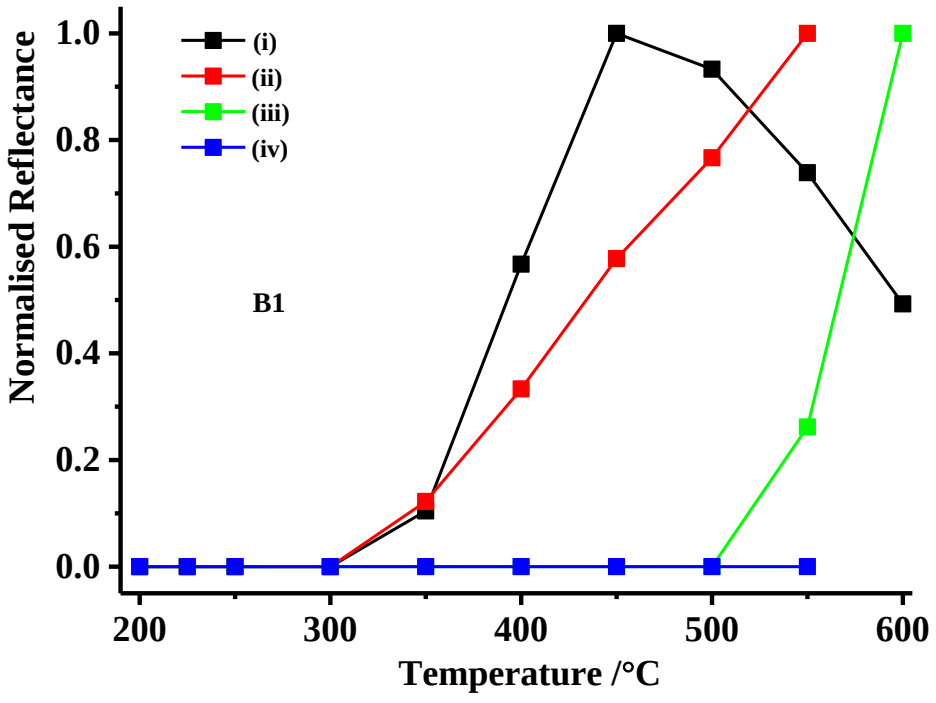

(a)

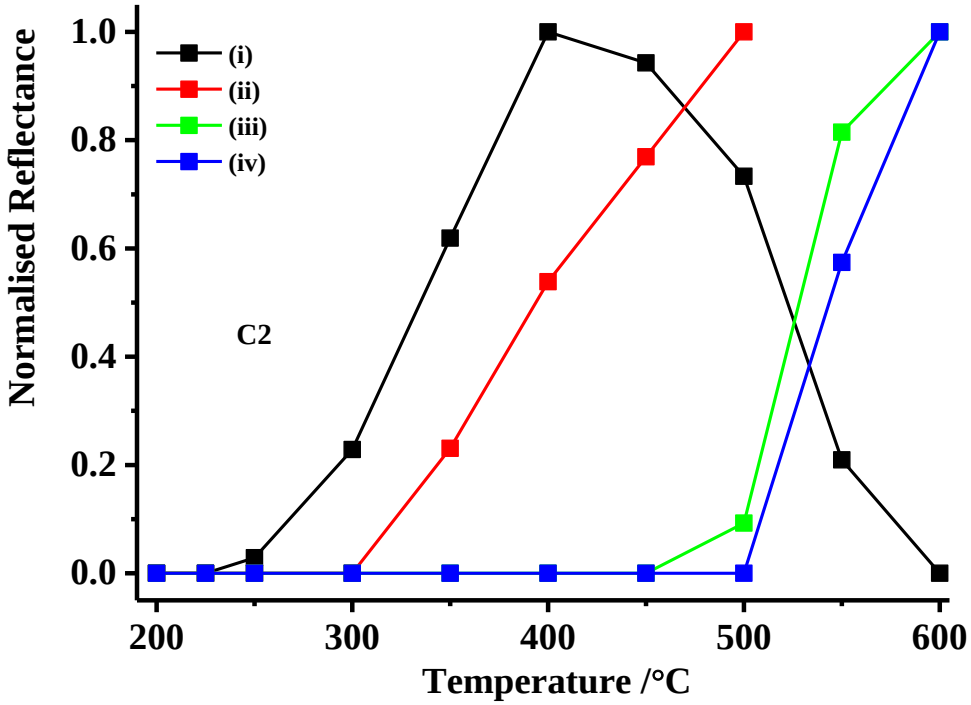
Normalised Reflectance
1.0
0.8
0.6
0.4
0.2
0.0
(i)
(ii)
(iii)
(iv)
C2
200
300
400
500
600
Temperature /°C

(b)

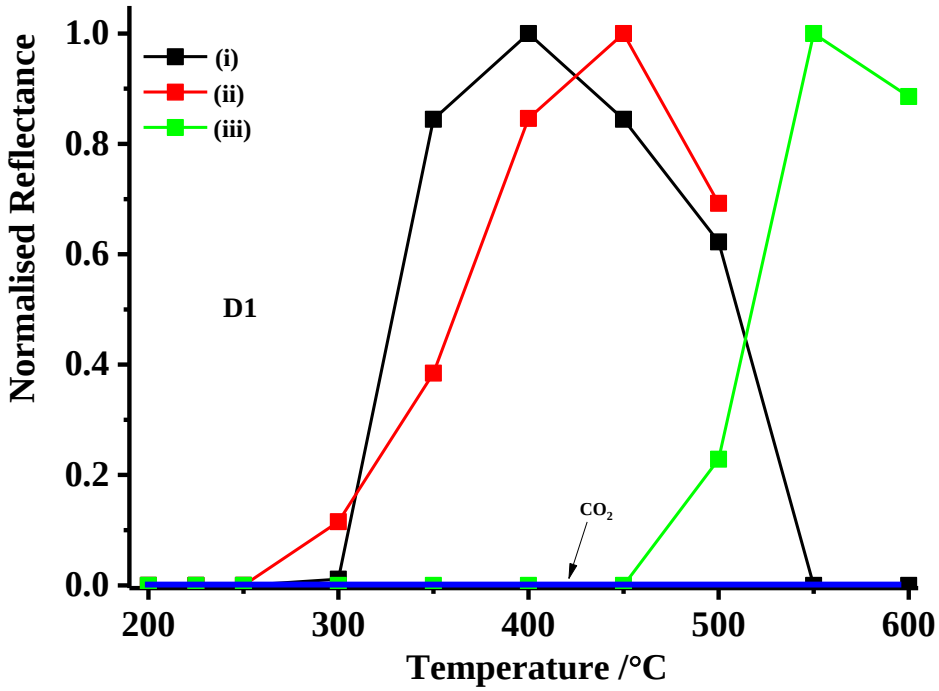
Normalised Reflectance
1.0
0.8
0.6
0.4
0.2
0.0
(i)
(ii)
(iii)
D1
CO2
200
300
400
500
600
Temperature /°C

(c)

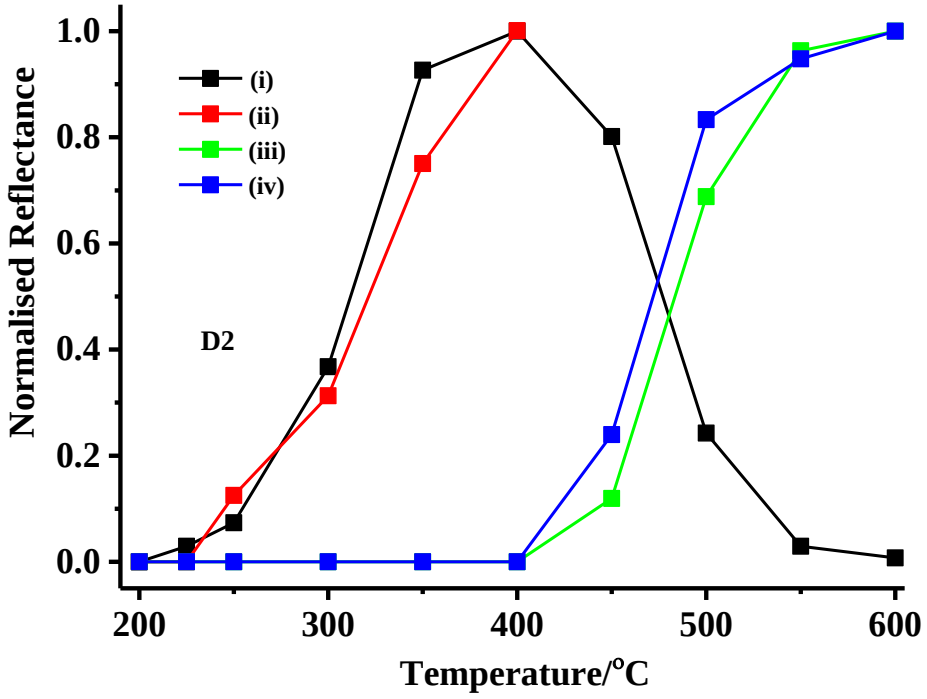

(d)

Figure 5.8. The intensities of the various features in the plots in figs. 5.7(a) – (d) normalised to their maximum values and plotted according to sample. (i) acetone at 1737 cm^{-1}, (ii) 2125 cm^{-1} due to Ce^{3+}, (iii) CO(g) at 2177 cm^{-1} and (iv) CO_2(g) at 2363 cm^{-1}.

5.4. The plasma experiments using the reflectance cell

5.4.1. Blank experiments

As mentioned in Chapter 4 section 4.4.1, the powder catalysts could only be employed in the reflectance cell as it was not possible to coat the catalyst onto the Macor caps of the transmission cell due to arcing. The preparation of the CeO_2 coated Macor/Ti mesh was discussed in section 2.10.

In the plasma reflectance experiments using the CeO_2 coatings, the reference spectra were taken with a pure N_2 feed at 30 cm^3 min^{-1}, after which the plasma was initiated at an input power of 16 W and further spectra collected as a function of time up to 20 minutes. For clarity, only the spectra collected after 2, 6, 10 and 20 minutes as shown in fig. 5.9. As may be seen from the figure, the spectra are featureless apart from two strong bands at 1210 cm^{-1} (broad) and 1150 cm^{-1}, that increase in intensity steadily with time, and the origin of these bands was discussed in Chapter 3.

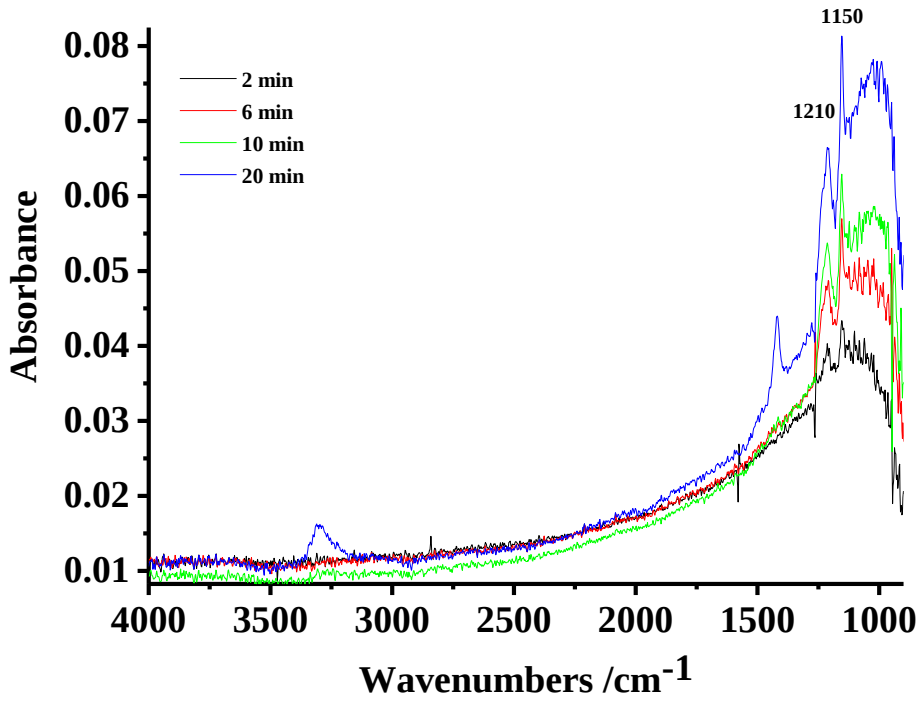

Figure 5.9. In situ FTIR spectra (4 cm^{-1} resolution, 100 co-added and averaged scans, 100 seconds per scanset) collected using the plasma reflectance cell at the times shown on the figure at an input power of 16 W using nitrogen as the feed gas and CeO_2 coating on the Macor/Ti mesh. The spectra collected immediately before the plasma was initiated was employed as the reference spectra and the spectra were corrected for the CaF_2 window reflection.

5.4.2. Experiments using N_2 and IPA vapour as the feed gas

Figure 5.10 shows spectra collected using the plasma reflectance cell with a gas feed of IPA + N_2 and CeO_2 coating on the Macor/Ti mesh at a total flow rate of 30 cm^3 min^{-1} and 16 W input power. The reference spectrum was collected under the same conditions, but without plasma. There are no absorptions due to physisorbed CO_2 or adsorbed carbonaceous species in the single beam spectra of CeO_2 in the reflectance cell-probably due to the much lower penetration depth of the IR beam compared to the thermal systems. Only the spectral region up to 2000 cm^{-1} is shown for clarity due to markedly sloping baselines above this frequency.

Figure 5.11(a) compares the spectrum collected after 8 minutes in fig. 5.10 to that collected in an analogous experiment using Macor after the same time and under the same experimental conditions as discussed in Chapter 3. Figure 5.11(b) shows the result of subtracting the spectrum collected after 8 minutes in fig. 5.10 from that taken after 20 minutes, and the analogous spectrum from the experiment employing Macor. On the basis of the Macor results as

mentioned in Chapter 3, the various bands in the spectra in figs. 5.10, 5.11(a) and (b) may be attributed to at least two species: a polymethylacetylene-like polymer containing moieties including CH_3, C=O, C=C and O-H groups formed via a cascade of Aldol/Pinacol/dehydration reactions initiated via the formation of acetone, and isophorone, produced via the Aldol condensation of acetone. There are also as yet unidentified products, as discussed previously.

The strong, signature bands of the polymer and isophorone shift in frequency depending upon the exact experimental conditions (as may be seen from fig. 5.12): for clarity and to aid comparison with the earlier work as mentioned in Chapter 3, these will be referred to as the 1750 cm^{-1} and 1666 cm^{-1} features, respectively. Using these bands as representative of the two species, it can be seen from figs. 5.11(a) and (b) that the relative amounts of the two primary products change with operational time: thus isophorone is the predominant product up to 8 minutes with both Macor and CeO_2, but with more polymer at Macor than CeO_2. Between 8 and 20 minutes, the amount of polymer produced increases relative to the isophorone at both catalysts, but again with more polymer at Macor than CeO_2.

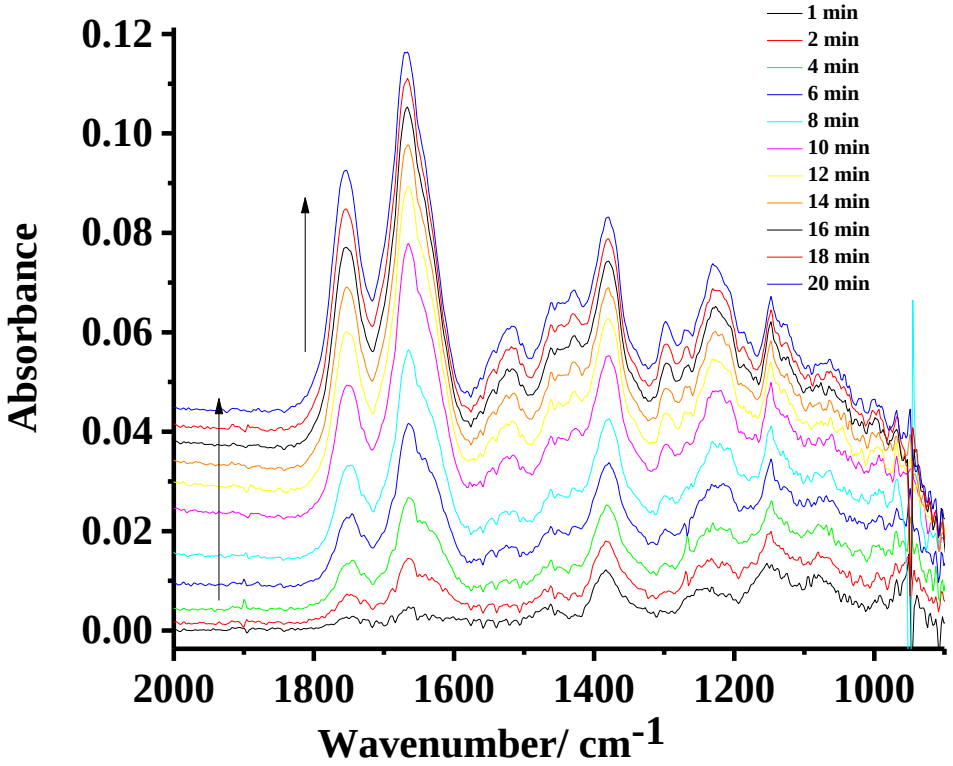

Figure 5.10. Spectra (4 cm^{-1} resolution, 100 co-added and averaged scans, 100 s per scanset) collected during an experiment in which IPA+N_2 was passed through the plasma reflectance cell at a total flow rate of 30 cm^3 min^{-1} and input power of 16 W. The reference spectrum was collected under the same conditions, but without plasma.

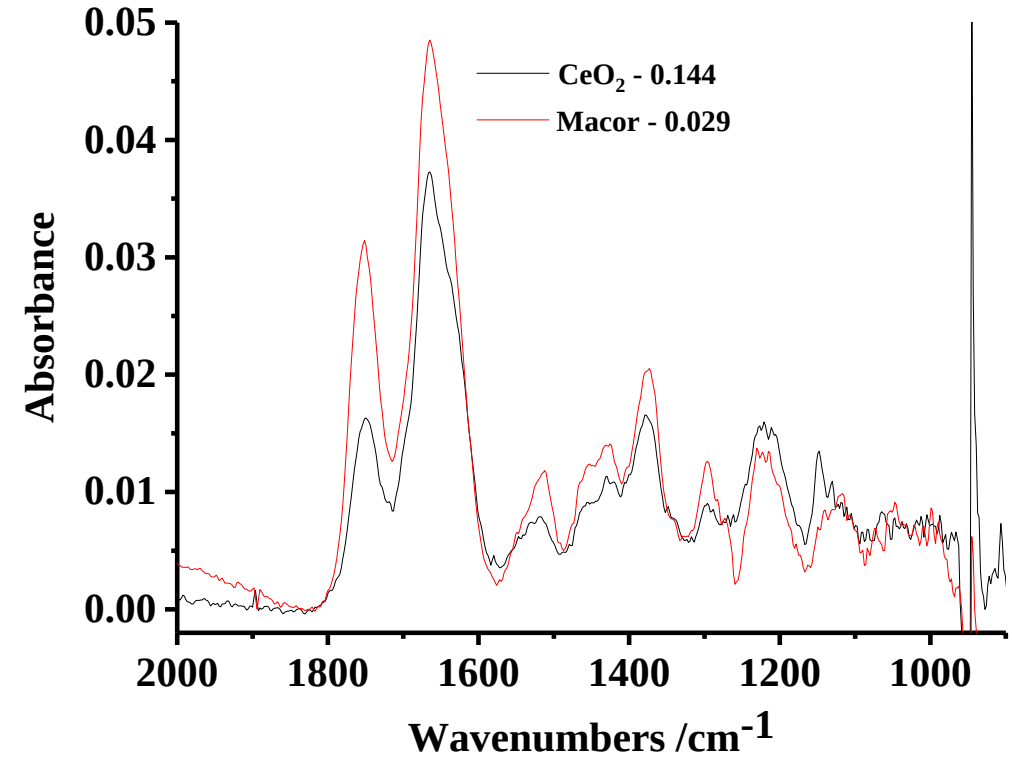

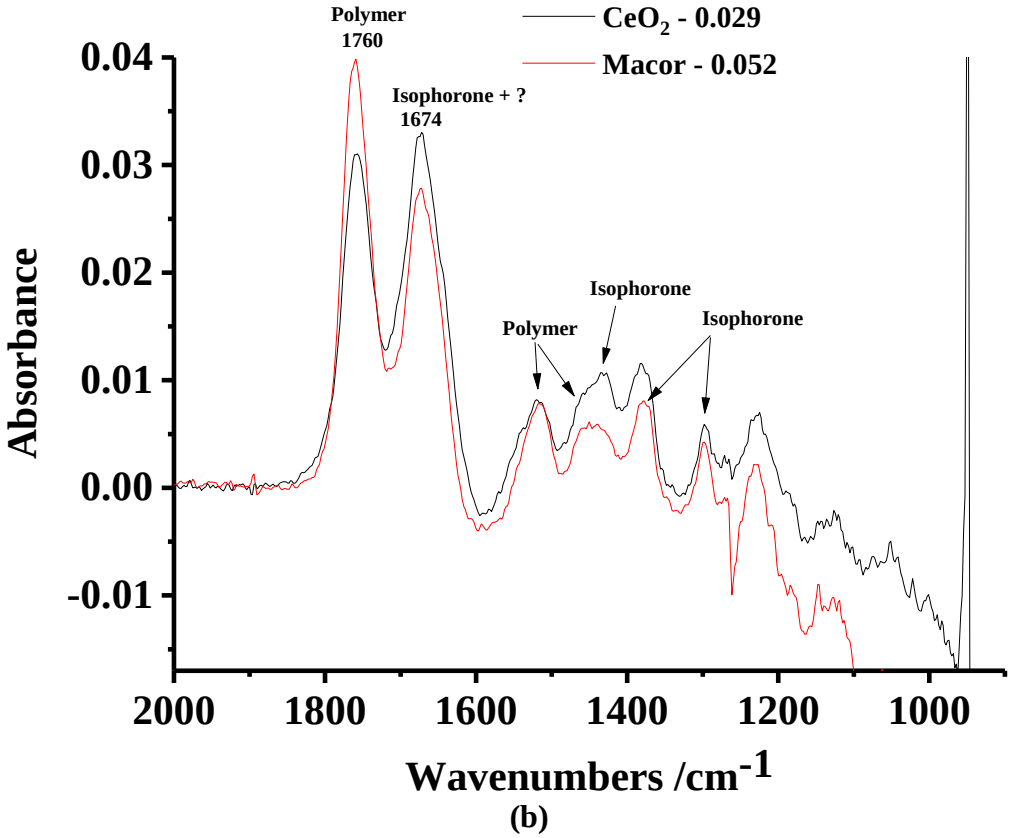

Figure 5.11. Spectra collected (a) after 8 minutes and (b) after 20 minutes during experiments carried out at 16 W input power and using a nitrogen+IPA feed at a total flow rate of 30 cm^3 min^{-1} with CeO_2 or Macor as the dielectric in the plasma reflectance cell. In (a) the analogous spectra collected after 1 minute were subtracted, and in (b) the spectra collected after 8 minutes were subtracted. The spectra were offset down as indicated to facilitate comparison.

It should be noted that, as discussed in Chapter 4 no conversion of IPA was observed at SnO_2 in the plasma reflectance cell, even at the higher input power of 20 W. The difference between the data obtained with SnO_2 on the one hand, and Macor & CeO_2 on the other is a key observation, as it shows that the solid surface is critical to the chemistry observed in the plasma. In other words, there is a conundrum: the formation of polymer and isophorone must require access to the catalyst surfaces: however, after the experiment in fig. 5.10 was completed, the CeO_2 surface was completely covered with the brown oil containing isophorone and the polymer. This was also generally observed after 20 minute experiments using Macor as well as CeO_2. Thus fig. 5.12 shows the spectra collected after 4, 8, 20 and 40 minutes in fig. 5.10, the spectra were all offset to zero at ca. 1600 cm^{-1} and scaled such that the intensities of the bands near 1666 cm^{-1} were the same (the scaling factors are shown on the figure) to allow for comparison. Figure 5.13(a) shows plots of the two signature features as a function of time normalised to their maximum values, and fig. 5.13(b) shows the raw data. It is clear from figs. 5.12, 5.13(a) & (b) that the production of both the polymer and isophorone continue throughout the experiment, the former steadily whilst the rate of the production of the latter decreases relative to the polymer after ca. 10 minutes, suggesting that the increasing coverage by the liquid film does not prevent the formation of these products. From fig. 5.12, it can be seen that the band maxima of the ca. 1750 and 1666 cm^{-1} features move steadily towards higher frequencies with processing time; however, a comparison with fig. 5.10 suggests that the isophorone peak does not shift but rather a peak grows alongside to higher frequency. With respect to the polymer band, the frequency of this feature is 1744 cm^{-1} after 4 minutes, increasing to ca. 1763 cm^{-1} after 40 minutes: the broad band centred near 1215 cm^{-1} and the ~1744 cm^{-1} feature suggest the formation of acetone [23] at least in the early stages of the experiment, in agreement with the proposed mechanism. The acetone feature is then obscured by the polymer band which grows in and moves to higher frequency as the conjugation(s) of the polymer molecule(s) comprising it change(s) [23].

By comparing the relative intensities of the various features in fig. 5.12 and their time dependences, it is possible to add to the assignments of the various bands to isophorone or the polymer orginally proposed in Chapter 3, and a summary is presented in table 5.3.

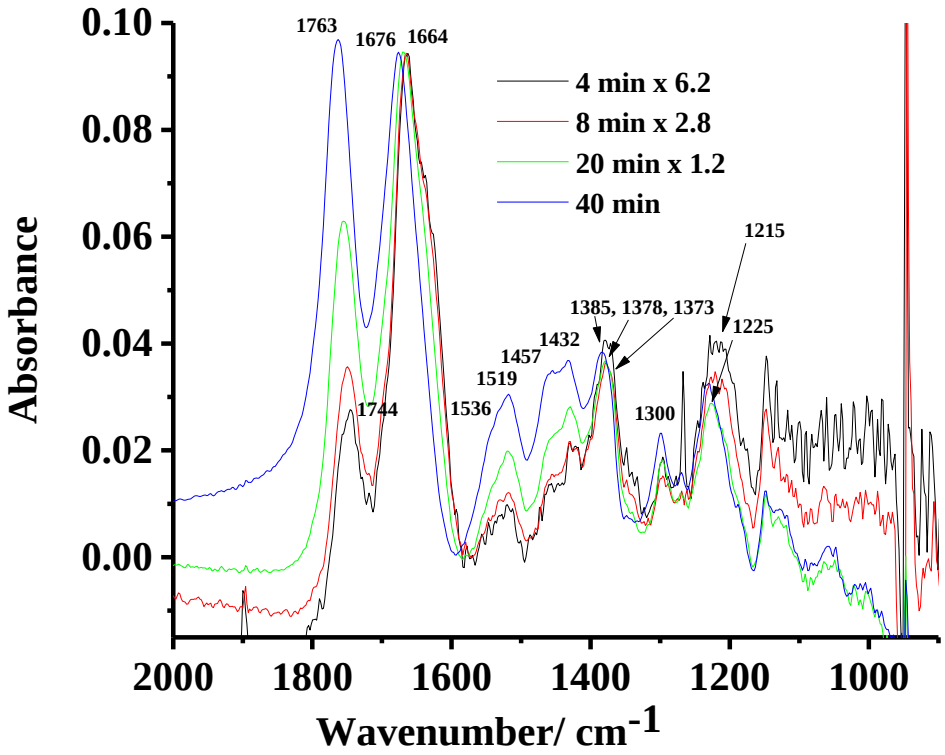

Figure 5.12. The spectra in fig. 5.10 collected after 4, 8, 20 and 40 minutes. The spectra were enhanced by the factors shown in the legend to facilitate comparison.

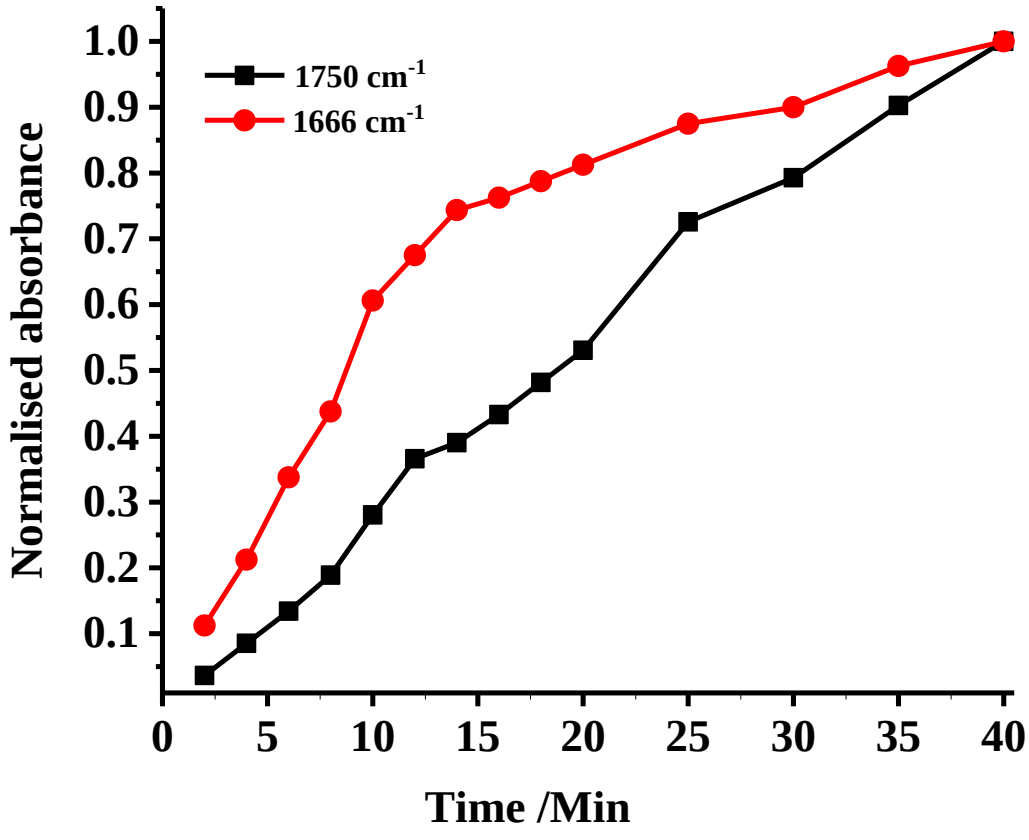

(a)

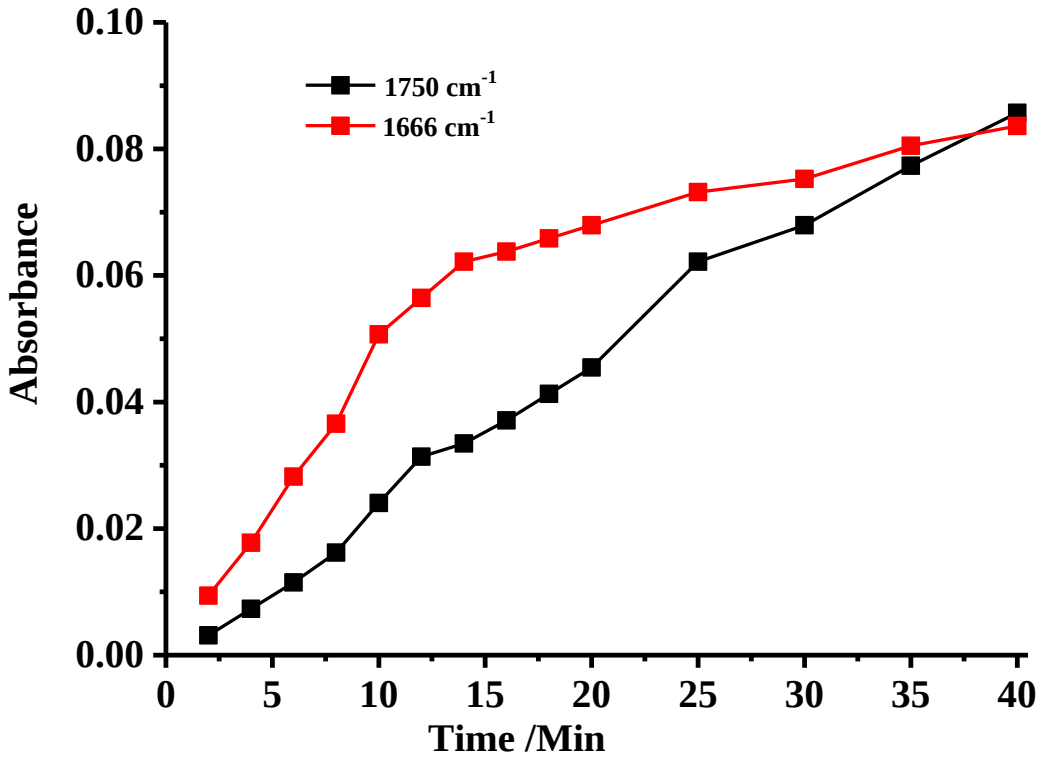

(b)

Figure 5.13. Plots of the 1750 and 1666 cm^{-1} bands in fig. 5.10 as a function of time: (a) the absorbances were normalised to their maximum values and (b) the raw data.

Polymer /cm^{-1}	**Isophorone /cm^{-1}**
2936	2936
2876	2876
1740 - 1765	
	1666
	1630 (sh)
1536	
1519	
1457	
1432	1430
1385	1378
	1373
	1215

Table 5.3. The principal features observed in the spectra in figs. 5.10 and 5.12.

Both Rodrigues et al [33] and Jia and Rousseau [34] have studied the CeO_2/plasma interface. Jia and Rousseau pre-adsorbed IPA and then flushed with dry air during plasma treatment: the authors incorrectly attributed peaks at 1159 and 1125 cm^{-1} to dissociatively and non-

dissociatively adsorbed IPA. In fact, these bands form, along with a third at 1110 cm^{-1} (which was also present in the spectra but not discussed) a signature triplet characteristic of liquid-phase IPA, i.e. IPA that has condensed on the windows and/or catalyst surface. The authors reported that IPA adsorbed and reacted at room temperature on the CeO_2 to form acetone, and more acetone was produced during the plasma treatment of the adsorbed species as well as adsorbed acetate. Jia and Rousseau employed a gas feed of air and IPA at ca. 500 cm^3 min^{-1} and observed the formation of physisorbed and dissociatively-adsorbed IPA which were converted to acetone and mesityl oxide in the plasma. Neither group reported seeing a polymeric product or isophorone.

5.5. Comparison of thermal and plasma data

It is clear that, whilst the presence of adsorbed carbonates/bicarbonates inhibits the thermal reaction of IPA at CeO_2, the plasma-driven process is not inhibited at all: for example, there are no additional features in figs. 5.11(a) and (b) that can be attributed to adsorbed carbonates.

Both the thermally and plasma – driven processes generate acetone, and both do so catalysed by the CeO_2.

5.6. Conclusion

The surface of polycrystalline CeO_2 comprises isolated OH groups, hydrogen bonded OH and various forms of adsorbed carbonate CO_x (bicarbonate, monodentate, bridge, bidentate etc.). One of the latter species is physisorbed CO_2, associated with several different surface sites. Interestingly, physisorbed CO_2 was observed even up to 600 °C, most probably due to its location in voids associated with Ce^{3+} species and their attendant oxygen vacancies. The behaviour of the adsorbed CO_x species as a function of temperature is complex and includes the interconversion of adsorbed species and desorption of CO_2. In contrast to the experiments using Macor, IPA adsorbs and reacts at CeO_2 on heating. The presence of the adsorbed carbonaceous species directly influenced the nature of the adsorbed IPA, with physisorbed IPA observed on samples with higher amounts of CO_x and alkoxide on samples that had been pretreated to reduce the coverage of species resulting from CO_2 adsorbed. The presence of such species also inhibited the oxidation of IPA to acetone and further to CO_2, with this process taking place at T > 200 °C on pretreated CeO_2 and > 300 °C at samples having significant coverage by CO_x. On the pretreated samples, CO_2 was produced from oxidation of acetone but

was not observed at samples with high coverage by CO_x. The spectra obtained at T > 400 °C in the thermal experiments suggested the presence of a roaming mechanism at the CeO_2 surface possibly associated with the Ce^{3+} sites, resulting in CH_4 and cold CO. This appears to be a unique observation and supports suggestions in the literature that such mechanisms that avoid the conventional transmission state may be more ubiquitous than formally believed. In the experiments exploring the non-thermal plasma driven conversion of IPA at CeO_2, the liquid products observed were essentially the same as those seen using Macor, ie a polymethyl acetylene-like polymer and isophorone, differing only in the relative amounts of these species.

5.7. References

1. Jasinski, P., Suzuki, T. and Anderson, H.U., 2003. Nanocrystalline undoped ceria oxygen sensor. *Sensors and Actuators B: Chemical*, *95*(1), pp.73-77.
2. Chelliah, M., Rayappan, J.B.B. and Krishnan, U.M., 2012. Synthesis and characterization of cerium oxide nanoparticles by hydroxide mediated approach. *Journal of Applied Sciences*, *12*(16), pp.1734-1737.
3. Lawrence, N.J., 2010. Synthesis and Catalytic Activity of Nanostructured Cerium Oxide.
4. Phokha, S., Pinitsoontorn, S., Chirawatkul, P., Poo-arporn, Y. and Maensiri, S., 2012. Synthesis, characterization, and magnetic properties of monodisperse CeO_2 nanospheres prepared by PVP-assisted hydrothermal method. *Nanoscale research letters*, *7*(1), p.425.
5. Zaki, M.I. and Sheppard, N., 1983. An infrared spectroscopic study of the adsorption and mechanism of surface reactions of 2-propanol on ceria. *Journal of Catalysis*, *80*(1), pp.114-122.
6. Binet, C., Daturi, M. and Lavalley, J.C., 1999. IR study of polycrystalline ceria properties in oxidised and reduced states. *Catalysis Today*, *50*(2), pp.207-225.
7. Ansari, S.A., Khan, M.M., Ansari, M.O., Kalathil, S., Lee, J. and Cho, M.H., 2014. Band gap engineering of CeO_2 nanostructure using an electrochemically active biofilm for visible light applications. *RSC Advances*, *4*(32), pp.16782-16791.
8. Ivers-Tiffee, E., Weber, A. and Herbstritt, D., 2001. Materials and technologies for SOFC-components. *Journal of the European Ceramic Society*, *21*(10-11), pp.1805-1811.
9. Schweke, D., Zalkind, S., Attia, S. and Bloch, J., 2018. The Interaction of CO_2 with CeO_2 Powder Explored by Correlating Adsorption and Thermal Desorption Analyses. *The Journal of Physical Chemistry C*, *122*(18), pp.9947-9957.

10. Boroumand, F., Moser, J.E. and Van Den Bergh, H., 1992. Quantitative diffuse reflectance and transmittance infrared spectroscopy of nondiluted powders. *Applied Spectroscopy*, *46*(12), pp.1874-1886.
11. Li, C., Sakata, Y., Arai, T., Domen, K., Maruya, K.I. and Onishi, T., 1989. Carbon monoxide and carbon dioxide adsorption on cerium oxide studied by Fourier-transform infrared spectroscopy. Part 1.—Formation of carbonate species on dehydroxylated CeO_2, at room temperature. *Journal of the Chemical Society, Faraday Transactions 1: Physical Chemistry in Condensed Phases*, *85*(4), pp.929-943.
12. Yoshikawa, K., Sato, H., Kaneeda, M. and Kondo, J.N., 2014. Synthesis and analysis of CO_2 adsorbents based on cerium oxide. *Journal of CO_2 Utilization*, *8*, pp.34-38.
13. Zhao, S.Y., Wang, S.P., Zhao, Y.J. and Ma, X.B., 2017. An in situ infrared study of dimethyl carbonate synthesis from carbon dioxide and methanol over well-shaped CeO_2. *Chinese Chemical Letters*, *28*(1), pp.65-69.
14. Morterra, C. and Orio, L., 1990. Surface characterization of zirconium oxide. II. The interaction with carbon dioxide at ambient temperature. *Materials chemistry and physics*, *24*(3), pp.247-268.
15. Ramis, G. and Lorenzelli, V., 1991. Low-temperature CO_2 adsorption on metal oxides: spectroscopic characterization of some weakly adsorbed species. *Materials Chemistry and Physics*, *29*(1-4), pp.425-435.
16. Zaki, M.I., Vielhaber, B. and Knoezinger, H.+., 1986. Low-temperature carbon monoxide adsorption and state of molybdena supported on alumina, titania, ceria, and zirconia. An infrared spectroscopic investigation. *The Journal of Physical Chemistry*, *90*(14), pp.3176-3183.
17. Slostowski, C., Marre, S., Dagault, P., Babot, O., Toupance, T. and Aymonier, C., 2017. CeO_2 nanopowders as solid sorbents for efficient CO_2 capture/release processes. *Journal of CO_2 Utilization*, *20*, pp.52-58.
18. Yoshikawa, K., Kaneeda, M. and Nakamura, H., 2017. Development of Novel CeO_2-based CO_2 adsorbent and analysis on its CO_2 adsorption and desorption mechanism. *Energy Procedia*, *114*, pp.2481-2487.
19. Christensen, P.A., Attidekou, P.S., Egdell, R.G., Maneelok, S. and Manning, D.A.C., 2016. An in situ FTIR spectroscopic and thermogravimetric analysis study of the dehydration and dihydroxylation of SnO_2: the contribution of the (100),(110) and (111) facets. *Physical Chemistry Chemical Physics*, *18*(33), pp.22990-22998.

20. Binet, C., Badri, A. and Lavalley, J.C., 1994. A spectroscopic characterization of the reduction of ceria from electronic transitions of intrinsic point defects. *The Journal of Physical Chemistry*, *98*(25), pp.6392-6398.
21. Zaki, M.I., Hussein, G.A.M., El-Ammawy, H.A., Mansour, S.A.A., Polz, J. and Knözinger, H., 1990. Effect of foreign ion additives on ceria surface reactivity towards isopropanol adsorption and decomposition: An infrared investigation. *Journal of molecular catalysis*, *57*(3), pp.367-378.
22. Kulkarni, D. and Wachs, I.E., 2002. Isopropanol oxidation by pure metal oxide catalysts: number of active surface sites and turnover frequencies. *Applied Catalysis A: General*, *237*(1-2), pp.121-137.
23. Christensen, P.A., Mashhadani, Z.T., Md Ali, A.H.B., Carroll, M.A. and Martin, P.A., 2018. The Production of Methane, Acetone,"Cold" CO and Oxygenated Species from IsoPropyl Alcohol in a Non-Thermal Plasma: An In-situ FTIR Study. *The Journal of Physical Chemistry A*, *122*(17), pp.4273-4284.
24. Herzberg, G. Molecular Spectra and Molecular Structure: I Spectra of Diatomic Molecules, 2nd Edn., Van Nostrand, New York, 1950, 126 – 127.
25. van Zee, R.D., Foltz, M.F. and Moore, C.B., 1993. Evidence for a second molecular channel in the fragmentation of formaldehyde. *The Journal of chemical physics*, *99*(3), pp.1664-1673.
26. Heazlewood, B.R., Jordan, M.J., Kable, S.H., Selby, T.M., Osborn, D.L., Shepler, B.C., Braams, B.J. and Bowman, J.M., 2008. Roaming is the dominant mechanism for molecular products in acetaldehyde photodissociation. *Proceedings of the National Academy of Sciences*, *105*(35), pp.12719-12724.
27. Bowman, J.M., 2006. Skirting the transition state, a new paradigm in reaction rate theory. *Proceedings of the National Academy of Sciences*, *103*(44), pp.16061-16062.
28. Houston, P.L. and Kable, S.H., 2006. Photodissociation of acetaldehyde as a second example of the roaming mechanism. *Proceedings of the National Academy of Sciences*, *103*(44), pp.16079-16082.
29. Sivaramakrishnan, R., Michael, J.V. and Klippenstein, S.J., 2009. Direct observation of roaming radicals in the thermal decomposition of acetaldehyde. *The Journal of Physical Chemistry A*, *114*(2), pp.755-764.
30. Harding, L.B., Georgievskii, Y. and Klippenstein, S.J., 2009. Roaming radical kinetics in the decomposition of acetaldehyde. *The Journal of Physical Chemistry A*, *114*(2), pp.765-777.

31. Donaldson, D.J. and Leone, S.R., 1986. Photofragmentation dynamics of acetone of 193 nm: State distributions of the CH_3 and CO fragments by time-and wavelength-resolved infrared emission. *The Journal of chemical physics*, *85*(2), pp.817-824.
32. Chorkendorff, I. and Niemantsverdriet, J.W., 2017. *Concepts of modern catalysis and kinetics*. 3rd. ED., John Wiley & Sons, p 110.
33. Rodrigues, A., Tatibouët, J.M. and Fourré, E., 2016. Operando DRIFT spectroscopy characterization of intermediate species on catalysts surface in VOC removal from air by non-thermal plasma assisted catalysis. *Plasma Chemistry and Plasma Processing*, *36*(4), pp.901-915.
34. Jia, Z. and Rousseau, A., 2016. Sorbent track: Quantitative monitoring of adsorbed VOCs under in-situ plasma exposure. *Scientific reports*, *6*, p.31888.

Chapter 6. Conclusions and future work

The work reported in this thesis focussed on the comparison of the thermally- and non-thermal plasma-driven conversion of IsoPropyl Alcohol (IPA) in dinitrogen at Macor, SnO_2 and CeO_2. IPA was chosen as a model Volatile Organic Compound (VOC) and domestic air pollutant: Macor was selected as a dielectric as it was expected to be inactive, being comprised predominantly of the oxides of aluminium, magnesium and silicon: it also has a reasonable dielectric constant and is thermally stable. SnO_2 was chosen primarily as a result of the significant body of infrared data already available in Newcastle, and CeO_2 for its known activity towards the conversion of IPA. The primary underlying objective of the research was to elucidate the chemistries taking place in the plasma glow and at the plasma/catalyst interface and so determine if and to what extent plasma-driven and thermally-driven processes differed, and ultimately to try and predict what materials would be active in non-thermal plasma processes.

In-situ transmission and reflectance cells, the attendant high voltage power supplies and optical bench were designed, fabricated and commissioned and shown to facilitate the study of non-thermal plasma chemistry. Macor was employed in both cells, but arcing occurred when the Macor was coated with SnO_2 or CeO_2 in the transmission cell and hence these materials were studied only in the reflectance cell.

A wholly unexpected result of the work was the fact that Macor was highly active in the NTP-driven conversion of IPA. The reaction of IPA in the non-thermal plasma occurred in two reaction zones: one remote from the Macor surface in the bulk of the plasma and one at the plasma/Macor interface. In the former region, HCN, acetone, methane and "cold" CO molecules at ca. 115K were produced continuously and carried away by the gas stream, attaining a steady state in the plasma glow. These species were produced either via a common intermediate or in the same process: the acetone did not react further in the gas phase, but did react at the Macor (see below). Whilst nitrogen was (obviously) essential for the formation of HCN, the other species were still produced when it was replaced by Ar, with acetylene replacing HCN as a product. Whilst undesirable, the production of HCN showed that nitrogen fixation was at least taking place. The methane and cold CO were postulated as being produced by the fragmentation of acetaldehyde (the latter was not detected but its involvement was based on significant literature precedent) via a loose transition state and roaming mechanism in which the CH_3-C bond elongates and the methyl moiety moves around to capture the terminal

hydrogen atom of the acetaldehyde (or the C-H bond elongates and the H atom roams), the reaction bypassing the conventional activation energy barrier. Such mechanisms were predicted to be more common that first perceived, a supposition supported by increasing examples in the literature and by the thermal studies on the reaction of IPA at CeO_2 (see below). Methane and cold CO were not observed in the studies using SnO_2 and CeO_2 but was probably due to the fact that the SnO_2 and CeO_2 could only be employed in the reflectance cell: the IR pathlength in the reflectance cell was ca. 5x lower than in the transmission cell and hence the absorbances of the gas phase species too low to be detected. The production of methane and cold CO from IPA has not been observed before.

At the plasma/Macor interface, the acetone produced in the bulk underwent Pinacol and Aldol –type processes catalysed by the Macor to produce an oil comprising a polymethylacetylene-like polymer with C=O, C=C, CH_3 and O-H moieties and isophorone. Given the fact that no such oil was produced when nitrogen was replaced by argon, it is likely that the polymer also contained nitrogen functionalities, although the role of nitrogen may have been confined to energy transfer. The concentrations of acetylene, methane, cold CO and acetone in the argon-fed NTP showed a clear oscillating profile which has yet to be explained.

No reaction was observed in the thermal experiments employing Macor up to 600 °C: in complete contrast, IPA did not react in the NTP experiments using SnO_2 but underwent a series of thermally-driven reactions at the SnO_2 commencing with physisorption of the IPA at room temperature in two distinct forms differentiated probably via their adsorption on different crystal facets. On heating, the IPA was partially desorbed whilst the remainder converted to two forms of isopropoxide: further heating produced acetone via adsorbed enolate and finally carbon dioxide. This study showed the power of infrared spectroscopy to elucidate mechanism.

In contrast to both Macor and SnO_2, conversion of IPA occurred in both the plasma-driven and thermally-driven experiments using CeO_2.

The presence of adventitious adsorbed carbonaceous species (carbonates, bicarbonates etc) had a significant inhibitory effect on the thermally-driven reaction of IPA, the inhibition decreasing with increasing pre-treatment of the samples. Interestingly, physisorbed CO_2 was observed at temperatures up to 600 °C due to their location in internal voids associated with Ce^{3+} species. IPA physisorbed on the CeO_2 at room temperature and was dehydrogenated to acetone on heating, the onset temperature for this process decreasing with increasing pre-treatment, i.e.

225 °C for the most pre-treated sample and 350 °C for the least pre-treated. Acetone production declined at temperatures > 400 °C, with the concommittant production of CO_2 being observed only for the most pretreated samples, suggesting that the active sites for CO_2 production were blocked by adsorbed carbonates.

At temperatures > 400 °C, methane and cold CO were produced, the onset temperature again decreasing with decreasing coverage of adsorbed carbonates. These species were not observed at SnO_2 or Macor and hence it appears that they were produced by a roaming mechanism, this time involving a surface-bound loose transition state.

All the CeO_2 samples exhibited a band at 2125 cm^{-1} which increased in intensity on heating and was attributed to Ce^{3+}: however, the role of these species in the observed chemistry remains obscure.

In the plasma-driven experiments using CeO_2, the products observed were essentially the same as those observed in the plasma experiments using Macor, i.e. a polymethylacetylene-like polymer and isophorone both produced via intermediate acetone, differing only in the relative amounts of the two products. The presence of adsorbed carbonates did not appear to inhibit the plasma reactions, but time did not allow the investigation of the effect of pre-treatment of the CeO_2 as in the thermal experiments. This work suggested that the coverage of the CeO_2 surface by the polymer and isophorone did not stop their formation, an observation supported by re-examination of the data obtained using Macor.

Future work should start with turning the reflectance cell through 180° to facilitate the use of catalyst powders and coatings. For safety reasons, this would require an external sample compartment, as well as a redesigned optical bench.

Clearly, an important question to answer is the why Macor exhibits such activity towards the plasma-driven conversion of IPA. In order to do this, additional analytical techniques should be employed, including GCMS to provide complementary, quantitative information, to determine what component, or combination of components, produce the polymer and isophorone. This could be achieved by investigating if and to what extent simpler materials can effect the same chemistry as Macor, eg. Al_2TiO_5 and $MgTiO_3$ with and without SiO_2.

The effect of the surface structure (different crystal facets) of active catalysts such be investigated with respect to the activity and selectivity of catalysed NTP processes via the identification of intermediates and their distribution and behaviour as a function of catalyst surface structure and compared to the analogous, thermally-driven systems.

The effect of the pre-treatment of the CeO_2 on the plasma-driven conversion of IPA should be investigated and the possible role of Ce^{3+} species elucidated to complete this work,

It is not clear from the work reported in this thesis that the liquid film produced at Macor and CeO_2 in the plasma-driven processes is entirely inert, and it would be informative to investigate the role of the liquid film. This would involve modifying the (upward facing) reflectance cell to include well-defined depressions and troughs to contain static and flowing liquids. Initially, the polymer + Isophorone would employ the liquid product, then the product diluted with suitable, inert solvents to decrease viscosity and then model liquids chosen for their properties including: dielectric constant (to exploit the discontinuity in electric field at the liquid/plasma interface), conductivity and viscosity.

In general, an understanding of the chemistry taking place in the bulk of the plasma would benefit from kinetic studies at the millisecond level, or better using time-resolved FTIR at timescales down to tens of ns. By identifying active intermediates and their lifetimes it may then be possible to employ appropriate theoretical modelling to produce valid, predictive models and so elucidate the mechanisms of the chemical conversions taking place. These models could then be used to identify new, effective catalysts and optimum experimental conditions for reactor design and development.

Finally, the work in this thesis wholly confirms the fact that possible catalysts for non-thermal driven catalytic processes cannot be identified based on materials active in thermally-driven processes. It also confirms the long-held belief that there are exciting and important chemistries waiting to be discovered using non-thermal plasma, and that infrared spectroscopy is an ideal tool to use to accomplish this.